Technische Universität München

Max-Planck-Institut für Physik
(Werner-Heisenberg-Institut)

Pulse Shapes and Surface Effects in Segmented Germanium Detectors

Daniel Lenz

Vollständiger Abdruck der von der Fakultät für Physik
der Technischen Universität München
zur Erlangung des akademischen Grades eines
Doktors der Naturwissenschaften (Dr. rer. nat.)
genehmigten Dissertation.

Vorsitzender:		Univ.-Prof. Dr. Alejandro Ibarra
Prüfer der Dissertation:	1.	Hon.-Prof. Allen C. Caldwell, Ph.D.
	2.	Univ.-Prof. Dr. Tobias Lachenmaier

Die Dissertation wurde am 15. März 2010
bei der Technischen Universität München eingereicht und
durch die Fakultät für Physik am 24. März 2010 angenommen.

Abstract:

It is well established that at least two neutrinos are massive. The absolute neutrino mass scale and the neutrino hierarchy are still unknown. In addition, it is not known whether the neutrino is a Dirac or a Majorana particle.

The GERmanium Detector Array (GERDA) will be used to search for neutrinoless double beta decay of ^{76}Ge. The discovery of this decay could help to answer the open questions. In the GERDA experiment, germanium detectors enriched in the isotope ^{76}Ge are used as source and detector at the same time. The experiment is planned in two phases. In the first, phase existing detectors are deployed. In the second phase, additional detectors will be added. These detectors can be segmented.

A low background index around the Q value of the decay is important to maximize the sensitivity of the experiment. This can be achieved through anti-coincidences between segments and through pulse shape analysis.

The background index due to radioactive decays in the detector strings and the detectors themselves was estimated, using Monte Carlo simulations for a nominal GERDA Phase II array with 18-fold segmented germanium detectors.

A pulse shape simulation package was developed for segmented high-purity germanium detectors. The pulse shape simulation was validated with data taken with an 19-fold segmented high-purity germanium detector. The main part of the detector is 18-fold segmented, 6-fold in the azimuthal angle and 3-fold in the height. A 19th segment of 5 mm thickness was created on the top surface of the detector. The detector was characterized and events with energy deposited in the top segment were studied in detail. It was found that the metalization close to the end of the detector is very important with respect to the length of the of the pulses observed. In addition indications for n-type and p-type surface channels were found.

Zusammenfassung:

Es ist bekannt, dass mindestens 2 Neutrinos Masse haben. Die absolute Skala der Neutrinomassen und die Hierarchie der Neutrinos sind aber noch immer unbekannt. Ausserdem weiss man nicht, ob Neutrinos Dirac oder Majorana Teilchen sind.

Das GERmanium Detector Array (GERDA) wird benutzt, um nach neutrinolosem Doppelbetazerfall von ^{76}Ge zu suchen. Die Entdeckung dieses Zerfalls könnte die offenen Fragen beantworten. Im GERDA Experiment werden mit dem Isotop ^{76}Ge angereicherte Germaniumdetektoren gleichzeitig als Quellen und Detektoren genutzt. Für das Experiment sind zwei Phasen geplant. In der ersten Phase werden existerende Detektoren eingesetzt. In der zweiten Phase werden zusätzliche, neue Detektoren hinzugefügt. Diese neuen Detektoren können segmentiert sein.

Ein niedriger Untergrundindex in dem Bereich des Q Wertes ist wichtig, um die Sensitivität des Experimentes zu maximieren. Ein niedriger Untergrundindex kann durch Antikoinzidenzen zwischen Segmentsignalen und durch Pulsformanalyse erreicht werden.

Der Untergundindex aufgrund von radioaktiven Zerfällen in den Detektoraufhängungen und in den Detektoren wurde für ein nominales Phase II array mit 18-fach segmentierten Germaniumdetektoren mihilfe von Monte Carlo Simulationen abgeschätzt.

Eine Pulsformsimulation für 18-fach segmentierte hochreine Germaniumdetektoren wurde entwickelt. Die Pulsformsimulation wurde mit Daten, die mit einem segmentierten Germaniumdetektor genommen wurden evaluiert. Der Hauptteil des Detektors wurde 18-fach segmentiert, 3-fach in der Höhe und 6-fach in dem azimuthalen Winkel. Ein 19. Segment mit 5 mm Dicke wurde an der Oberseite des Detektors geschaffen. Der Detektor wurde charakterisiert und Ereignisse mit Energiedeposition in dem 19. Segment wurden genau studiert. Es wurde herausgefunden, dass die Metallisierung nahe der Stirnflächen des Detektors sehr wichtig ist bezüglich der Länge der beobachteten Pulse. Zusätzlich wurden Hinweise auf die Existenz von Oberflächenkanälen gefunden.

Contents

1. Introduction

The neutrino was postulated by Pauli in 1930 as a very light, neutral particle to save energy and angular momentum conservation in nuclear beta decay. In 1934, Fermi constructed a new theory describing beta decay. Since then, the neutrino was assumed to be a charge- and massless Dirac particle. In 1938, shortly after Fermi's new theory was established, Furry pointed out that the neutrino could also be a Majorana particle [1], i.e. its own anti-particle. In 1939, Furry published a paper about the possibility of neutrinoless double beta decay [2], assuming the neutrino to be a Majorana particle. It was not until 1956 that neutrinos were observed directly [3]. The interpretation of the solar neutrino deficit as a consequence of neutrino oscillations requires that neutrinos have finite masses. Since only mass differences can be determined from oscillation measurements, the absolute neutrino mass scale is still unknown. Furthermore, the question whether the neutrino is a Dirac or a Majorana particle remains open.

Today, three ways are used to infer the absolute neutrino mass. An upper limit on the sum of the neutrino masses can be derived from structure formation in the early universe. The limits are model dependent, but an upper bound of the order of 1 eV was established. The exact measurement of the endpoint of the spectrum of tritium beta decay sets an upper limit of 2.3 eV [4,5] on the electron neutrino mass. Experiments on neutrinoless double beta decay set limits on the effective Majorana neutrino mass from which limits of the electron neutrino mass are deduced. These are on the order of 2 eV.

The first experimental searches for neutrinoless double beta decay date back to the 1950s. A multitude of experiments using different isotopes has been conducted since then. The best effective Majorana mass limits are from the Heidelberg-Moscow [6] and IGEX [7] experiments. Both experiments used the germanium isotope ^{76}Ge. Since germanium is a semiconductor, it is used as source and detector at the same time, yielding intrinsically a high efficiency. The main limitation of these experiments is the background index.

The GERmanium Detector Array, GERDA [8], is designed for the search for neutrinoless double beta decay of ^{76}Ge. It is under construction in the Gran Sasso National Laboratory (LNGS) in Italy. The background index, b, targeted is of the order of $10^{-2}\mathrm{cts}/(\mathrm{keV}\cdot\mathrm{kg}\cdot\mathrm{y})$ in the first phase of the experiment and of $10^{-3}\mathrm{cts}/(\mathrm{keV}\cdot\mathrm{kg}\cdot\mathrm{y})$ in the second. The background is kept small by minimizing the amount of radioactivity close to the detectors, by large passive shields and in the second phase potentially by the usage of segmented germanium detectors. The targeted limit on the effective Majorana neutrino mass is about 110 meV at 90% C.L. in Phase II.

To reach this sensitivity, b has to be below $10^{-3}\mathrm{cts}/(\mathrm{keV}\cdot\mathrm{kg}\cdot\mathrm{y})$ and the detectors have to be very well understood. Techniques have been developed to suppress background events, such as the segmentation of the germanium detectors and pulse shape analysis, i.e. the analysis of the time response of the detectors. The anti-coincidences of segments to discriminate background events is a robust technique. In contrast, pulse shape analysis always strongly depends on the samples used to train any discrimination method. The available data samples are never purely signal-like or background-like. In addition, the signal-like events in those samples are not distributed homogeneously throughout the detector.

One goal was to develop and evaluate a detailed pulse shape simulation. The simulated pulses can then be used as a controllable input to pulse shape analyses. The pulse shape simulation was evaluated with data taken with an 19-fold segmented n-type high purity germanium detector operated in a vacuum cryostat.

A second goal was to study effects appearing close to the surface of germanium detectors. Therefore, the 19-fold segmented germanium detector, "Super Siegfried", was procured with a single, 5 mm thick, segment on top, which was used to study surface effects.

Furthermore, the background index due to radioactive decays in the detectors and detector strings, expected for the second phase of the GERDA experiment, was estimated using Monte Carlo methods.

The thesis is structured as follows: In Chapter 2 an overview of the current status of neutrino physics is given. In addition, ways to measure the neutrino mass are presented.

In Chapter 3 and Chapter 4, double beta decay and some general experimental considerations for double beta decay experiments are reviewed. In addition, past and future double beta decay experiments are discussed.

In Chapter 5, the concepts of background reduction in the GERDA experiment, the GERDA experiment and its status as of Sept. 2009 are presented.

In Chapter 6, the different mechanisms of interactions of radiation with matter in the energy range important for this thesis are described. The properties of semiconductor- and especially of germanium-detectors are described in Chapter 7.

The background index due to radioactive decays in the detectors and in the detector strings for a nominal GERDA Phase II array was estimated using Monte Carlo simulations. This is presented in Chapter 8. In Chapter 9, the influence of angular correlations between deexcitation photons from the decay of ^{60}Co onto the GERDA background index is investigated.

The newly developed pulse shape simulation is described in Chapter 10. The evaluation of the pulse shape simulation with data taken with the 19-fold segmented n-type high purity germanium detector is explained in Chapter 12.

In Chapter 11 the 19-fold segmented Super Siegfried detector is characterized. The properties of events happening close to the top surface are closely investigated in Chapter 14.

2. Neutrinos

After Pauli's postulation of the neutrino, most people believed that neutrinos were massless. Many experimental observations confirmed that view. The standard theoretical description of particles and interactions, the *Standard Model of particle physics* (SM) reflects this. The SM describes the elementary particles and the electro-weak and strong forces in the framework of gauge theory. Its development started in the 1960ies by Glashow, Salam and Weinberg [9–11]. An accumulation of observations finally established that neutrinos mix and oscillate and thus, that they are massive. These observations are discussed in this chapter. Two popular ways to describe the theoretical implications are briefly reviewed. In section 2.4, methods to measure the neutrino mass and current mass limits are summarized.

2.1. The Standard Model Neutrino

Three so called families are known in the SM. Each family contains a leptonic doublet consisting of a charged lepton and a neutral neutrino. Their flavors are electron (e), muon (μ) and tau (τ):

$$\begin{pmatrix} e^- \\ \nu_e \end{pmatrix} \qquad \begin{pmatrix} \mu^- \\ \nu_\mu \end{pmatrix} \qquad \begin{pmatrix} \tau^- \\ \nu_\tau \end{pmatrix}. \tag{2.1}$$

The number of families is not predicted by the SM. However, analyses of the decay-width of the Z^0-boson [12,13] reveal, that only three different types of light neutrinos exist. The V-A structure of the weak interaction requires that the leptonic doublets are left-handed. In addition there are right-handed singlets not taking part in weak interactions,

$$\begin{pmatrix} l^- \\ \nu_l \end{pmatrix}_L \quad , \quad l_R \,. \tag{2.2}$$

Neutrinos are implemented in the SM as massless, left-handed Dirac particles. Right-handed neutrinos are not included in the SM. The lepton number, L, is conserved in each family.

2.2. Neutrino Oscillations

If neutrinos have mass, there is a spectrum of neutrino mass eigenstates ν_i. The neutrino flavor eigenstates ν_α with $\alpha = e, \nu, \tau$ are mixtures of the mass eigenstates and can be written

as

$$|\nu_\alpha\rangle = \sum_i U^\star_{\alpha,i} |\nu_i\rangle, \tag{2.3}$$

with U being a unitary matrix, called Pontecorvo-Maki-Nakagawa-Sakta (PMNS) matrix. To calculate the time evolution of a neutrino created in state $|\nu_\alpha\rangle$, the Schrödinger equation is applied to the $|\nu_i\rangle$ components of $|\nu_\alpha\rangle$, since propagation is described in mass eigenstates:

$$|\nu_i(\tau_i)\rangle = e^{-im_i\tau_i}|\nu_i(0)\rangle, \tag{2.4}$$

with m_i being the mass of ν_i and τ_i being the time in the frame of reference of ν_i. Rewriting the phase in terms of time t and distance travelled L in the laboratory frame and assuming a highly relativistic neutrino, $t \approx L$, results in

$$e^{-im_i\tau_i} = e^{-i(E_i - p_i)L}, \tag{2.5}$$

where E_i and p_i are the energy and momentum of the neutrino mass eigenstate ν_i. Assuming furthermore, that ν_α is produced with a definite momentum, that all mass eigenstates ν_i have a common momentum, p, and that the masses are small compared to the momentum, $E_i = \sqrt{p_i^2 + m_i^2} \approx p + \frac{m_i^2}{2p}$ holds and the evolution of the state can be described by

$$|\nu_\alpha(L)\rangle \approx \sum_i U^\star_{\alpha,i} e^{-i(m_i^2/2E)L}|\nu_i\rangle, \tag{2.6}$$

where $E \approx p$ is the average energy of the various mass eigenstates of the neutrino. Inverting Eq. (2.3) and inserting it into Eq. (2.6) results in

$$|\nu_\alpha(L)\rangle \approx \sum_\beta \left[\sum_i U^\star_{\alpha,i} e^{-i(m_i^2/2E)L} U_\beta\right] |\nu_\beta\rangle. \tag{2.7}$$

A neutrino created in state $|\nu_\alpha\rangle$ travelling a distance L becomes a superposition of all flavors. The probability to find the neutrino in the flavor state $|\nu_\beta\rangle$ after it traveled a distance L is $|\langle\nu_\beta|\nu_\alpha(L)\rangle|^2$.

2.2.1. Formalism for Two Flavors

The previously derived formulas are now applied to the case of two neutrino flavors. The unitary matrix U can be written as a standard rotation matrix

$$U = \begin{pmatrix} \cos\Theta & \sin\Theta \\ -\sin\Theta & \cos\Theta \end{pmatrix}, \tag{2.8}$$

where Θ is the one mixing angle. For a non-zero mixing angle, the probability to change the flavor of a neutrino $P(\nu_\alpha \to \nu_\beta)$ is

$$P(\nu_\alpha \to \nu_\beta) = \sin^2 2\Theta \sin^2\left(\Delta m_{12}^2 \frac{L}{4E}\right), \tag{2.9}$$

with $\Delta m^2_{12} = |m^2_1 - m^2_2|$. This formula is given in natural units and is valid in vacuum. In real units it becomes

$$P(\nu_\alpha \to \nu_\beta) = \sin^2 2\Theta \sin^2 \left(1.27 \Delta m^2_{12}[\mathrm{eV}^2] \frac{L[\mathrm{km}]}{E[\mathrm{GeV}]} \right). \tag{2.10}$$

The probability to change the flavor depends on the value of Θ and the value of Δm^2_{12}. Furthermore, it depends on the neutrino energy and the distance traveled between source and detector. For fixed values of E and Δm^2_{12}, the probability to detect a neutrino emitted as ν_α as ν_β is changing periodically with the distance L travelled. This is where the name "neutrino oscillation" comes from.

2.2.2. Formalism for Three Flavors

For three neutrino flavors, one possible parameterization of the unitary matrix U is

$$U = \begin{pmatrix} 1 & 0 & 0 \\ 0 & c_{23} & s_{23} \\ 0 & -s_{23} & c_{23} \end{pmatrix} \begin{pmatrix} c_{13} & 0 & s_{13}e^{-i\delta} \\ 0 & 1 & 0 \\ -s_{13}e^{i\delta} & 0 & c_{13} \end{pmatrix} \begin{pmatrix} c_{12} & s_{12} & 0 \\ -s_{12} & c_{12} & 0 \\ 0 & 0 & 1 \end{pmatrix} \begin{pmatrix} e^{\frac{i\alpha_1}{2}} & 0 & 0 \\ 0 & e^{\frac{i\alpha_2}{2}} & 0 \\ 0 & 0 & 1 \end{pmatrix}, \tag{2.11}$$

with s_{ij} being the sines, c_{ij} being the cosines of the three mixing angles, δ being the Dirac CP violating phase and α_i the Majorana phases. The term $e^{i\delta}$ is always accompanied by s_{13}, such that small values of θ_{13} could make it impossible to observe CP violating effects in the lepton sector. The terms in α_i are only important if the neutrino is a Majorana particle. Overall, there are eight free parameters to describe neutrino oscillations; three mixing angles, two mass differences (the third one is constrained) and three CP violating phases. The probability of observing a neutrino, emitted as ν_α having travelled a distance L in vacuum as ν_β becomes

$$\begin{aligned} P(\nu_\alpha \to \nu_\beta) = \delta_{\alpha\beta} \quad &- \quad 4 \sum_{i>j} Re(U^\star_{\alpha i} U_{\beta i} U_{\alpha j} U^\star_{\beta j}) \sin^2(\Delta m^2_{ij} \frac{L}{4E}) \\ &+ \quad 4 \sum_{i>j} Im(U^\star_{\alpha i} U_{\beta i} U_{\alpha j} U^\star_{\beta j}) \sin(\Delta m^2_{ij} \frac{L}{4E}) \cos(\Delta m^2_{ij} \frac{L}{4E}), \end{aligned} \tag{2.12}$$

with Δm_{ij} being the mass difference of the neutrino eigenstates i, j and E being the average energy of the mass eigenstates.

2.2.3. Solar Neutrinos

The sun is a main sequence star in the phase of stable hydrogen burning. It produces ν_e from nuclear fusion reactions where the combined effective reaction can be written as

$$4p \to {}^4He + 2e^+ + 2\nu_e,$$

with an average neutrino energy $\langle E_{\nu_e} \rangle \approx 0.6$ MeV. The reactions producing neutrinos and the resulting fluxes on earth according to the BS05(OP) model, the so called *Standard Solar Model* (SSM) [14], are given in Tab. 2.1. The fluxes expected on earth as a function of the energy are shown in Fig. 2.1. Here, neutrino oscillations are not taken into account.

Reaction	Abbr	Flux ($cm^{-2}s^{-1}$)
$pp \rightarrow de^+\nu$	pp	$5.99(1.00 \pm 0.01) \cdot 10^{10}$
$pe^-p \rightarrow d\nu$	pep	$1.42(1.00 \pm 0.02) \cdot 10^{8}$
$^3He\,p \rightarrow {}^4He\,e^+\nu$	hep	$7.93(1.00 \pm 0.16) \cdot 10^{3}$
$^7Be\,e^- \rightarrow {}^7Li\,\nu + (\gamma)$	^{7}Be	$4.84(1.00 \pm 0.11) \cdot 10^{9}$
$^8B \rightarrow {}^8Be^\star\,e^+\nu$	^{8}B	$5.69(1.00 \pm 0.16) \cdot 10^{6}$
$^{13}N \rightarrow {}^{13}C\,e^+\nu$	^{13}N	$3.07(1.00^{+0.31}_{-0.28}) \cdot 10^{8}$
$^{15}O \rightarrow {}^{15}N\,e^+\nu$	^{15}O	$2.33(1.00^{+0.33}_{-0.29}) \cdot 10^{8}$
$^{17}F \rightarrow {}^{17}O\,e^+\nu$	^{17}F	$5.84(1.00 \pm 0.52) \cdot 10^{6}$

Table 2.1.: Reactions producing neutrinos in the sun and their abbreviations. The fluxes on earth are predicted by the BS05(OP) model [14] without neutrino oscillations.

A widely used unit in solar neutrino experiments is the *Solar Neutrino Unit* (SNU), where

$$1\ \text{SNU} = 10^{-36}\text{captures per target atom per second.} \tag{2.13}$$

In 1968, Davis *et al.* published the first measurement of the solar neutrino flux [15]. A tank filled with 600 tons of C_2Cl_4 was used to detect solar neutrinos by the reaction

$$^{37}Cl + \nu_e \rightarrow {}^{37}Ar + e^-. \tag{2.14}$$

The threshold for this reaction is $E_\nu > 814$ keV, implying that the dominant part of the neutrinos observed originates from the ^{8}B process, but also the ^{7}Be, pep, ^{13}N and ^{15}O processes contribute. The ^{37}Ar created in the capture process is instable with a half-life of $T_{1/2} = 34.8$ days. After an exposure time of $(2-3) \cdot T_{1/2}$, the ^{37}Ar was extracted chemically and the number of ^{37}Ar atoms were counted using low background proportional counters. The measured rate was $2.56 \pm 0.16(\text{stat.}) \pm 0.16(\text{syst.})$ SNU. This was about a third of the expected SSM neutrino flux. This was the birth of the "solar neutrino problem". Many years later, the gallium based experiments GALLEX, GNO and SAGE confirmed the neutrino deficit, using a similar reaction on gallium:

$$^{71}Ga + \nu_e \rightarrow {}^{71}Ge + e^-. \tag{2.15}$$

This reaction has an energy threshold of only 233 keV and is, thus, sensitive to the pp neutrino contribution, providing the highest flux. The unstable ^{71}Ge was chemically extracted

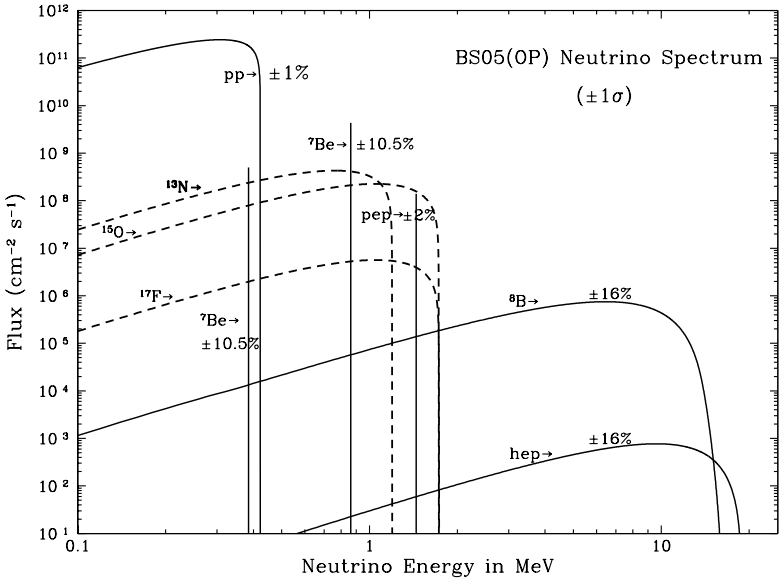

Figure 2.1.: Energy dependent flux of the solar neutrinos on earth as predicted by the SSM [14].

Experiment	Measured ν_e Flux [SNU]
GALLEX	$76.4 \pm 6.3\,(\text{stat.})\,^{+4.5}_{-4.9}\,(\text{syst.})$
GNO	$62.9^{+5.5}_{-5.3}\,(\text{stat.})\,\pm 2.5\,(\text{syst.})$
SAGE	$70.8^{+5.3}_{-5.2}\,(\text{stat.})\,^{+3.7}_{-3.2}\,(\text{syst.})$

Table 2.2.: Results of the measurements of the solar electron neutrino flux from the gallium experiments GALLEX [16], GNO [17] and SAGE [18].

from the gallium and counted. The three experiments yielded comparable results (Tab. 2.2). All three experiments see significantly less than the predicted 126 ± 6 SNU [19]. However, the factor 3 from Davis *et al.* was not reproduced, hinting at an energy dependence of the phenomenon.

In the 1980ies, the Kamiokande (and later the Super Kamiokande) experiment published their first measurements of the solar neutrino flux. Kamiokande was a water Čerenkov experiment using neutrino electron (νe) scattering ($\nu_x + e^- \rightarrow \nu_x + e^-$) as the detection method. The scattered electron produces Čerenkov light which is detected by photo multipliers. The direction of the scattered electron is correlated with the direction of the incoming neutrino. Using this information, it was possible for the first time to identify the sun as the source of the neutrinos [20]. Unfortunately, Kamiokande had a high energy threshold of about 7 MeV (5 MeV for Super Kamiokande) and was, thus, mainly sensitive to the low flux of ^{8}B neutrinos. In principle, (νe) scattering occurs for all neutrino flavors. However, for electron neutrinos there are additional charged current interactions which actually

dominate. The total cross section for ν_μ e or ν_τ e scattering compared to the one of ν_e e is

$$\sigma(\nu_{\mu,\tau}\,e) \approx \sigma(\nu_e\,e)/6,$$

making (Super) Kamiokande sensitive to ν_e predominantly. The ^{8}B neutrino flux measured by the Super Kamiokande collaboration is $(2.38 \pm 0.05(\text{stat.})^{+0.16}_{-0.15}(\text{sys.})) \cdot 10^6 \text{cm}^{-2}\text{s}^{-1}$ [21]. The measured flux is again significantly less (about 40%) than the predicted SSM flux (see Tab. 2.1).

It was attempted to change the solar model, to account for the observed low neutrino count rates. In most non-SSMs the core temperature of the sun was reduced by about 5%, as this would reduce the neutrino flux to the measured values. Unfortunately, other solar properties would change and would not be in agreement with observations any longer. In addition, the effect would not be energy dependent, i.e. the reduction should be approximately the same for all experiments. It was not possible to construct a solar model which could account for the low solar neutrino fluxes and, at the same time, other observed properties. A detailed review is found in [22].

In 1999, the Sudbury Neutrino Observatory (SNO) started data taking. SNO used a kiloton of ultra-pure heavy water (D_20) in a spherical vessel surrounded by ultra pure water. It measured the ^{8}B neutrino spectrum with neutrino nucleon (νN) and νe scattering using charged current (CC) as well as neutral current (NC) interactions:

$$\begin{aligned}
\nu_i + d &\rightarrow \nu_i + p + n && \text{NC}\,(\nu N), && (2.16)\\
\nu_e + d &\rightarrow e^- + p + p && \text{CC}\,(\nu_e N), && (2.17)\\
\nu_i + e &\rightarrow \nu_i + e && \text{NC}\,(\nu e), && (2.18)\\
\nu_e + e &\rightarrow \nu_e + e && \text{CC}\,(\nu_e e). && (2.19)
\end{aligned}$$

The experimental situation for ν_i e scattering was similar to the one of Kamiokande. The NC (νN) reactions are equally sensitive to all neutrino flavors. The signal coming from the reaction is a 6.25 MeV γ-ray due to neutron capture in deuterium. The threshold of this reaction is 2.2 MeV. However, the neutron capture efficiency is low and the γ energy is close to the detection threshold of 5 MeV. This results in an overall low detection probability. To enhance the neutron capture efficiency and the γ-ray energy to 8.6 MeV, two tons of NaCl were added to the heavy water in a second experimental phase. The measured fluxes were [23] :

$$\begin{aligned}
&4.94 \pm 0.21^{+0.38}_{-0.34} \cdot 10^6 \text{cm}^{-2}\text{s}^{-1} && \text{NC}\,(\nu\,\text{N}),\\
&1.68 \pm 0.06^{+0.08}_{-0.09} \cdot 10^6 \text{cm}^{-2}\text{s}^{-1} && \text{CC}\,(\nu_e\,\text{N}),\\
&2.35 \pm 0.22 \pm 0.15 \cdot 10^6 \text{cm}^{-2}\text{s}^{-1} && (\nu e).
\end{aligned} \qquad (2.20)$$

The CC $(\nu\,\text{N})$ and the νe scattering results favor independently a too low ν_e flux compared to the prediction from the SSM (see Tab. 2.1). The (νe) scattering result is in agreement

with the previous Super-Kamiokande result. The flux as measured by the NC $(\nu\mathrm{N})$ reaction is in agreement with the ν_e flux predicted by the SSM of $5.69(1.00 \pm 0.16) \cdot 10^6$ cm^{-2}s^{-1}. This confirmed the picture that electron neutrinos are properly produced in the sun, but change their flavor before reaching the earth.

2.2.4. Atmospheric Neutrinos

Cosmic rays hitting the atmosphere create a particle shower in which pions are created. Charged pions decay predominantly into a muon and a muon neutrino. A deficit in the measured muon neutrino flux compared to the expectation was found by two experiments. In the IMB experiment (1986) [24], a detector built to search for proton decay, the deficit was attributed to unknown systematic errors. The second experiment was Kamiokande. It had the capability to clearly distinguish ν_e and ν_μ induced events and attributed the deficit to "some as-yet-unaccounted-for physics such as neutrino oscillation" [25]. In 1994, Kamiokande discovered that the flux of high energy muon neutrinos depends on the zenith angle which is best explained by ν_μ oscillating to ν_τ [26]. Small mixing angles (as in the quark sector) were expected at that time. Since the ν_μ deficit observed required large mixing angles, this evidence was not considered convincing. Finally, in 1998, an analysis of the flux and zenith-angle distribution of the upward coming muons in Kamiokande [27] showed clearly, that the data is consistent with $\nu_\mu \rightarrow \nu_\tau$ oscillation and that the mixing angle is close to maximum. The competing theories of neutrino decoherence and neutrino decay could be excluded by Super-Kamiokande [28] in 2004, using $L/E = 500$ km/GeV data exhibiting the first oscillation minimum. This minimum cannot be explained by neutrino decay which is excluded by 3.4σ. The neutrino decoherence model is disfavored even more strongly [27].

2.2.5. Reactor Neutrinos

Electron anti-neutrinos from the decay of radioactive fission products inside a nuclear reactor provide a good opportunity to study neutrino oscillation in a controlled environment. Optimized detector positions (L/E) to the reactors allow to probe different neutrino oscillation parameter ranges. All reactor experiments are so called disappearance experiments. These experiments measure the $\bar{\nu}_e$ flux. Since $\bar{\nu}_e$ oscillate to $\bar{\nu}_X$, a deficit in the $\bar{\nu}_e$ flux is expected.

The KamLAND Experiment

The KamLAND experiment consists of a one kiloton ultra-pure liquid-scintillator detector and is located at the Kamiokande site in Japan. It is a long-baseline reactor neutrino experiment with a flux-weighted average distance of 180 km to several reactors. KamLAND uses the inverse beta decay reaction

$$\bar{\nu}_e + p \rightarrow e^+ + n \tag{2.21}$$

to detect anti-neutrinos. The observed signal are two 511 keV photons from positron annihilation and a delayed 2.2 MeV γ-ray from neutron capture on a proton. Using this signature in coincidence reduces the background significantly. KamLAND detects anti-neutrinos with an energy $E_{\bar{\nu}_e} > 1.8\,\mathrm{MeV}$ and is sensitive down to $\Delta m^2_{12} \sim 10^{-5}\,\mathrm{eV}^2$. KamLAND published first results in 2003 [29] with an exposure of $162\,\mathrm{ton}\cdot\mathrm{yr}$. The ratio of observed to expected (assuming no oscillation) events was

$$\frac{N_{\mathrm{obs}} - N_{\mathrm{BG}}}{N_{\mathrm{NoOsc}}} = 0.611 \pm 0.085(\mathrm{stat}) \pm 0.041(\mathrm{syst}). \tag{2.22}$$

This deficit is a clear sign for neutrino oscillation. A precise analysis of the latest KamLAND and solar neutrino data using the formalism for the oscillation between two neutrino flavors gave $\Delta m^2_{12} = 7.59^{+0.21}_{-0.21} \times 10^{-5}\mathrm{eV}^2$ and $\tan^2\theta_{12} = 0.47^{+0.06}_{-0.05}$ [30].

Chooz, Double Chooz, Daya Bay and RENO

Special interest in the PMNS matrix element U_{e3} exists, since θ_{13} mediates the effect of CP violation in the lepton sector. Several experiments try to measure this angle. The Chooz experiment is already completed and gives at the moment the most stringent limits on θ_{13}. The Chooz detector was located $\approx 1000\,\mathrm{m}$ away from two reactor cores. It had an average value of $L/E \sim 300\,\mathrm{MeV/m}$. To detect neutrino interactions, the same signature as in the KamLAND experiment was used. No evidence (at 90% C.L.) for neutrino oscillation in the $\bar{\nu}_e$ disappearance mode was seen. Oscillations of $\bar{\nu}_e \to \bar{\nu}_X$ are excluded for $\Delta m^2_{13} \geq 8 \cdot 10^{-4}\ \mathrm{eV}^2$ at maximum mixing and $\sin^2(2\theta_{13}) \geq 0.17$ at large Δm^2_{13} values [31]. To reduce the systematic uncertainty, a second, similar detector closer to the reactors is under construction. This experiment is called Double-Chooz and aims at a sensitivity of $\sin^2 2\theta_{13} < 0.02 - 0.03$ at 90%C.L. within 3 years of measuring time. The same double-detector concept will be used by two other experiments: RENO which aims at the same sensitivity as Double-Chooz and Daya Bay which has a targeted sensitivity of $\sin^2 2\theta_{13} < 0.01$ at 90%C.L.. All three double-detector experiments are currently under construction.

2.2.6. Accelerator Neutrinos

Neutrino beams consist predominantly of muon (anti-)neutrinos from pion decay produced in interactions of protons on a nuclear target. Neutrinos from accelerators offer the chance of disappearance as well as appearance experiments. As the energy of the neutrinos and the beam intensity is typically higher than in reactor experiments, higher Δm^2 regions and smaller mixing angles are probed. Long-baseline experiments allow precision measurements.

Disappearance Experiments

Two disappearance experiments, K2K and MINOS used a two detector (close-far) concept. Both measured a ν_μ deficit in the far detector. MINOS, with a baseline of $\approx 735\,\mathrm{km}$ measured $\Delta m^2_{23} = 2.43 \pm 0.13 \cdot 10^{-3}\,\mathrm{eV}^2$ and set a lower limit on $\sin^2(2\theta_{23}) > 0.90$ at 90% C.L.

in a two flavor analysis. Furthermore, neutrino decay and decoherence was excluded at the 3.7σ and 5.7σ level [32], respectively. K2K published results compatible with those of MINOS [33].

Appearance Experiments

Karmen and LSND [34] were two experimental searches for $\bar{\nu}_e$ in an $\bar{\nu}_\mu$ beam. Karmen did not see $\bar{\nu}_e$ appearance and set a two flavor based limit on Δm^2_{12} and $\sin^2(2\theta_{12})$ [35]. LSND in contrast found $\bar{\nu}_e$ events. Interpreting these events as caused by two flavor neutrino oscillation gives $\Delta m^2_{12} \approx 0.2 - 10\,\mathrm{eV}^2$ and $\sin^2(2\theta_{12}) \approx 0.003 - 0.03$ [36]. This is not compatible with solar and atmospheric neutrino experiments. The scenario of sterile neutrinos could bring their result in accordance with other experimental results. The recently completed experiment MiniBooNE at Fermilab partially rejected the sterile neutrino scenario [37].

Two further experiments, T2K [38] and NOvA [39], are under construction to search for ν_e appearance, to measure θ_{13} and the CP violating phase δ. Another appearance experiment is Opera [40]. Opera was built to search for ν_τ in a ν_μ beam coming from CERN. Observing neutrino appearance would be an important step to prove the correctness of neutrino oscillation, since so far only disappearances were observed.

2.2.7. Interpretation of Experimental Results

Evidence of neutrino oscillation has been established through a large number of experiments, using solar, atmospheric, reactor and accelerator neutrinos. From the six free parameters that determine the properties of neutrino oscillation (Eq. (2.11)) all Δm^2_{ij} and angles have been measured or constrained (Tab. 2.3). Only the CP violating phase δ is completely unknown due to the smallness of θ_{13}. The mechanism of neutrino mixing and oscillation

Parameters	Best fit value
$\Delta m^2_{21}(10^{-5}\,\mathrm{eV}^2)$	$7.65^{+0.23}_{-0.20}$
$\lvert\Delta m^2_{31}\rvert(10^{-3}\,\mathrm{eV}^2)$	$2.40^{+0.12}_{-0.11}$
$\sin^2\theta_{12} \approx \sin^2\theta_\odot$	$0.34^{+0.022}_{-0.016}$
$\sin^2\theta_{23} \approx \sin^2\theta_{atm}$	$0.50^{+0.07}_{-0.06}$
$\sin^2\theta_{13}$	$0.01^{+0.016}_{-0.011}$

Table 2.3.: Summary of the neutrino oscillation parameters. The parameters are obtained from a three-flavor analysis of all data from solar, atmospheric, reactor (KamLAND and CHOOZ) and accelerator (K2K and MINOS) experiments [41].

is well understood and the large mixing angle (LMA) scenario has been established. Still

unknown are the absolute masses of the neutrino eigenstates and whether the neutrino hierarchy is normal ($m_3 > m_1$) or inverted ($m_3 < m_1$). The mechanism describing neutrino mixing is equivalent to the one in the quark sector. However, the Cabibbo-Kobayashi-Maskawa (CKM) quark mixing matrix is almost diagonal with significant mixing only between the first and second generation, while the PMNS matrix has large off-diagonal elements. This might indicate a completely different underlying physical mechanism. Many competing theories try to explain the structure of the PMNS matrix [42–44].

2.3. Massive Neutrinos

Massive neutrinos are not part of the original SM. But there is an easy way to introduce neutrino masses by adding right handed Dirac neutrino singlets to the theory. However, other possibilities are favored by some theoretical physicists. Most fashionable is the introduction of Majorana neutrinos. Within this framework the small absolute masses of neutrinos can be explained and lepton number violating processes are allowed. The two approaches will be briefly reviewed in the following.

2.3.1. Dirac Neutrino Mass Term

Dirac fermions are described using 4-component spinors ψ, obeying the Dirac equation

$$(i\gamma^\mu \frac{\partial}{\partial x^\mu} - m)\psi = 0, \tag{2.23}$$

where γ^μ are the Dirac matrices and m is the fermion mass. Applying the chiral projection operators, defined as

$$P_{L,R} = \frac{1}{2}(1 \mp \gamma_5), \tag{2.24}$$

$$\tag{2.25}$$

to a spinor ψ results in the chiral projections $\psi_{L,R}$. Each spinor can be written as a sum of its chiral projections

$$\psi = \underbrace{(P_L + P_R)}_{=1}\psi = \psi_L + \psi_R. \tag{2.26}$$

A Dirac mass term in the Lagrangian is written as

$$\mathcal{L} = m_D\overline{\psi}\psi = m_D(\overline{\psi}_L\psi_R + \overline{\psi}_R\psi_L), \tag{2.27}$$

with $m_D = \lambda v$, where λ is the Yukawa coupling to the Higgs-field and v is the vacuum expectation value (VEV) of the Higgs field. The adjoint spinor $\overline{\psi}$ is given by $\overline{\psi} = \psi^\dagger\gamma^0$. Eq. (2.27) demonstrates that right handed particles are needed to allow for a Dirac mass term in the Lagrangian.

The neutrino masses are much smaller than those of the corresponding charged leptons. This is possible if the Yukawa couplings λ are very small. But there is no fundamental reason why the couplings of the neutrinos should be so much smaller (at least $O(10^6)$) than those of the charged leptons. Such a strong mass splitting is, in addition, not observed in the quark sector. Therefore, the approach of Majorana neutrinos is often preferred to account for the smallness of the neutrino masses.

2.3.2. Majorana Neutrino Mass Term

Introducing the charged conjugate spinor $\psi^c = i\gamma^2\gamma^0\overline{\psi}^\dagger$, there are three more spinor combinations which behave like Lorentz-scalars and which allow to include a mass term in the Lagrangian in a gauge invariant way. Note, that such terms are only allowed for electrically neutral particles, since otherwise charge conservation is violated. The three possible spinor combinations are $\overline{\psi}^c\psi^c$, $\overline{\psi}\psi^c$ and $\overline{\psi}^c\psi$. For neutral particles, $\overline{\psi}^c\psi^c$ is identical to $\overline{\psi}\psi$ which generates Dirac masses. $\overline{\psi}\psi^c$ and $\overline{\psi}^c\psi$ are hermitian conjugates. In summary there is only one additional mass term to be considered,

$$\mathcal{L} = \frac{1}{2}\left(m_M\overline{\psi}\psi^c + m_M^\star\overline{\psi}^c\psi\right), \tag{2.28}$$

where m_M is a complex Majorana mass. Decomposing the spinors into their chiral components yields two hermitian mass terms,

$$\mathcal{L}^L = \frac{1}{2}m_L\left(\overline{\psi}_L\psi_L^c + \overline{\psi}_L^c\psi_L\right), \tag{2.29}$$

$$\mathcal{L}^R = \frac{1}{2}m_R\left(\overline{\psi}_R^c\psi_R + \overline{\psi}_R\psi_R^c\right), \tag{2.30}$$

where $m_{L,R}$ are left and right handed real Majorana masses. Since left handed neutrinos form a SU(2) doublet, the Majorana mass term Eq. (2.29) is not gauge-invariant and m_L is set to zero.

2.3.3. General Mass Term

The most general mass term allowed is a combination of Dirac and Majorana mass terms:

$$\begin{aligned} 2\mathcal{L} &= m_D\left(\overline{\psi}_R\psi_L + \overline{\psi}_L^c\psi_R^c\right) + m_R\overline{\psi}_R\psi_R^c + h.c. \\ &= \left(\overline{\psi}_L^c, \overline{\psi}_R\right)\begin{pmatrix} 0 & m_D \\ m_D & m_R \end{pmatrix}\begin{pmatrix} \psi_L \\ \psi_R^c \end{pmatrix} + h.c., \end{aligned} \tag{2.31}$$

where $h.c.$ is the hermitian conjugate. Only the ψ_L and ψ_R^c contribute to the known neutrino interactions and not ψ_R or ψ_L^c. The notation is changed to $\psi_L = \nu_L$, $\psi_L^c = \nu_L^c$ and $\psi_R = N_R$, $\psi_R^c = N_R^c$. With this notation Eq. (2.31) becomes

$$2\mathcal{L} = \left(\overline{\nu}_L^c, \overline{N}_R\right)\begin{pmatrix} 0 & m_D \\ m_D & m_R \end{pmatrix}\begin{pmatrix} \nu_L \\ N_R^c \end{pmatrix} + h.c.. \tag{2.32}$$

The mass eigenstates are obtained by diagonalizing the mass matrix. They are

$$\nu_l = \nu_L - \frac{m_D}{m_R} N_R^c, \tag{2.33}$$

$$\nu_h = N_R^c + \frac{m_D}{m_R} \nu_L, \tag{2.34}$$

with ν_l the light and ν_h the heavy neutrino eigenstate. ν_h is sometimes called sterile neutrino. Assuming that $m_R \gg m_D$, two mass eigenvalues m_l, m_h are obtained

$$m_l = \frac{m_D^2}{m_R} \qquad \text{and} \qquad m_h = m_R \left(1 + \frac{m_D^2}{m_R^2}\right) \approx m_R. \tag{2.35}$$

Thus, small observable masses m_l compatible with experiment are obtained for a suitably large Majorana mass m_R and a Dirac mass m_D of the order of the weak scale. This mechanism is known as the *seesaw* mechanism. The Lagrangian can now be rewritten as

$$2\mathcal{L} = -m_l \bar{\nu}_l^c \nu_l + m_h \bar{\nu}_h^c \nu_h + h.c.. \tag{2.36}$$

2.4. Measurement of Neutrino Masses

There are three major ways to experimentally determine the absolute neutrino mass. From cosmological observations, the sum of the three neutrino mass eigenstates m_ν^{cosmo} can be extracted. These limits on the sum of the neutrino masses is model dependent, but an approximate model independent limit can be derived. Another method is the precise measurement of the shape of the endpoint of the energy spectrum from single beta decay. This method is sensitive to the effective electron neutrino mass $\langle m_{\nu_e} \rangle$. Neutrinoless double beta decay experiments are sensitive to the effective Majorana mass of the neutrino $\langle m_\nu \rangle$ and will be addressed in section 3.2.

Cosmology

Cosmological observations are sensitive to

$$m_\nu^{\text{cosmo}} = \sum_i m_{\nu_i}. \tag{2.37}$$

They cannot distinguish between Dirac or Majorana neutrinos. To convert cosmic microwave background (CMB) data into a constraint on m_ν^{cosmo}, it is necessary to adopt a certain cosmological model, e.g. the *Standard Model of Cosmology* (SMC). This includes the assumption of a flat universe, i.e. the energy density of the universe is one:

$$\Omega = \Omega_\Lambda + \Omega_{CDM} + \Omega_B + \Omega_\nu = 1. \tag{2.38}$$

Here, Ω_Λ is the energy density due to the cosmological constant, Ω_{CDM} is the energy density of cold dark matter, Ω_B is the baryonic energy density and Ω_ν is the energy density

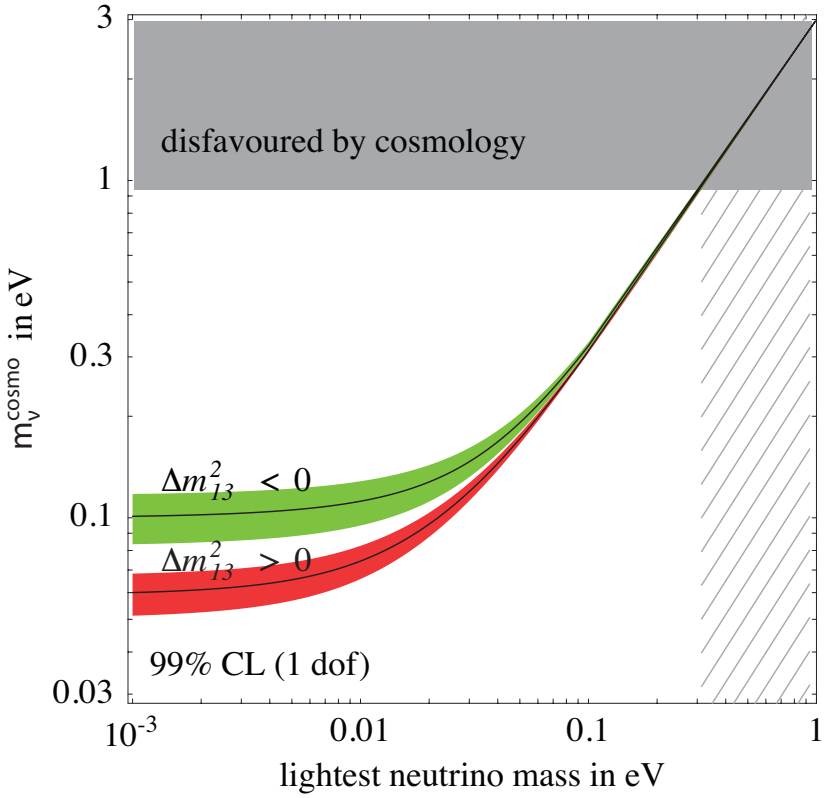

Figure 2.2.: Expected region of m_ν^{cosmo} (at 99% C.L.) from neutrino oscillation as a function of the lightest neutrino mass. The central lines show how the ranges would shrink if the best-fit values of oscillation parameters were confirmed with negligible uncertainties. The top gray band represents the limit $m_\nu^{cosmo} < 0.94\,\text{eV}$. The hatched region gives a limit on the lightest neutrino mass derived from the limit on m_ν^{cosmo}, taking into account the neutrino mass splitting observed in neutrino oscillation experiments. Figure adapted from [45].

of the neutrinos. The SMC is consistent with all observations. Fitting the Wilkinson Microwave Anisotropy Probe (WMAP) CMB anisotropy data within the framework of the SMC results in a 99% C.L. limit on $m_\nu^{cosmo} < 0.94\,\text{eV}$ [45], see Fig. 2.2. Taking into account different data sets and fitting different models results, in general, in limits of the order of $m_\nu^{cosmo} < 1\,\text{eV}$. The inclusion of data on the large scale structures (LSS) can narrow down the allowed masses of neutrinos. More precise measurements of the CMB anisotropy, as planned with the Planck satellite, will improve the mass limit.

In Fig. 2.2 m_ν^{cosmo} is shown as a function of the mass of the lightest neutrino eigenstate, taking into account the parameters extracted from neutrino oscillation experiments.

Beta Decay

The effective electron neutrino mass is

$$\langle m_{\nu_e} \rangle = \sqrt{\sum_i |U_{ei}|^2 m_i^2}, \tag{2.39}$$

where the sum is taken over all mass eigenstates and U_{ei} are the elements of the PMNS matrix. Note, that cancellation due to CP phases cannot happen, since only absolute values of the matrix elements U_{ei} enter. The value $\langle m_{\nu_e} \rangle$ can be measured in β decay experiments. The Dirac or Majorana nature of the neutrino cannot be inferred from such measurements The MAINZ [46] and the TROITSK [5] experiments measured the endpoint energy and the shape of the spectrum of tritium beta decay. The best limit was derived by the MAINZ experiment with $\langle m_{\nu_e} \rangle < 2.3\,\text{eV}$ (90% C.L.) [4]. The KATRIN experiment, currently under construction, will probe the effective electron neutrino mass down to 0.35 eV (at 90%C.L.) [47] using similar techniques as the MAINZ experiment. Fig. 2.3 shows the expected regions of $\langle m_{\nu_e} \rangle$ as a function of the mass of the lightest neutrino.

The effective muon and tau neutrino masses are defined analogously to $\langle m_{\nu_e} \rangle$. A limit on the effective muon neutrino mass was derived from decays of positively charged pions at rest, $\pi^+ \to \mu^+ \nu_\mu$. Since the pion mass m_{π^+} and the muon mass m_μ are known and the muon momentum, p_μ, can be measured, the effective muon neutrino mass can be constrained from

$$\langle m_{\nu_\mu} \rangle^2 = m_\pi^2 + m_\mu^2 - 2m_\pi \sqrt{p_\mu^2 + m_\mu^2}. \tag{2.40}$$

The derived limit is $\langle m_{\nu_\mu} \rangle < 0.17\,\text{MeV}$ (90% C.L.) [48]. An improvement of this limit could come from the planned experiment NuMass [49]. Using a similar approach the aimed sensitivity is $\langle m_{\nu_\mu} \rangle < 8\,\text{keV}$.

The effective tau neutrino mass can be constrained using tau decays in collider experiments. The best limit on the effective tau neutrino mass is $\langle m_{\nu_\tau} \rangle < 18.2\,\text{MeV}$ at 95% C.L. [50].

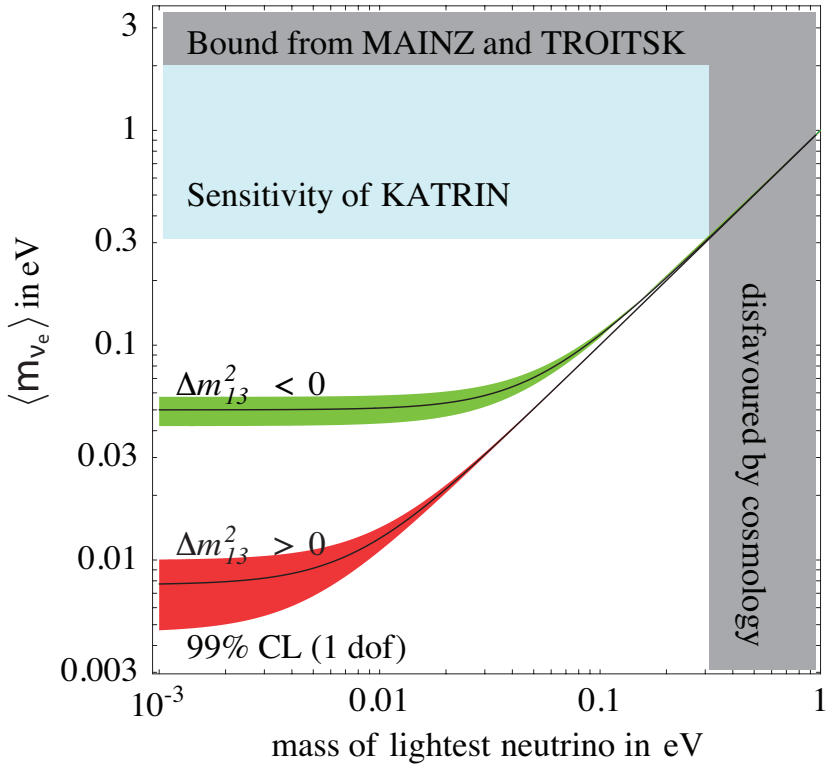

Figure 2.3.: Expected region for $\langle m_{\nu_e} \rangle$ (at 99% C.L.) from neutrino oscillation as a function of the mass of the lightest neutrino. The central lines represent the best-fit values of oscillation parameters. Dark shaded bands indicate the regions excluded by cosmology and the MAINZ and TROITSK experiments. The sensitivity of KATRIN is indicated as a light shaded band. Figure adapted from [45].

3. Double Beta Decay

Double beta decay is a rare, second order, weak process. A nucleus of charge Z and atomic number A decays into a daughter nucleus of charge $Z \pm 2$ and the same atomic number A. The change in Z depends on the type of beta decay. From here on $\beta^-\beta^-$ decay is considered, since the small phase space for $\beta^+\beta^+$ decays makes them even rarer. In the case of $\beta^-\beta^-$ decay two neutrons decay coherently into two protons. There are two possibilities:

$$2\nu\beta\beta: \quad (Z,A) \rightarrow (Z+2,A) + 2e^- + 2\bar{\nu}_e, \tag{3.1}$$

$$0\nu\beta\beta: \quad (Z,A) \rightarrow (Z+2,A) + 2e^-. \tag{3.2}$$

The first possibility Eq. (3.1) is called neutrino accompanied double beta decay ($2\nu\beta\beta$) and the second one Eq. (3.2) is called neutrinoless double beta decay ($0\nu\beta\beta$). In principle, double beta decay can occur in nearly every beta decaying isotope. But the competing single beta decay will make it impossible to observe double beta decays. Therefore, these types of decays are only observable if single beta decay is highly suppressed due to large angular momentum differences in initial and final state or if it is energetically forbidden. The latter is the case if the daughter nucleus is heavier than the mother nucleus, see Fig. 3.1, which only occurs for even-even nuclei due to their strong binding energy. About 35 candidate isotopes for double beta decay are known. In Sec. 3.1 is discussed $2\nu\beta\beta$ and 3.2 addresses $0\nu\beta\beta$.

3.1. Neutrino Accompanied Double Beta Decay

In $2\nu\beta\beta$ two electrons and two electron anti-neutrinos are emitted, see Eq. (3.1). The corresponding Feynman graph is shown in Fig. 3.2. Since it is a four body decay the total kinetic energy, the Q value of the $2\nu\beta\beta$, is shared between the four leptons. The two neutrinos cannot be detected. The energy spectrum of the two electrons is continuous. The maximum of the spectrum is approximately at $Q/3$. The $2\nu\beta\beta$ is allowed in the framework of the SM and has been observed for several isotopes. The decay rate of $2\nu\beta\beta$ decay is given by

$$\Gamma_{2\nu\beta\beta} = 1/T_{1/2}^{2\nu\beta\beta} = G_{2\nu}(Q,Z)|\mathcal{M}_{2\nu}|^2, \tag{3.3}$$

where $G_{2\nu}(Q,Z)$ is the phase space factor and $\mathcal{M}_{2\nu}$ is the nuclear matrix element. The phase factor $G_{2\nu}$ is very sensitive to Q; it scales with Q^{11}.

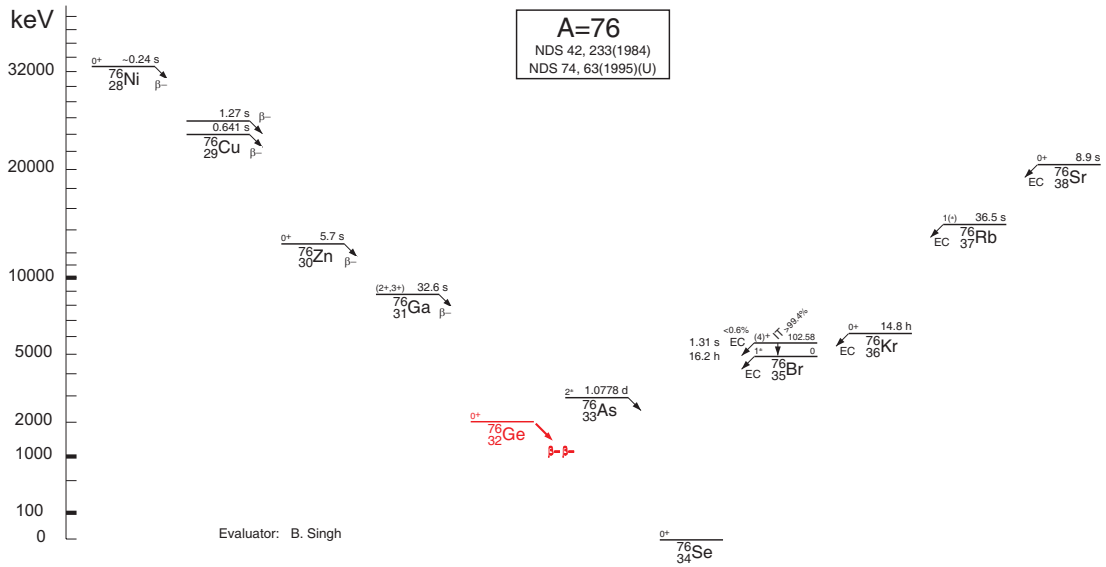

Figure 3.1.: Isobars for A=76 [51]. The isotope ^{76}Ge is stronger bound than the one of ^{76}As, but less strong bound than ^{76}Se. Therefore, ^{76}Ge cannot undergo single beta decay but double beta decay into ^{76}Se is possible.

3.2. Neutrinoless Double Beta Decay

Neutrinoless double beta decay is forbidden in the SM. It violates lepton number conservation by two units, $\Delta L = 2$. The observation of 0νββ would imply "physics beyond the standard model of particle physics". The immediate conclusion drawn from an observation of 0νββ would be that neutrinos are Majorana particles, i.e. their own anti-particles [52]. Furthermore, the neutrino has to be massive, since the helicity of the neutrino has to change during the process. Currently, 0νββ decay is the only experimentally feasible way to distinguish between Dirac and Majorana neutrinos.

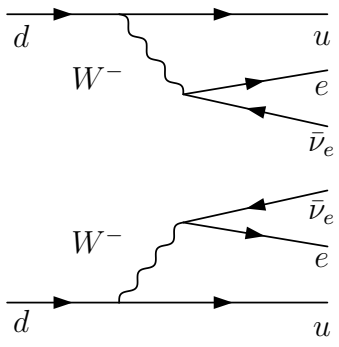

(a)

Figure 3.2.: Feynman diagram for 2νββ decay which is allowed in the SM.

3.3. Physics Potential of Neutrinoless Double Beta Decay

There are several possible mechanisms to mediate $0\nu\beta\beta$. Therefore, the observation of $0\nu\beta\beta$ decay might have an impact on many aspects of particle physics. The most commonly discussed mechanisms are the exchange of

- light Majorana neutrinos, see Fig. 3.3(a);
- (composite [53]) heavy Majorana neutrinos [54];
- SUSY particles in R-parity violating SUSY, see Fig. 3.3(b) and Fig. 3.3(c) [55];
- leptoquarks, see Fig. 3.3(d) and Fig. 3.3(e) [56].

There are also theoretical models which allow for small right handed currents in the weak interaction. In this case the exchanged neutrino could be massless since no helicity change is needed. It is difficult to distinguish between these scenarios. There have been suggestions to use angular correlations between the emitted electrons [57] to identify the realized mechanism but it is not possible to disentangle all models.

The most popular model is the exchange of light Majorana neutrinos. In this case, the neutrino has to be a massive particle. From here on, only the exchange of light Majorana neutrinos is considered unless stated otherwise. The decay rate of neutrinoless double beta decay is then given by

$$\Gamma_{0\nu\beta\beta} = 1/T_{1/2}^{0\nu\beta\beta} = G_{0\nu}(Q,Z)|\mathcal{M}_{0\nu}|^2\langle m_\nu\rangle^2, \tag{3.4}$$

with $G_{0\nu}$ denoting the phase space factor, which scales with Q^5, $\langle m_\nu\rangle$ being the effective Majorana neutrino mass and $\mathcal{M}_{0\nu}$ the nuclear matrix element for $0\nu\beta\beta$. The effective Majorana neutrino mass is the coherent sum over the neutrino mass eigenstates and their corresponding PMNS matrix elements:

$$\langle m_\nu\rangle = \left|\sum_i m_i U_{ei}^2\right| = \left|m_1 U_{e1}^2 + m_2 U_{e2}^2 e^{i(\alpha_2-\alpha_1)} + m_3 U_{e3}^2 e^{i(-\alpha_1-2\cdot\delta)}\right|. \tag{3.5}$$

The effective Majorana neutrino mass is different from the effective electron neutrino mass (Eq. (2.39)) observed in single beta decay experiments. Note, that cancellation can occur due to the CP phases in the effective Majorana neutrino mass.

3.4. Neutrino Mass Measurements from Neutrinoless Double Beta Decay

The observable quantity in neutrinoless double beta decay experiments is the decay rate. The decay rate is related to the effective Majorana neutrino mass via Eq. (3.4). To extract

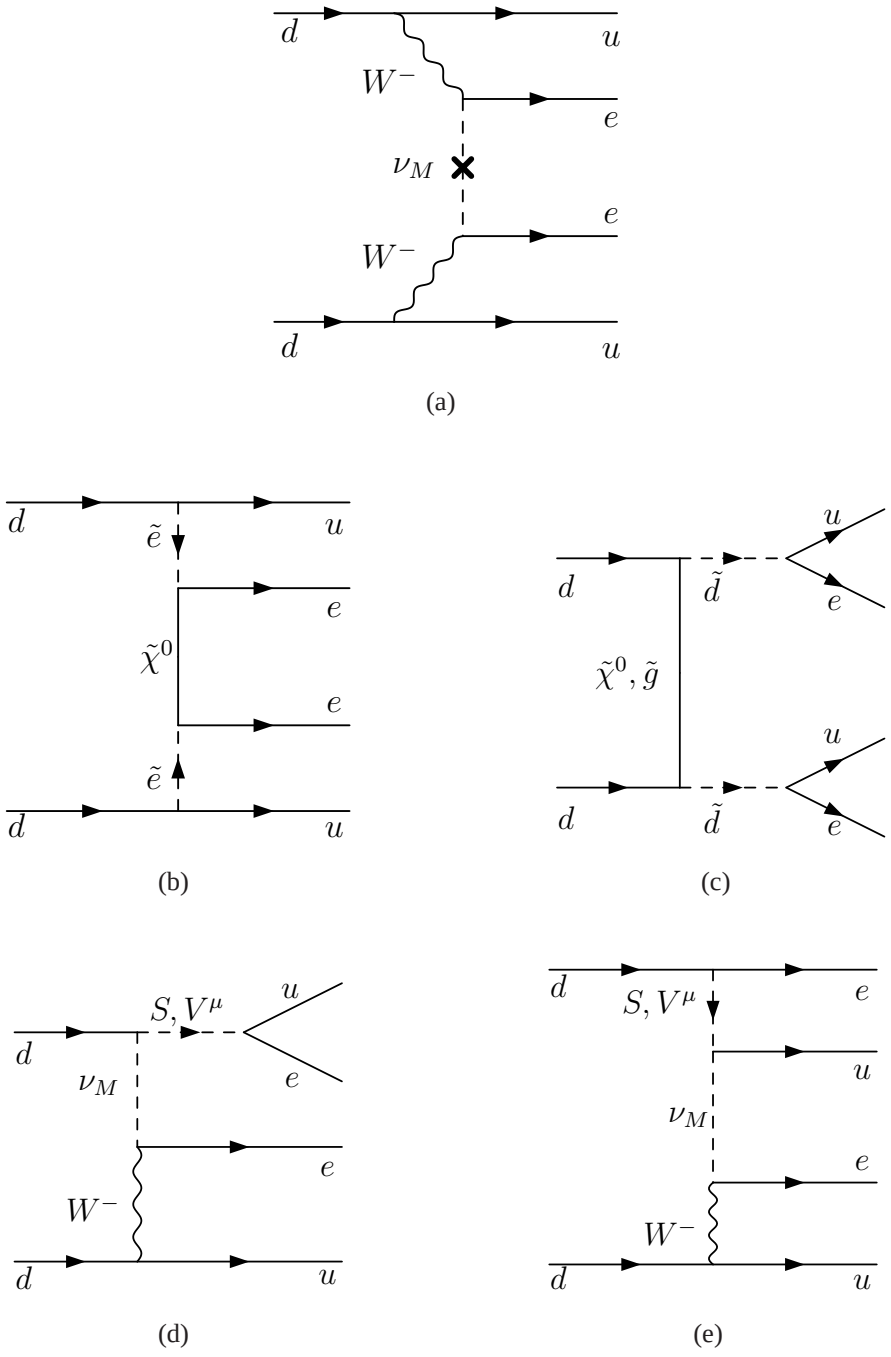

Figure 3.3.: Feynman diagrams for $0\nu\beta\beta$, mediated by (a) the exchange of a light Majorana neutrino ν_M,(b)(c) a neutralino $\tilde{\chi}^0$ or gluino $\tilde{g}$ in R-parity violating supersymmetric theories, or (d)(e) a light Majorana neutrino ν_M in combination with a leptoquark S, V^ν.

the effective Majorana neutrino mass, the quantities $G_{0\nu}(Q,Z)$ and $\mathcal{M}_{0\nu}$ have to be known. The phase space factor $G_{0\nu}(Q,Z)$ can be calculated reliably, but different values were obtained depending on the assumptions made; for a comprehensive review see [58]. The value of the nuclear matrix element $\mathcal{M}_{0\nu}$, is more uncertain. There are two competing descriptions of nuclei used for the prediction of nuclear matrix elements. One is the Interacting Shell Model (ISM) and the other one is the proton neutron - Quasi particle Random Phase Approximation (pn-QRPA). The resulting nuclear matrix elements agree for most elements within a factor of two or better [59,60]. The remaining disagreements, however, introduce the biggest uncertainty into the extraction of the effective Majorana neutrino mass from the decay rates.

The effective Majorana neutrino mass can be related to the lightest neutrino mass eigenstate, using the PMNS matrix parameters deduced from neutrino oscillation experiments. Fig. 3.4 shows the effective Majorana neutrino mass as a function of the lightest neutrino mass eigenstate. The outer curves represent the best fit and 3σ-uncertainty in the oscillation parameters. Normal as well as inverted hierarchy is shown. In the normal hierarchy scenario, the state corresponding to the largest mass contributes with a small mixing angle. If the mass of the lightest state is small, $\langle m_\nu \rangle$ is small as well. In contrast, in the inverted hierarchy, the heavy neutrinos contribute most and $\langle m_\nu \rangle$ is larger.

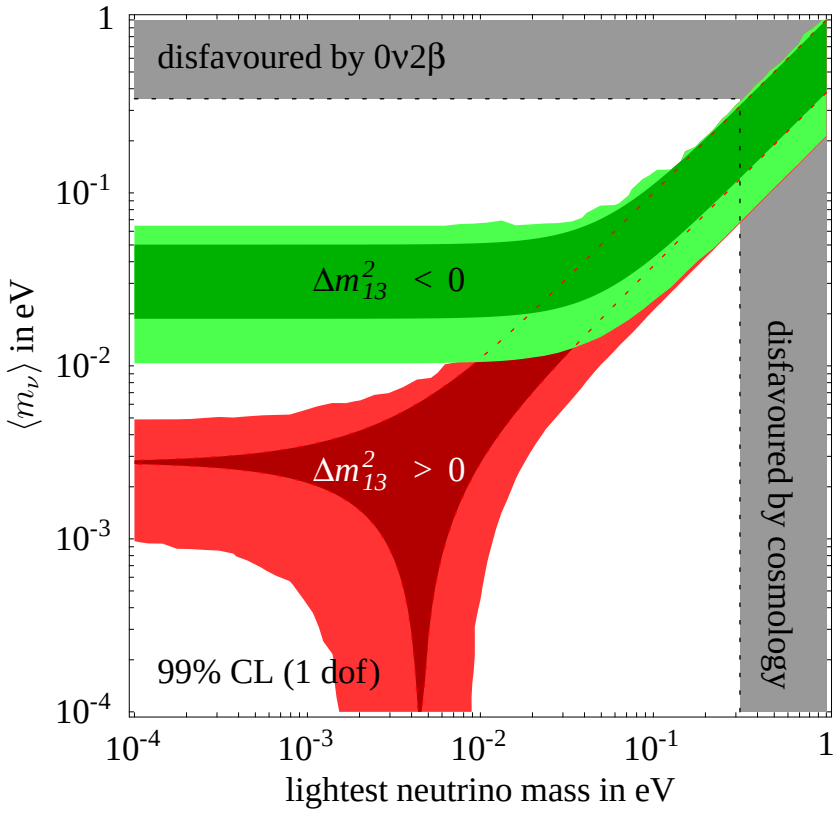

Figure 3.4.: Expected region (at 99% C.L.) from neutrino oscillations of the effective Majorana neutrino mass $\langle m_\nu \rangle$ as a function of the lightest neutrino mass. The darker area shows how the ranges would shrink if the best-fit value of oscillation parameters were confirmed with negligible uncertainties. The spread in the bands comes from the so far unconstrained CP violating phases. Figure adapted from [45].

4. Double Beta Decay Experiments

In neutrinoless double beta decay, two electrons are emitted and a Majorana neutrino is exchanged (Fig. 3.3(a)). The energy released is shared between the two electrons and can be measured; nuclear recoil can be neglected. The energy spectra of the two-electron-systems in $2\nu\beta\beta$ and $0\nu\beta\beta$ are shown in Fig. 4.1. The small peak at the Q value of the decay is due to $0\nu\beta\beta$.

4.1. Experimental Considerations

The expected number of signal events N_s from neutrinoless double beta decay is given by

$$N_s = M \cdot \frac{N_A}{M_A} \cdot \kappa \cdot \varepsilon_{sig} \cdot (1 - e^{-t \ln(2)/T_{1/2}}), \tag{4.1}$$

where M is the total source material mass in grams, N_A is Avogadro's number, M_A and κ are the atomic mass and the mass fraction of the isotope under study and ε_{sig} is the signal efficiency. $T_{1/2}$ is the half-life of the isotope under study and t is the measuring time.
Using a Taylor approximation for $e^{-t \ln(2)/T_{1/2}} = 1 + \frac{-t \ln(2)}{T_{1/2}}$ yields

$$\begin{aligned} N_s &= M \cdot \frac{N_A}{M_A} \cdot \kappa \cdot \varepsilon_{sig} \cdot \frac{t \ln(2)}{T_{1/2}}, \\ \Leftrightarrow \quad T_{1/2} &= \kappa \cdot \varepsilon_{sig} \cdot \ln(2) \frac{N_N \cdot t}{N_s}, \end{aligned} \tag{4.2}$$

with $N_N = M \cdot \frac{N_A}{M_A}$ being the total number of germanium nuclei. The expected number of background events is given by

$$N_b = b \cdot M \cdot t \cdot \delta E, \tag{4.3}$$

in terms of the background index b in counts$/(\mathrm{kg} \cdot \mathrm{keV} \cdot \mathrm{y})$ and the energy search window δE around the Q value. If the expected number of signal events N_s is smaller than the typical fluctuation in the numbers of background events $N_s < \sqrt{N_b}$, no signal can be extracted and only a limit on the half-life can be given. For larger N_b the sensitivity scales as

$$\kappa \cdot \varepsilon_{sig} \cdot \ln(2) \frac{N_N \cdot t}{\sqrt{N_b}} = \kappa \cdot \varepsilon_{sig} \cdot \ln(2) \cdot \frac{N_A}{M_A} \left(\frac{M \cdot t}{b \cdot \delta E} \right)^{1/2}. \tag{4.4}$$

If $N_b = 0$ the sensitivity scales linearly with t.

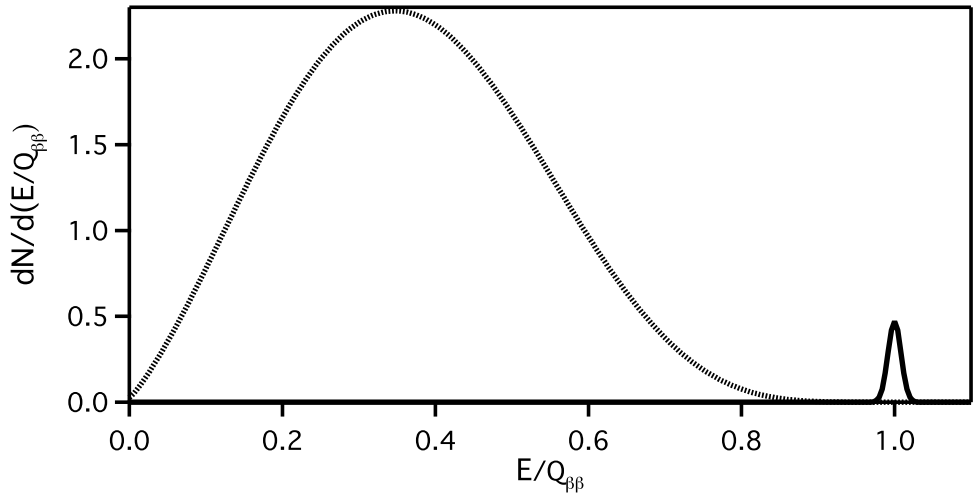

Figure 4.1.: Schematic drawing of the expected energy spectra from $2\nu\beta\beta$ and $0\nu\beta\beta$. The dashed continuous spectrum results from $2\nu\beta\beta$, whereas the peak at the end point of the $2\nu\beta\beta$ spectrum is due to $0\nu\beta\beta$ [61].

Some experimental guidelines can be gained from Eq. (4.4). Probing long half-lifes (or low effective Majorana masses) requires:

- a large product $M \cdot \kappa$;
- a high signal efficiency ε_{sig};
- a long measurement time t;
- a good energy resolution to allow for a small search window δE;
- and a low background index b.

In addition, the Q value of the decay should be as high as possible, since the phase space $G_{0\nu}$ scales with Q^5, see Eq. (3.4). The most energetic gamma line in natural radioactive decays is at $E = 2.614\,\mathrm{MeV}$. A Q value higher than this energy would significantly reduce the background from γ radiation.

4.2. Neutrinoless Double Beta Decay Experiments

The measurement of an energy spectrum is common to all double beta decay experiments. A peak is expected at the Q value of the decay. The width of the peak is determined by the energy resolution. A reasonable search window is chosen and the number of $0\nu\beta\beta$ signal events over background is extracted. If the energy resolution is not good enough the spectrum of $2\nu\beta\beta$ and $0\nu\beta\beta$ is fitted simultaneously. The number of $0\nu\beta\beta$ events is

Isotope	Q[MeV]	nat. Abundance[%]	$T_{1/2}^{2\nu\beta\beta}$ [y]	Properties
^{48}Ca	4.27	0.2	$(4.2 \pm 1.2) \cdot 10^{19}$	$CaWO_4$ scintillates
^{76}Ge	2.039	7.8	$(1.3 \pm 0.1) \cdot 10^{21}$	semiconductor and bolometer
^{70}Zn	1.001	0.6	–	CdZnTe is semiconductor
^{114}Cd	0.534	28.7	–	
^{116}Cd	2.809	7.5	$(3.2 \pm 0.3) \cdot 10^{19}$	$CdWO_4$ is scintillator
^{124}Sn	2.287	5.8	–	semiconductor
^{128}Te	0.868	31.7	$(7.2 \pm 0.3) \cdot 10^{24}$	TeO_2 is bolometer
^{130}Te	2.530	34.1	$(2.7 \pm 0.1) \cdot 10^{21}$	
^{136}Xe	2.480	8.9	$> 8.1 \cdot 10^{20} (90\% C.L.)$	is a scintillator
^{150}Nd	3.367	5.6	$7.0^{+11.8}_{-0.3} \cdot 10^{18}$	stays stable inside liquid scintillator

Table 4.1.: A selection of possible double beta decay isotopes. Given are the Q value and the natural abundance as well as the half-life of the $2\nu\beta\beta$ decay (if available) and some properties which make them experimentally interesting. Half-life values are all taken from [62].

extracted from deviations of the spectrum with respect to the $2\nu\beta\beta$ expectation near the endpoint. The properties of the isotope under investigation determines the experimental techniques. Selected isotopes and their properties are listed in Tab. 4.1. As explained above, all experiments try to optimize the sensitivity. This can be done in different ways. But all experimental approaches can be classified in two groups:

1. the source is used as detector, or
2. the source is not the detector.

4.2.1. The Source is the Detector

The big advantage of constructing a detector from the source material is that the electrons do not have to reach the detector and a high signal efficiency ε_{sig} is possible. Some of the materials used are semiconductors, allowing for very good energy resolution. The drawback of these detectors is that it is often difficult to reconstruct event topologies and thus, to actively reject background events or reveal the $0\nu\beta\beta$ mediating mechanism. A selected list of experiments using different isotopes and experimental techniques is now discussed.

Germanium is a low temperature semiconductor with very good intrinsic energy resolution. It has been used for many years in gamma spectroscopy. Germanium can be produced with extremely high purity, allowing for a low intrinsic background rate. Unfortunately, ^{76}Ge has a natural abundance of only 7.8% and has to be enriched, which makes it very expensive. Due to its low Q value, several gamma lines from natural radioactivity contribute to the background in ^{76}Ge experiments. Past experiments of this kind were the IGEX [7] and the Heidelberg-Moscow [6] experiments. These experiments are discussed in Sec. 4.3. Detectors from these experiments will be reused in the GERDA experiment [8]. A detailed description of the GERDA experiment is given in Chapter 5.

The Cobra experiment [63] uses CdZnTe as the source material. Cobra is special since five candidate isotopes are under study at the same time. The source material CdZnTe is a semiconductor which works at room temperature. However, the energy resolution (FWHM) is limited, only about 12 keV at 2.8 MeV. On the other hand, the CdZnTe detectors can be used as time projection chambers and thus have the chance to reconstruct event topologies. The Cobra experiment collected 4.34 kg days of data in a first underground run in the Gran Sasso National Laboratory (LNGS). Limits on the half-life (at 90 % C.L.) of $1.19 \cdot 10^{17}$ y and $2.68 \cdot 10^{15}$ y for the isotopes ^{64}Zn and ^{120}Te, respectively could be obtained [64].

The CUORE experiment [65] will use TeO_2 bolometers with an energy resolution of about 8 keV at 2614 keV. The detectors will be operated at a temperature between 8 mK and 10 mK. The isotope ^{130}Te is the $0\nu\beta\beta$ decay candidate. The ^{130}Te abundance is relatively high, about 34.1 %. The CUORE experiment is planned for 988 $5x5x5\,\mathrm{cm}^3$ bolometers, each with a mass of 760 g. The expected background rate is $0.01 \mathrm{counts}/(\mathrm{keV}\cdot\mathrm{kg}\cdot\mathrm{y})$ yielding a predicted sensitivity to $T_{1/2}^{0\nu\beta\beta}(^{130}\mathrm{Te}) \approx 2.5 \cdot 10^{26}$y. A test facility called CUORICINO has been successfully tested with 40.7 kg TeO_2 [66]. The CUORE experiment is under construction in the underground facility of the LNGS.

EXO is an experiment based on liquid Xenon. The double beta decay candidate isotope is ^{136}Xe. The electrons created in Xenon will drift under the influence of an applied electric field towards charge collection wires and the energy is measured. The scintillation light emitted by the Xenon is also detected. From the time difference of the two signals the interaction position can be reconstructed. EXO will use 80% enriched liquid Xenon. Xenon is advantageous to reduce background, since it is easy to purify. Furthermore, it is dense and thus has a strong self-shielding effect. The Q value of ^{136}Xe is 2.48 MeV, above most of the lines of natural radioactivity. The ultimate goal of EXO is, in addition, to tag and trap the resulting barium daughter nucleus [67].

Another project suggested is SNO++. A liquid scintillator is foreseen to replace the heavy water used in the SNO experiment. The main goal is to measure pep neutrinos from the sun. However, dissolving the isotope ^{150}Nd into the liquid scintillator would allow SNO++ to search for double beta decay of ^{150}Nd. The Q value of ^{150}Nd is 3.37 MeV. Adding 1% natural Nd to the liquid scintillator will provide 560 kg of ^{150}Nd. The SNO++ detector will have a limited energy resolution. Therefore, the main background to $0\nu\beta\beta$ decay will be $2\nu\beta\beta$. Simulations of the expected background spectra show that no peak at the endpoint of the energy spectrum would be visible. However, the energy spectrum from $2\nu\beta\beta$ would be distorted enough to extract a signal.

4.2.2. The Source is not the Detector

The experiment NEMO [68] was an experiment where source and detector were different. It was run in several phases, the last phase being NEMO-3 [69]. The concept of the exper-

iment is to hang foils made from material of possible double beta decay isotopes inside a tracking detector. The foils are very thin such that the two electrons have a high probability to escape the foils. The escaped electrons are tracked in gas filled drift cells operated in Geiger mode inside a magnetic field. The energy and time of flight are measured with a calorimeter made from plastic scintillator. The full three dimensional tracks of the electrons and their energies are reconstructed. NEMO offers the opportunity to reconstruct event kinematics and angular distributions. An additional advantage of this detector concept is that several source materials can be studied at the same time.

The energy resolution of NEMO is rather limited, ranging between 11 % to 14.5 % (FWHM) at 1 MeV to about 8% FWHM at 3 MeV. In contrast to "source is detector" experiments, NEMO has a low efficiency to detect the decay. Therefore, large amounts of source materials are needed. But since the foils have to be very thin it is very difficult to use large masses which requires a large detector. A proposed NEMO-like experiment, Super-NEMO will be operated with only one $0\nu\beta\beta$ candidate to provide a strong source. A detector for approximately 100 kg of ^{150}Nd or ^{82}Se and an improved energy resolution of $\sim 7\%$ FWHM at 1 MeV is under study [70].

4.3. The Heidelberg-Moscow and IGEX Experiments

The Heidelberg-Moscow and the IGEX experiments were both build to search for neutrinoless double beta decay of the Germanium isotope ^{76}Ge. They were the most sensitive germanium $0\nu\beta\beta$ experiments so far. In both experiments, high purity p-type crystals were operated underground in conventional copper cryostats with lead shields.

The IGEX experiment was carried out in the Canfranc underground laboratory in Spain. From 1991 to 2000 data with a total exposure of $8.8\,\mathrm{kg}\cdot\mathrm{y}$ ($117\,\mathrm{mole}\cdot\mathrm{y}$) were collected. The background count rate was $0.17\,\mathrm{cts}/(\,\mathrm{keV}\cdot\mathrm{kg}\cdot\mathrm{y}\,)$. The corresponding energy spectrum is shown in Fig. 4.2(a). A limit on the half-life of $T_{1/2}^{0\nu\beta\beta} > 1.6\cdot 10^{25}\,\mathrm{y}$ at 90% C.L. was deduced [71].

The Heidelberg-Moscow experiment was operated from 1990 to 2003. The total exposure was $71.1\,\mathrm{kg}\cdot\mathrm{y}$. The data shown in Fig. 4.2(b) correspond to data taken between August 1990 and May 2000. In this dataset a background index in the around the Q value of $0.19\pm 0.01\,\mathrm{cts}/(\,\mathrm{keV}\cdot\mathrm{kg}\cdot\mathrm{y}\,)$ was achieved and a limit on the half-life of $T_{1/2}^{0\nu\beta\beta} \geq 1.9\cdot 10^{25}$y at 90% C.L. was set [72]. In a later publication, parts of the Heidelberg-Moscow collaboration re-analyzed the data and claimed a signal with corresponding $T_{1/2}^{0\nu\beta\beta} = 1.61\cdot 10^{25}\,\mathrm{y}$ [73]. Later, this claim was renewed after an analysis of the full dataset from 1900-2003 [74]. The claim of evidence for $0\nu\beta\beta$ is controversial [75–80].

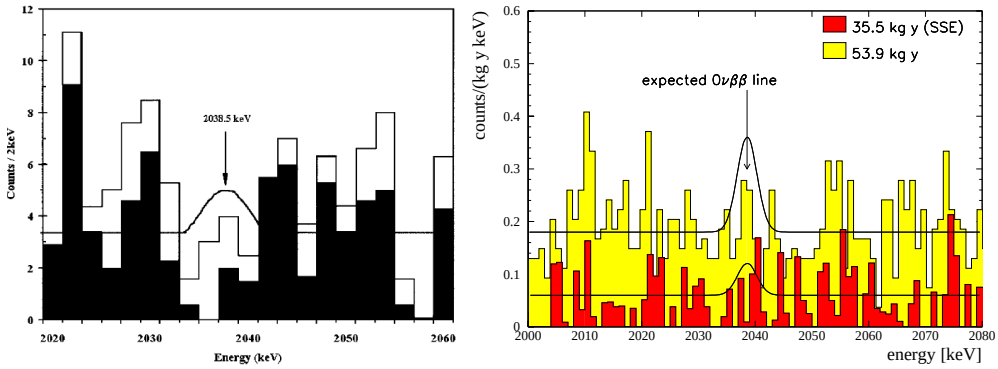

(a) (b)

Figure 4.2.: (a) The energy spectrum around the Q value of ^{76}Ge measured by the IGEX experiment for a total exposure of 8.8 kg · y is shown [71]. The open and black histograms correspond to the energy spectrum without and with the application of pulse shape analysis, respectively. The Gaussian curve represents the 90 % C.L. upper limit on the number of 0νββ events. (b) The corresponding energy spectrum measured in the Heidelberg-Moscow experiment. The total exposure was 53.9 kg · y and 35.5 kg · y. The yellow histogram represents all data and the red one represents single site events, identified by pulse shape analysis [72]. The black curves represent the excluded signals with $T_{1/2}^{0\nu\beta\beta} \geq 1.3 \cdot 10^{25}$ y (90% C.L.) and $T_{1/2}^{0\nu\beta\beta} \geq 1.9 \cdot 10^{25}$ y (90% C.L.), respectively.

5. GERDA Experiment

The GERmanium Detector Array, GERDA [8], is an experiment designed for the search of $0\nu\beta\beta$ of ^{76}Ge. It is currently under construction in the underground laboratory of the Gran Sasso National Laboratory (LNGS) in L'Aquila, Italy. The main improvement compared to previous $0\nu\beta\beta$ experiments is the reduction of the background index by up to a factor of 100 in the region of interest (ROI) around the Q value of the decay. The main features of GERDA are the operation of bare germanium detectors directly submerged in liquid argon and the minimization of other high-Z materials in the vicinity of the detectors.

The first goal of the GERDA collaboration is to test the claim of discovery of $0\nu\beta\beta$ made by parts of the Heidelberg-Moscow collaboration [73,74]. The GERDA experiment is designed to be operated in two phases. In the first phase (Phase I), p-type high purity germanium detectors enriched in ^{76}Ge from IGEX and the Heidelberg-Moscow experiment are reused. With an exposure of approximately $15\,\mathrm{kg}\cdot\mathrm{y}$ at a background index of $10^{-2}\mathrm{counts}/(\mathrm{keV}\cdot\mathrm{kg}\cdot\mathrm{y})$, the claim will be tested [81]. In the second phase (Phase II) additional detectors and a lower background index of $10^{-3}\mathrm{counts}/(\mathrm{keV}\cdot\mathrm{kg}\cdot\mathrm{y})$ will enhance the sensitivity and a limit of $\langle m_\nu \rangle \leq 110\,\mathrm{meV}$ at 90% C.L. can be set. These new detectors could be segmented n-type detectors, as studied for this thesis.

The concept of GERDA is based on ideas from [82] and is explained in section 5.1. The technical realization is explained subsequently and in section 5.3, the status of construction as of September 2009 is described.

5.1. The GERDA Concept

As explained in Sec. 4.1, the requirements to probe long half-lifes are a large number of source nucleii, high signal efficiency ε_{sig}, good energy resolution ΔE (FWHM) and a low background index b in the ROI. Eight detectors with a total mass of 17.9 kg made from germanium enriched up to $\kappa = 0.86$ in ^{76}Ge are used in Phase I. In Phase II additional detectors with a similar mass fraction of ^{76}Ge will be deployed. Since the source is the detector a high signal detection efficiency of up to $\varepsilon_{sig} = 87\%$ [81] will be reached. Germanium detectors have a very good energy resolution, usually much better than $\Delta E \leq 5\,\mathrm{keV}$ at 2 MeV.

The sensitivity of low background experiments is limited by the background index. The experience from recent experiments shows that the dominant source of background was

radioactive decay. The goal is to significantly reduce this source. Additional sources will be muons and muon induced neutrons and the decay of cosmogenical produced isotopes inside the detectors. The strategy to reduce the background index is to:

- construct the experiment underground;
- install a muon veto;
- install large multi layer shields;
- achieve an ultrapure environment;
- have little high-Z material close to the detectors;
- store and handle the detector in an ultra clean environment.

5.2. Technical Realization

The experiment consists of a steel cryostat inside a water tank embedded in a superstructure with a cleanroom on top, see Fig. 5.1.

5.2.1. Hall A of the Gran Sasso Underground Laboratory

The location of the GERDA experiment is Hall A of the underground laboratory of the Gran Sasso National Laboratory. The average overburden of rock is approximately 3400 meters of water equivalent. Cosmic ray protons and neutrons are blocked completely. The flux of cosmic ray muons is reduced compared to the surface by a factor of 10^6 and the expected rate is 1 muon $\mathrm{m}^{-2}\,\mathrm{h}^{-1}$ [83].

5.2.2. Muon Veto

An active muon veto was constructed to reduce the background index from prompt and muon induced events. The muon veto consists of two independent systems. Plastic scintillator panels of size 5×5 m and a thickness of 5 cm are mounted on top of the clean room.

Muons crossing the water tank create Čerenkov light. Photo-multiplier-tubes (PMTs) collect the Čerenkov light. To increase the detection efficiency for Čerenkov light, the water tank was lined with VM2000 wavelength shifting and reflecting foil. The muon rejection efficiency of the Čerenkov veto alone was estimated from Monte Carlo to be better than 99%. The total muon background index, b_μ, was estimated to be less than $b_\mu < 1 \cdot 10^{-4} \mathrm{counts}/(\mathrm{keV} \cdot \mathrm{kg} \cdot \mathrm{y})$ [84], assuming that the background contribution from long-lived unstable nuclei induced by muons can be efficently reduced by dedicated cuts on delayed coincidences.

5.2.3. Multi Layer Shielding

Large multi layer passive shields are used to reduce the particle flux reaching the detectors. The individual shielding layers consist of the outer layer, a water buffer and the inner layer, the liquid argon. The water tank is made from stainless steel and has a diameter of 10 m and a height of 9 m and contains 590 m^3 of ultra-pure water. The water shields effectively natural γ-radiation from outside the watertank. In addition, it acts as a neutron moderator and reduces the neutron flux from the rock. Simulations have shown that a background index due to external neutrons is negligible compared to that of internal γ-sources.

The liquid argon cryostat is also made from stainless steel and has a copper lining on the inside. It has a diameter of 4.2 m and holds 70 m^3 of liquid argon. Radiation produced inside the cryostat is absorbed efficiently by the liquid argon.

5.2.4. The Detector Array

Conventional cryostats and copper cooling fingers are removed in GERDA and bare germanium detectors are operated directly submerged in liquid argon to achieve an ultra-clean environment and to reduce high-Z material close to the detector. Argon can be produced with high radio purity and adds very little to the background index. Most material close to the detectors, apart from argon, is either copper or teflon, since these materials can be reliably produced with good radio purity. All materials used, have been screened and their contamination (or upper limits on the contamination) are known. They have to fulfill strict requirements concerning radio purity; often a contamination as low as μBq/kg is needed.

The detector array consists of individual detector strings. All components in the detector strings have been reduced to a minimum of mass. Phase I and Phase II strings differ mainly in the detector holder structure. The Phase I detector array will consist of eight enriched and five non-enriched p-type coaxial detectors. An example of a high purity copper holder is shown in Fig. 5.2(a). The amount of copper and Teflon per detector holder is reduced to about 80 g copper and 13 g Teflon, depending on the exact crystal dimensions.

In Phase II additional n-type 18-fold segmented high purity or p-type unsegmented Broad Energy high purity germanium (BEGe) detectors will be deployed. In case of segmented detectors the Phase II crystal holders will be similar to the one shown in Fig. 5.2(b). The copper and Teflon mass would be reduced even further to about 30 g copper and 7.5 g Teflon.

A detailed description of a detector string is given in Sec. 8.2.

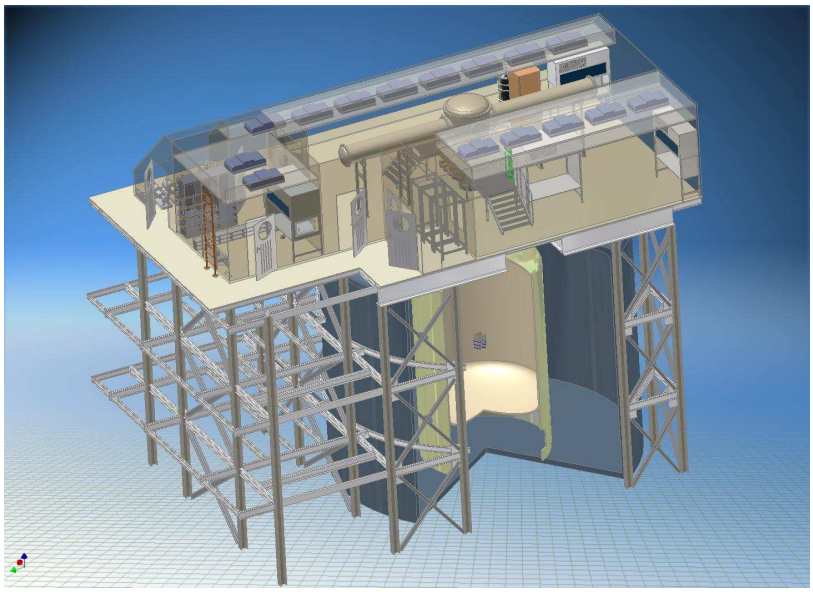

Figure 5.1.: Engineers view of the GERDA experiment. The detector array is visible inside the cryostat. The cryostat is surrounding the watertank. On top of the superstructure is the clean room with the lock system, allowing access to the filled cryostat.

5.2.5. Superstructure, clean room and lock system

The superstructure consists of a platform and three sections of laboratory infrastructure. On top of the platform a class 10000 clean room was built. The detectors will be stored in a dedicated storage system inside the cleanroom. The detector handling and mounting will happen in class 100 flow-boxes inside the cleanroom. The assembled detector strings will be inserted through a lock system into the cryogenic volume.

5.3. Status as of September 2009

By September 2009, the construction of the cryostat, the watertank and the superstructure were completed. The clean room on top of the superstructure was fully erected but construction inside was ongoing. A photo of the GERDA experiment taken in early summer 2009 is shown in Fig. 5.3.

The muon veto construction was partly finished. The mounting of the reflecting foil and all PMTs inside the watertank was finished in August 2009, see Fig. 5.4. The construction of the scintillator plates to be placed on top of the clean room was ongoing.

The detectors for Phase I were all refurbished and tested. A FWHM of 2.5 keV at 1332.5 keV

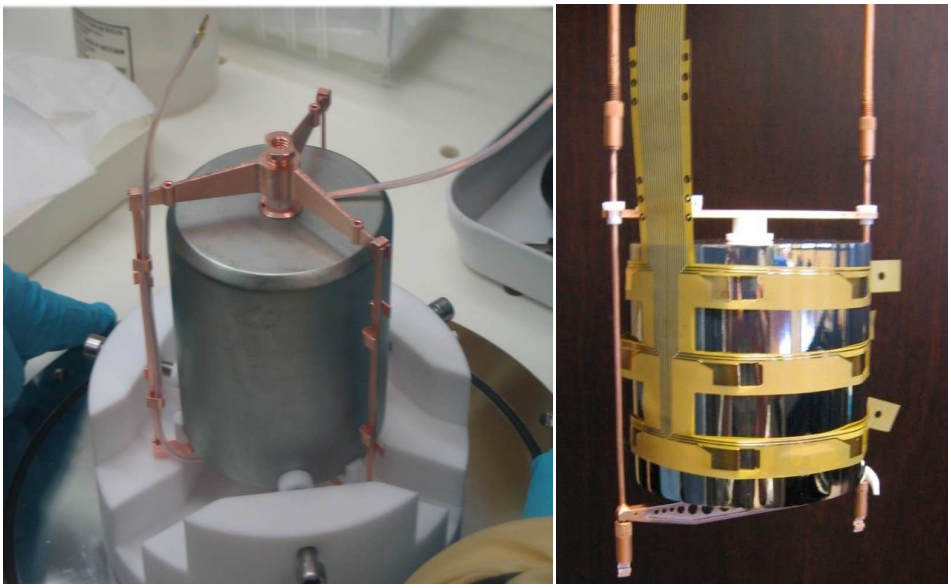

(a) (b)

Figure 5.2.: (a) Photo of an enriched GERDA Phase I crystal mounted into its high purity copper holder. High voltage and signal cable are visible. (b) Phase II detector candidate, 18-fold segmented, made from natural germanium in its low mass copper holder and connected with a Kapton signal cable.

Figure 5.3.: Photo of the GERDA experiment taken in early summer 2009. The watertank inside the superstructure and the clean room on top can be seen.

Figure 5.4.: Inside of the watertank and outside of the cryostat coated with wavelength shifting and reflective foil. The circle indicates the position of one of the PMTs which are hard to see.

was obtained in a test facility. Fig. 5.2(a) shows a Phase I detector mounted into a Phase I detector holder.

37.5 kg enriched Ge in the form of GeO_2 was purchased and is currently stored underground. The final descision on the design of the Phase II detectors has not been made. They could be either 18-fold segmented true coaxial n-type detectors (Fig. 5.2(b)) or BEGe detectors.

The commissioning of the GERDA experiment is planned for 2009/10.

6. Interaction of Electrons, Positrons and Photons with Matter

The energies relevant here are of the order of several keV up to several MeV.

6.1. Electrons and Positrons

Electrons and positrons with energies up to several MeV interact with matter mainly through two mechanisms: ionization and Bremsstrahlung.

The energy loss $-\frac{dE}{dx}$ due to **ionization** can be described by [85]

$$-\frac{dE}{dx} = 4\pi N_A r_e^2 m_e c^2 \frac{Z}{A} \cdot \frac{1}{\beta^2} \left(\ln \frac{\gamma m_e c^2}{2I} - \beta^2 - \frac{\delta^*}{2} \right), \tag{6.1}$$

where Z, A are the atomic charge and number of the absorber, m_e is the electron mass, r_e is the classical electron radius, $N_A = 6.022 \cdot 10^{23}\text{mol}^{-1}$ is Avogadro's number, I is the average excitation energy, characteristic for each absorber material, β is the velocity of the electron in units of c, γ is its Lorentz factor, c is the speed of light and δ^* a parameter which describes how much the extended transverse electric field of the incident relativistic particle is screened by the charge density of the atomic electrons.

The energy loss due to **Bremsstrahlung** in the electric field of the nucleus can be expressed as [85]

$$-\frac{dE}{dx} = 4\alpha N_A \frac{Z^2}{A} r_e^2 E_e \ln \frac{183}{Z^{1/3}}, \tag{6.2}$$

where E_e is the energy of the electron or positron and α is the fine structure constant.

Ionization is dominant at lower energies, whereas Bremsstrahlung becomes more important with increasing energy. The energy at which both processes are contributing equally to the energy loss is called critical energy. The critical energy is material dependent. For elements with $Z > 13$, it is [85]

$$E_{crit} = \frac{550\,\text{MeV}}{Z}. \tag{6.3}$$

After a positron has lost all its kinetic energy it will **annihilate** with an electron from the surrounding resulting in two 511 keV photons.

6.2. Photons

Photons with energy E_γ interact with matter through three different mechanisms. These mechanisms are the photoelectric effect, Compton scattering and electron-positron pair production. In all cases the photon energy is passed to electrons or positrons which subsequently lose energy through the mechanisms discussed in the previous section.

In the **photoelectric effect** the photon is absorbed by an atomic shell electron which leaves its shell. The energy of this electron is

$$E_{e^-} = E_\gamma - E_b \tag{6.4}$$

where E_b is the binding energy of the electron. The vacant shell is filled by an electron from the surrounding and a photon is emitted. If the photon is re-absorbed, an Auger electron can be emitted. The cross section of the photoelectric effect, σ_{photo}, is inversely proportional to the initial photon energy.

The result of a **Compton interaction** is a scattered photon and a recoil electron. The energy of the recoil electron is given by

$$E_{e^-} = h\nu \left(\frac{\frac{h\nu}{m_e}(1-\cos\theta)}{1+\frac{h\nu}{m_e}(1-\cos\theta)} \right). \tag{6.5}$$

where $h\nu$ is the energy of the incoming photon and the angle θ is the scattering angle of the outgoing photon with respect to the direction of the incoming photon. The energy transfer is maximal when the photon is back-scattered, at $\theta = 180^\circ$. The corresponding energy defines the so called "Compton edge". The cross section for Compton scattering, $\sigma_{Compton}$, at energies above about 10 keV is proportional to $\ln(E_\gamma)/E_\gamma$.

If the photon energy exceeds twice the electron rest mass, the photon can create an **electron-positron pair** in the electric field of a nucleus. For low energies, the pair-production cross section, σ_{pair}, is proportional to $\ln E_\gamma$. For energies $E_\gamma \gg \frac{1}{\alpha Z^{1/3}}$, it is nearly constant. The resulting positron loses its energy and annihilates with an electron from the surrounding, resulting in two 511 keV photons.

The mass attenuation coefficient, μ, describes the absorption of radiation in matter and depends on the sum of all relevant cross sections: $\mu = \frac{N_A}{A} \cdot (\sigma_{photo} + \sigma_{Compton} + \sigma_{pair})$. As an illustration, Fig. 6.1 shows μ in dependence of E_γ for germanium. The cross sections of the different photon-interaction processes depend on E_γ and Z of the absorber material. In germanium, photons with energies below 200 keV interact mostly through the photoelectric effect. The interaction of photons with energies of $200 - 8000$ keV is dominated by Compton scattering. More energetic photons will create electron-positron pairs.

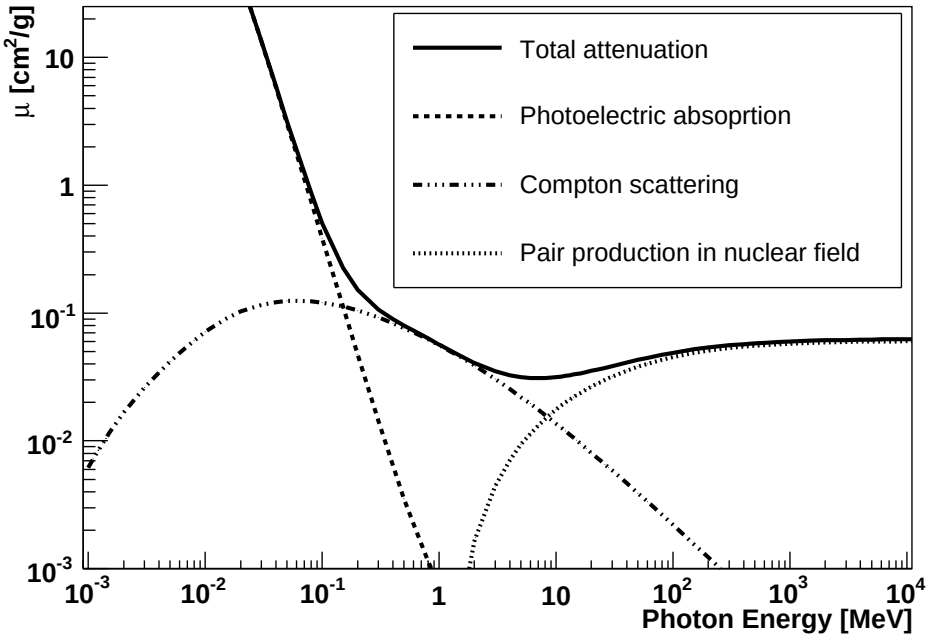

Figure 6.1.: Mass attenuation coefficient of germanium in cm^2/g as a function of the initial photon energy [86]. For energies below 200 keV, the photoelectric effect dominates. Between 200 keV and about 8 MeV, Compton scattering is the dominant interaction mechanism. Above 8 MeV, electron-positron pair-creation is most important.

7. Semiconductor Detectors

There is a wide variety of literature explaining the principles and details of semiconductor detectors. For a comprehensive and elaborated report see [87]. The properties of (germanium) semiconductors important for this work are described in the following.

7.1. Material Properties

Depending on the energy gap between valence and conduction band, materials are classified as conductors, semiconductors or insulators. The band gap of insulators is usually larger than 5 eV; semiconductors have a band gap of the order of 1 eV. Therefore, in semiconductors electrons can be lifted easily from the valence to the conduction band.

Semiconductors are classified into n- and p-type, depending on the impurities. Assuming a semiconductor with four valence electrons (e.g. silicon or germanium), impurities with three valence electrons (e.g. boron) will act as acceptors, producing p-type material. The acceptor levels lie about 0.05 eV above the valence band. Little energy is needed to lift electrons to the acceptor levels, creating a net positive charge in the valence band. The holes can move freely in the valence band.

If the impurities are elements with five valence electrons (e.g. phosphorus) they act as donors and yield n-type material. The donor levels lie about 0.05 eV below the conduction band. In this case, little energy is needed to lift the electrons to the conduction band, creating a net negative charge in the conduction band.

Any border between p-type and n-type material forms a junction where electrons in the conduction band of the n-type material diffuse to the p-type material. The diffusion results in a net space charge distribution causing an electric field which prevents further diffusion of electrons and holes. The area covered by the electric field is called the “depletion zone”, since the number of free charge carriers is significantly reduced.

7.2. Detector Concepts

Detectors can be constructed out of n-type or p-type material called the bulk. The simplest detector has one p-n junction forming a diode. From here on, an n-type bulk is assumed.

Two basic geometries are in use, planar and cylindrical detectors. For planar detectors, the two sides have to form the electrodes defining the potential. For cylindrical detectors, a central bore or a point-contact has to take the place of one of the sides.

The p^+ electrode[1] is usually implemented as an boron implantation. It is very thin, of the order of μm. The n-side of the detector usually gets an n^+-electrode. In silicon it consists of a thin phosphorus implantation, in germanium this is not possible and lithium is drifted into the material. Drifted layers are much thicker than implantations.

The electrodes are metallized, typically with aluminum. These contacts allow the application of an external potential across the p-n junction. The lower potential is attached to the p-side of the junction. This causes electrons and holes to drift away from the junction and the depletion zone grows. Biasing a diode this way is called "reverse biasing". Full depletion is reached when the depletion zone extends over the full volume of the detector. The current observed under those conditions is called leakage current.

Charges created inside the depletion zone do not recombine and drift towards the electrodes causing a small current. The induced charges in the electrodes are collected. The active volume of a detector is defined as the volume for which charges are efficiently collected. The electrodes themselves are conductive and do not contribute to the active volume. Detectors are typically operated at voltages above the full depletion voltage in order to achieve high electric fields and high charge carrier velocities.

The potential on the surface between the electrodes is a priori undefined. The full potential difference has to drop across such a surface requiring it be highly resistive. The surface itself is called intrinsic surface. In some cases it is covered with a protective layer called passivation layer.

7.3. Germanium Detectors

Germanium detectors can be produced with extremely high purity, i.e. an extremely low active impurity-density of the bulk of the order of $10^{10}\,\mathrm{cm}^{-3}$. The depletion depth d for planar germanium detectors is given by

$$d = \left(\frac{2\varepsilon_R V}{eN}\right)^{1/2}, \tag{7.1}$$

where V is the reverse bias voltage, N is the net impurity concentration, ε_R is the dielectric constant and e is the electron charge. Applying a bias voltage of several kV allows to deplete several centimeters of germanium. The operation of large germanium detectors is thus possible.

[1] The "+" indicates that the impurity density is higher than the impurity density of the bulk.

The largest volume for a given depletion depth can be achieved a in cylindrical geometry with the depletion zone growing in radial direction. Three different cylindrical geometries exist: *true coaxial*, *closed-end coaxial* and *point-contact* geometry. In the first two cases, an inner bore hole exists and electrodes are established inside the bore and on the mantle. In the true coaxial geometry, the bore completely penetrates the cylinder, whereas for closed-end coaxial geometries the bore only reaches a certain depth. A point-contact detector has no bore and one of the electrodes is established as a small area on one of the end-plates of the cylinder. In the following only true coaxial detectors are considered.

The two end-plates of a true coaxial detector are relatively large and are very critical to the operation of such devices. Any problem with these end-plates can lead to an increase of the observed leakage current.

The electrodes of a germanium detector are implemented as boron implants on the mantle and a lithium drift layer inside the bore. The drift layer has a thickness of the order of hundreds of micrometers forming a sizeable dead layer reducing the active volume.

The specific properties of germanium have consequences for the signatures of specific interactions. In the photoelectric effect, the photon is absorbed and an electron is created. The electron deposits its energy locally, i.e. 90 % of the electron energy is deposited within a sphere of radius of the order of a mm [88]. Compton scattering most likely causes multiple energy deposits, separated by distances of the order of centimeters; the mean free path of a 2 MeV photon in germanium is of the order of 4 cm. This distance guides the choice of detector size and segmentation.

The band gap of germanium at 80 K $E_{\text{gap}} = 0.73\,\text{eV}$ is small and decreasing with increasing temperature to approximately 0.67 eV at 273 K. At room temperature, thermal excitation causes electrons to populate the conduction band. Applying an external electric field would cause a large electric current which would prevent any small current from an energy deposition to be detected. Therefore, germanium detectors have to be cooled to liquid nitrogen temperatures during operation. Normally, germanium detectors are operated in a vacuum cryostat and cooled via a cooling finger dipped into liquid nitrogen. The actual crystal temperature depends on the quality of the thermal coupling and the insulation.

7.3.1. Signal Development

In this section the process of signal formation inside a germanium detector is briefly reviewed.

Electron and Hole creation

Energy is deposited inside germanium detectors by the processes described in Sec. 6. Electrons are lifted from the valence to the conduction band and electron-hole pairs are created. The band gap of germanium E_{gap} is only 0.73 eV at 80 K. However, to create an electron-hole pair the energy $E_{e^-h^+} = 2.95\,\text{eV}$ (at 80 K) is needed. The difference is caused by the need to excite phonons in the lattice; germanium has an indirect band gap. The energy $E_{e^-h^+}$ to create an electron-hole pair is independent of the energy of the incident particle, the deposited energy, E_{dep} and the energy deposition mechanism. The mean number of electron-hole pairs, $\langle N \rangle$, is

$$\langle N \rangle = \frac{E_{\text{dep}}}{E_{e^-h^+}}. \tag{7.2}$$

Electric Field

The electric field inside a true coaxial detector is determined by the electrically active bulk impurity density $\rho(\mathbf{r})$ and the boundary conditions, i.e. the applied potential on the electrodes. It can be calculated by solving Poisson's equation in cylindrical coordinates

$$\frac{1}{r}\frac{\partial \varphi}{\partial r} + \frac{\partial^2 \varphi}{\partial r^2} + \frac{1}{r^2}\frac{\partial^2 \varphi}{\partial \phi^2} + \frac{\partial^2 \varphi}{\partial z^2} = -\frac{1}{\varepsilon_0 \varepsilon_R}\rho(\mathbf{r}), \tag{7.3}$$

where φ is the electric potential and ε_0 is the vacuum permittivity and ε_R is the dielectric constant of germanium.

Mobility

The drift velocity vector of the charge carriers, $\mathbf{v}_{e/h}$, and the electric field $\mathbf{E}(\mathbf{r})$ are related by

$$\mathbf{v}_{e/h} = \mu_{e/h}\mathbf{E}(\mathbf{r}), \tag{7.4}$$

where $\mu_{e/h}$ is the mobility of electrons and holes, respectively. The mobilities are determined by bulk impurities, lattice defects and lattice excitations. At such low bulk impurities as in almost perfect high purity germanium crystals, the mobility is dominated by the scattering of charge carriers off phonons, i.e. lattice vibrations. As these are temperature dependent, so are the mobilities $\mu_{e/h}$:

$$\mu_{e/h} \propto T^{-a}, \tag{7.5}$$

where a is found to vary between 1.6 and 2.8 [89].

Equation 7.4 is a simplification, as the mobility of the charge carriers is also influenced by the orientation of the crystal lattice. This is described in more detail in Chapter 10.

Diffusion

A large number of electron-hole pairs is created at each energy deposition. During the drift towards the electrods diffusion takes place. The diffusion can be described by the Einstein relation:

$$\kappa_{e/h} = kT\,\mu_{e/h}/\mathrm{e} \tag{7.6}$$

where $\kappa_{e/h}$ is the transverse diffusion constant for electrons or holes, kT is the thermal energy and e is the electron charge. The transverse diffusion constant was calculated as $\mu_e = 210\,\mathrm{cm}^2/\mathrm{s}$ and $\mu_h = 230\,\mathrm{cm}^2/\mathrm{s}$ for holes and electrons [90]. Measurements show an upper limit on the lateral diffusion of $\sim 130\,\mathrm{cm}^2/\mathrm{s}$ [90].

Induced Signals on Electrodes

Electric signals are induced on the electrodes of a detector by all moving charge carriers inside the detector. The currents or induced charges on one electrode are calculated using the Shockley-Ramo Theorem [91,92]:

$$Q(t) = Q_0 \cdot [\,\varphi_\mathrm{W}(\mathbf{r}_h(t)) - \varphi_\mathrm{W}(\mathbf{r}_e(t))\,], \tag{7.7}$$

$$I(t) = Q_0 \cdot [\,\mathbf{E}_\mathrm{W}(\mathbf{r}_h(t)) - \mathbf{E}_\mathrm{W}(\mathbf{r}_e(t))\,], \tag{7.8}$$

where $Q_0 = N \cdot e$ is the net electric charge, $\varphi_\mathrm{W}(\mathbf{r}_{e/h}(t))$ and $\mathbf{E}_\mathrm{W}(\mathbf{r}_{e/h}(t))$ are the weighting potential and the weighting field at the position $\mathbf{r}_{e/h}(t)$. The weighting potential can be calculated by solving the Laplace equation

$$\frac{1}{r}\frac{\partial\varphi}{\partial r} + \frac{\partial^2\varphi}{\partial r^2} + \frac{1}{r^2}\frac{\partial^2\varphi}{\partial\phi^2} + \frac{\partial^2\varphi}{\partial z^2} = 0 \tag{7.9}$$

with the boundary condition that the potential on the electrode under consideration is one and the potential on all other electrodes is zero.

7.3.2. Energy Resolution

The energy resolution of a germanium detector is influenced by three effects. The full width at half maximum (FWHM) W_T expected from a fixed energy deposit is written as

$$W_T^2 = W_D^2 + W_X^2 + W_E^2, \tag{7.10}$$

where W_D^2 represents the broadening due to inherent statistical fluctuations of the number of charge carriers and is given by

$$W_D^2 = (2.35)^2 F\,E_{e^-h^+}\,E_\mathrm{dep}, \tag{7.11}$$

where F is the Fano factor which is of the order of 0.1. The W_X^2 is due to incomplete charge collection and also scales linearly with E_{dep}. The third term, W_E^2, represents the contribution from electronic noise. This contribution is independent of E_{dep}.

Typically cylindrical germanium detectors have a FWHM of $0.8-1.2$ keV at 122 keV rising to $1.7-2.3$ keV at 1332 keV.

7.3.3. Segmented Detectors

The mantle electrode of cylindrical detectors can be segmented to gain information about the location of energy deposits. All segments have to be at the same potential for the detector to operate properly.
The segmentation technique depends on the bulk material. For the n-type detectors considered here, the boron implantation on the mantle is structured to form multiple electrodes. The smallest possible structures have dimensions on the several millimeter scale. The technique is quite elegant and does not disturb the crystal structure.

For p-type detectors, the n^+ electrode on the mantle is lithium drifted. The segmentation is achieved by milling through the lithium layer. This requires a ditch of a width and depth of the order of a millimeter each. This rather "destructive method" disturbs the crystal and is expected to distort the electric field inside the detector.

7.3.4. Surface Channel Effect

The end-faces of a cylindrical detector are problematic surfaces which are very important for the smooth operation of such a device. The problem was recognized from the beginning of germanium detector development. The passivation layer contains a large number of electronic states in the band gap of the bulk. If they are empty, they form a positive space charge which must be compensated by an equal number of negative charges within the bulk. This causes the energy bands to bend and form a slightly conducting, undepleted area under the passivation layer. This region is called n-type "surface channel". The surface channel distorts and decreases the electric field close to the end of the detector. The bias voltage drops across a very small distance above the remaining region of depletion. This locally causes a very strong electric field. Figure 7.1 illustrates the effect.

Electrons created close to the n-contact can be collected easily at that contact, even if they are created within the region affected by the surface channel, see Fig. 7.2(a). Electrons created close to the p-contact and the upper surface have to drift a long way through the region affected by the n-type surface channel. In the extreme, they might drift towards the intrinsic surface and then along the surface where the field is extremely low. In this case it is quite probable that some of the electrons are lost. The amplitude of the signal seen at the n-contact is reduced, since this signal is mostly induced by the electrons. The signal

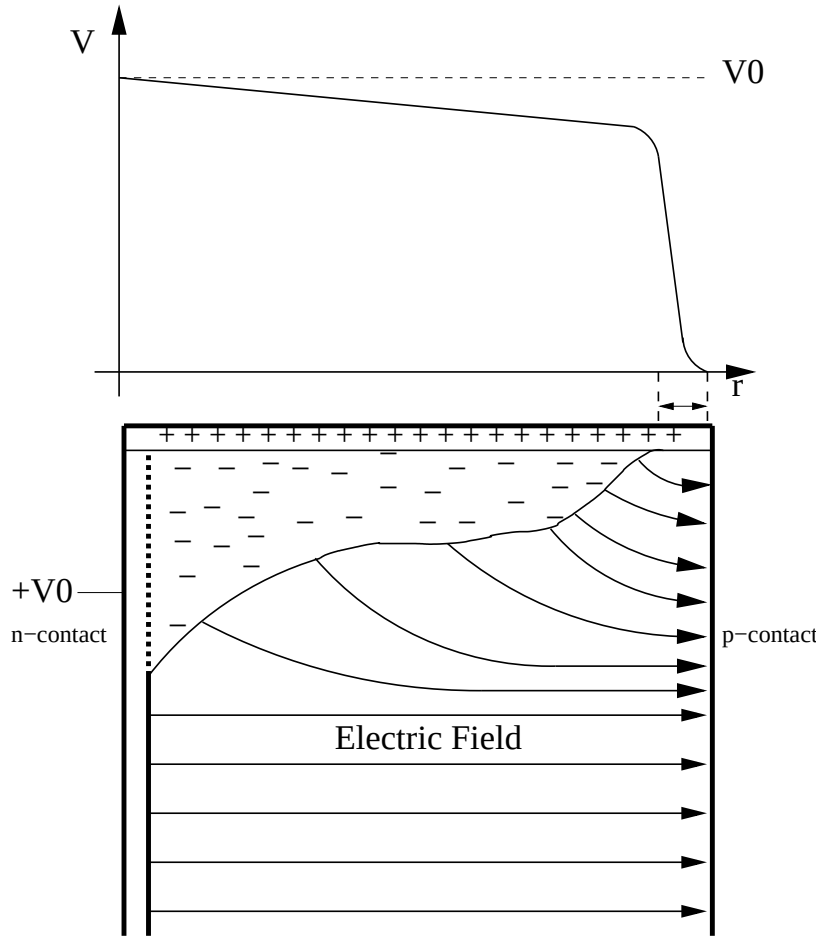

Figure 7.1.: Illustration of the effects of an n-type surface channel. The positively charged states in the passivation layer are compensated by negative charges close to the surface. The area with negative charges is undepleted. The electric field is distorted and is very strong close to the outer edge, i.e. the p-contact, of the detector. Figure adapted from [93].

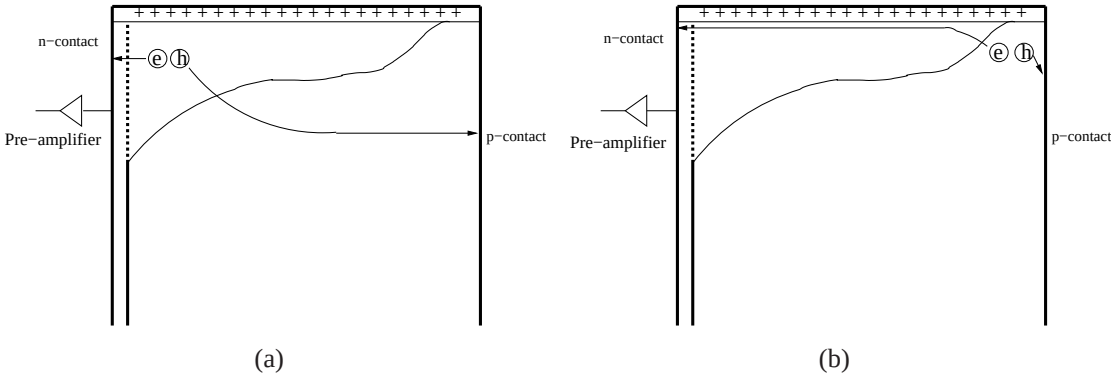

Figure 7.2.: The path of electrons and holes in a detector with an n-type surface channel. (a) shows electron-hole pairs created in the surface channel region close to the n-contact. The electrons have a short distance inside the surface channel region and have the possibility to reach the read-out contact. (b) Electron-hole pairs are created close to the p-contact. The electrons have to travel a long distance along the surface through the surface channel region. Charge carriers are lost in the surface channel region. The induced signal at the n-contact is reduced. The signal is also reduced at the p-contact, but less since here the signal is mostly induced by holes. Figure adapted from [93].

is less reduced at the p-contact, since here mostly holes contribute. Effectively, “inactive” or “dead layers” are observed in regions from which the charge carriers cannot reach the read-out electrode. These are not necessarily the regions where the actual surface channel is located.

The exact mechanism of charge carrier loss is not understood so far. Low surface mobility had been suggested [93]. This effect, however, is not sufficient to cause the observed loss of signal amplitude [94]. Two other mechanisms have been proposed [94]: The probability for charge trapping on the surface could be largely enhanced and/or the electric field strength and distribution could be distorted sufficiently to explain the effect.

Experimental evidence for surface channel effects have been reported previously [95]. The experimental result is illustrated in Fig. 7.3. An electric field was applied perpendicular to the top surface. This field enhances or reduces the potential across the detector surface and thus increases or decreases the effect of the surface channel. Applying a voltage of the right polarity can reduce the affected volume and thus also the inactive region.

Surface channel effects are influenced by many details of the detector production and operation. During production the end-surfaces undergo several chemical treatments and this influences the later behavior of the detector. Operational parameters like the residual gas atmosphere in the cryostat [93], the operational temperature and temperature cycles also influence the detector performance [94].

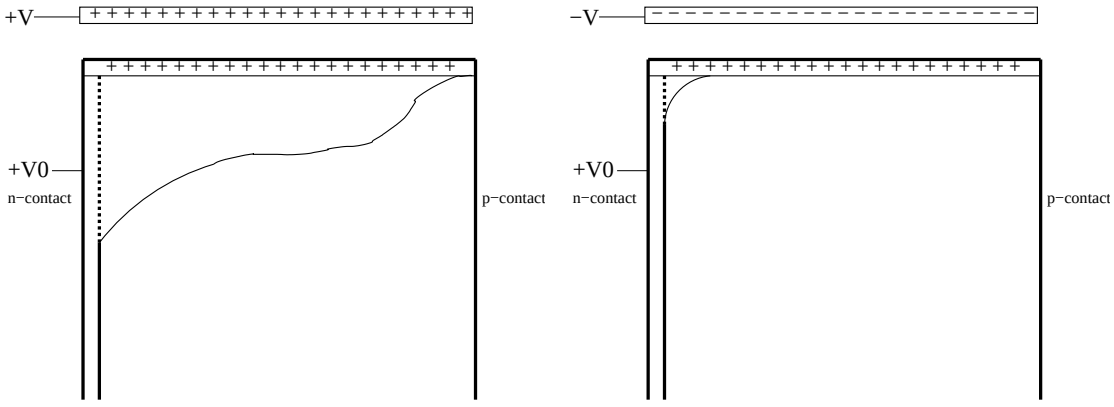

(a) (b)

Figure 7.3.: (a) Applying an external electric field increasing the potential induced by the states in the passivation layer increases the thickness of the surface channel region. (b) Choosing the opposite field polarity decreases the thickness the surface channel region. Figure adapted from [93].

Detectors with surface channels normally have high noise and a large leakage currents. However, even detectors with normal noise and leakage currents were observed to have a surface channel [94].

8. Background in the GERDA Experiment from the Detector Array

Any energy deposit of about 2 MeV seen in the germanium detectors of the GERDA experiment which is not due to $0\nu\beta\beta$, is background. A low background index b in the energy window δE around the Q value of $0\nu\beta\beta$ is extremely important to maximize the sensitivity, see Sec. 4.1.

An estimate of the background index due to the decay of unstable nuclei in the detector strings and the detectors is given in this chapter.

8.1. Background Sources

The important background sources known are given in Sec. 5.1. Considered here are unstable nuclei in the GERDA detector strings and the detectors themselves. The calculation were performed for all isotopes in the ^{232}Th and the ^{238}U decay chains and, in addition, for ^{60}Co, ^{68}Ge and ^{110m}Ag.

8.2. Simulated GERDA setup

The setup of the GERDA experiment simulated was the nominal Phase II detector array. It consisted of 7 detector strings, each string with three 18-fold segmented detectors. The strings were arranged hexagonally. The array was placed inside a volume of liquid argon, representing the filled cryostat. The outer GERDA infrastructure was implemented in the Monte Carlo (MC) software framework MAGE [96], but this is not relevant for this analysis.

The simulated setup of the GERDA experiment was in some parts significantly less detailed than the real design. Especially parts several 10th of centimeters away from the active detectors were simplified. Technical details in the design were neglected but the correct material fractions were taken into account. The simplifications were necessary to control computational and programming time. They should not significantly change the simulated energy deposits in the detectors since photons of an energy of the order of MeV were considered. The mean free path of such photons is of the order of several centimeters in the materials used and the detailed structure would not be “resolved” by these photons.

The generated α and β particles, not penetrating deeply, would be sensitive to the detailed structure, but they cannot reach the active detectors in any case.

8.2.1. Detector Strings

Each of the seven detector strings consisted of an upper part and a lower part. The function of the upper part was to hold the string inside the liquid argon, to maintain the correct position inside the detector array and to transfer the signals from the detector out of the cryogenic volume.

As the upper part was intended to be permanently located inside the cryogenic volume of the GERDA experiment and the lower part of the string was constructed such that it can be assembled outside the cryogenic volume and then attached to the upper part of the string, they were represented by different Monte Carlo volumes.

The upper part consisted of a cable chain and signal cables inside. At the lower end a junction system was located. The upper end of the lower part of the string was the counterpart of the junction system. The complete junction system was called “the matrix”. Underneath were some front-end electronics (FEE), a spacer to separate the FEE from the active volumes and the detectors in their holders. Kapton signal cables and coaxial high-voltage cables connected the FEE and the detectors.

A drawing of a string as implemented in MAGE is shown in Fig. 8.1. All parts of the strings and their implementation into MAGE are subsequently described and their masses and materials are given in Tab. 8.1.

8.2.2. Cable Chains

The cable chain was made of stainless steel. The simulated cable chain was implemented as a simple hollow box. The wall thickness was 0.8 mm. The simulated volume had a length of 3.058 m and a mass of 1.19 kg. It was fully contained inside the liquid argon volume. The part of the chain further up is irrelevant here.

8.2.3. Matrix and Electronics

The exact geometry of the matrix included many small volumes unsuitable for MC simulation. Therefore, a simplified geometry of the matrix was implemented in MAGE. A single volume with a compound material and the correct material fractions was created. The volume was subdivided to represent the junction-sled, the junctions-pins, junction-spacer and junction-cable, see Fig. 8.2.

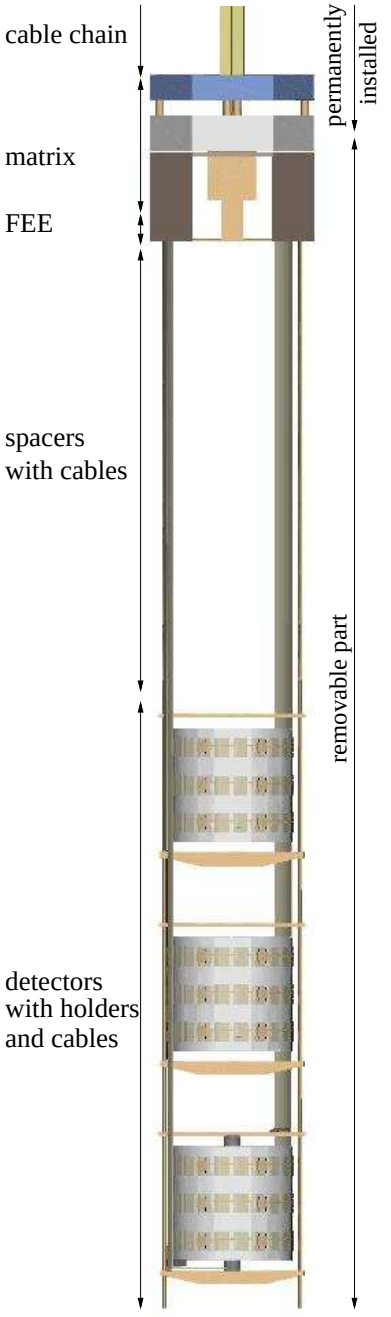

Figure 8.1.: A detector string as implemented in the MAGE framework. Shown are the lower part of the cable chain, the matrix, the FEE, the spacer and the detectors in their holders with cables.

Part	Occurrence in String	Material	Mass [g/per part]
detectors	3	enriched Ge	1616.00
Kapton cable†	3	Kapton	0.35
		Copper	2.64
holder	3	Copper	32.04
		Teflon	4.79
signal-cable guide	3	Teflon	1.34
high-voltage-cable guide	3	Teflon	1.44
Kapton connection-cable	1	Kapton	1.06
		Copper	2.90
high-voltage coaxial cable	1	Teflon	0.66
		Copper	0.98
spacers	1	Copper	12.50
junction-board	1	Copper	60.00
electronics-box	1	misc	10.00
electronics Kapton cable	1	Kapton	5.53
	1	Copper	1.22
matrix:			
junction-sled	1	Copper	491.00
		Iglidur	4.00
junction-pins	1	Copper	142.00
		Murtfeldt	67.00
		Brass	4.41
junction-spacer	1	Copper Screws	20.00
junction-cable	1	Copper	440.00
	1	Teflon	34.00
cable chain	1	Stainless Steel	1193.00
cable	1	Copper	126.99
		Teflon	0.97

Table 8.1.: Table of materials and masses per part used in the simulation of the nominal Phase II array setup of the GERDA experiment. The first column lists the part, the second the number of parts per string. The third and forth columns list the materials and the amount of each material used per part. The masses are absolute masses and were extracted from technical designs. These masses were used to calculate the background index. The masses in the Monte Carlo simulation are somewhat different due to the simplifications made. †Since the Kapton signal cable and the high-voltage Kapton cable were not simulated independently their total mass is given here.

The design of the FEE had not been specified at the time of the simulation. Therefore, a simple copper board, the "junction-board" with a copper box on top, the "electronics-box" was representing the FEE. A Kapton cable, the "electronics Kapton cable", connected the FEE with the matrix. The junction-board was located 30 cm above the top of the uppermost detector in the string. It had a thickness of 1 mm. The electronics-box had the dimensions of $2\,\text{cm} \times 2\,\text{cm} \times 1\,\text{cm}$.

A technical drawing of the matrix, and the geometry implemented into the simulation are shown in Fig. 8.2.

The junction-sled volume contained copper and Iglidur, a plastic which allowed for a sliding connection between the removable and permanent parts of the string.

The junction-pins, 180 pogo pins, provided the electrical connection between removable and permanent part of the detector string. The simulated volume contained the material of the pins, brass, copper and of the plastic body. The 180 pogo pins were assumed to have a total mass of 4.41 g, i.e. each had a mass of 24.5 mg. The brass was assumed to be 61% Cu, 37% Zn and 2% Pb. The plastic body was made from Murtfeldt. In addition some copper from contacts, screws and plates was distributed in the volume.

The junction-spacer volume contained material from the copper that was used to maintain a vertical gap in the matrix. This space was needed to connect the signal cables to the junction-pins.

The junction-cable volume contained copper and Teflon. It represented the connection between the matrix and the cable chain and the cables inside the cable chain.

8.2.4. Spacers and Holders

The spacers were simulated as two cylindrical copper rods with a radius of 0.9 mm. They represented the top part of the holding structure connecting the junction-board to the copper holders. The two spacer volumes contain a mass of 12.45 g.

The complete holding structure of a detector consisted of a low mass copper holder, two Teflon plugs inserted 2 mm into the inner bore-hole on the top and bottom of the detector and two Teflon parts to hold and guide the signal and high voltage cables. The signal-cable-guide was located at the top and the high-voltage cable guide on the bottom of the copper holder. A CAD drawing of the holder structure and its implementation into MAGE are shown in Fig. 8.3.

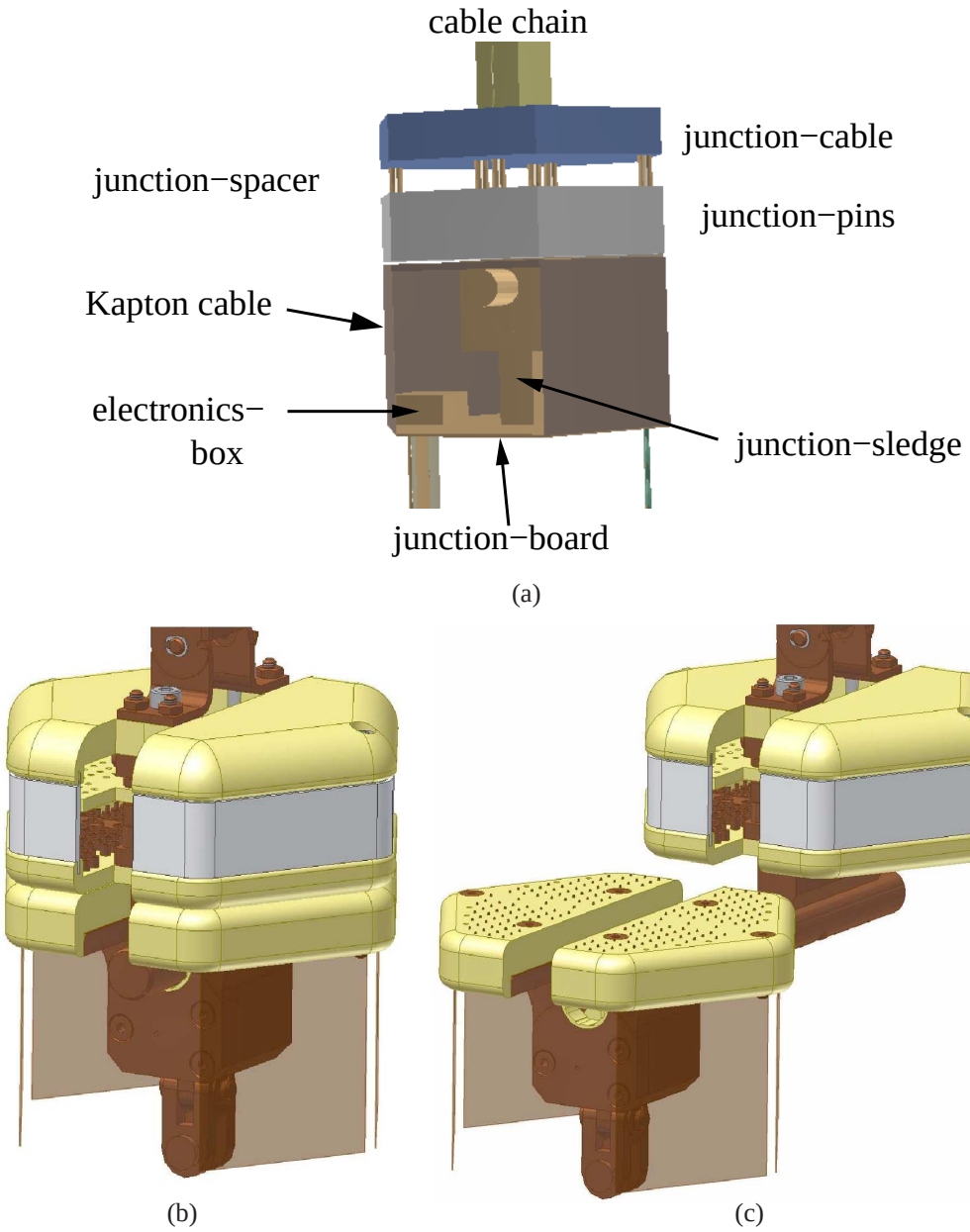

Figure 8.2.: (a) The matrix as implemented into the MAGE framework. Indicated are the cable chain, the junction-cable volume, the junction-spacer volume, the junction-pins volume and the junction-sled volume. Also indicated are the FEE, i.e. the electronics box the Kapton cable and the junction-board. (b) Technical drawing of the closed matrix. (c) Technical drawing of the open matrix.

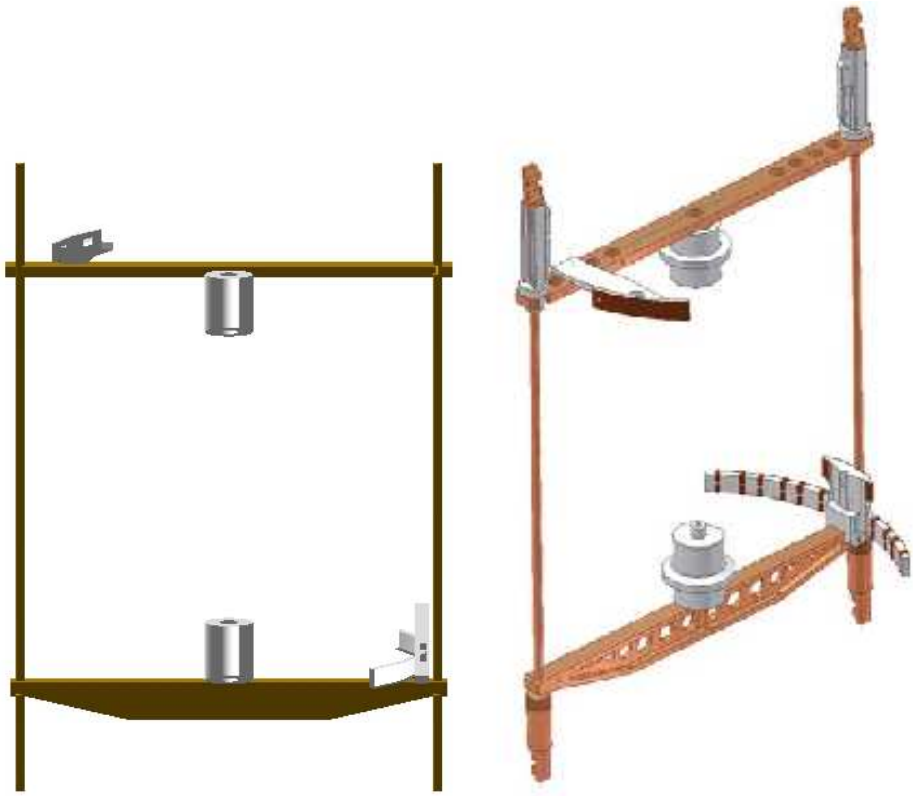

(a) (b)

Figure 8.3.: (a) The low mass copper and Teflon holder structure as implemented in MAGE. (b) A CAD drawing of the structure. All white parts were made of Teflon and all other parts were made of copper. The total mass of the holder was 39.61 g including the cable guides. The copper mass was 32.04 g and the Teflon mass was 7.57 g.

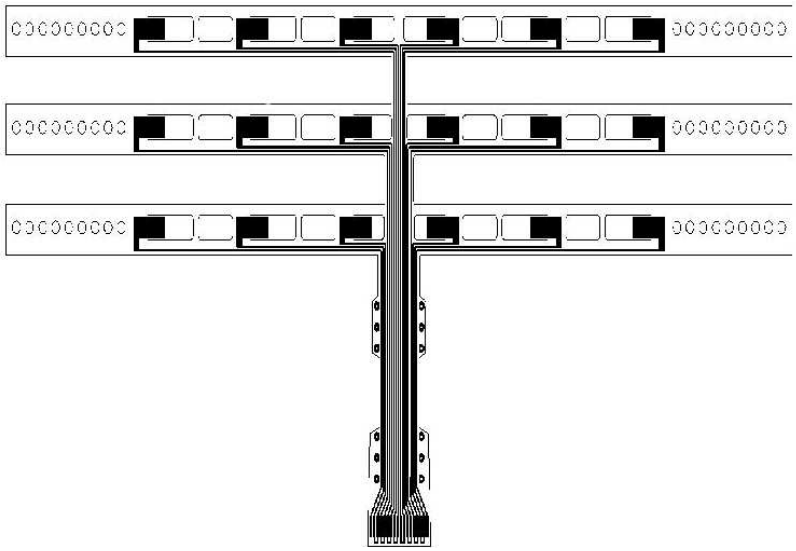

Figure 8.4.: Layout of the low mass Kapton cable used to read out the segments. The black color represents the copper signal lines, everything else was made from Kapton.

8.2.5. Detectors

Each of the 21 detectors was represented by a cylindrical volume with height of 70 mm, inner radius of 0.5 mm and the outer radius of 37.5 mm. The volume was subdivided according to the detector segmentation into 18 segments. On the top, bottom, inner and outer surface of the volume a 1 μm thick dead layer was modelled.

Each detector volume represented a mass of 1.616 kg, total. The isotope fraction of ^{76}Ge simulated was $\kappa = 0.86$. The total mass of enriched germanium in the array was 33.94 kg.

The detectors had a vertical distance of 6 cm to the next detector inside a string. The clearance between the neighboring detectors, from string to string, was 1.5 cm.

8.2.6. Cables

The signal cables to read out the 18 segments were low mass Kapton cables with copper traces on the outside. The amount of Kapton was reduced to a minimum by cutting away all unnecessary areas. The layout of the Kapton signal cable is shown in Fig. 8.4.

All Kapton of all cables simulated had a thickness of 25 μm. The simulated copper traces on the outside of the cables had a thickness of 35 μm and a width of 400 μm.

The overall mass contained in the Kapton of the signal cable was 0.28 g. The amount of copper per signal cable simulated was 2.64 g.

The Kapton cables used had extensions up to the FEE. For the simulation, extra volumes called “Kapton connection-cables” were created. They contained 1.06 g of Kapton and the simulated traces contained 2.90 g of copper.

The high-voltage connection from the FEE to the detectors was maintained through a coaxial cables. The high-voltage connection was implemented into the simulation as a compound material of Teflon and copper, called “high-voltage coaxial cable” and connected to another volume, the “high-voltage Kapton cable”, which connected to the detector. The high-voltage coaxial cable had a mass of 1.64 g per string. The high-voltage Kapton cable had a mass of 0.07 g per detector.

Above the matrix three woven ribbon twisted pair signal cables made of 20 pairs of copper lines, a copper line for grounding in between each pair and Teflon were guided inside the cable chain. All copper lines had a radius of 0.09 mm. The volumes representing the cables were implemented in the simulation as a flat box of a compound material of copper and Teflon. The length of the volume was 3.06 m. The volume contained a total mass of copper of 126.99 g and 0.97 g of Teflon per string.

8.3. Event Generation

Radioactive decays in each of the previously described volumes were simulated. Each simulated decay yielding an energy deposit in a detector is called “event”. The simulation was carried out using the MAGE framework. The MAGE version, from 01.Feb.2008 14:52 was used together with GEANT4.9.1 [97,98]. The *DarkMatter* realm was used for decays inside the crystal, otherwise the *BBdecay* realm was used.

The complete decay chains of ^{232}Th and ^{238}U were simulated. Additionally ^{60}Co, ^{110m}Ag and ^{68}Ge were simulated for materials where screening results indicate the presence of these elements (see Tab. 8.2). The decays were generated using the G4ParticleGun generator which does not include angular correlation between photons emitted in the decays.

Generally, $10 \cdot 10^6$ decays were generated for each isotope in each volume. Only for contamination inside the crystals $1 \cdot 10^6$ decays were generated. All decays were randomly distributed in a given volume with exception of the Iglidur in the junction-sled volume. Iglidur is only used in the upper part of the junction-sled to facilitate the sliding connection of the matrix. Thus, radiation from Iglidur is absorbed by the surrounding copper. The decays of Iglidur were placed into a hollow sphere with inner radius of 0.6 cm and outer radius of 0.62 cm. The center of the sphere was shifted in z-direction with respect to the center of the junction-sled by 34 mm. Thus, the position of the decays agreed approximately with the position of the Iglidur in the junction-sled.

The output of MAGE were energy depositions and their positions inside the detector, "hits". Under real conditions only the sum of all energy deposits inside a segment (crystal) is measured. Therefore, the energies of all hits belonging to a given segment (crystal) were summed up. The sum of the hit energies inside a segment was called "segment energy" and the sum of the energy deposited inside one crystal was referred to as "core energy". A threshold of 10 keV for segment and core energy was applied.

8.4. Energy Resolution

The energy resolution $\sigma(E)$ was simulated as

$$\sigma(E) = \frac{\sqrt{a^2 \cdot E + b^2}}{\sqrt{\ln 2\sqrt{8}}}, \tag{8.1}$$

with E being the segment or core energy in keV. The term in a describes the Fano noise. The value of a was set to $a = 0.0405$ according to measurements with germanium detectors previously performed. The term in b is the contribution from the noise in the pre-amplifier, with $b = 1.31$. A plot of the FWHM$(E) = 2.35 \cdot \sigma(E)$ is shown in Fig. 8.5. The FWHM at 1.332 MeV was 3.35 keV and at 2.039 MeV was 3.78 keV.

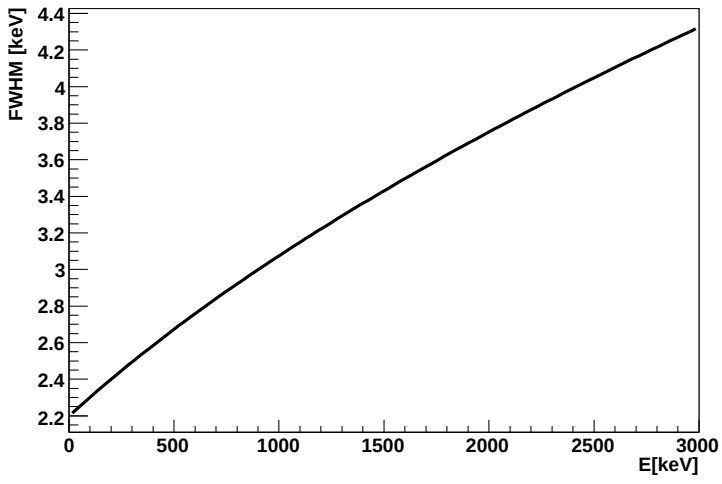

Figure 8.5.: Diagram of the assumed FWHM as a function of the measured energy according to Eq. (8.1).

8.5. Calculation of Background Indices

The background index b originating from a particular part and contamination is

$$b_{ROI} = SP \cdot \frac{A}{\delta E} \cdot \frac{m_{mat}}{m_{Ge}} \cdot C, \tag{8.2}$$

where $SP = N_{sel}/N_{all}$ is the survival probability, i.e. the ratio between selected events and initially produced events. A is the specific activity of the material in Bq/kg (taken from Tab. 8.2), $\delta E = 20\,\text{keV}$ is the width of the energy window defining the region of interest (ROI) around $Q_{\beta\beta}$, m_{mat} is the mass of the part which is evaluated (see Tab. 8.1), $m_{Ge} = 33.94\,\text{kg}$ is the total mass of enriched germanium in the array and C is the number of seconds per year. The activities used for the different materials are listed in Tab. 8.2.

The decay chains were assumed to be in secular equilibrium, unless screening results indicated otherwise. In this cases, only subsets of the chains were assumed to be in secular equilibrium.

The individual activities of each part were assumed to be constant during the calculation of the background index, i.e. no half-life was taken into account. As an exception, the background index from the decay of ^{68}Ge was calculated taking the half-life into account, since it is only $T_{1/2} = 270.8\,\text{days}$. The number of ^{68}Ge decays, ΔN, was calculated using the radioactive decay law

$$\Delta N = N_0 \cdot (1 - e^{-t \cdot \ln 2 / T_{1/2}}), \tag{8.3}$$

with N_0 being the initial number of ^{68}Ge atoms. The initial number $N_0 = 165$ ^{68}Ge atoms per kg of enriched germanium was estimated from MC simulations, taking into account the underground storage time. An underground storage time of 900 days was assumed for the enriched germanium. The number of decays of ^{68}Ge into ^{68}Ga and of ^{68}Ga into ^{68}Zn was assumed to be equal, since the half life of ^{68}Ga is only 67 minutes. The SP was taken from the simulation and the background contribution was calculated for the first and second year of GERDA Phase II.

8.6. Background Suppression

8.6.1. Energy Cuts

Due to the good energy resolution of germanium detectors a small ROI can be chosen. For this analysis the cut on the core energy of $2029\,\text{keV} < E_{\text{core}} \leq 2049\,\text{keV}$ was chosen to calculate the background index b_{ROI}.

8.6.2. Anti-Coincidence Cuts

Background events can be identified by coincidences between two or more detectors. To reduce these background events a crystal anti-coincidence cut, a single crystal (SC) cut is applied and the background index b_{SC} is calculated.

Background events can also be identified using the segmentation of germanium detectors. The electrons form $0\nu\beta\beta$ interact with the germanium by ionization and Bremsstrahlung, as described in Chapter 7. The energy deposit of the electrons inside the germanium detectors is mostly local, i.e. within a sphere with less than a millimeter radius [88]. These events are called single site events (SSE). Most background events are induced by photons. Photons at theses energies will mostly interact through Compton scattering and deposit their energy in a sphere of several centimeters radius [88]. These events are called multi site events (MSE). Background events are mostly MSE and $0\nu\beta\beta$ events are mostly SSE. It is possible to suppress MSE considerably, choosing the proper segment size and requiring segment anti-coincidence, i.e. selecting single segment (SS) events.

The limitations of this method are geometrical and physical ones:

- background events can be MSE but contained within one segment,
- signal events can be SSE but on a segment boundary yielding two segment events,
- background events can be SSE,
- signal events can be MSE if Bremsstrahlung photons are emitted.

8.7. Results

The background indices b_{ROI}, b_{SC} and b_{SS} for each part are given in Tab. 8.3. A detailed decomposition into the contribution from each isotope and each part is presented in Appendix A.

The total background index for the array, is the sum of the b's for all the different sources. For the case of an energy cut only, it comes to $b_{ROI} = (561.70 \pm 4.36) \cdot 10^{-4} \mathrm{cts}/(\mathrm{keV} \cdot \mathrm{kg} \cdot \mathrm{y})$ in the first year. Applying the detector anti-coincidence cut, the background index b_{ROI} is reduced by about a factor of two to $b_{SC} = (239.81 \pm 3.01) \cdot 10^{-4} \mathrm{cts}/(\mathrm{keV} \cdot \mathrm{kg} \cdot \mathrm{y})$. Taking into account segment anti-coincidences the background index b_{SC} was further reduced by a factor of five to $b_{SS} = (46.88 \pm 1.10) \cdot 10^{-4} \mathrm{cts}/(\mathrm{keV} \cdot \mathrm{kg} \cdot \mathrm{y})$. The biggest contribution to the background index came from the internal ^{68}Ge decays. This contribution drops in the second year about 60%. The second biggest contribution are the decays inside the Kapton cables surrounding the detectors.

Many assumption had to be made to calculate the numbers given here. The quoted uncertainties only represent the statistical uncertainty from the MC. Wherever reality differs significantly from the assumptions concerning the activities of parts, significant changes in the values given follow.

8.8. Background Identification through Pulse Shape Analysis

The distinction between MSE and SSE is also possible from an analysis of the induced pulse shapes on the electrodes. SSE have a different structure of the pulse than MSE. Pulse shape analyses (PSA) were carried out using pulse shapes from an 18-fold segmented high purity germanium detector. It was shown that an additional factor of two could be gained in the suppression of certain background components compared to segment anti-coincidence cuts alone [99].

The shortcomings of this method are, the above mentioned physical limitations, i.e. $0\nu\beta\beta$ events can be MSE and background events can be SSE.

Pulses of SSE are normally collected using photon induced double escape peak (DEP) and Single Compton scattering events. They are used to mimic $0\nu\beta\beta$ pulses. However, DEPs are normally not located close to the Q value of $0\nu\beta\beta$ of ^{76}Ge. Furthermore, the interaction positions inside the crystals are not uniformly distributed, but predominantly located near the surfaces.

These problems could, in principle, be overcome using single Compton events, but it is difficult and extremely time consuming to collect these data sets. Therefore, it is necessary to complement the data with simulated pulses.

Material	Activity [mBq/kg]	Isotope
Enriched Germanium	$0.01 \cdot 10^{-3}$	^{226}Ra(U)
	$0.006 \cdot 10^{-3}$	^{228}Th(Th)
	$4.89 \cdot 10^{-3}$	^{68}Ge
	$0.18 \cdot 10^{-3}$	^{60}Co
Copper(Lens)	≤ 0.016	^{226}Ra (U)
	≤ 0.019	^{228}Th (Th)
	≤ 0.010	^{60}Co
Teflon	≤ 0.16	^{226}Ra (U)
	≤ 0.16	^{228}Th (Th)
Kapton	9	(U)
	≤ 4	(Th)
	≤ 2	^{60}Co
high-voltage coaxial cable	≤ 9	^{238}U (U)
	≤ 1.3	^{226}Ra (U)
	≤ 51	^{210}Pb (U)
	6	^{228}Th (Th)
	7	^{110m}Ag
Electronics	$10^{\star}$	(U)
	$10^{\star}$	(Th)
	$10^{\star}$	^{60}Co
Iglidur	≤ 22.6	^{226}Ra (U)
	≤ 15.9	^{228}Ra (Th)
	≤ 25.6	^{228}Th (Th)
Pogo Pins	53	^{226}Ra (U)
	1400	^{210}Pb (U)
	39	^{228}Ra (Th)
	19	^{228}Th (Th)
Murtfeldt	≤ 3.4	^{234m}Pa (U)
	≤ 0.019	^{226}Ra (U)
	0.15	^{228}Th (Th)
	≤ 0.061	^{60}Co
Copper Screws	≤ 2	^{226}Ra (U)
	$\leq 4000^{\ddagger}$	^{210}Pb (U)
	≤ 1	^{228}Ra (Th)
	≤ 1	^{228}Th (Th)
	≤ 0.5	^{60}Co
Stainless Steel (Cable Chains)	≤ 72	^{238}U (U)
	0.97	^{226}Ra (U)
	≤ 2.9	^{228}Ra (Th)
	2.2	^{228}Th (Th)
	190	^{60}Co

Table 8.2.: Table of specific activities of materials used inside the GERDA experiment. The given activities are screening results, except values marked with *, these are assumptions. †Values calculated using the known half lifes and the initial number of atoms per kg enriched germanium estimated from Monte Carlo simulations. ‡The ^{210}Pb limit is that high since the screening was done on a detector with a thick front dead layer. Therefore, the ^{210}Pb is not used, but the screening result for ^{226}Ra is used for calculations and secular equilibrium is assumed.

Part	b_{ROI} $[10^{-4}\text{cts}/(\text{keV}\cdot\text{kg}\cdot\text{y})]$	b_{SC} $[10^{-4}\text{cts}/(\text{keV}\cdot\text{kg}\cdot\text{y})]$	b_{SS} $[10^{-4}\text{cts}/(\text{keV}\cdot\text{kg}\cdot\text{y})]$
Crystal:			
first year	326.07 ± 4.03	153.94 ± 2.77	18.65 ± 0.96
second year	129.48 ± 1.59	61.16 ± 1.10	7.58 ± 0.38
Cables:			
Kapton Cables	109.95 ± 0.51	43.51 ± 0.34	12.78 ± 0.19
Kapton connection-cable	21.88 ± 0.22	8.67 ± 0.15	3.57 ± 0.10
high-voltage coaxial cable	55.14 ± 0.46	10.43 ± 0.20	2.41 ± 0.10
Holder:			
copper holders	10.20 ± 0.07	2.89 ± 0.04	0.99 ± 0.02
Teflon plugs	11.38 ± 0.09	4.65 ± 0.06	1.59 ± 0.03
signal-cable guides	2.14 ± 0.02	0.79 ± 0.01	0.34 ± 0.09
high-voltage-cable guides	2.68 ± 0.02	1.02 ± 0.02	0.44 ± 0.01
spacers	0.12 ± 0.01	0.06 ± 0.01	0.03 ± 0.01
Matrix:			
junction-board	0.09 ± 0.01	0.06 ± 0.01	0.03 ± 0.01
FEE	6.74 ± 0.47	4.23 ± 0.37	2.05 ± 0.26
electronics Kapton cable	2.11 ± 0.16	1.36 ± 0.13	0.65 ± 0.09
junction-sled	3.36 ± 0.31	2.17 ± 0.25	0.91 ± 0.16
junction-pins	7.21 ± 0.65	4.57 ± 0.51	2.24 ± 0.36
junction-spacer	0.60 ± 0.07	0.37 ± 0.06	0.13 ± 0.03
junction-cable	0.31 ± 0.10	0.23 ± 0.02	0.07 ± 0.01
Cables above Matrix:			
cable chain	1.71 ± 1.21	0.85 ± 0.85	-
cable	0.01 ± 0.01	0.01 ± 0.01	-
Sum: (first year)	561.70 ± 4.36	239.81 ± 3.01	46.88 ± 1.10
Sum: (second year)	365.11 ± 2.31	147.03 ± 1.61	35.81 ± 0.69

Table 8.3.: The table summarizes the background index coming from different parts of the detector strings, with different selection cuts applied.

9. Angular Correlation of Photons in ^{60}Co Decays

As angular correlations between photons were in general not simulated, possible effects of such correlations were studied for the test case of ^{60}Co.

The isotope ^{60}Co decays to an excited state of ^{60}Ni which subsequently de-excites by the emission of two photons. The angular correlation between the two photons is well established [100,101]. The case of the collinear emission into one hemisphere is of special interest since such events could mimic $0\nu\beta\beta$ if both photons hit one detector (segment).

The effect of the angular correlation between the de-excitation photons was analyzed. Distributions of observables of Monte Carlo events with and without the correlation implemented were compared for that purpose. Monte Carlo events for ^{60}Co were generated with the DECAY0 code [102]. In early versions the angular correlation was neglected. Since the 18.10.2006 release, the angular correlation is implemented in the event generation process.

9.1. Differences Between Simulated ^{60}Co Decays Generated by old and new DECAY0

Events were generated with two different versions of the event generator DECAY0. The versions dated 04.10.2004 and 18.10.2006 were used. The latter had the angular correlation between the de-excitation photons implemented.
The angle enclosed by the two photons is labeled Θ. Fig. 9.1 shows the distributions of $\cos\Theta$ for events generated with the old and the new version of DECAY0. The 10^6 events generated with the old DECAY0 version resulted in a flat distribution, whereas the 10^6 events generated with the new DECAY0 version show a clear correlation. Here, events with $\cos\Theta$ close to -1 or 1 are more probable, implying that the photons were emitted preferably collinear. The increase in probability to find collinear photons is about 10%.
The possible implication of angular correlation were studied for a GERDA type detector, see Chapter 5. The setup simulated contained a detector plus some cryostat material around it [103]. The scenario is similar to the GERDA array scenario.

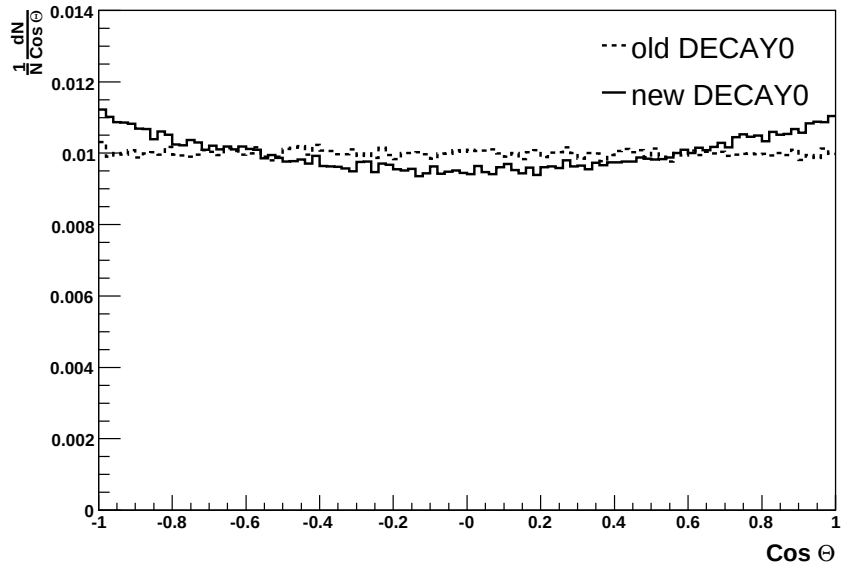

Figure 9.1.: Comparison of the angular correlations of photons in 10^6 ^{60}Co decays, each, generated by an old [04.10.2004] (dashed line) and a new [18.10.2006] (solid line) DECAY0 version.

The first scenario investigated was a ^{60}Co source with a cylindric shape of radius and height 2 mm simulated at a distance of 10 cm above the cryostat. 10^6 decays were simulated with both the 04.10.2004 and the 18.10.2006 DECAY0 versions.

Events with a total energy deposition of $E_{\text{core}} > 50$ keV were accepted and only segments with an energy deposition of $E_{\text{seg}} > 20$ keV were considered.

20359 decays from the 04.10.2004 and 20340 decays from the 18.10.2006 DECAY0 version were accepted as events. These two numbers agree within statistical uncertainties.

In the second scenario, 10^7 decays of ^{60}Co randomly distributed inside the detector were investigated. The sample generated with the 04.10.2004 DECAY0 version yielded 9153633 accepted events and 9156322 were accepted for the 18.10.2006 DECAY0 version. These numbers also agree within statistical uncertainties.

Four observables were studied: the total number of segments hit in each event, the segment multiplicity, the total amount of energy deposited in each event, the energy deposited in each segment and the occupancy of each segment, i.e. the fraction of events in which energy is deposited in the segments.

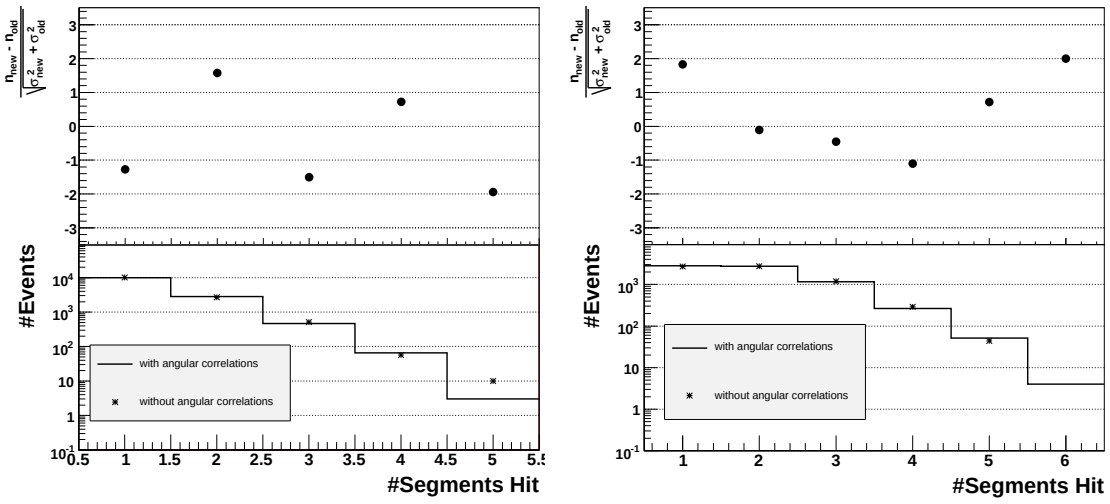

(a) (b)

Figure 9.2.: ^{60}*Co decay 10 cm above cryostat.* Two total energy regions, (a) below and (b) above 1 MeV, are considered. Bottom: Segment multiplicities for the two Monte Carlo samples. Top: The normalized differences between segment multiplicities. The differences are normalized by the combined statistical uncertainties as seen in the distribution.

9.1.1. ^{60}Co Decays in an External Source

The segment multiplicity of both samples and their normalized differences are shown in Fig. 9.2. The differences were normalized by the combined statistical uncertainties. Two energy regions, corresponding to a total energy deposit below (Fig. 9.2(a)) and above (Fig. 9.2(b)) 1 MeV, are shown. All differences are below the two sigma level.

Fig. 9.3(a) shows the total energy spectra and their normalized differences. No significant energy dependent difference between the two samples is seen. Fig. 9.3(b) shows the normalized residual distribution. A Gaussian was fitted to the distribution. The fit yields a mean of -0.08 ± 0.12 and a sigma of 1.08 ± 0.1 implying that the differences between the two MC samples are due to statistical fluctuations only.

The energy deposited in all 18 segments was studied; the results for two arbitrary segments, 4 and 13, are shown in Fig. 9.4 (a) and (b), respectively. As no events with an energy above 1.33 MeV were observed in these two segments, the energy spectrum is shown up to 1.33 MeV only. The normalized residual distribution for the segments was fitted by a Gaussian, yielding a mean of 0.02 ± 0.17 and a sigma of 1.12 ± 0.12 for segment 4 and a mean of 0.0 ± 0.1 and sigma of 1.0 ± 0.1 for segment 13, respectively. No significant difference between the two different MC samples is seen.

In Fig. 9.5 (a) and (b) the segment occupancies are given for both Monte Carlo samples. The bottom segments (1-6) have the lowest occupancy, whereas the top segments (13-18) have the highest occupancy. As the source is located above the detector, this is expected.

Fig. 9.5(c) shows the differences between occupancies for all segments and 9.5(d) shows the normalized residual distribution. The fit of the normalized residuals distribution yields a mean of 0.17 ± 0.29 and a sigma of 1.04 ± 0.27, implying that the differences can be explained by purely statistical fluctuations.

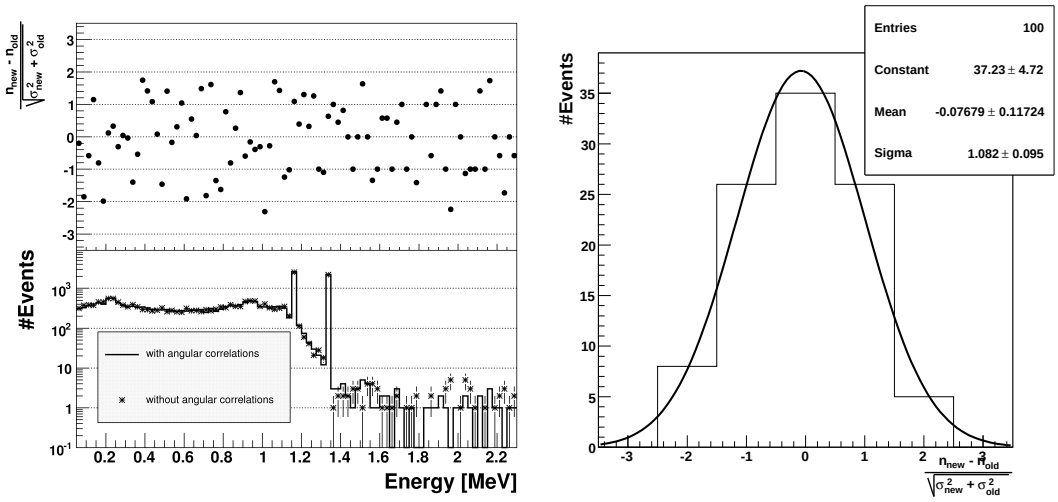

(a) (b)

Figure 9.3.: ^{60}*Co decay 10 cm above cryostat.* (a) Bottom: The total energy spectra of the two samples.(a) Top: The normalized differences of the spectra are plotted. The normalization was done using the combined statistical uncertainties. (b) The normalized residual distribution is shown in.

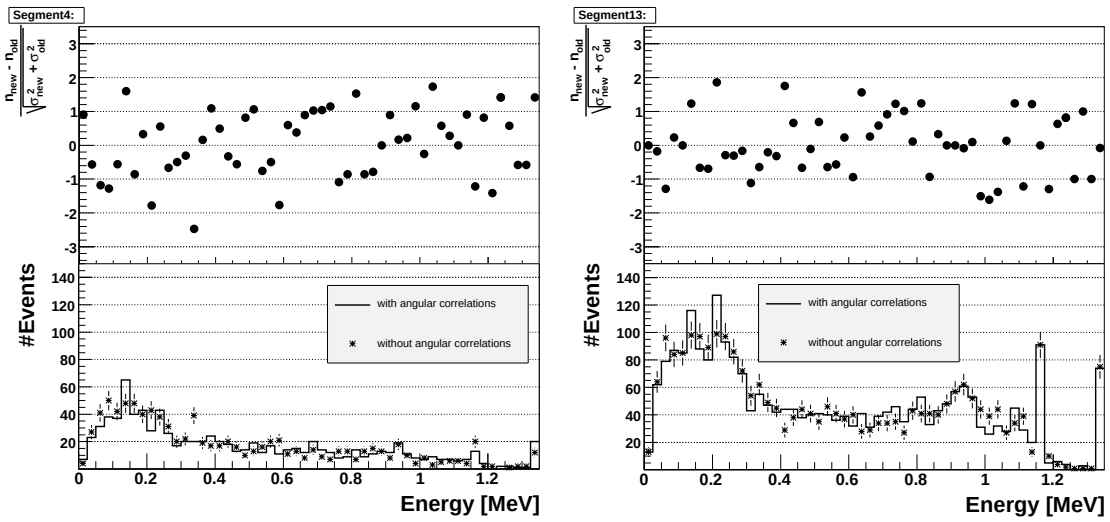

(a) (b)

Figure 9.4.: ^{60}*Co decay 10 cm above cryostat.* Bottom: Energy spectra of the two samples in the segments 4 (a) and 13 (b). Top: Normalized differences of the spectra. The normalization was done using the combined statistical uncertainties.

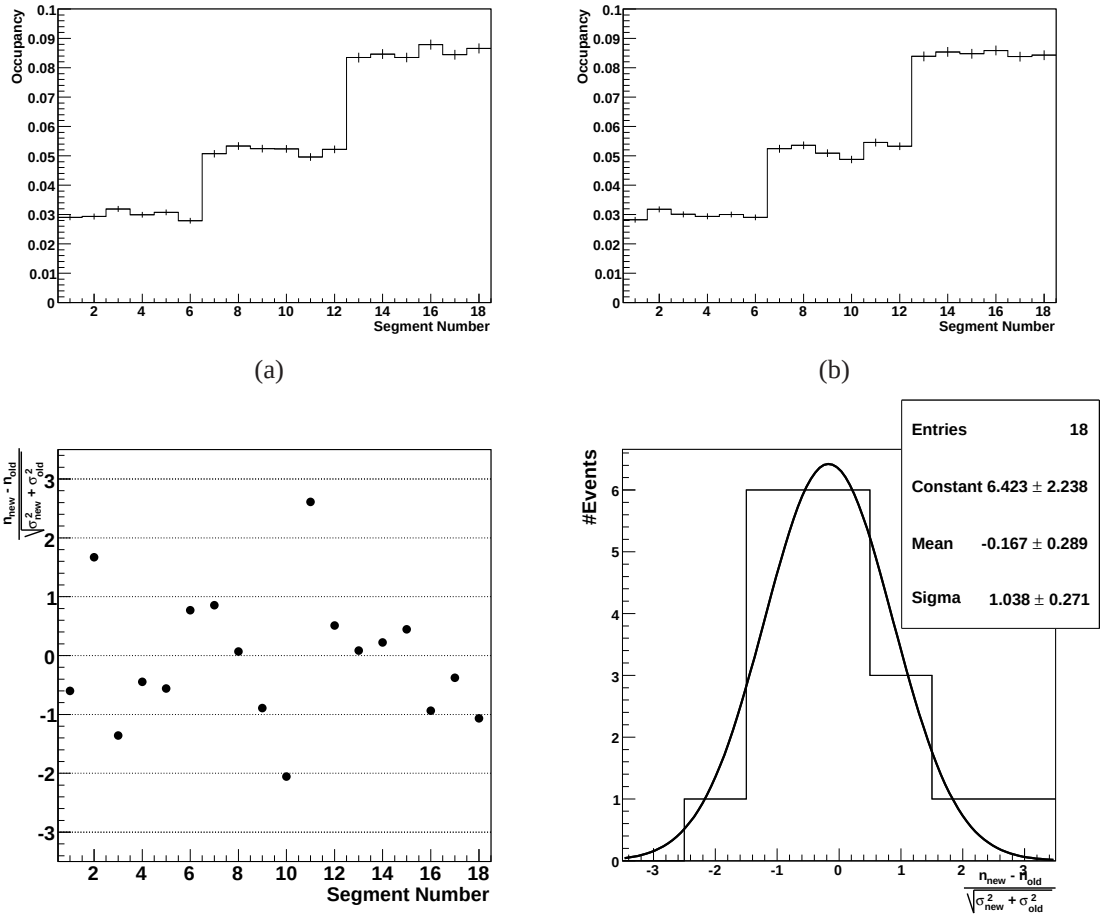

Figure 9.5.: ^{60}*Co decay 10 cm above cryostat.* Segment occupancy for ^{60}Co decays from (a) the old [04.10.2004] and (b) the new [18.10.2006] DECAY0 version. In (c) the normalized occupancy differences as a function of the segment numbers are shown and (d) shows the normalized residual distribution.

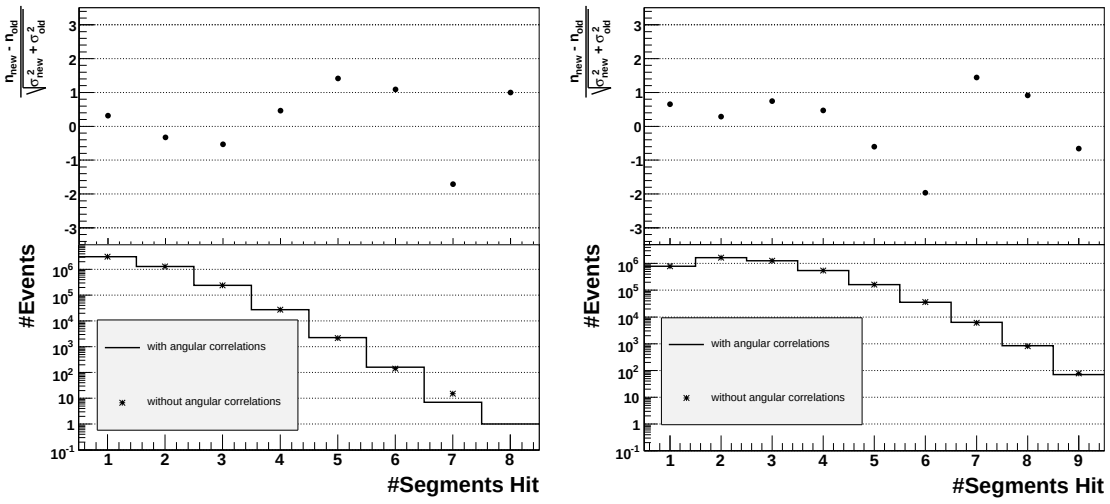

(a) (b)

Figure 9.6.: ^{60}*Co decay inside the detector.* Two total energy regions, below (a) and above (b) 1 MeV, are considered. Bottom: Segment multiplicities for the two Monte Carlo samples. Top: The normalized differences between segment multiplicities. The differences are normalized by the combined statistical uncertainties.

9.1.2. ^{60}Co Decays Inside the Detector

The same observables as before were studied.
Fig. 9.6 shows the distribution of the segment multiplicities and their normalized differences. The differences were normalized by the combined statistical uncertainties. Two energy regions, corresponding to a total energy deposit of below (Fig. 9.6(a)) and above (Fig. 9.6(b)) 1 MeV, are shown. The differences are all below the two sigma level.

Fig. 9.7(a) shows the total energy spectra and their normalized differences. No significant energy dependent difference between the two samples is seen. Fig. 9.7(b) shows the normalized residual distribution. A Gaussian was fitted to this distribution. The fit yielded a mean of 0.05 ± 0.11 and a sigma of 1.0 ± 0.1 implying that the differences between the two MC samples can be explained by statistical fluctuations only.

The energy deposition in all 18 segments was studied; two arbitrary segments, 2 and 14 are shown in Fig. 9.8 (a) and (b), respectively. Since ^{60}Co is simulated to decay inside the detector, the detectable energy in one segment can reach $E_{seg} = Q_{^{60}Co} = 2.8$ MeV. The normalized residuals distribution for each segment was plotted and fitted by a Gaussian. For segment 2, this yields a mean of -0.01 ± 0.10 and a sigma of 0.9 ± 0.1. For segment 14, a mean of -0.12 ± 0.36 and sigma of 1.34 ± 0.37 was found. Thus, the difference between the samples can be explained by purely statistical fluctuation within the two different MC samples.

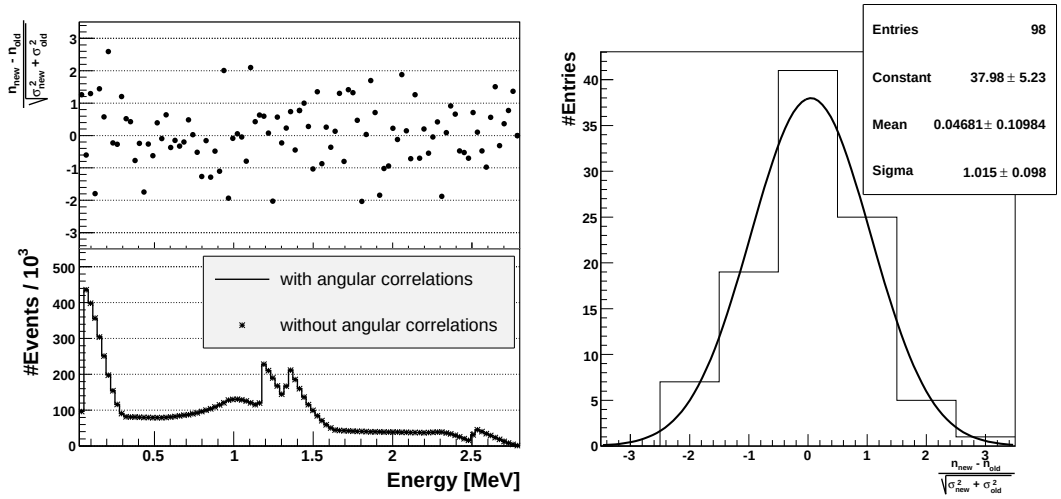

(a) (b)

Figure 9.7.: ^{60}*Co decay inside the detector.* (a) Bottom: The total energy spectra of the two samples. The normalized differences of the spectra is plotted in (a) Top: The normalization was done using the combined statistical uncertainties. (b) The normalized residual distribution.

In Fig. 9.9(a) and (b) the segment occupancy is shown. Since decays of ^{60}Co inside the detector were considered, the occupancy has a different structure than in Fig. 9.5. The occupancy of the segments 7–12, the middle segments layer of the detector is about 20% higher than in the upper and lower segment layers of the detector. The de-excitation photons can escape the detector. The photons leaving the top and bottom of the detector will contribute to a lower occupancy in the upper and lower segments layer. In Fig. 9.9(c) the normalized differences between the occupancies for all segments is shown. The normalized residuals distribution (Fig. 9.9(d)) has a mean of 0.27 ± 0.29 and a sigma of 1.11 ± 0.28, implying that the differences between the samples generated with the new and old DECAY0 version are in good agreement with statistical fluctuations.

9.2. Conclusion on Angular Correlations in ^{60}Co Decays

None of the observables considered was significantly affected by the introduction of angular correlations. The effect of the angular correlation between the two de-excitation photons from ^{60}Co decays is not observable with this kind of segmented detector used in GERDA. Therefore, it is justified to simulate background events in GERDA using event generators neglecting the angular correlation between the two de-excitation photons.

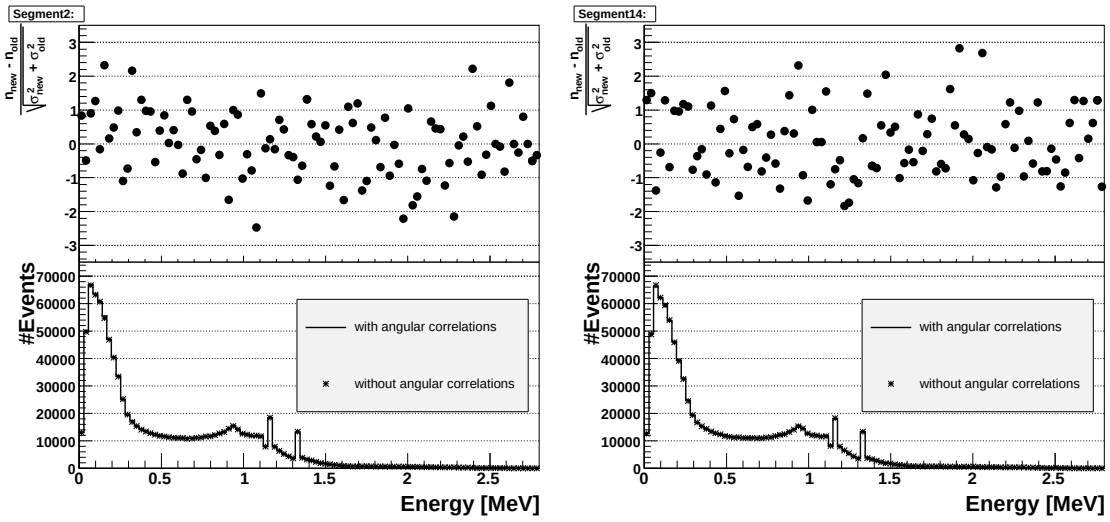

(a) (b)

Figure 9.8.: ^{60}*Co decay inside the detector.* Bottom: Energy spectra of the two samples in the segments (a) 2 and (b) 14. Top: Normalized differences of the spectra. The normalization was done using the combined statistical uncertainties.

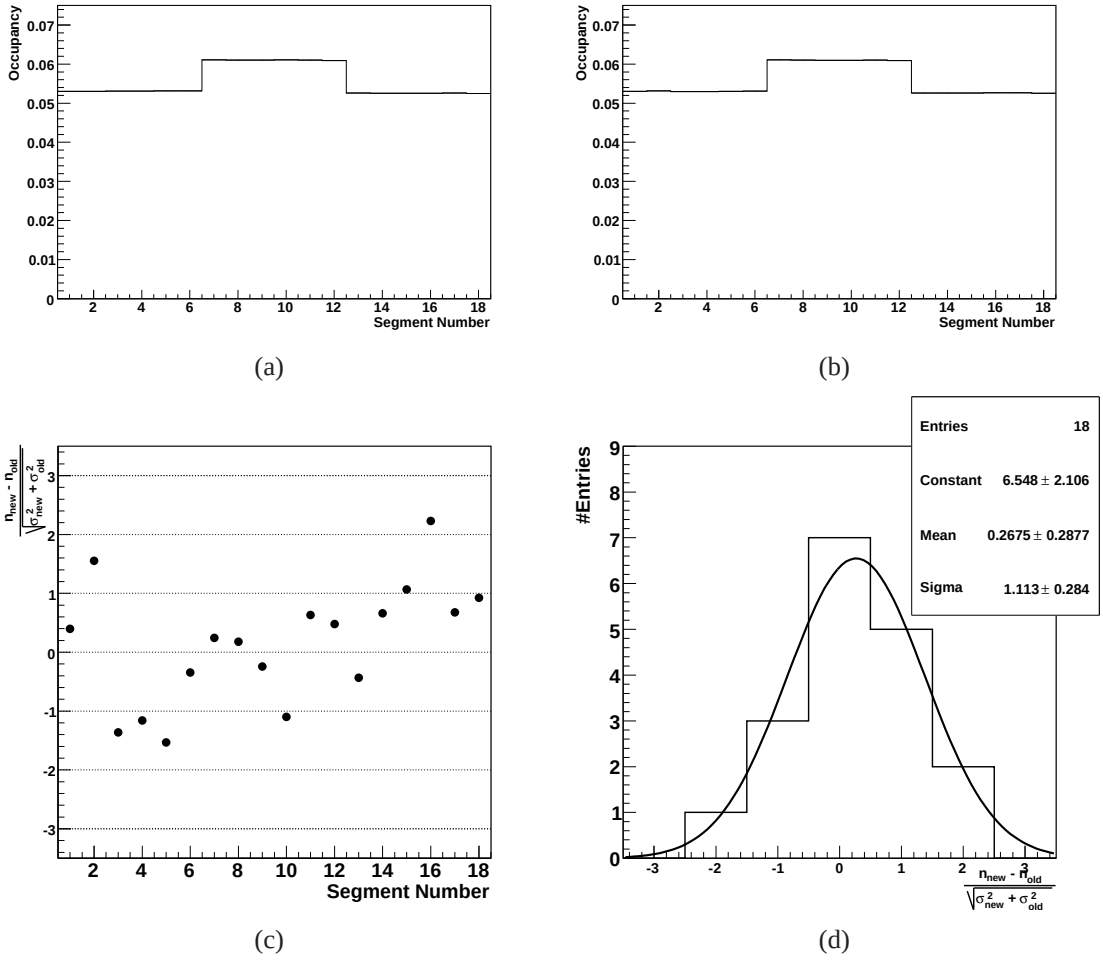

Figure 9.9.: ^{60}*Co decay inside the detector.* Segment occupancies for ^{60}Co decays from (a) the old [04.10.2004] and (b) the new [18.10.2006] DECAY0 version. (c) Normalized differences in the segment occupancies and (d) the normalized residual distribution.

10. Pulse Shape Simulation

A pulse shape simulation comprising the calculation of the electric field and the weighting potentials as well as the induced charges in the electrodes is presented. The effects of the active bulk-impurity density on the electric field are also demonstrated.

10.1. The Basic Principle

The procedure of the pulse shape simulation is as follows:

1. The interactions of particles with a germanium detector are simulated using the Monte Carlo framework MAGE [96]. The result is a list of interactions, hits, with location of the energy deposit.

2. The hits are clustered such that energy deposits within a given distance are combined. The default distance is 1 mm. The location of the cluster is set to be the bary-center of the hits.

3. The number of electron-hole pairs is calculated.

4. The electric field and the weighting potentials at the position of the charges are obtained from previously calculated grid maps.

5. The velocity of the charges are calculated, taking into account the effect of the crystal structure.

6. The time development of the pulse shapes induced in all electrodes are calculated.

7. The effects from the read-out chain, such as noise and limited bandwidth are folded into the pulse shapes.

10.2. Hit Clustering

According to the requirements of a particular simulation, hits can be clustered. Per default, two hits closer to each other than the best hypothetical radial resolution of the detector,1 mm, calculated as the speed of the charge carriers multiplied by the time resolution of the electronics, are clustered. For a given simulation, the space over which hits are to be clustered, r_{cl}, can be adjusted. The position of each cluster is the bary-center of the original hits. The energy of the cluster, E_{cl}, is the sum of the energies of the original hits. Any hit

closer to the new bary-center than r_{cl} will be added to the cluster and a new bary-center is calculated. The cluster is used to calculate the amplitude of the corresponding pulse. If more then one cluster is left for a given event, the pulses are added at each step.

10.3. Calculation of Electric Field and Weighting Potential

The signal development was briefly described in Sec. 7.3.1 . The electric field determines the drift of the electrons and holes in the detector. The Shockley-Ramo Theorem, Eq. (7.7), describes the induced charges or currents on the electrodes using the weighting potentials or weighting fields.

The electric field inside a cylindrical true coaxial germanium detector can be calculated analytically for simple impurity density distributions. The weighting potentials of the segments of the envisioned 18-fold segmented detectors cannot be calculated analytically. The electric field and the weighting potentials were calculated with the same numerical algorithm.

The electric field and the weighting potentials are calculated in three dimensions.

The electric field , $\mathbf{E}(\mathbf{r})$, at the position $\mathbf{r} = (r, \phi, z)$ is calculated solving Poisson's equation,

$$\nabla^2 \varphi(\mathbf{r}) = -\frac{1}{\varepsilon_0 \varepsilon_R} \cdot \rho(\mathbf{r}), \tag{10.1}$$

where φ is the electric potential, ε_0 is the vacuum permittivity, $\varepsilon_R = 16$ is the dielectric constant of germanium and ρ is the active bulk-impurity density. The Dirichlet-boundary conditions are applied, i.e. the electrical potential has a finite value on the core electrode and is zero on the segment electrodes. It is assumed that the electric field was not influenced by the electron-hole pairs drifting inside the detector.

The weighting potentials φ_0 were calculated solving Laplace's equation,

$$\nabla^2 \varphi_0(\mathbf{r}) = 0, \tag{10.2}$$

with the boundary condition that the weighting potential equals unity on the considered electrode and zero otherwise. Since true coaxial detectors were considered Poisson's and Laplace's equation were expressed as

$$\frac{1}{r}\frac{\partial \varphi}{\partial r} + \frac{\partial^2 \varphi}{\partial r^2} + \frac{1}{r^2}\frac{\partial^2 \varphi}{\partial \phi^2} + \frac{\partial^2 \varphi}{\partial z^2} = -\frac{1}{\varepsilon_0 \varepsilon_R}\rho(r, \phi, z), \tag{10.3}$$

$$\frac{1}{r}\frac{\partial \varphi_0}{\partial r} + \frac{\partial^2 \varphi_0}{\partial r^2} + \frac{1}{r^2}\frac{\partial^2 \varphi_0}{\partial \phi^2} + \frac{\partial^2 \varphi_0}{\partial z^2} = 0. \tag{10.4}$$

Poisson's and Laplace's equation are both solved numerically on a grid. The numerical technique employed is the method of Successive Over-Relaxation (SOR).

This method uses three-dimensional numerical derivatives. Eq. (10.3) is rewritten as

$$\varphi(r,\phi,z) = \frac{1}{C}\quad\left(-\frac{\rho(r,\phi,z)}{\varepsilon_0\varepsilon_R} - \frac{1}{r}\frac{\varphi(r+1)-\varphi(r-1)}{2h_r} - \frac{\varphi(r+1)+\varphi(r-1)}{h_r^2}\right. \tag{10.5}$$

$$\left. - \frac{1}{r^2}\frac{\varphi(\phi+1)+\varphi(\phi-1)}{h_\phi^2} - \frac{\varphi(z+1)+\varphi(z-1)}{h_z^2}\right), \tag{10.6}$$

with $(r-1)$, $(r+1)$ being two points on the grid, next to the considered grid point and h_r is the distance between the two points in r and the same nomenclature for ϕ and z, and $C = -\frac{2}{h_r^2} - \frac{2}{r^2 h_\phi^2} - \frac{2}{h_z^2}$. The value of the potential φ at the position (r,ϕ,z) is defined by the impurity density $\rho(r,\phi,z)$ and the potential at its six nearest neighbors.

In order to iteratively calculate the field based on this formula, a starting potential has to be set. The initial potential is chosen in accordance with the boundary conditions as $\varphi(r) = V_{bias} - V_{bias}\cdot r/r_{max}$, where V_{bias} is the applied bias voltage and r_{max} is the outer radius. The calculation for each iteration is performed inside out. The potential at the iteration $n+1$ at each position (r,ϕ,z) becomes

$$\varphi(r,\phi,z)_{n+1} = \frac{1}{C}\quad\left(-\frac{\rho(r,\phi,z)}{\varepsilon_0\varepsilon_R} - \frac{1}{r}\frac{\varphi(r+1)_n-\varphi(r-1)_n}{2h_r} - \frac{\varphi(r+1)_n+\varphi(r-1)_n}{h_r^2}\right. \tag{10.7}$$

$$\left. - \frac{1}{r^2}\frac{\varphi(\phi+1)_n+\varphi(\phi-1)_n}{h_\phi^2} - \frac{\varphi(z+1)_n+\varphi(z-1)_n}{h_z^2}\right). \tag{10.8}$$

This technique is called "Gauss-Seidel method". The convergence of this method can be accelerated considerably by introducing a constant C_{SOR} with $1 \le C_{SOR} \le 2$ and modifying the procedure as

$$\varphi(r,\phi,z)'_{n+1} = C_{SOR}\cdot(\varphi(r,\phi,z)_{n+1} - \varphi(r,\phi,z)_n) + \varphi(r,\phi,z)_n\ . \tag{10.9}$$

This method is called "Successive Over-Relaxation".

The iteration is repeated until the change of the potential in one iteration is

$$\frac{\sum_{r,\phi,z}|\varphi(r,\phi,z)'_{n+1} - \varphi(r,\phi,z)_n|}{\sum_{r,\phi,z}|\varphi(r,\phi,z)_n|} < X, \tag{10.10}$$

with $X \le 10^{-5}$, typically.

The weighting potentials are calculated analogously.

Numerical differentiation in the same approximation as before of the electric and weighting potentials yields the electric and weighting fields.

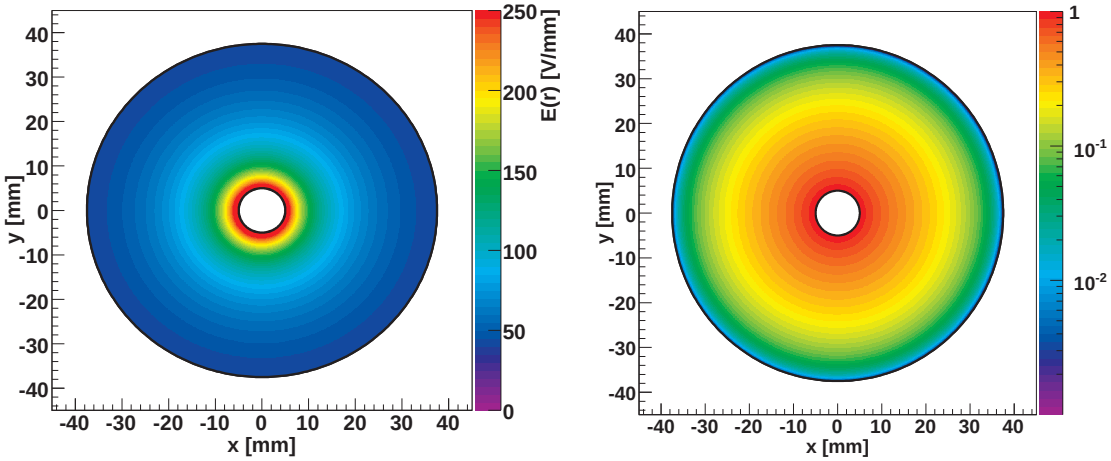

(a) (b)

Figure 10.1.: (a) Radial component of the electric field inside a true coaxial 18-fold segmented germanium detector, calculated with the Successive Over-Relaxation method. The impurity density $\rho = 0.1 \cdot 10^{10}\,\mathrm{cm}^{-3}$ was assumed and an electric potential of $+3000V$ was applied on the core electrode. (b) The weighting potential of the core electrode of the detector; it equals unity on the core electrode and and zero on any other electrode.

The radial electric field for a uniform impurity density of $0.1 \cdot 10^{10}\,\mathrm{cm}^{-3}$ and the weighting potential of the core electrode are shown in Fig. 10.1. The weighting potential of a segment electrode in horizontal cross section and in vertical cross section are shown in Fig. 10.2.

The impurity density determines the electric field in the detector at a fixed bias voltage, see Eq. (10.1). The radial dependence $E(r)$ for a true coaxial n-type germanium detector, for different impurity densities is shown in Fig. 10.3. The electric field magnitude and shape changes significantly for different impurity densities. Low ρ values yield large $E(r)$ at small r, dropping towards large r. Large ρ values yield large $E(r)$ at large r, and low $E(r)$ at small r.

Unfortunately, the impurity density is not constant throughout a typical detector. It often varies within a factor of three from top to bottom. Furthermore, the impurity density often changes over the radius of the crystal [104]. Since the detector is not always cut from the exact center of the crystal, a radial impurity change can be transformed to a radial and azimuthal change in the detector.

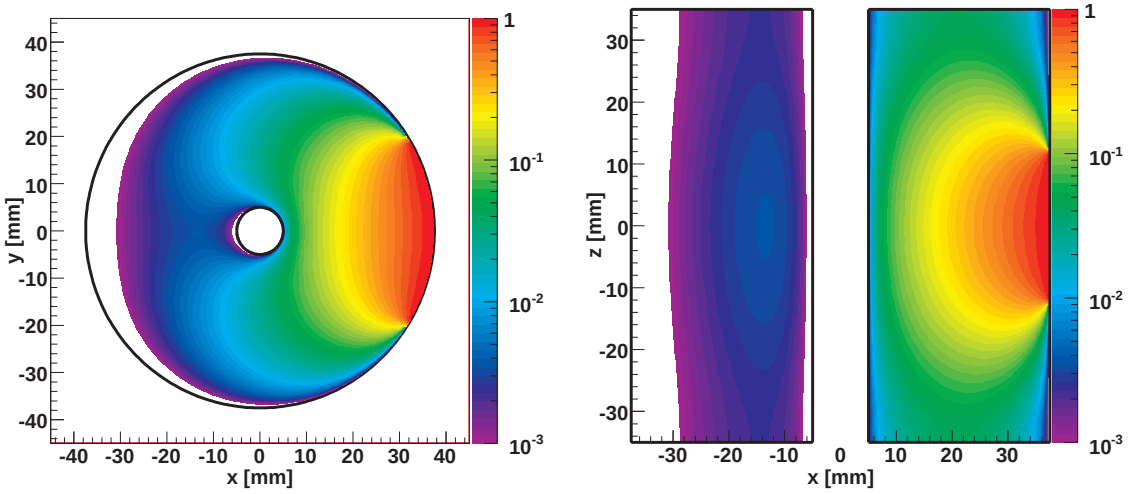

(a) (b)

Figure 10.2.: Weighting potential of a central segment electrode of a true coaxial 18-fold segmented germanium detector in (a) horizontal cross section (z=0) and in (b) vertical cross section (y=0). The weighting potential equals unity on the considered electrode and zero on all other electrodes.

10.4. Drift Velocities and Mobility

The mobilities of the electrons μ_e and holes μ_h as defined in Eq. (7.4) are the proportionality constants between the electric field, $\mathbf{E}(\mathbf{r})$, and the drift velocity, $\mathbf{v}(\mathbf{r})$,

$$\mathbf{v}(\mathbf{r}) = \mu_{e,h}\mathbf{E}(\mathbf{r}), \tag{10.11}$$

where $\mathbf{r}$ indicates the position.

The temperature of a group of electrons or holes is defined according to the formalism of Maxwell-Boltzmann distributions. Since germanium detectors are typically operated around 100 K, the temperatures of electrons and holes are higher than the temperature of the crystal lattice. In this case the mobility becomes a complex tensor and depends on the crystal lattice orientation. In particular, $\mathbf{v}(\mathbf{r}) \nparallel \mathbf{E}(\mathbf{r})$ is possible. This effect is called “transverse anisotropy”.

The crystal structure of germanium is face-centered cubic (FCC). The crystal axes, given in Miller indices, are $\langle 100 \rangle$, $\langle 110 \rangle$ and $\langle 111 \rangle$. Along the axes $\mathbf{v}(\mathbf{r}) \parallel \mathbf{E}(\mathbf{r})$ due to the crystal symmetry. The magnitude of the mobility is different on different crystal axis, though. This effect is called “longitudinal anisotropy”.

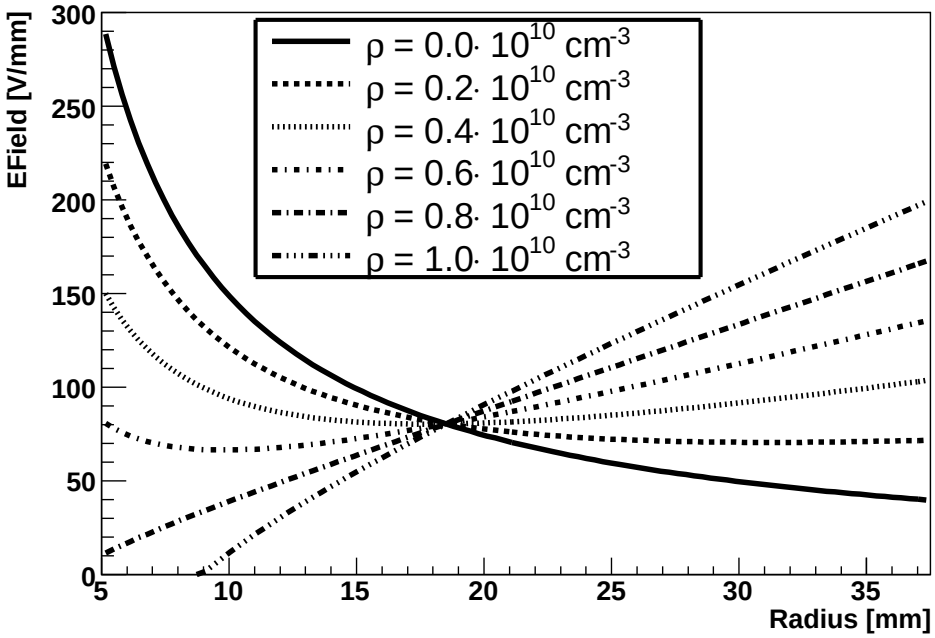

Figure 10.3.: Change of the radial electric field strength as a function of the radius for different active bulk impurity densities ρ and fixed applied electric potential of 3000 V. For each calculation the impurity density was constant throughout the detector. At $\rho = 1.0 \cdot 10^{10}\,\mathrm{cm}^{-3}$ the detector is not fully depleted anymore.

Reference	Carrier	Direction	$\mu_0 \left[\frac{\mathrm{cm}^2}{\mathrm{V\cdot s}}\right]$	$E_0 \left[\frac{\mathrm{V}}{\mathrm{cm}}\right]$	β	$\mu_n \left[\frac{\mathrm{cm}^2}{\mathrm{V\cdot s}}\right]$
Ref. [105]:	Electron	$\langle 111 \rangle$	42420	251	0.87	62
		$\langle 100 \rangle$	40180	493	0.72	589
Ref. [106]:	Hole	$\langle 111 \rangle$	107270	100	0.58	-
		$\langle 100 \rangle$	66333	181	0.744	-
Ref. [107]:	Electron	$\langle 111 \rangle$	38536	538	0.641	510
		$\langle 100 \rangle$	38609	511	0.805	-171
	Hole	$\langle 111 \rangle$	61215	182	0.662	-
		$\langle 100 \rangle$	61824	185	0.942	-

Table 10.1.: Parameters describing the drift velocity along the $\langle 111 \rangle$ and $\langle 100 \rangle$ axes, using the parameterization from Eq. (10.12).

The longitudinal anisotropy was measured for the axes $\langle 100 \rangle$ and $\langle 111 \rangle$. The mobilities along these directions were extracted using the parameterization [87],

$$v = \frac{\mu_0 E}{[1 + (\frac{E}{E_0})^{\beta}]^{1/\beta}} - \mu_n E, \tag{10.12}$$

where μ_0, μ_n, E_0 and β are parameters determined by a fit. The parameter μ_0 characterizes a simple linear relation between E and v. The deviation from the linear relation is modeled through the parameters E_0 and β. The parameter μ_n was introduced [105] to account for the "Gunn effect" which occurs at electric field strength above 300 V/mm.

Values of μ_0, E_0, β and μ_n as extracted from fits are given in Table 10.1.

The anisotropy in any direction is related to the longitudinal anisotropy between the $\langle 100 \rangle$ and $\langle 111 \rangle$ directions. The drift velocity in any direction can be calculated accordingly. The details of the calculation can be found in [108].

The mobilities of the electrons and holes along the axes, as used in the simulation, are shown in Fig. 10.4 and are those taken from [107].

Diffusion processes in the drift of the electrons and holes were neglected, since their effects are small. A maximal transverse diffusion of about 0.2 mm is estimated and should not significantly change the observed pulse shape.

10.5. Time Development of the Induced Charges

The position of the charges at each time step, Δt, was calculated with a fourth order Runge-Kutta method. The time step chosen for the simulation was 1 ns. The induced charges Q

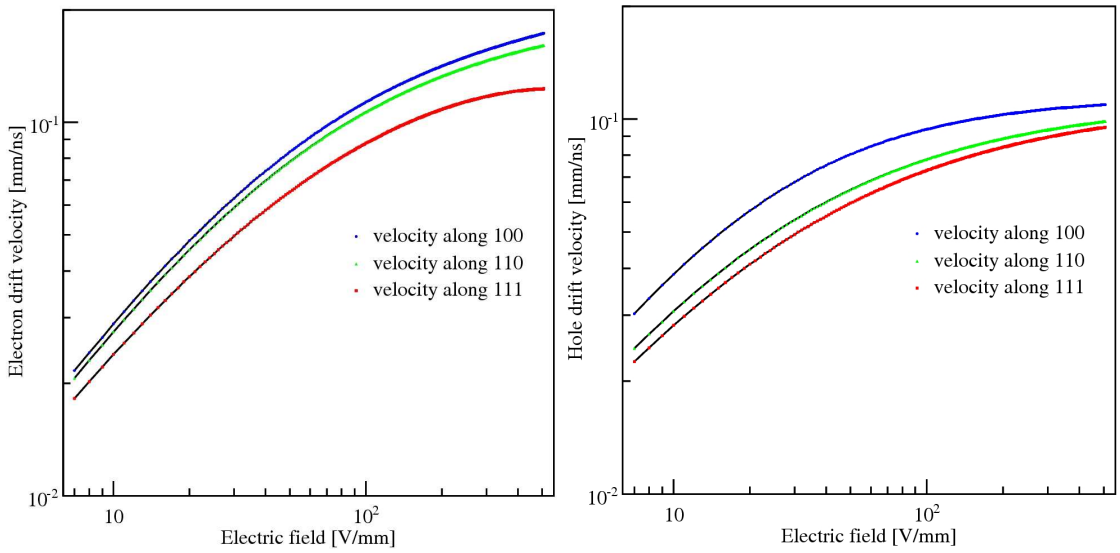

(a) (b)

Figure 10.4.: The drift velocities of the (a) electrons and (b) holes along the crystal axes as a function of the radial electric field strength. The parameter values from [107] were used. The velocities along axes $\langle 100 \rangle$ and $\langle 111 \rangle$ are extracted from the fit, the velocities along $\langle 110 \rangle$ are calculated.

in all segments were calculated according to Eq. (7.7) at each position, resulting in a raw pulse, the time development of the pulses, i.e. Q(t) or I(t).

10.6. Raw Pulses

The raw core and segment charge pulses for a simulation with unity charge deposited at different radii r and fix azimuthal angle $\phi = 0°$ is shown in Fig. 10.5. The big difference between pulses induced by energy depositions at different radii is obvious.

10.7. Effects of the Electronics

The raw pulses from the simulation are different than pulses recorded with a data acquisition system. The amplitude and shape of the pulses are changed through the limited bandwidth and the noise in the read-out chain. An example of the simulated electronic effects can be found in [108].

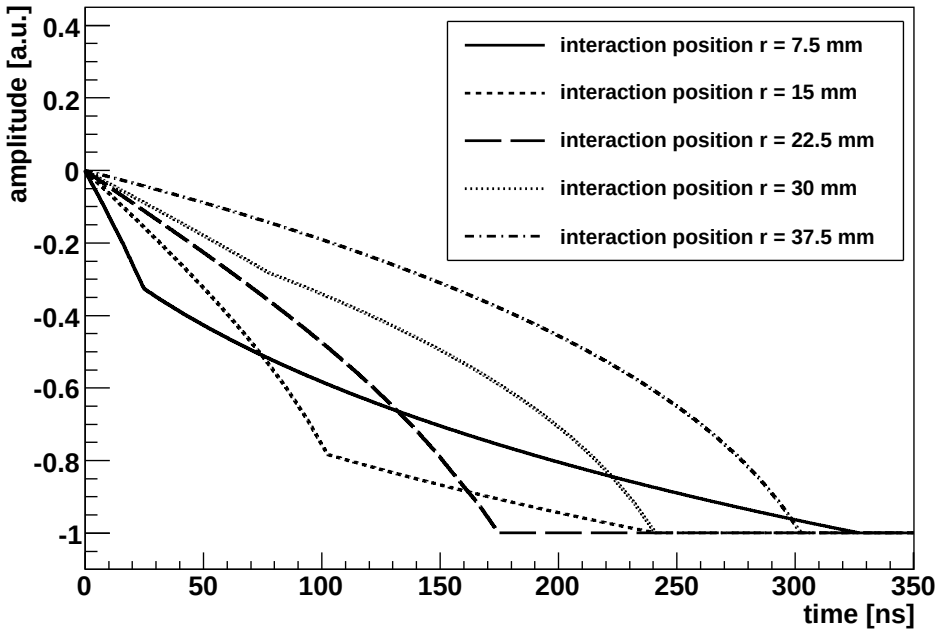

(a)

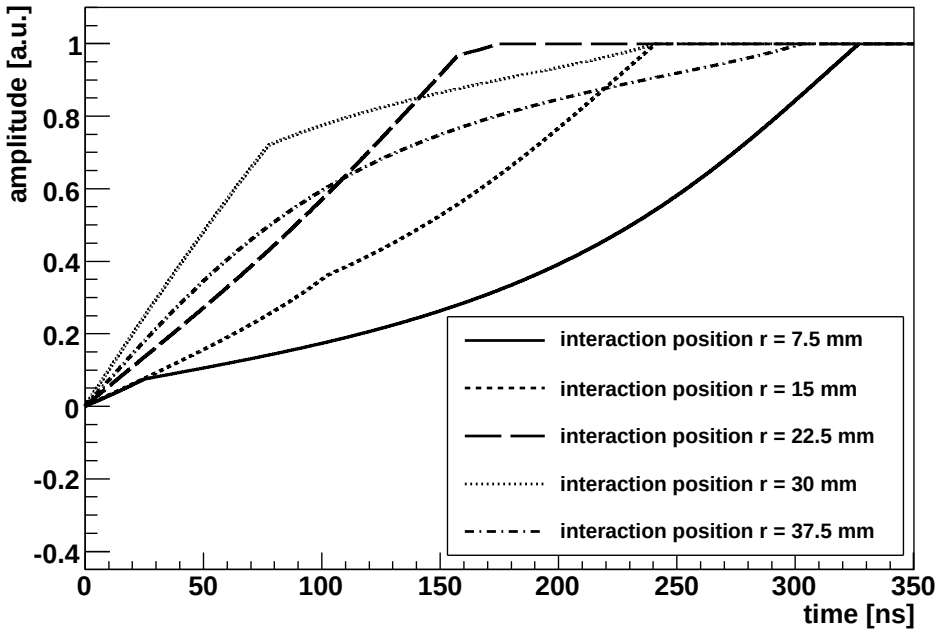

(b)

Figure 10.5.: Raw pulses from the simulation with point-like charges and interaction positions at fixed ϕ and different radii r for (a) the core and (b) the corresponding segment.

11. The Special Detector Super Siegfried

The intrinsic surfaces at the end-faces of true coaxial detectors are critical for their operation. The full bias voltage has to drop cross these surfaces. Therefore, they have to be highly resistive. To protect them, they are covered by passivation layers. A special detector with a single 5 mm thick segment was procured to study surface effects in detail.
The general characterization measurements are included in this chapter while results concerning the top surface are reported in Chapter 14.

11.1. Detector

The Super Siegfried (SuSie) detector is a cylindrical true coaxial n-type high purity germanium detector. The detector has a height of 70 mm. The radius of the inner bore hole is 5.05 mm and the outer radius is 37.5 mm. At the ends the bore holes have a conical shape. The detector has a mass of 1634.5 g. It has an 18+1-fold segmentation, see Fig. 11.1(a).

The p^+ electrodes on the outside are boron implants. The segmented implantation was carried out by Canberra France. A single 5 mm thick segment, unsegmented in the azimuthal angle ϕ, on one side of the detector, defining the top of the detector, was created. The remaining outer p^+ layer is six-fold segmented in ϕ and three-fold segmented in z. The lower two layers have a thickness of 23.33 mm, whereas the third layer has a thickness of 18.33 mm. The segments of the detector are not fully metallized. Only a circular area with approx. 2 mm radius in the middle of the segment, is metallized and available for contacting.

The detector has a concentration of electrically active impurities, according to the crystal manufacturer, between $\rho = 0.44 \cdot 10^{10}\mathrm{cm}^{-3}$ at the top and $\rho = 1.30 \cdot 10^{10}\mathrm{cm}^{-3}$ at the bottom of the detector. The core capacitance at different applied bias voltages was measured by Canberra France in Lingolsheim as shown in Fig. 11.2. The capacitance decreases with increasing bias voltage. It stops decreasing around +2250V applied to the core electrode and stays nearly constant at higher bias voltages. From that measurement, the depletion voltage was estimated to be 2250V and the operation voltage was set to 3000V.

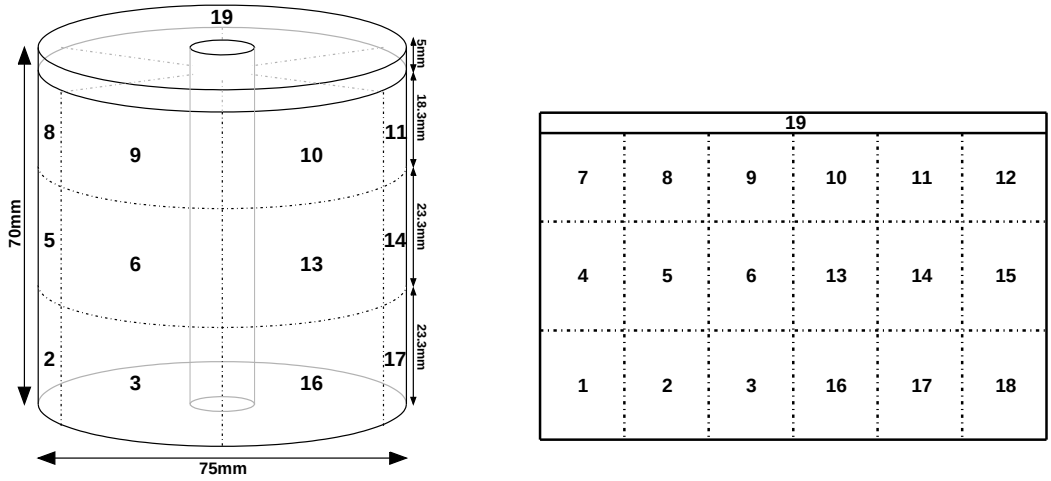

(a) (b)

Figure 11.1.: (a) Schematic drawing of the 18+1-fold segmentation of the detector. (b) The segment numbering scheme.

11.2. Test Setup

The SuSie detector is fitted with a “Snap-Contacts” cable [103]. The contact to the top segment was made using a about 2 cm long metallic strip fixed to the segment. The read-out cable was soldered to the metal strip. The position of the contact is above the segment boundary between segment 10 and 11, at 255°. The segment numbering is shown in Fig. 11.1(b).

The detector was operated inside a conventional aluminum cryostat. Fig. 11.3(a) shows the detector in its holder covered by a protective Teflon foil. The detector holder consisted of three vertical copper bars, each connected to a copper bar on top, pressing on a Teflon plug in the bore hole of the detector. The copper bars were separated by 120°. The vertical bars had a diameter of 5 mm. The copper bars on top were 3 mm thick and 7 mm wide.

The detector holder was wrapped in aluminum foil, which acts as an infrared shield, see Fig. 11.3(b). The detector was cooled via a cold finger dipped into liquid nitrogen. The temperature of the detector was monitored using a Pt 100 resistor installed on the holder of the detector, close to the cold finger. The operational temperature was between -170°C and -160°C. The cryostat was pumped to a pressure of approximately $5 \cdot 10^{-6}$ mbar. The test stand was located in an air-conditioned room, such that environmental temperature and humidity were controlled and stable.

The field-effect transistor (FET) for the core signal was placed inside the cryostat while the FETs for the segments were integrated in the pre-amplifiers outside. The cryostat had four

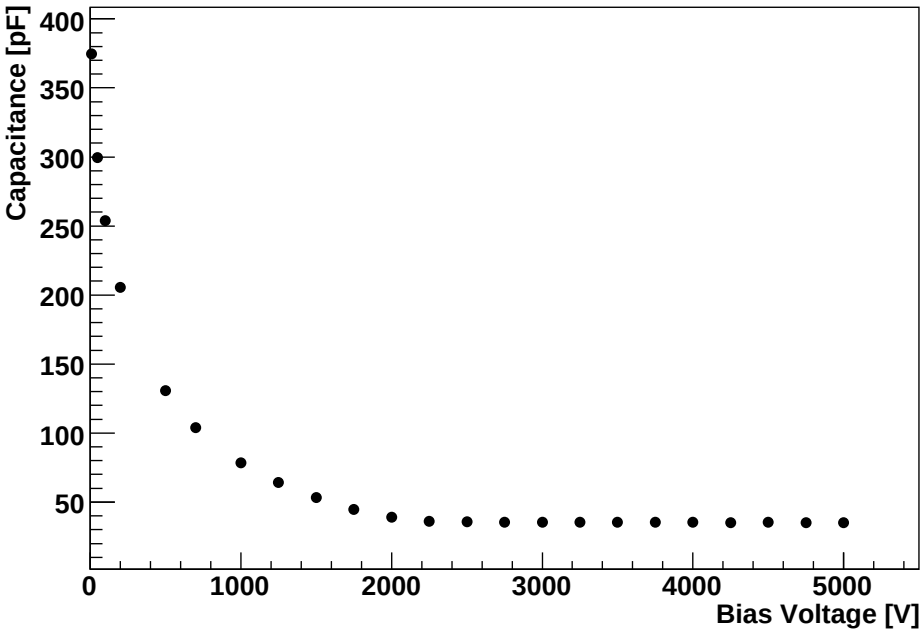

Figure 11.2.: Voltage dependence of the total detector capacitance as measured by Canberra France.

feed-throughs. Two 7-channel feed-throughs were located on one side of the cryostat and a 9-channel feed-through and the high-voltage feed-through on the opposite side. Segments 1–9 and segment 19, the Pt 100 and drain and feedback from the core FET were connected through the two 7-channel feed-throughs. Segments 10–18 were connected through the 9-channel feed-through. A schematic drawing of the feed-throughs is given in Fig. 11.4(a). The cables inside of the cryostat were all unshielded.

Canberra PSC 823 pre-amplifier were used for all signals. The 19 segment pre-amplifiers were housed in two copper boxes next to the feed-throughs of the cryostat. The core pre-amplifier was housed in an aluminum box, fixed to one of the copper boxes, see Fig. 11.5. The cold FET of the core pre-amplifier was AC coupled while all segments were DC coupled, see Fig. 11.4(b).

A 75 MHz XIA Pixie-4 data acquisition system [109] (DAQ) with five four-channels modules was used to record data. For each event, the energy, time and pulse shape information for each channel can be stored. The energy in Analog to Digital Converter (ADC) counts, E_i^{ADC}, is calculated for each channel i, from a trapezoidal filter applied to the pre-amplified signals.

The test stand in its environment is shown in Fig. 11.5.

(a) (b)

Figure 11.3.: (a) Photo of the detector in its holder, mounted in the cryostat on the base plate and wrapped by a protective Teflon foil. (b) The detector and holder wrapped in an aluminum foil which acts as infrared shield.

11.3. Measurements and Data Sets

Measurements were performed to characterize the Super Siegfried detector, to investigate its surface properties and to verify the pulse shape simulation described in Chapter 10.

Three different sources were used: a 50 kBq ^{60}Co source, a 35 kBq ^{228}Th source and a 42 kBq ^{152}Eu source. If the ^{228}Th or the ^{60}Co source were used, they were always placed centrally above the cryostat pointing at the center of the detector. The ^{152}Eu source was always collimated and used in different positions. The collimator consisted of a 2 cm thick tungsten rod with a hole of 1 mm radius. The ^{152}Eu was used to perform scanning measurements.

An event was triggered if the core signal exceeded a threshold of 25 ADC counts, corresponding to approximately 10 keV, in an trapezoidal trigger filter. The DAQ read out core and all segments simultaneously if an event passed the trigger. Most of the time, only the time and energy information for each channel was stored (ET Mode). For some measurements, the pulse shape of all channels were stored additionally (PS Mode). For all analyzes, a threshold of 20 keV was applied to reduce trigger turn on effects. The recorded data sets and their purposes are listed in Tab. 11.1.

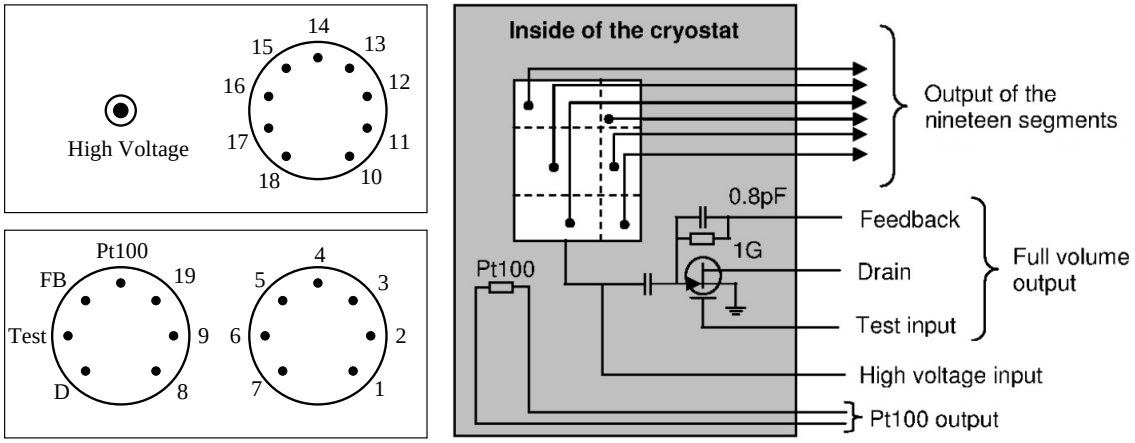

Figure 11.4.: (a) Feed-throughs of the SuSie test stand. Channels 1–9, channel 19, the Pt 100, the test, feedback (FB) and drain (D) from the core were connected through the two 7-channel feed-throughs. Channels 10–18 were connected through the 9-channel feed-through. (b) Schematics of the front-end electronics.

11.4. Monte Carlo Simulation

A simplified version of the test stand geometry implemented in GDML2.10.0.p01 was used to generate Monte Carlo (MC) samples using the MaGe [96] framework in conjunction with GEANT4.9.0.p01 [97,98]. The characteristics of the vacuum cryostat were taken from a previous simulation of the same cryostat [110]. The vacuum cryostat had a thickness of 2 mm and was simulated as aluminum alloy. The tungsten collimator was assumed to be 100% tungsten.

The simulated crystal was a true coaxial detector and had a size of 70 mm in height, an inner radius of 5 mm and an outer radius of 37.5 mm. The conical ends of the inner bore hole were taken into account. The whole detector acted as active material, no dead layers were taken into account. The 19th segment has a thickness of 5 mm and the layer of segments below the 19th segment has a thickness of 18.33 mm. The two lower layers had a thickness of 23.33 mm.

The detector holder including Teflon plugs were simulated with the opening angle between the three copper bars on top being exactly 120°.

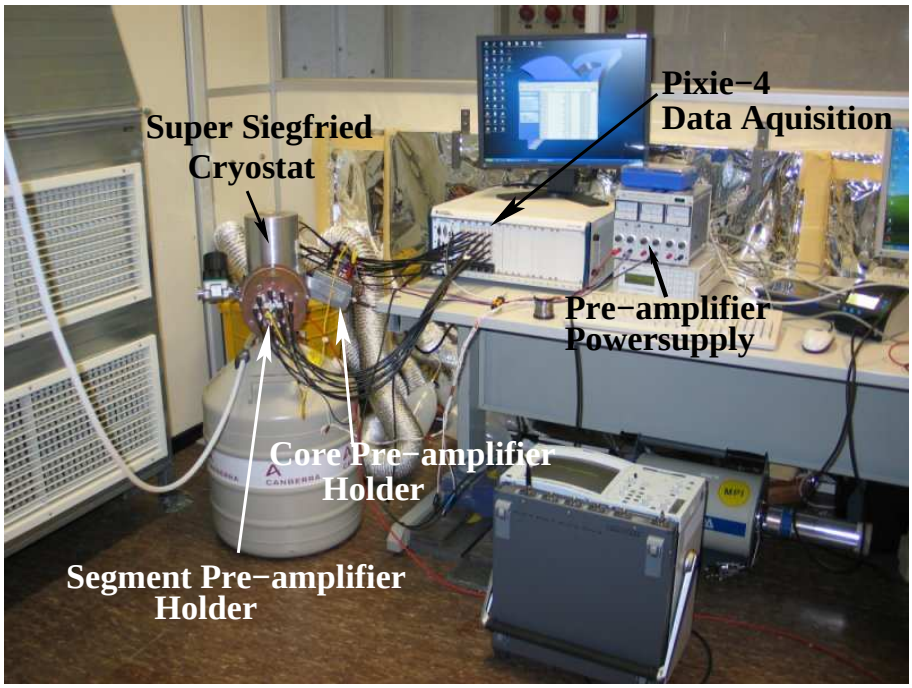

Figure 11.5.: Test setup inside the laboratory. Indicated are the cryostat, one of the boxes containing segment pre-amplifiers, the box containing the core pre-amplifier, the DAQ and the power supply for the pre-amplifiers.

Source	Type	Purpose	Mode
^{60}Co	Single	estimate depletion voltage through bias voltage change from 0-5000V in 500V steps	ET + PS
^{60}Co	Single	calculation of resolution, segment to segment cross-talk correction	PS
^{228}Th	Single	calculation of resolution,detector characterization, surface channel characterization	ET + PS
^{152}Eu	Scan z from side	determination of crystal position inside cryostat determination of segment boundaries in z direction	ET
^{152}Eu	Scan middle layer in ϕ from side	determination of segment boundaries in ϕ determination of crystal axis	PS
^{152}Eu	Scan 19th segment in ϕ from side	calculation of rise times in segment 19 characterization segment 19	PS
^{152}Eu	Scan 19th segment in ϕ from top	estimated of dead layer thickness	ET
^{152}Eu	Scan 19th segment in r from top	estimated of dead layer thickness	PS

Table 11.1.: The recorded data sets, their purpose and the data taking mode, pulse shape (PS) or energy and time (ET) are listed. The type of measurement “Single” indicates that the source was centered on top of the cryostat and a single data set was taken. “Scan” indicates that several data sets with either fixed radius and varying angle or height or fixed angle and varying radius were taken.

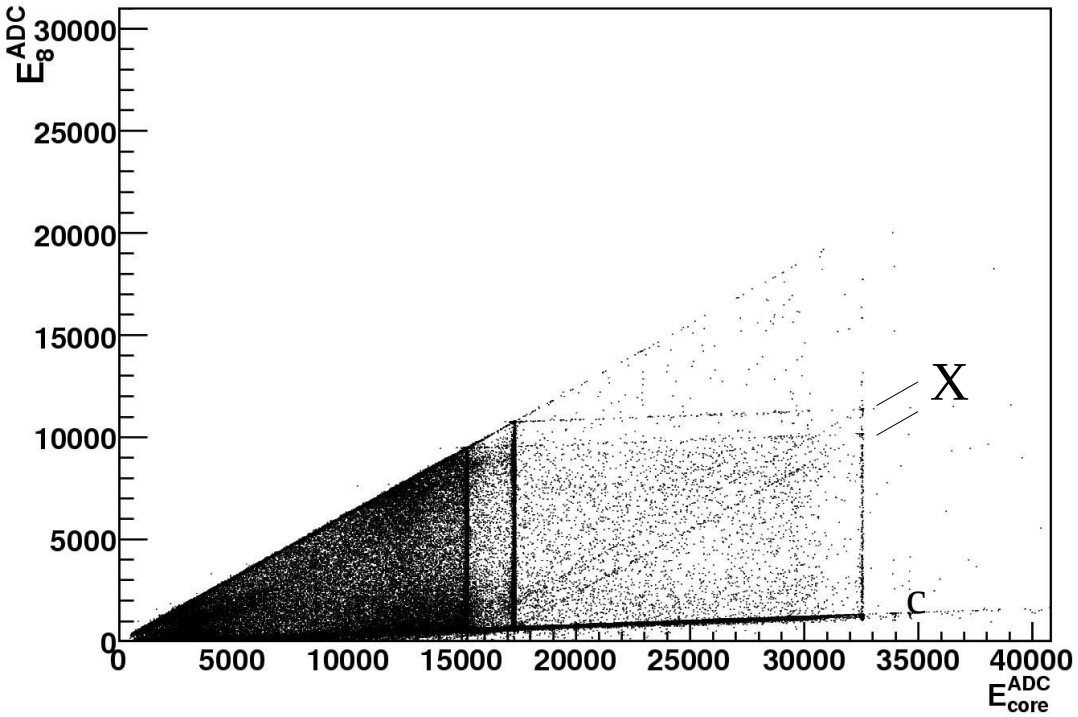

Figure 11.6.: Scatter plot of the energy in ADC counts seen for ^{60}Co in segment 8, E_8^{ADC}, as a function of the energy in ADC counts seen by the full detector, E_{core}^{ADC}. Each dot corresponds to one event. Cross-talk between the read-out channels of the core and segment 8 is visible as the slope of the line marked with c. For the explanation of "X" please refer to the text on page 100.

11.5. Calibration and Cross-Talk Correction

The electronics configuration as described in Sec. 11.2 results in the transmission of amplified core signals in close proximity to the transmission of unamplified segment signals. The energy in ADC counts in segment 8, E_8^{ADC}, as a function of the core energy in ADC counts E_{core}^{ADC} is shown in Fig. 11.6. The core channel caused strong cross-talk into the segment channels. Due to the cross-talk, an independent calibration of all channels using known photon lines in single segment events and under the assumption of linearity like,

$$E_i = S_i \cdot E_i^{ADC}, \tag{11.1}$$

with E_i, $i = \text{core}, 1, \ldots, 19$, being the calibrated energy and S_i being the calibration factor of channel i, could not be carried out.

Since only core to segment cross-talk was observed but not the reverse effect, it was not necessary to determine a full cross-talk matrix. The calibration and cross-talk corrections were carried out under two assumptions:

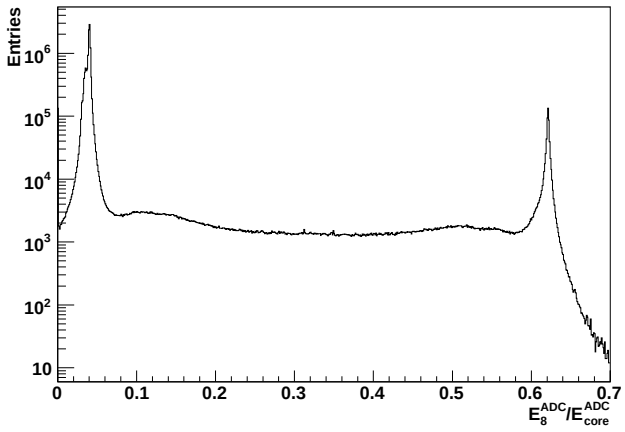

Figure 11.7.: Distribution of $E_8^{ADC}/E_{\text{core}}^{ADC}$. Two peaks are clearly visible. The first one at around $\kappa_8 = 0.04$ corresponds to the cross-talk from the core to segment 8. The other one at $R_8 \approx 0.62$ reflects the different responses of the read-out chains.

- the core can be calibrated independently;
- the cross-talk from core to segments is always positive.

These assumptions can be expressed in two equations:

$$E_{\text{core}} = S_{\text{core}} \cdot E_{\text{core}}^{ADC} \tag{11.2}$$

$$E_i = E_i^{ADC} \cdot a_i - E_{\text{core}}^{ADC} \cdot b_i, \tag{11.3}$$

where a_i and b_i are coefficients. The two cases $E_i = 0$ and $E_i = E_{\text{core}}$ yield two equations and a_i and b_i can be determined. E_i then becomes

$$E_i = \frac{E_i^{ADC} - E_{\text{core}}^{ADC} \cdot \kappa_i}{R_i - \kappa_i} \cdot S_{\text{core}} \tag{11.4}$$

with κ_i being the cross-talk correction coefficient, $\kappa_i = E_i^{ADC}/E_{\text{core}}^{ADC}$ if $E_i = 0$ and with $R_i = E_i^{ADC}/E_{\text{core}}^{ADC}$ if $E_i = E_{\text{core}}$, reflecting the different responses of the read-out chains. The coefficients κ_i and R_i can be obtained from the $E_i^{ADC}/E_{\text{core}}^{ADC}$ spectra, shown for segment 8 in Fig. 11.7. The first peak at $E_8^{ADC}/E_{\text{core}}^{ADC} = 0.04$ corresponds to κ_8, the second peak at $E_8^{ADC}/E_{\text{core}}^{ADC} \approx 0.62$ corresponds to R_8. The core to segment cross-talk correction factors κ_i for all affected segments are given in Tab. 11.2. The strongest cross-talk was observed between core and segment 8. In general segment channels connected to the same feed-through as the core signal suffered most from core to segment cross-talk, i.e. segment 8, 9 and 19.

segment	6	7	8	9	12	14	19
κ_i	0.0043	0.0015	0.04	0.014	0.0028	0.0083	0.0278

Table 11.2.: Core to segment cross-talk correction factors κ_i for all affected segments.

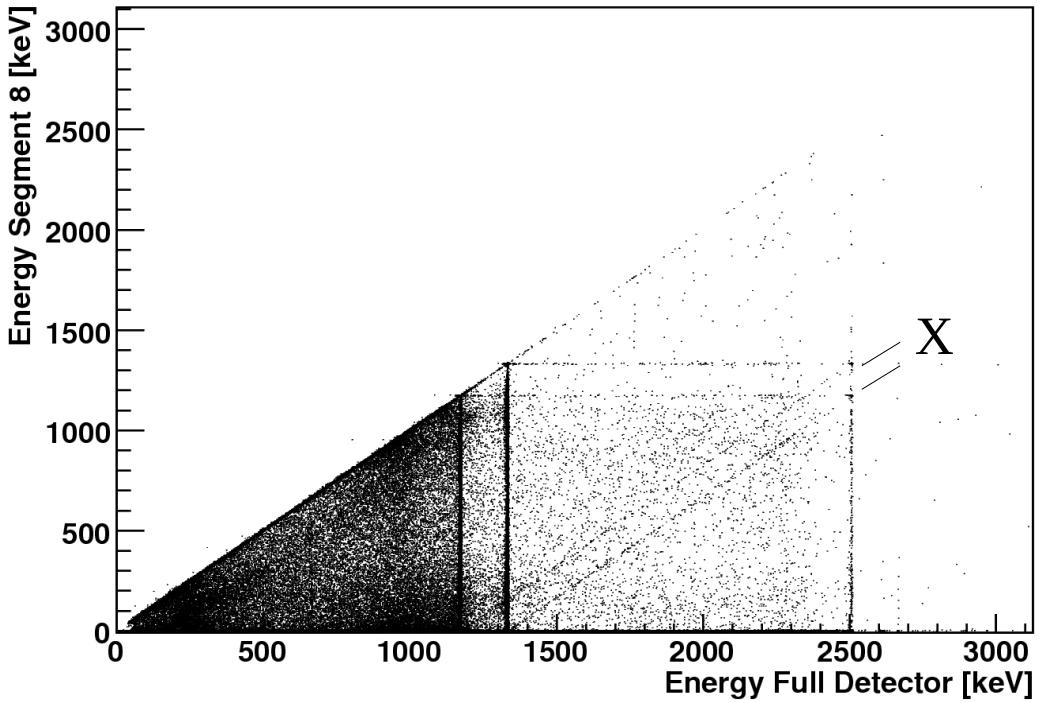

Figure 11.8.: Scatter plot of the energy seen for ^{60}Co in segment 8 as a function of the energy seen by the full detector. Each dot corresponds to one event. The same data as in Fig. 11.6 is shown but the energy calibration and cross-talk correction was carried out according to Eq. (11.4). For the explanation of "X" please refer to the text.

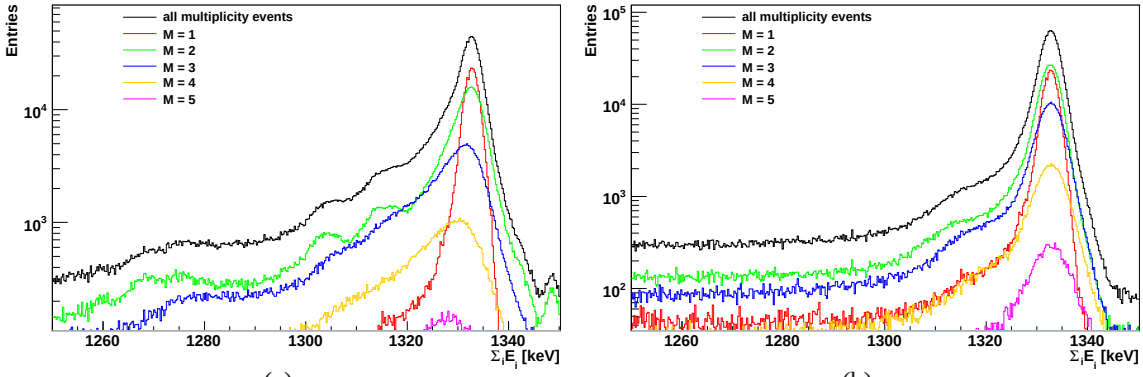

(a) (b)

Figure 11.9.: Segment energy sum decomposed into spectra with different segment multiplicities. (a) The uncorrected spectra are shown. Events with segment multiplicities $M > 1$ have their peak mean value shifted to lower energies. (b) The same plot is shown with segment to segment cross-talk correction applied. The resolution is improved and the spectra have the same peak mean value for all multiplicities.

The energy in segment 8 as a function of the core energy after calibration and cross-talk correction is shown in Fig. 11.8. The energy calibration worked and the cross-talk was successfully corrected.

Events with all energy deposited in segment 8 are located on the upper diagonal line. The vertical lines corresponded to events where the full energy is deposited in the detector, but only a fraction of that energy is deposited in segment 8. The horizontal lines are events where one of the two ^{60}Co photons is fully absorbed inside segment 8 and additional energy is deposited elsewhere in the detector. The two lower diagonal lines, marked with X, correspond to events, where one ^{60}Co photon is fully absorbed inside the detector not in segment 8, and additional energy is deposited in segment 8. Above the upper diagonal line no events are expected, since it is unphysical that the segments measured more energy than the core. However, some events are located there and will be discussed later in Chapter 14.

Direct segment to segment cross-talk not mediated by the core is not taken into account by the procedure described above. The sum of the energies of all segments, $\sum_i E_i$, for events with different segment multiplicities, M, is shown in Fig. 11.9. Negative segment to segment cross-talk is seen. Single segment events ($M = 1$) have the nominal peak position at 1332.5 keV. The energy peaks of higher M events are non-Gaussian, are shifted to lower $\sum_i E_i$ and the FWHM of the peaks is larger. The negative segment to segment cross-talk is also visible in events with $M = 2$ when plotting the energy in segment i, E_i, as a function of the energy in segment j, E_j, see Fig. 11.10(a).

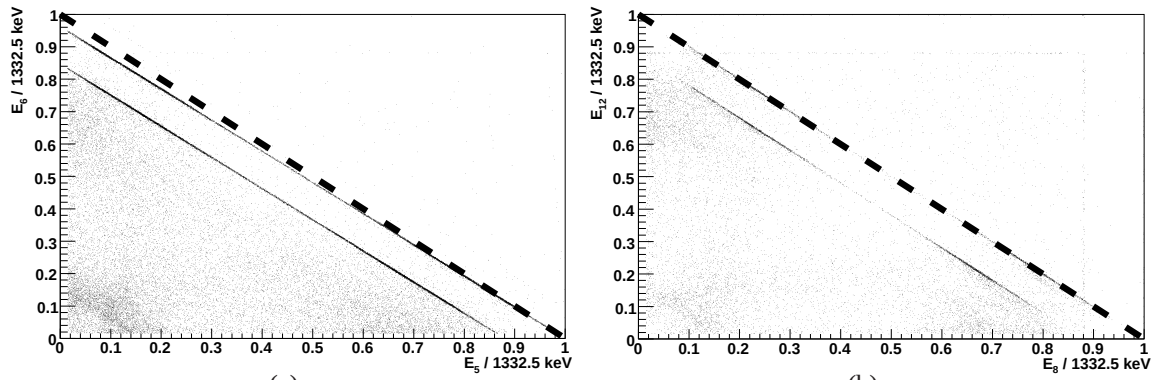

(a) (b)

Figure 11.10.: Events with multiplicity $M = 2$. (a) Energy deposit in segment 5 and segment 6 and (b) segment 8 and segment 12. Each dot corresponds to one event. The energy seen by each segment was divided by 1332.5 keV to normalize to the according ^{60}Co gamma line. The correlation between energy deposit in segment 5 and segment 6 exhibits cross-talk. The thick dashed line indicates where events with a total energy deposit of 1332.5 keV were expected to be without segment to segment cross-talk. No segment to segment cross-talk was observed between segment 8 and segment 12.

Negative segment to segment cross-talk can be corrected in the following way:

$$E_i^{true} = E_i^{meas} + \sum_{i \neq j, j=1}^{19} E_j^{meas} \cdot \delta_{ij}, \tag{11.5}$$

where E_i^{true} is the true energy deposited in the segment, E_i^{meas} is the measured energy in the segment and δ_{ij} are the cross-talk factors for cross-talk from segment j into segment i. The δ_{ij} were obtained from events with multiplicity $M = 2$ and a core energy between $(1173.24 - 1 \cdot \sigma)\,\text{keV} \leq E_{\text{core}} \leq (1173.24 + 1 \cdot \sigma)\,\text{keV}$ corresponding to one ^{60}Co peak and between $(1332.5 - 1 \cdot \sigma)\,\text{keV} \leq E_{\text{core}} \leq (1332.5 + 1 \cdot \sigma)\,\text{keV}$ corresponding to the other ^{60}Co peak, where σ was obtained from a fit to the corresponding photon line in the core energy spectrum. The segment energies of the events were normalized by the energy of the corresponding photon line. All possible combinations of normalized energy deposits in segment i vs. segment j were obtained. The unbinned data was fitted with a first order polynomial to describe the correlation between the segment energies. The factors δ_{ij} were calculated using the functions as shown in Fig. 11.11.

The $\sum_i E_i$ spectra for different M improved after the correction, see Fig. 11.9(b). The FWHM of the different multiplicity spectra before and after cross-talk correction are given in Tab. 11.3. The method yielded corrected segment to segment spectra, shown in Fig. 11.12. The method explained here gives compatible results as the method explained in [111].

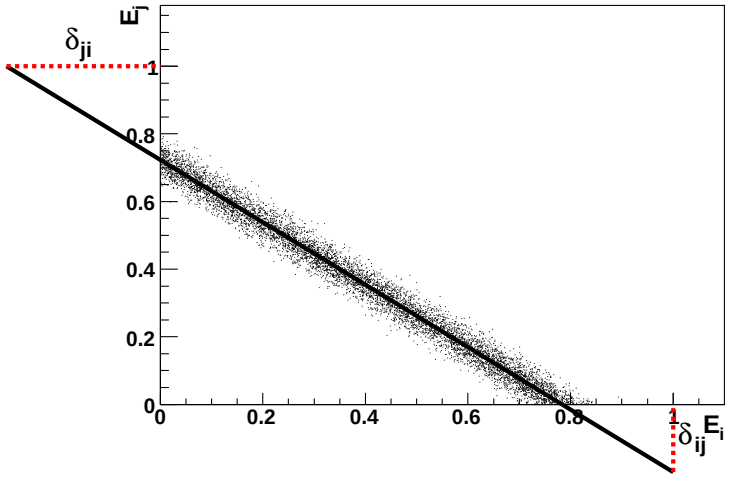

Figure 11.11.: Schematic drawing explaining the extraction of the segment to segment cross-talk correction factors δ_{ij} and δ_{ji}. The data was fitted with a polynomial of first order. The fitted function was used to calculate δ_{ij} and δ_{ji}.

Multiplicity	Mean^{meas}[keV]	Mean^{true}[keV]	ΔE^{meas}[keV]	ΔE^{true} [keV]
all	1332.30 ± 0.01	1332.66 ± 0.01	5.23 ± 0.01	4.62 ± 0.01
1	1332.52 ± 0.01	1332.52 ± 0.01	3.54 ± 0.01	3.54 ± 0.01
2	1332.08 ± 0.01	1332.58 ± 0.01	6.36 ± 0.01	4.68 ± 0.01
3	1329.76 ± 0.02	1332.62 ± 0.01	9.50 ± 0.04	5.79 ± 0.01
4	1327.51 ± 0.04	1332.58 ± 0.01	11.97 ± 0.09	6.93 ± 0.03
5	1324.98 ± 0.37	1332.41 ± 0.05	15.04 ± 0.37	8.54 ± 0.11
6	1323.22 ± 0.96	1332.70 ± 0.14	16.32 ± 1.15	7.73 ± 0.32

Table 11.3.: Mean value and energy resolution, ΔE, of the peak in the $\sum_i E_i$ spectrum for different M for the 1332.5 keV ^{60}Co peak before, *meas*, and after, *true*, segment to segment cross-talk corrections.

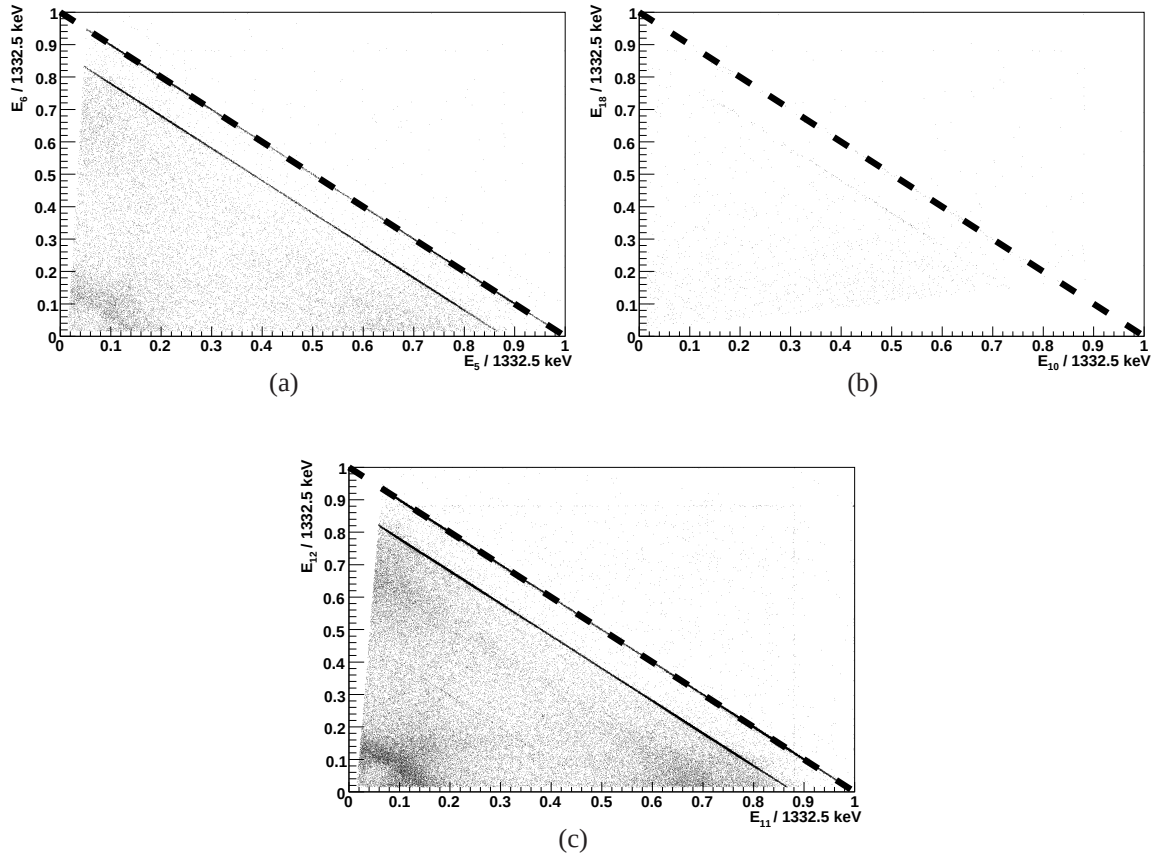

Figure 11.12.: Two segment events with energy deposit in: (a) segment 5 and segment 6, (b) segment 10 and segment 18 and (c) segment 11 and segment 12 after segment to segment cross-talk correction. Each dot corresponds to one event. The energy seen in each segment was divided by 1332.5 keV to normalize to the corresponding ^{60}Co gamma line. The thick dashed line indicates where events from the 1332.5 keV ^{60}Co should cluster without segment to segment cross-talk. The areas without events in (a) and (c) at low E_5 and low E_{11} values, respectively, and in (b) at low E_{18} values are due to the fact that the energy is shifted towards higher values during cross-talk correction, but the DAQ did not record negative values for energies.

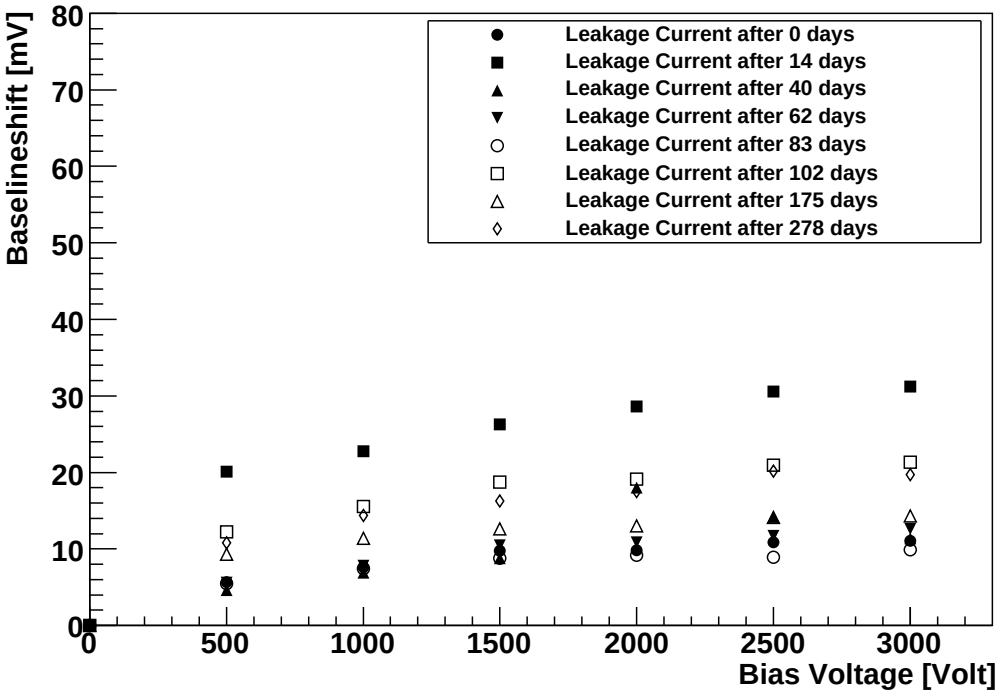

Figure 11.13.: Voltage dependence of the sum of the segment baseline shifts at different dates.

11.6. Basic Detector Properties

11.6.1. Leakage Current

The leakage current was monitored regularly using the baseline dependence of the DC coupled segment pre-amplifiers on the bias voltage. The shifts were not calibrated; however 1 meV of shift corresponds to the order of one picoampere of leakage current. The bias voltage was ramped up in 500 V steps. The sum of the baseline shifts as a function of the applied bias voltage for measurements at different times is shown in Fig. 11.13. A slight increase in the baseline shift with increasing bias voltage is visible and expected. Fig. 11.14 shows the baseline shift of the whole detector and segment 19 over time. No systematic increase in leakage current with ongoing operation is observed, implying that no detector damage developed. The variations can come from different operational temperatures.

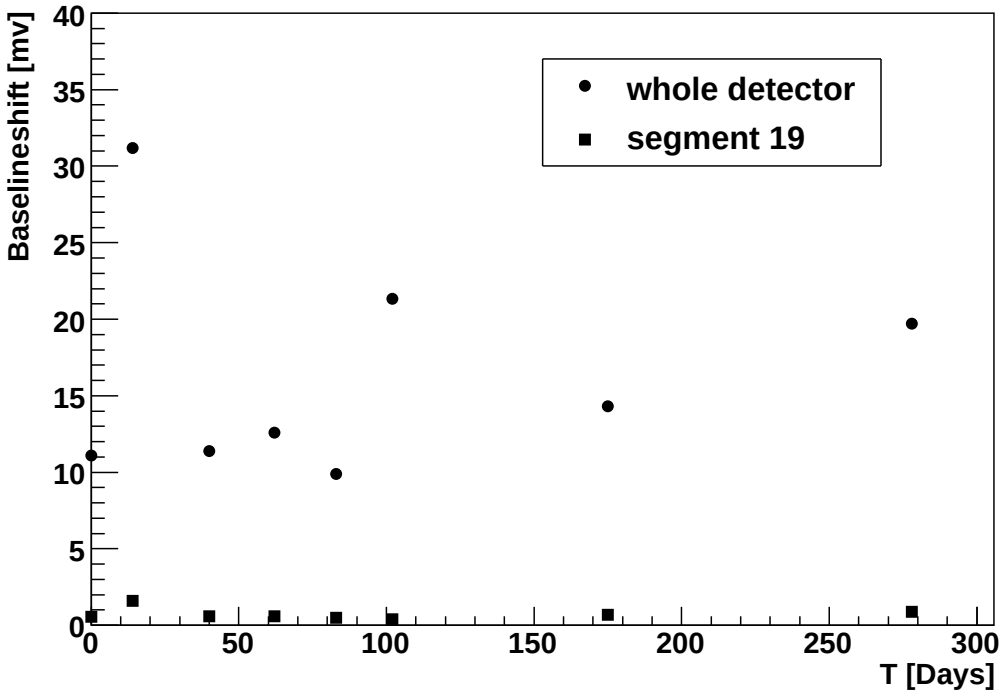

Figure 11.14.: Sum of the segment baseline shifts and shift of the 19th segment as a function of days expired.

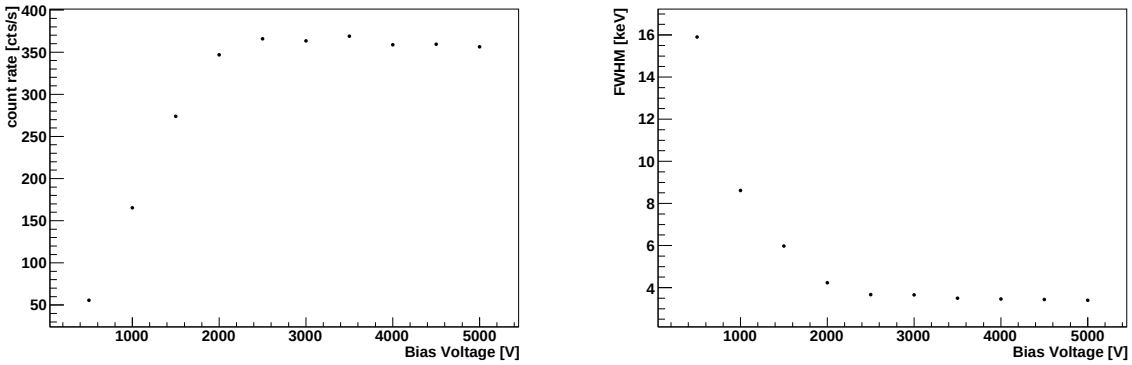

(a) (b)

Figure 11.15.: (a) Count rate of the core and (b) FWHM as a function of the bias voltage. Error-bars are included but invisible due to marker size.

11.6.2. Bias Voltage

The count rate, i.e. the number of counts in a certain energy window per time interval, was extracted from the ^{60}Co data sets at different bias voltages. The voltage dependence of the count rate of events under the 1332.5 keV peak is presented in Fig. 11.15(a). It is clearly visible how the count rate increased with increasing bias voltage and then saturated around 2500 V. Partially depleted semi-conductor detectors have a reduced charge collection efficiency, therefore, the count rate rises until full depletion is reached. The onset of the plateau is consistent with a full depletion at 2250 V as determined in Sec. 11.1.

In Fig. 11.15(b) the resolution (FWHM) as a function of the applied voltage is shown. Clearly visible how the resolution dropped with increasing voltage and stabilizes around 2500 V when full charge collection efficiency at full depletion was reached.

11.6.3. Linearity

A linear detector response was assumed for the calibration described in Sec. 11.5. The energies measured in ADC counts versus the energies of known photon lines in the ^{228}Th spectrum including background are shown in Fig. 11.16(a). The line represents a linear fit to the data. The deviations from the fit , i.e. the residuals in ‰ are given in Fig. 11.16(b).

11.7. Determination of Segment Boundaries

The segment boundaries were extracted from the count rate of the segments as a function of the source position in azimuthal angle ϕ. The ^{152}Eu scan ϕ for the central layer and scan z data sets at $\phi = 170\,^{\circ}$ were used.

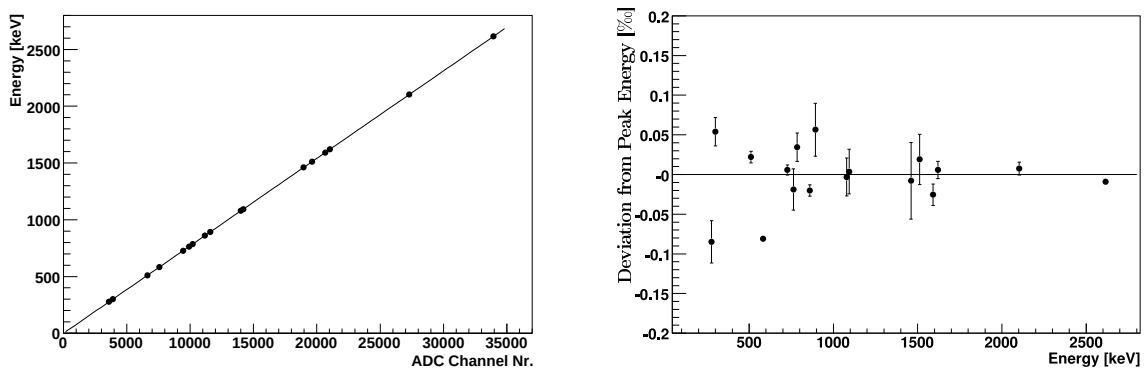

(a) (b)

Figure 11.16.: (a) Linearity and (b) the residuals of the response to lines in the ^{228}Th spectrum including background. The line in (a) represents the linear fit.

The count rate was calculated from the number of events under the 121.78 keV gamma line of ^{152}Eu. The number of events under the peak were calculated from a Gaussian plus first order polynomial fit representing the photon peak and background. The count rate for core and segments as a function of ϕ is shown in Fig. 11.17. The count rate for core did vary between 1.4 cts/s and 1.9 cts/s. No trend is visible. At 50°, 170° and 280° the count rate dropped, because there the vertical copper bars of the detector holders were partially absorbing and scattering the photons.

The count rate of the segments was zero if the source was not positioned in front of the corresponding segment. It was around 1.6 cts/s if the source was positioned in front of the segment. The count rate was fitted with a box smeared with a Gaussian representing the size of the irradiated spot. Due to a lack of scanning points this method did not succeed in the precise determination of the boundaries.

Instead, it was assumed that the segment boundaries are at the positions where the count rate dropped to half of the averaged count rate of the central scan points in the segments, omitting the scan points in front of a vertical holder bars. This just corresponds to the simple geometrical picture of a source located exactly in front of the segment boundary.

The weighted-mean of the count rate of the central scan points was calculated. A linear interpolation was used to extract the positions where half of the weighted mean of the count rate were reached. These positions defining the segment boundaries are given in Tab. 11.4. The uncertainties were estimated by varying the positions and the weighted mean of the count rates by their assigned uncertainties.

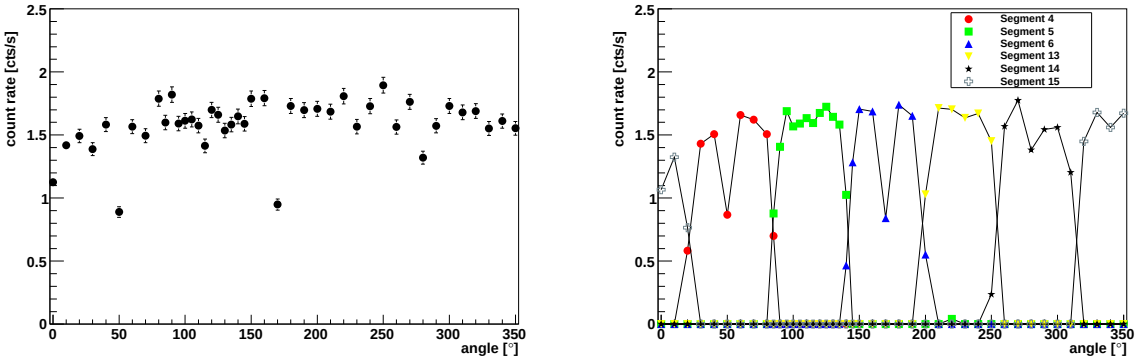

(a) (b)

Figure 11.17.: Count rate of (a) the core electrode and (b) the segment electrodes as a function of the azimuthal angle ϕ. The count rate was extracted from the number of events under the 121.78 keV ^{152}Eu peak. It dropped at 50°, 170° and 280°. The three copper bars of the detector holder absorbed and scattered the low energy photons. The lines in (b) do not have any physical meaning and are only shown to guide the eye.

The 121.78 keV photons from the ^{152}Eu source are not all absorbed right at the surface. Therefore, the effect of the anisotropic drift of the charge carriers inside the crystal can effectively change the size of the segments from the geometrical 60°.

The segment boundaries in height z are extracted in the same way, using the z-scan data set. The count rate as a function of source position in z is shown in Fig. 11.18. The position of the segment boundaries in height z is shown in Tab. 11.5.

Segments	$\phi_1[^\circ]$	$\phi_2[^\circ]$	$\phi_2 - \phi 1[^\circ]$
1,4,7	22.0 ± 1.0	84.5 ± 1.0	62.5 ± 1.41
2,5,8	84.6 ± 1.0	142.5 ± 1.0	57.9 ± 1.41
3,6,9	142.2 ± 1.0	197.5 ± 1.0	55.3 ± 1.41
16,13,10	198.2 ± 1.0	254.2 ± 1.0	56.0 ± 1.41
17,14,11	254.2 ± 1.0	315.0 ± 1.0	60.8 ± 1.41
18,15,12	315.0 ± 1.0	19.6 ± 1.0	64.6 ± 1.41

Table 11.4.: Segment boundaries,ϕ_1 and ϕ_2, in the azimuthal angle ϕ, extracted from the count rate of segments 4,5,6,13,14,15. It was assumed that the boundary position in the azimuthal angle ϕ is independent of the z position.

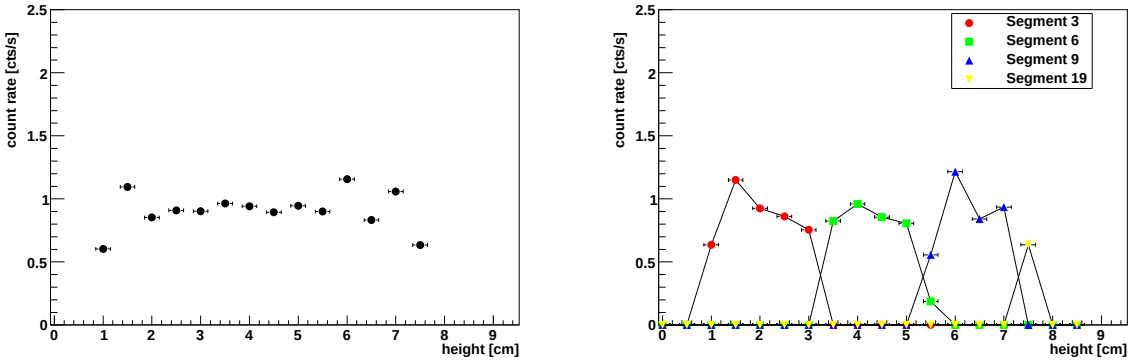

(a) (b)

Figure 11.18.: Count rate extracted form the number of events under the 121.78 keV gamma peak from ^{152}Eu as a function of the position of the source in the height z is shown. In (a) the core count rate and in (b) the segment count rate is shown. The line in (b) is just to guide the eye and has no physical meaning.

Segments	Lower boundary [cm]	Upper boundary [cm]	Thickness [cm]
1,2,3,16,17,18	0.87 ± 0.15	3.19 ± 0.15	2.32 ± 0.21
4,5,6,13,14,15	3.25 ± 0.15	5.32 ± 0.15	2.07 ± 0.21
7,8,9,10,11,12	5.42 ± 0.15	7.25 ± 0.15	1.83 ± 0.21
19	7.25 ± 0.15	7.75 ± 0.15	0.50 ± 0.21

Table 11.5.: Segment boundaries in height z, measured for the segments 3,6,9,19. It is assumed that the boundary position in z is independent of the ϕ position.

11.8. Spectra and Resolution

11.8.1. Energy Spectra

The energy spectra of the ^{60}Co data set of core and all 19 segments are shown in Fig. 11.19. The core spectrum is shown in the top left corner. The arrangement of the segment spectra corresponds to the segmentation shown in Fig. 11.1(b). The core spectrum shows the typical ^{60}Co photon peaks at 1173.2 keV and at 1332.5 keV and the summation peak at 2505 keV. The single escape peak (SEP) from the 1173.2 keV line at 662 keV is visible. The SEP from the 1332.5 keV line is hidden in the Compton background. There are gamma lines from natural radioactivity in the surrounding, at 1460 keV, 1765 keV and at 2615 keV from decays of the isotopes ^{40}K, ^{214}Bi and ^{208}Tl, respectively. In the segment spectra, only the ^{60}Co lines are visible.

Since the source was located above the cryostat, the bottom layer of segments has the fewest entries, but under the two ^{60}Co peaks there are always $O(10^3)$ events.

11.8.2. Influence of the Read-Out Chain

The broadening of the spectral lines due to electronics noise was measured for each read-out chain using a BNC PB-5 pulse generator connected to the test inputs of the corresponding pre-amplifiers. Pulses with a rise time of 200 ns and a rate of 100 Hz were used. When connecting the pulser to a segment pre-amplifier, an inverted pulse was sent to the core channel to trigger the DAQ.

The peak due to the pulser was recorded together with a ^{60}Co spectrum used for calibration. The core spectrum with the pulser induced peak at 1286 keV is shown in Fig. 11.20. It was fitted with a Gaussian plus first order polynomial. The resolution was extracted from the fit. It was 1.99 ± 0.01 keV for the core, varied between 2.19 ± 0.02 and 3.07 ± 0.06 for regular segments and was 7.33 ± 0.13 keV for segment 19. The resolution of each channel is given in Tab. 11.6.

11.8.3. Energy Resolution of Core and Segments

Resolutions (FWHM) were extracted from fits of a first order polynomial plus Gaussian to the photon peaks. The resolution was 3.05 ± 0.02 keV at 1332.5 keV for the core and between 2.6 keV and 3.4 keV at 1332.5 keV for the segments. The resolution of segment 19 was 7.61 ± 0.22 keV at 1332.5 keV. The resolutions for core and all segments are given in Tab. 11.6.

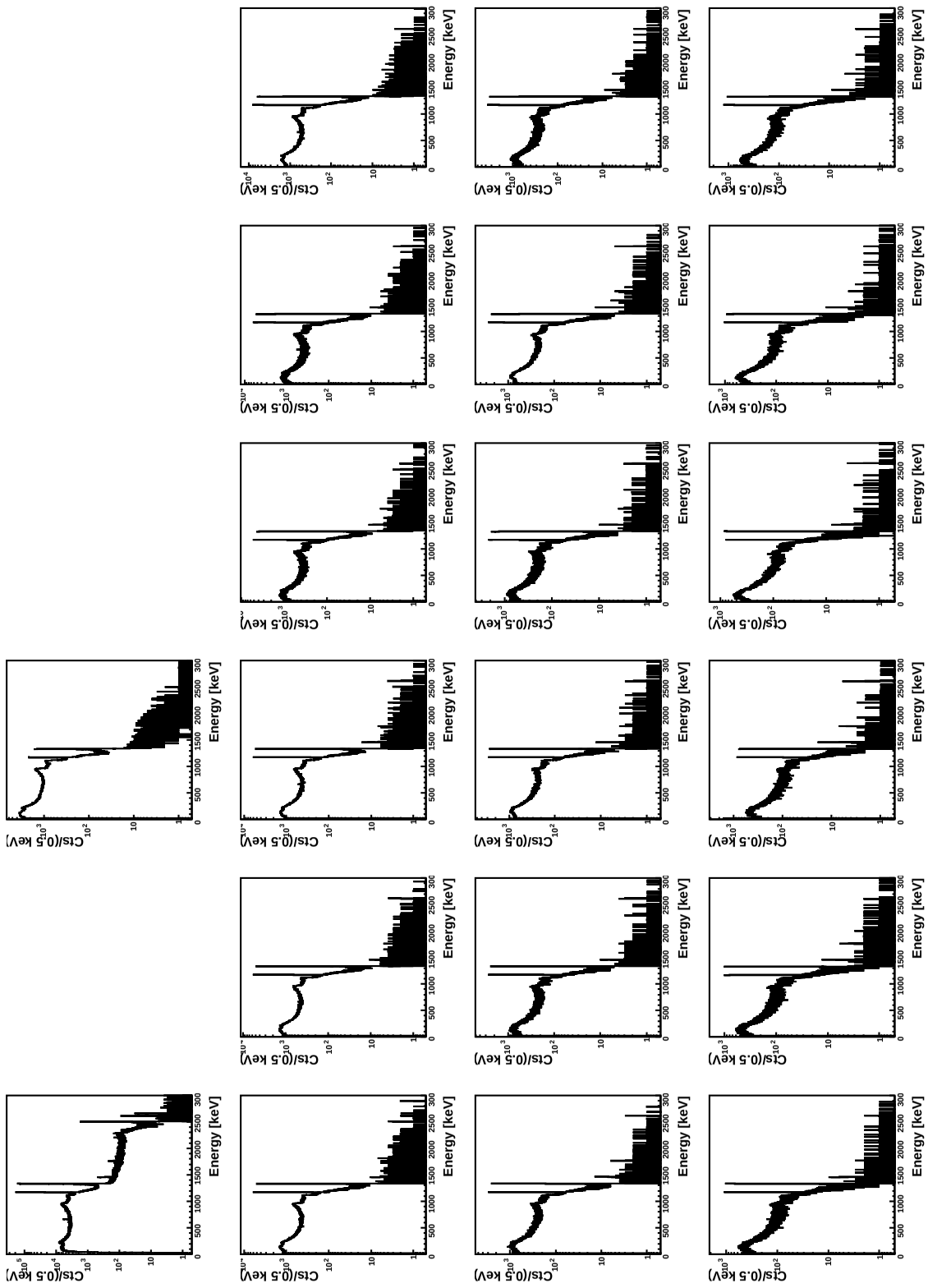

Figure 11.19.: ^{60}Co energy spectra of the core (top left) and all 19 segments when read out simultaneously. The arrangement of the segment energy spectra corresponds to the segmentation scheme shown in Fig. 11.1(b).

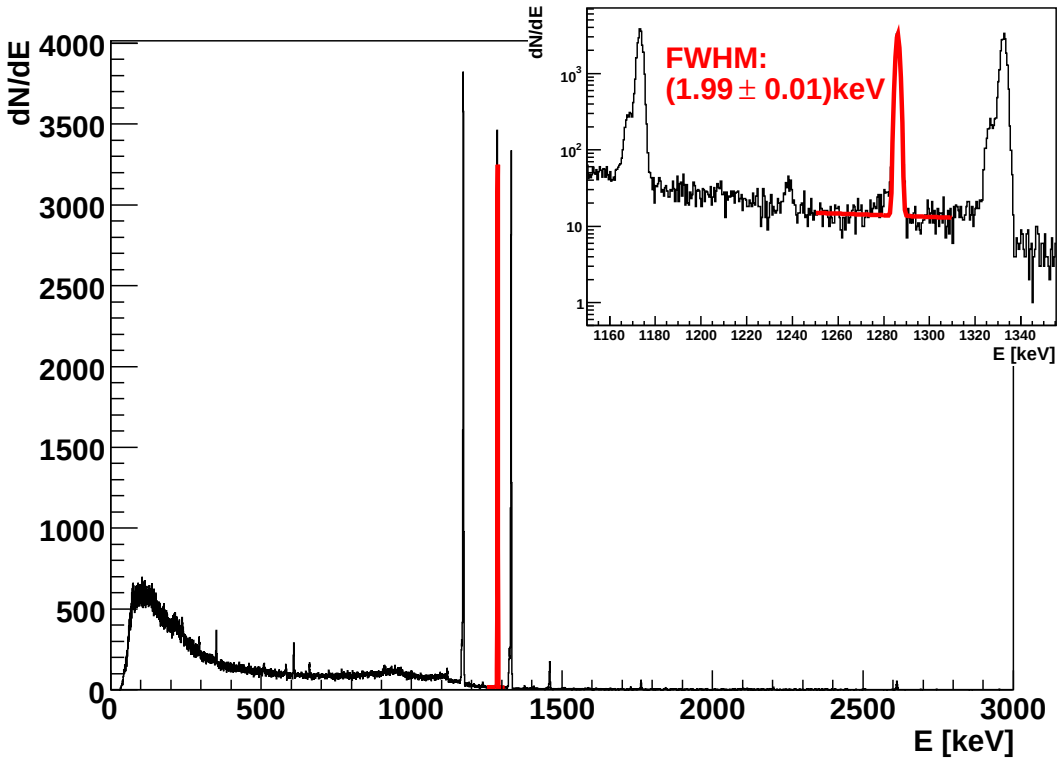

Figure 11.20.: Core spectrum of a ^{60}Co source with an additional peak at 1286 keV from a pulser signal applied to the test input of the core pre-amplifier. The non-Gaussian peaks of ^{60}Co will be discussed in Chapter 14.

11.8.4. Energy Resolution as Function of the Measured Energy

The core resolution as a function of the energy is shown in Fig. 11.21. Data from the ^{60}Co and the ^{228}Th data sets were combined.

The resolution as a function of the energy was fitted according to Eq. (7.10). The electronics contribution was measured as explained in section 11.8.2 and fixed in the fitting procedure. From the fit a Fano factor of 0.176 ± 0.01 was extracted.

11.8.5. Energy Resolution as Function of the Azimuthal Angle ϕ

The energy resolution at 121.78 keV as a function of the azimuthal angle ϕ was extracted from the ^{152}Eu scanning data set. The 121.78 keV gamma line was fitted with a Gaussian plus first order polynomial and the FWHM was calculated for the core and the segments. The result shown in Fig. 11.22.

Segment	Energy Resolution (FWHM) at 1332.5 keV [keV]	Resolution (FWHM) measured with Pulser [keV]	Resolution (FWHM) corrected for electronics contribution [keV]
core	3.05 ± 0.02	1.99 ± 0.01	1.99 ± 0.02
1	2.81 ± 0.07	2.22 ± 0.05	1.72 ± 0.05
2	2.77 ± 0.07	2.49 ± 0.05	1.21 ± 0.09
3	3.19 ± 0.08	2.94 ± 0.06	1.24 ± 0.10
4	2.64 ± 0.03	2.32 ± 0.04	1.26 ± 0.05
5	2.96 ± 0.04	2.66 ± 0.04	1.30 ± 0.06
6	2.80 ± 0.04	2.42 ± 0.04	1.98 ± 0.06
7	3.12 ± 0.03	2.84 ± 0.04	1.29 ± 0.05
8	3.16 ± 0.03	2.51 ± 0.03	1.92 ± 0.04
9	3.11 ± 0.03	2.53 ± 0.03	1.81 ± 0.04
10	3.11 ± 0.03	2.47 ± 0.03	1.89 ± 0.04
11	2.61 ± 0.02	2.19 ± 0.02	1.42 ± 0.02
12	3.37 ± 0.03	3.02 ± 0.03	1.50 ± 0.04
13	3.23 ± 0.04	2.75 ± 0.05	1.69 ± 0.06
14	2.71 ± 0.03	2.30 ± 0.04	1.43 ± 0.05
15	3.22 ± 0.04	2.35 ± 0.04	2.20 ± 0.06
16	2.80 ± 0.04	2.28 ± 0.05	1.63 ± 0.06
17	2.50 ± 0.06	2.21 ± 0.05	1.17 ± 0.08
18	2.70 ± 0.05	2.32 ± 0.06	1.38 ± 0.08
19	7.61 ± 0.22	7.33 ± 0.13	2.05 ± 0.26

Table 11.6.: Energy resolution of all segments and the total detector at 1332.5 keV. The ^{60}Co source was located centrally above the cryostat. The resolution measured with a pulser connected to the test input of the corresponding pre-amplifier is given in the third column. In column four the energy resolution corrected for the electronics resolution is given.

The resolution of the core at 121.78 keV is nearly constant and fluctuated around 1.5 keV. The resolution of the segments differed from segment to segment between 2 keV and 3 keV. Within one segment the resolution was nearly constant.

As each segment is connected to a different read-out chain, the contributions from the electronic is different for each segment. This dominates the variation from segment to segment, see Tab. 11.6.

11.8.6. Energy Resolution as Function of Height z

The energy resolution as a function of the source position in the height z was measured. The source was positioned in the middle of the segment in ϕ. The position in z was varied in 0.5 cm steps.

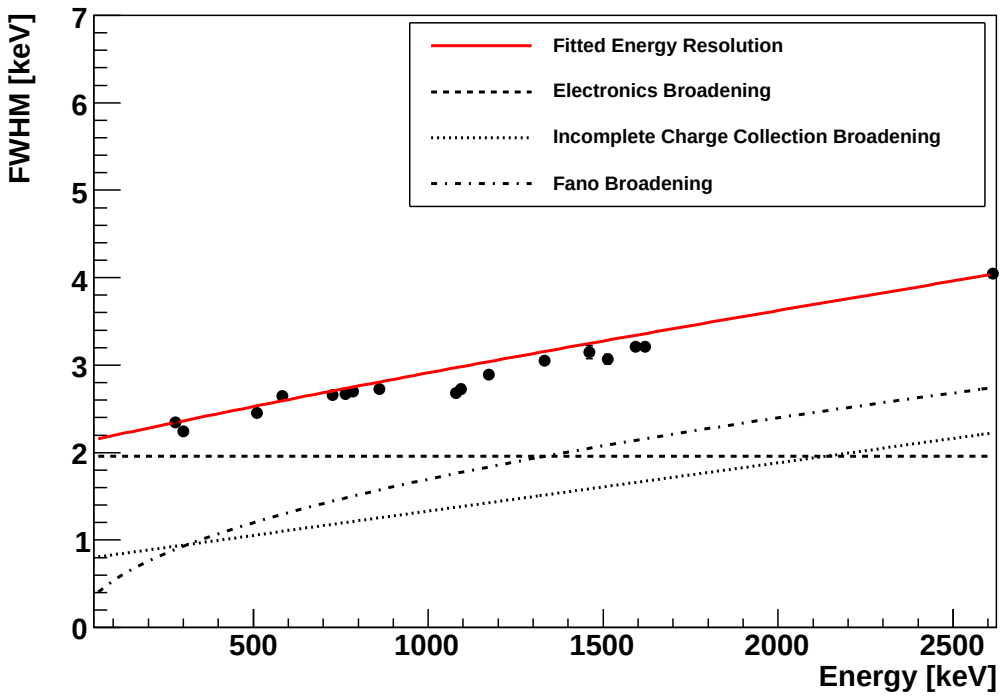

Figure 11.21.: Energy dependence of the detector. The Fano factor extracted from the fit was $= 0.176 \pm 0.01$.

The FWHM was extracted from a fit of a first order polynomial plus Gaussian to the 121.78 keV photon peak of ^{152}Eu. The FWHM is shown in Fig. 11.23(a) for the core and in Fig. 11.23(b) for the four segments concerned.

The core energy resolution was, again, approximately 1.5 keV. The energy resolution of the segments differed from segment to segment between 2 keV and 3.5 keV. The energy resolution of segment 6 measured in the ϕ scan and in the z scan agreed within statistical uncertainties. The resolution of segment 19 was 8.49 ± 0.69 keV.

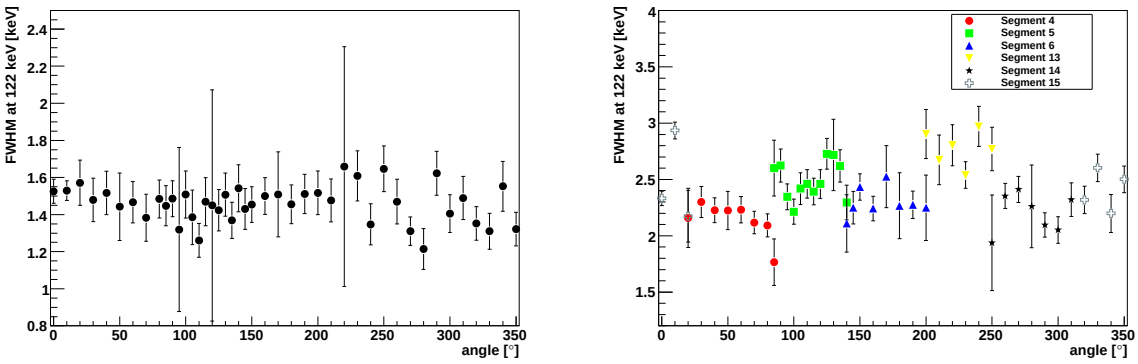

(a) (b)

Figure 11.22.: The FWHM at 121.78 keV extracted from the ^{152}Eu data set as a function of the azimuthal angle ϕ. In (a) it is shown for the core and in (b) for all segments.

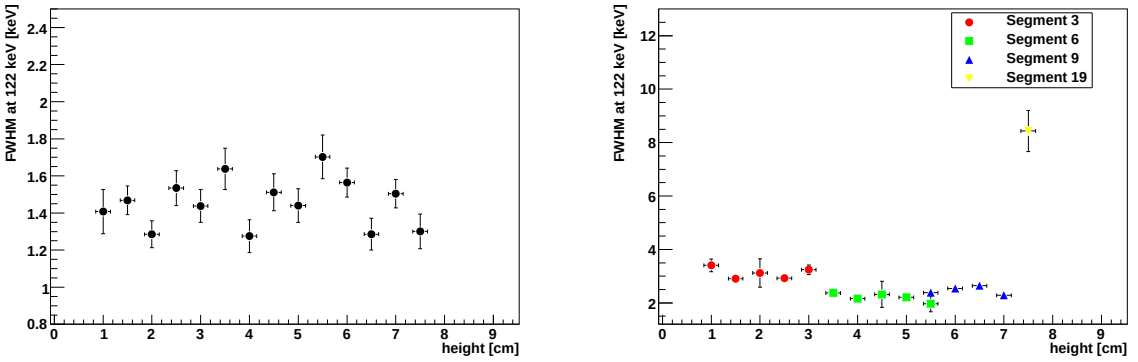

(a) (b)

Figure 11.23.: The FWHM at the 121.78 keV peak from the ^{152}Eu source (a) of the core electrode and (b) the segment electrodes as a function of the source position in the height z.

axis	first extremum [°]	second extremum [°]	third extremum [°]	fourth extremum [°]
$\langle 100 \rangle$	83.4	173.4	263.4	353.4
$\langle 110 \rangle$	38.4	128.4	218.4	308.4

Table 11.7.: Position of the extrema extracted from a fit to the $10\% - 90\%$ rise time distribution as a function of the azimuthal angle ϕ. The minima correspond to the axis $\langle 100 \rangle$ and the maxima correspond to the axis $\langle 110 \rangle$.

11.9. Pulse Shapes

Pulse shapes are the raw signals after pre-amplification and were recorded with the DAQ in PS-mode. An example of an 1408 keV single segment event from a ^{152}Eu source positioned at 120° is shown in Fig. 11.24. The core and segment five show a clear pulse. In segment 8, 9 and 19 the effect of core to segment cross-talk can be seen. A small induced positive pulse was recorded. Since the induced pulses corresponded to an energy less than 20 keV the calculated energy in these segments were set to zero. Mirror charges were visible in segment one, two, three, four and 6. In segment 9 the cross-talk and a mirror charge interfere.

11.9.1. Determination of Crystal Axes

The crystal axes were determined from the rise time distributions of the pulses as a function of the scanning angle ϕ.

The 121.78 keV peak was fitted with a Gaussian plus first order polynomial. Single segment events with a core energy, E_{core}, in the range $E_{\text{core}} \pm 3\sigma$, with σ as extracted from the fit, were selected. The rise time from 10% to 90% of E^{ADC} was calculated for each core and segment pulse. The resulting $10\% - 90\%$ rise time distributions were fitted with a Gaussian. The mean of the Gaussian is plotted as a function of the azimuthal angle ϕ and is shown in Fig. 11.25.

The fastest drift of charge carriers inside germanium is along the $\langle 100 \rangle$ axis, whereas the slowest drift is along the $\langle 110 \rangle$ axis (see Sec.10.4). Correspondingly, the shortest rise time is along the $\langle 100 \rangle$ axis and the longest along the $\langle 110 \rangle$ axis. The $10\% - 90\%$ rise time as a function of ϕ was fitted with

$$t_{10\%-90\%} = a + b \cdot \sin(c \cdot \phi + d), \tag{11.6}$$

where a, b, d were free parameters and c was fixed to 4 to account for the 4-fold symmetry. From the fitted function of the core the rise time minima and maxima were extracted. The position of the crystal axes is given in Tab. 11.7. Allowing c to be a free parameter in the fit yielded only slightly different values for the crystal axes.

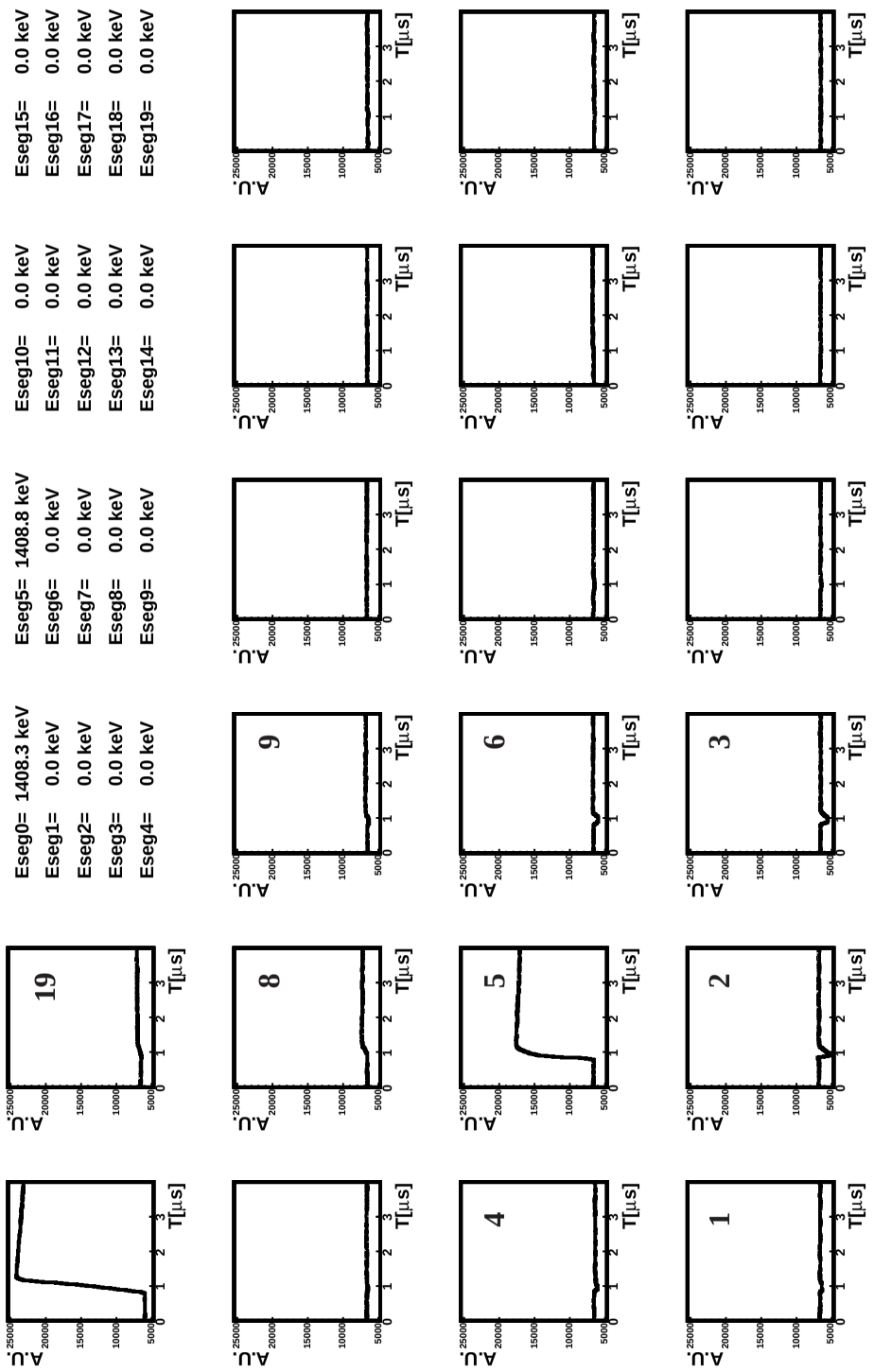

Figure 11.24.: Pulse shapes from core and all 19 segments read out simultaneously. The ^{152}Eu source was located at a position of $\phi = 120°$, in the middle of segment 5. The corresponding energies were calculated and listed in the top right corner.

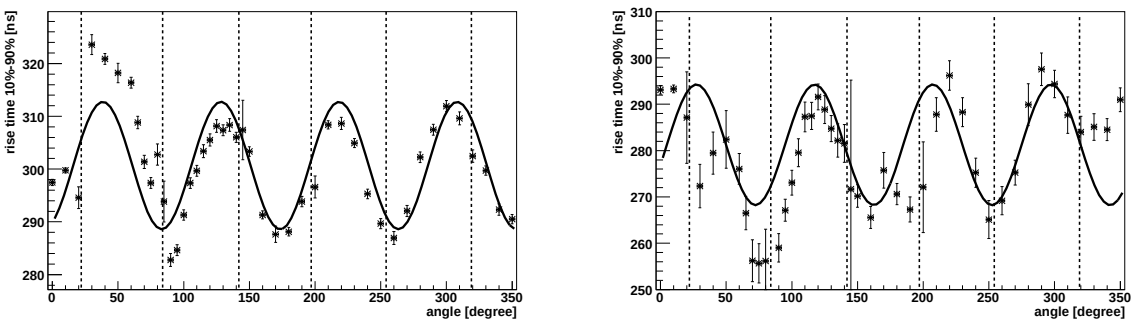

(a) (b)

Figure 11.25.: 10% – 90% rise time of (a) the core and (b) the segment signals as a function of the angular position of the ^{152}Eu source. The positions of the segment boundaries are indicated by the dashed lines.

12. Verification of the Pulse Shape Simulation

The pulse shape simulation described in Chapter 10 needs to be verified before its predictions can be trusted. The various steps of the simulation have to be separated as much as possible. Unfortunately, the electric field itself cannot be measured. Thus an experimental verification is impossible. Therefore, the iterative approach adopted was tested against an analytical calculation for the simple case of a radial field created for a constant impurity density ρ.

The only measurable objects are the pulse shapes produced by a detector under certain conditions. The verifications process can only rely on comparisons between measured and simulated pulses where the experimental conditions have to be simulated as well as possible.

As there are many parameters influencing the simulation, the goal is to determine whether the different contributions can be distinguished.

12.1. Comparison Between Analytical and Numerical Calculation of the Electric Field

The simple case where the electric field is calculated for a constant impurity density ρ, can easily be solved analytically. The numerical method described in Chapter 10 was tested on a $100 \times 100 \times 100$ grid against the analytical solution E_{ana} in the range of impurity densities from $\rho = 0\,\text{cm}^{-3}$ to $\rho = 0.83 \cdot 10^{10}\,\text{cm}^{-3}$. This represents a reasonable range for the detectors in question. The maximum deviation in field strength was below 1 % in all cases.

The resulting radial field for $\rho = 0.62 \cdot 10^{10}\,\text{cm}^{-3}$ is depicted in Fig. 12.1. The shapes and magnitudes are in good agreement. Only small differences are observed. The numerical results for $E(r)$ has an inflection point at r close to the outer surface. The analytical solution does not have this inflection. However, the effect is small.

The deviation is $(E_{\text{ana}} - E_{\text{num}})/E_{\text{ana}}$ in % shown in Fig. 12.2. The deviation decreases from inside out, but for the point at the maximal radius. The maximum deviation occurs at the outer edge of the detector at $r = 37.5\,\text{mm}$. This is due to the procedure employed

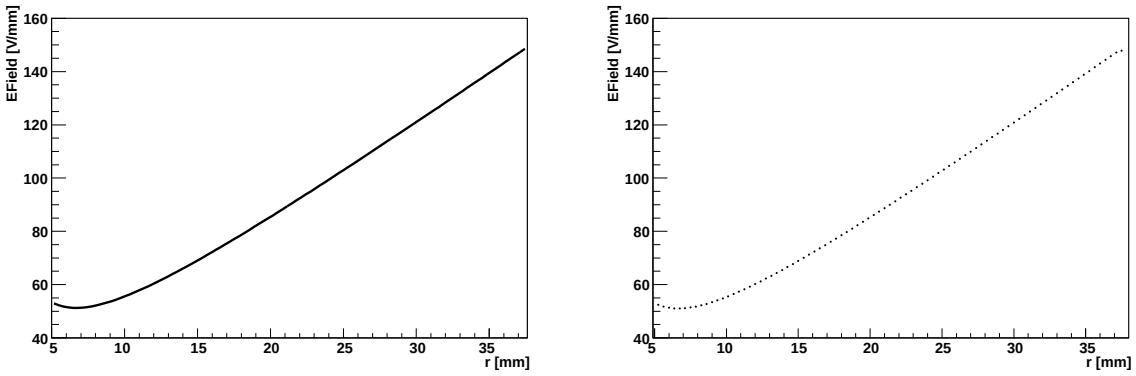

(a) (b)

Figure 12.1.: Radial electric field strength as a function of the radius, calculated (a) analytically and (b) with the method of Successive Over-Relaxation.

where the electric field is derived from the potential inside out with a three point estimation, which cannot be applied at the boundaries.

12.2. Influence of the Impurity Density on the Pulse Shapes

Two simulations were carried out with the detector axis fixed according to Sec. 11.9.1, i.e. the $\langle 100 \rangle$ axis at $\phi = 353.4^\circ$ and the $\langle 110 \rangle$ axis at $\phi = 38.4^\circ$. The impurity densities in the two simulation were $\rho = 0.83 \cdot 10^{10}\,\mathrm{cm}^{-3}$ and $\rho = 0\,\mathrm{cm}^{-3}$. The applied electrical potential was 3000V.

Pulse shapes were simulated for single energy deposits at a radius of $r = 37.4\,\mathrm{mm}$, close to the detector boundary, for varying ϕ. The impact of any impurity density change is expected to be large since the drift length of the electrons inside the detector is maximal. For each pulse the 10%-90% rise time was calculated.

In Fig. 12.3 the negative core and positive segment pulses for the single energy deposit at $\phi = 350^\circ$ and $\phi = 40^\circ$ are shown. The two positions were chosen since these are the closest position with data to the $\langle 100 \rangle$ axis and $\langle 110 \rangle$ axis.

The amplitude, the time and the radius r are implicitly connected through the Shockley-Ramo Theorem Eq. (7.7) and Eq. (10.12). The amplitude is calculated at each time step with the Shockley-Ramo Theorem, using the weighting potentials, which are position dependent. The position depends on $\mathbf{v}(r)$ which depends on $E(r)$. Thus, the shape of $E(r)$ influences the pulses shapes. For $\rho = 0.83 \cdot 10^{10}\,\mathrm{cm}^{-3}$, at large r, the radial electric field is

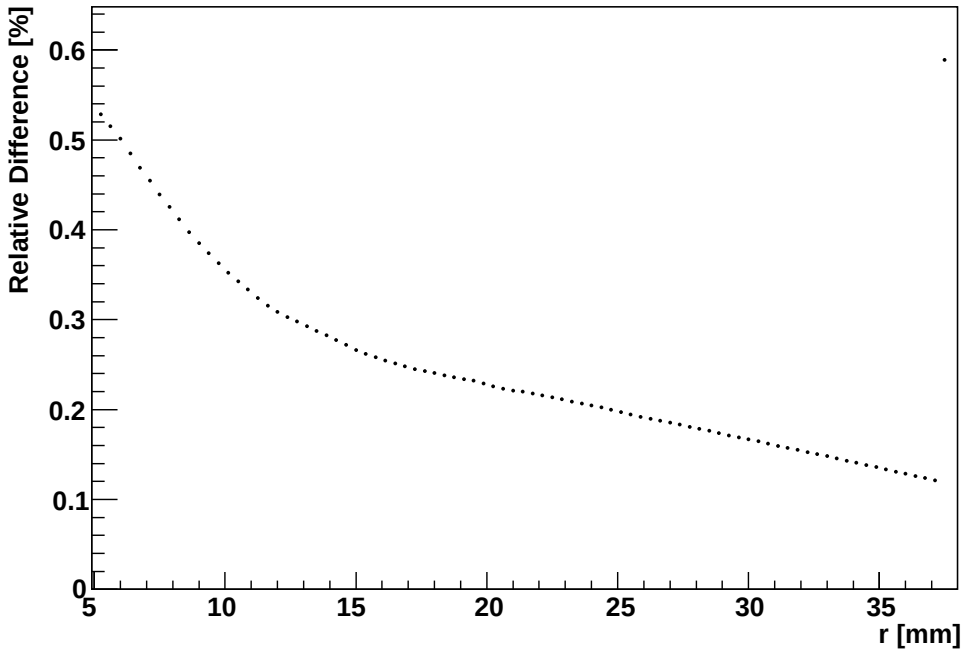

Figure 12.2.: Relative difference between the radial electric fields calculated analytically and with the method of Successive Over-Relaxation.

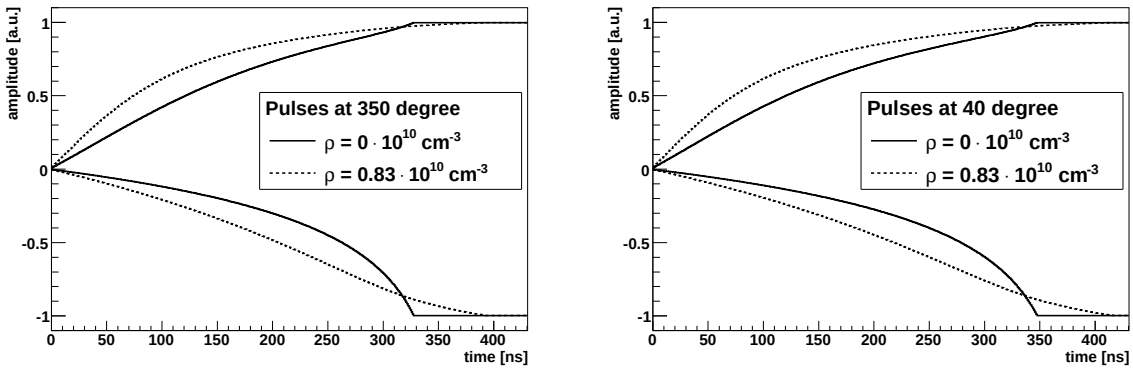

(a) (b)

Figure 12.3.: Induced pulse shapes of the core (negative pulse) and segment (positive pulse) at (a) $\phi = 350^\circ$ and (b) $\phi = 40^\circ$ at an impurity density of $\rho = 0\,\mathrm{cm}^{-3}$ and $\rho = 0.83 \cdot 10^{10}\,\mathrm{cm}^{-3}$, caused by a single point-like charge at $r = 37.4\,\mathrm{mm}$.

$E(r) > 150\,\mathrm{V/mm}$. It is small at small r, see Fig. 10.3. The difference in the weighting potentials of holes and electrons give the induced pulse magnitude, see Eq. (7.7). Therefore, the core pulse drops quickly and the segment pulse shape rises quickly. At small r, $E(r)$ is very low and thus $\mathbf{v}(r)$ is low. Therefore, the pulse is very long and has a small slope.

The situation is opposite in a detector with $\rho = 0\,\mathrm{cm}^{-3}$. The field $E(r)$ is low at large r and increases with decreasing r. Thus, the $\mathbf{v}(r)$ of the electrons and holes is low at large r and the difference in the weighting potential of electrons and holes is growing slowly. The amplitude of the pulse increases slowly. At low r, $\mathbf{v}(r)$ increases and the difference in weighting potential between electrons and holes is increasing rapidly, yielding a sharp end of the pulse.

The 100% rise time, $t_r^{100\%}$, of the pulses is different. At $\phi = 350^\circ$, along the $\langle 100 \rangle$ axis, at an impurity density of $\rho = 0\,\mathrm{cm}^{-3}$ ($\rho = 0.83 \cdot 10^{10}\,\mathrm{cm}^{-3}$) the rise time is $t_r^{100\%} = 329\,\mathrm{ns}$ ($t_r^{100\%} = 396\,\mathrm{ns}$). Along the $\langle 110 \rangle$ axis at $\phi = 40^\circ$ the rise time is $t_r^{100\%} = 349\,\mathrm{ns}$ ($t_r^{100\%} = 418\,\mathrm{ns}$). The difference at fixed impurity density and different position is caused by the longitudinal anisotropy, and is of the order of 20 ns. The difference at fixed position is caused purely by the difference in the impurity density. It is, for these extreme cases, of the order of 70 ns.

The 10%-90% rise times, $t_r^{10\%-90\%}$ as a function of the azimuthal angle ϕ is shown in Fig. 12.4. The 10%-90% rise time was chosen since it is the typical variable to describe the pulse length. In data $t_r^{100\%}$ cannot be determined due to noise. The sinusoidal pattern in the $t_r^{10\%-90\%}$ distribution is caused by the longitudinal anisotropy, the crystal axes effect. The change of the 10%-90% rise time due to the longitudinal anisotropy is of the order of 20 ns. The difference in the $t_r^{10\%-90\%}$ distribution due to the different impurity densities is large, approximately 60 ns or about 20%.

12.3. Full Spatial Simulation vs. Single Energy Deposit

To answer the question, whether the data can be compared to the simple scenario of one point-like charge or whether the actual spatial distribution of interactions is needed, the results from the previous scenario were compared with results from the ^{152}Eu case.

A simulation was carried out for photons with an energy of $E_\gamma = 121.78\,\mathrm{keV}$. The interactions of the photons were simulated using MAGE. The pulse shapes of single segment events, i.e. events where all energy is deposited in one segment, were added and normalized yielding a single averaged pulse shape.

The difference between the pulse shape from a single energy deposit and the average pulse shape from the energy deposits of photons with $E_\gamma = 121.78\,\mathrm{keV}$ is shown in Fig. 12.5.

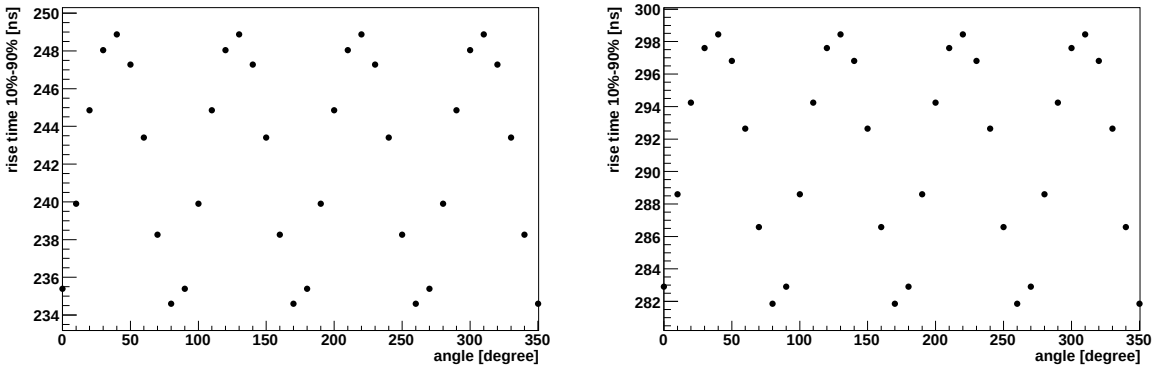

(a) (b)

Figure 12.4.: 10%-90% rise time of the pulses as a function of the angle: (a) for $\rho = 0\,\mathrm{cm}^{-3}$ and (b) for $\rho = 0.83 \cdot 10^{10}\,\mathrm{cm}^{-3}$ for a single point-like charge at $r = 37.4\,\mathrm{mm}$. Observe the different scales on the Y-axes.

Pulse shapes from many interaction positions are represented in the single averaged pulse shape (see Fig. 10.5 for the change of the pulse shape depending on the interaction positions). Therefore, the clear features of the pulse shape from the single energy deposit were smoothed. The full rise time of the pulses is the same. However, the 10% and 90% rise time is different.

In Fig. 12.6 the averaged pulse shapes are shown for core and segment at $\rho = 0\,\mathrm{cm}^{-3}$ and at $\rho = 0.83 \cdot 10^{10}\,\mathrm{cm}^{-3}$. After averaging the difference in the shapes is still clearly visible. In the $t_r^{10\%-90\%}$ distribution extracted from the averaged pulses, see Fig. 12.7, the effect of the longitudinal anisotropy is still present. The difference in the $t_r^{10\%-90\%}$ distribution between the pulses simulated from an electric field with impurity density of $\rho = 0\,\mathrm{cm}^{-3}$ and of $\rho = 0.83 \cdot 10^{10}\,\mathrm{cm}^{-3}$ has decreased from about 70 ns to 26 ns.

The significant differences between the results for the simple point-like charge and the ^{152}Eu scenario imply that the data has to be compared to the averaged simulated pulse from the ^{152}Eu simulation, tanking into account all interaction positions.

12.4. Comparison Between Simulated and Measured Pulses

The pulse shape simulation as described in Chapter 10 requires input parameters like assumptions about the mobility of the charge carriers and the exact distribution of the active impurity density $\rho(r)$, as well as the relative position of the crystal axes with respect to the segment boundaries.

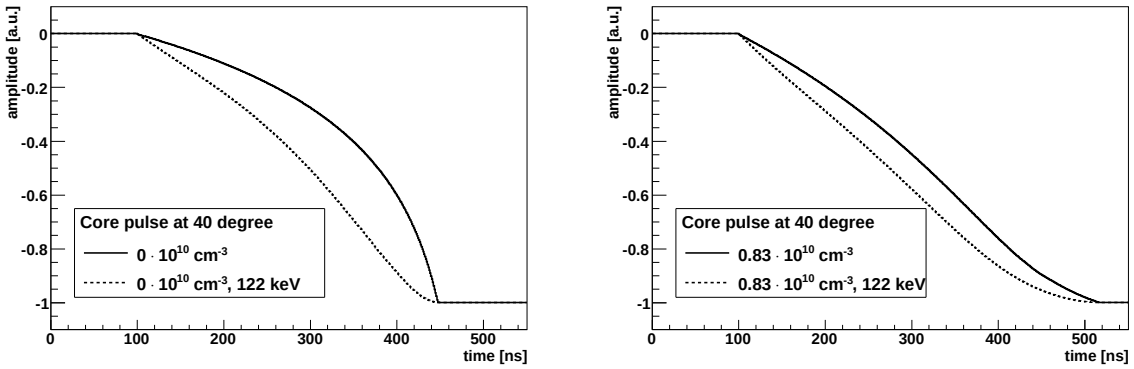

(a) (b)

Figure 12.5.: Comparison of the core pulse shapes from a single energy deposit (solid line) and from the $E_\gamma = 121.78\,\mathrm{keV}$ photons averaged pulse shape (dashed line) (a) for $\rho = 0 \cdot 10^{10}\,\mathrm{cm}^{-3}$ and (b) for $\rho = 0.83 \cdot 10^{10}\,\mathrm{cm}^{-3}$.

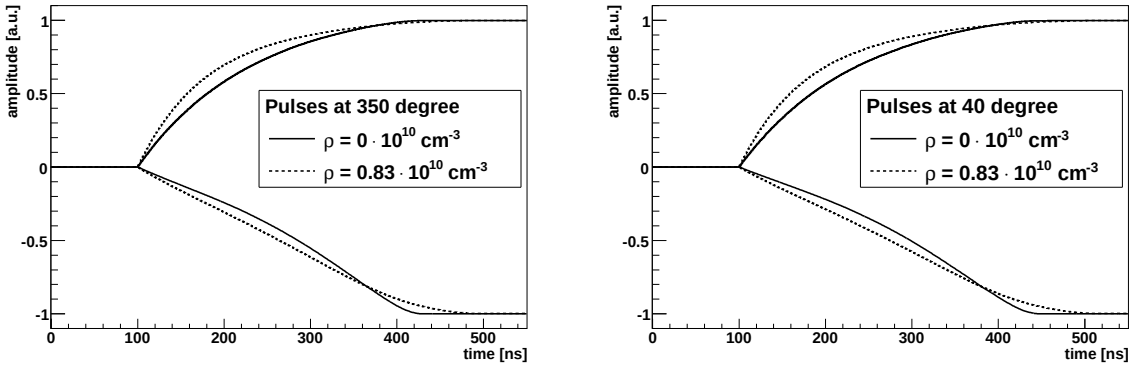

(a) (b)

Figure 12.6.: Averaged induced pulse shapes of the core and segment at (a) $\phi = 350^\circ$ and (b) $\phi = 40^\circ$ at an impurity density of $\rho = 0\,\mathrm{cm}^{-3}$ and $\rho = 0.83 \cdot 10^{10}\,\mathrm{cm}^{-3}$, caused by photons with $E_\gamma = 121.78\,\mathrm{keV}$ hitting the detector.

Deviations between simulated and measured pulses can arise due to imperfect input regarding all of these detector characteristics.

The data used was taken with a well understood detector, see Chapter 11 and 14. The impurity density of that detector was between $\rho = 0.44 \cdot 10^{10}\text{cm}^{-3}$ and $\rho = 1.30 \cdot 10^{10}\text{cm}^{-3}$ at the top and at the bottom of the detector, according to the manufacturer. According to measurements the SuSie detector was fully depleted at 3000 V. Thus, ρ can only vary between $0\,\text{cm}^{-3}$ and $0.83 \cdot 10^{10}\,\text{cm}^{-3}$. The crystal axes were determined previously, see Sec. 11.9.1.

Unfortunately, it is impossible to create point-like charges inside the detector to verify the radial dependence as shown in Section 10.6. The best available source to produce well located charge deposition was ^{152}Eu. The linear attenuation coefficient of the 121.78 keV photon line of ^{152}Eu in germanium is $\mu_{121.78} = 1.9252\,\text{cm}^{-1}$ [112].

12.4.1. Data Selection and Preparation

The data sets from the ^{152}Eu scan, see Tab. 11.1, of the middle layer were used. Events were selected if the following requirements were fulfilled:

1. the event was a single segment event and the event was in the segment where the source was located in front of;
2. the core energy was $117\,\text{keV} < E_{\text{core}} < 125\,\text{keV}$;
3. the difference between core and segment energy, E_i, was $|E_{\text{core}} - E_i| < 5\,\text{keV}$.

The peak to background ratio in each data set was better than 5 : 1 after the selection cuts.

It was not possible to compare single data pulses to the simulation due to noise levels and the uncertainty on the interaction position, see sec. 12.3. Therefore, pulses were averaged in the following way.

The time shift of the core pulses due to the sampling of the DAQ was estimated and was found to be less than 13 ns. Thus, no time shift correction was applied. The baselines of the selected pulses were removed and the pulses were normalized and added.

Averaged data pulses were obtained for the core and for the segment for each scan point. The averaging reduced the noise. More than 600 individual pulse shapes were summed up at each scan point.

A linear interpolation between the averaged data points was applied to re-sample the averaged data pulses at a 1 GHz sampling frequency. An uncertainty in the pulse amplitude for each sampling point was estimated using the baseline of the pulses. The deviation from zero in the first 500 ns was calculated. The resulting distribution was fitted with a Gaussian. The full width half maximum from the fit was assigned as the uncertainty at each sampling point.

12.4.2. Pulse Shape Simulation

The Monte Carlo simulation of photons with energy $E_\gamma = 121.78\,\text{keV}$ as described in Sec. 12.3 was used. Photons were simulated in steps of 10° at $z = 0$.

In the pulse shape simulation the $\langle 100 \rangle$ axis was set to 83.4° and the $\langle 110 \rangle$ axis was set to 38.4°, as for the SuSie detector, see Sec. 11.9.

Several electric fields with different impurity densities were calculated. The impurity density was uniform throughout the crystal. It was changed in steps between $\rho = 0\,\text{cm}^{-3}$ to $\rho = 0.83 \cdot 10^{10}\,\text{cm}^{-3}$. For each electric field the same simulation was carried out. The pulses were simulated with a sampling frequency of 1 GHz.

The pulses from the simulation were normalized and added with the same requirements as for the data pulses. Here, single segment events were selected after pulse shape simulation. This implicitly takes the influence of the crystal axes into account.

A simple model for the pre-amplifiers was used. A fixed decay time of $50\,\mu\text{s}$ was added to the averaged pulse shapes. Furthermore, each averaged pulse was modified to take into account different bandwidth , $BW \approx 1/(2\pi \cdot \tau)$, of the transmission, where τ is a time constant.

12.4.3. Comparison Between Data and Simulation

The averaged data and averaged simulated pulses were compared by fitting the simulated pulses to the data pulses using,

$$C_{meas}(t) = A \cdot C_{sim}(t/T_{scale} + T_O), \tag{12.1}$$

where A is an amplitude scale factor, T_O describes the time offset and T_{scale} is a time scaling factor. Thus, a $T_{scale} < 1$ implies that the simulated pulse was stretched and $T_{scale} > 1$ implies that the simulated pulse was compressed.

The simulated averaged pulses with different τ were fitted to the averaged data pulses for each scan angle. The χ^2 per degree of freedom, χ^2/ndf, of the fit to the core pulse as a function of the azimuthal scan angle ϕ and as a function of the simulated time constant τ for an assumed impurity density of $\rho = 0.6 \cdot 10^{10}\,\text{cm}^{-3}$ is shown in Fig. 12.8(a). The χ^2/ndf as function of the angle did not exhibit any correlation between χ^2/ndf and segment boundaries or crystal axes.

The sum of all χ^2/ndf values over all 36 angles, $\sum_\phi \chi^2/\text{ndf}$ was calculated. It is shown in Fig. 12.8(b). The minimum was at $\sum_\phi \chi^2/\text{ndf} = 262.2$. The best simulated τ was 35 ns, corresponding to a bandwidth of $BW \approx 4.5\,\text{MHz}$. The best τ was also estimated for all segment pre-amplifier. The best bandwidth for the segments ranged from 1.8 MHz to 2.9 MHz.

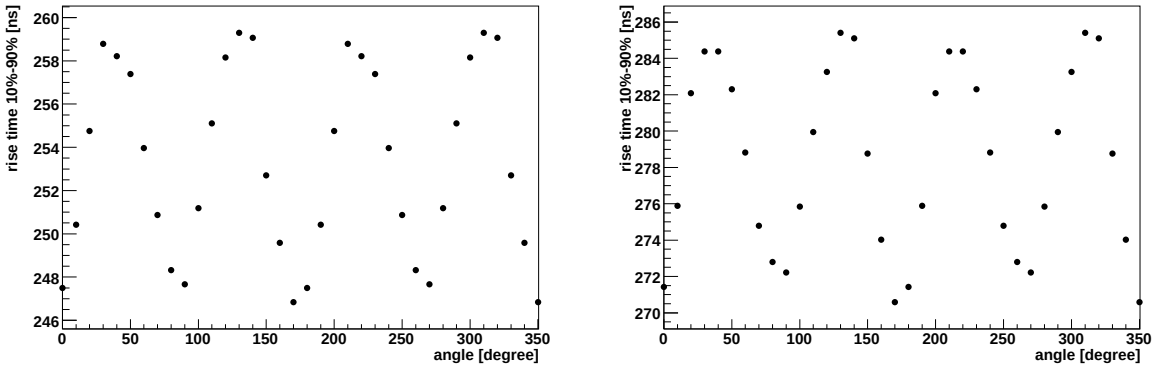

(a) (b)

Figure 12.7.: 10%-90% rise time of the pulses as a function of the angle. In (a) for $\rho = 0\,\mathrm{cm}^{-3}$ and (b) for $\rho = 0.83 \cdot 10^{10}\,\mathrm{cm}^{-3}$ for photons with $E_\gamma = 121.78\,\mathrm{keV}$. Observe the different scales on the Y-axes.

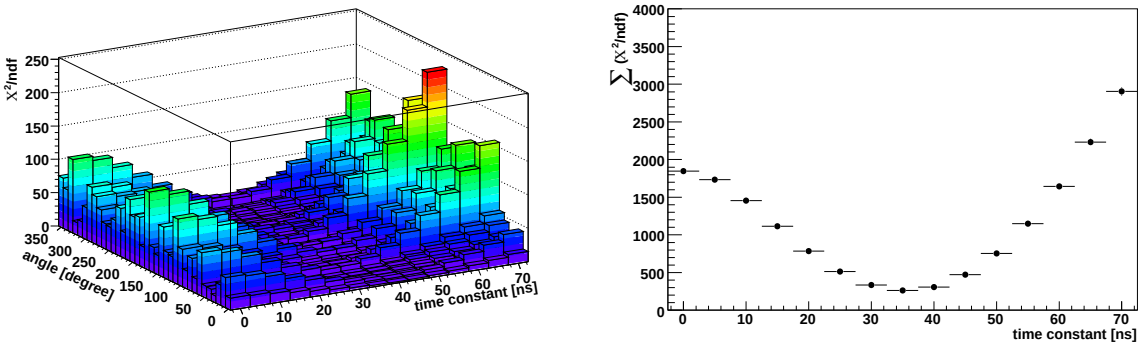

(a) (b)

Figure 12.8.: (a) χ^2/ndf from a fit with a function extracted from the simulated averaged core pulses to the averaged core data pulses as a function ϕ and as a function τ. (b) The $\sum_\phi \chi^2/\mathrm{ndf}$ as a function of τ.

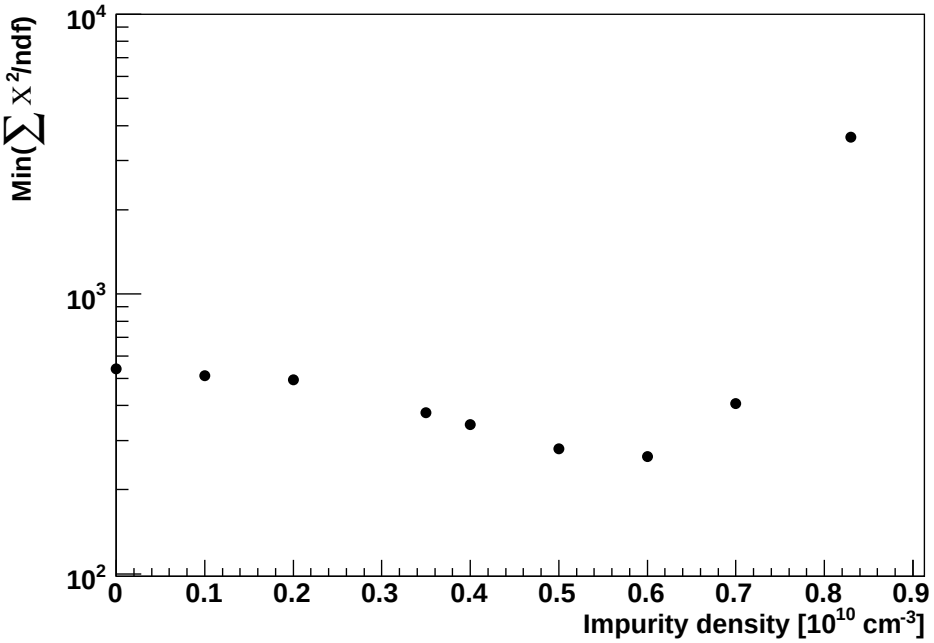

Figure 12.9.: The minimum of the individual sums of χ^2/ndf values over all angles, as a function of the impurity density used to calculate the electric field that was used to simulate the pulses.

The previously described procedure was repeated for the simulated range in ρ. The minimum $\sum_\phi \chi^2/\mathrm{ndf}$ as a function of the impurity density is shown in Fig. 12.9. The best impurity density was $\rho = 0.6 \cdot 10^{10}\,\mathrm{cm}^{-3}$. The impurity density of $\rho = 0.6 \cdot 10^{10}\,\mathrm{cm}^{-3}$ is in the range of the impurity density given by the manufacturer. Furthermore, it is close to the impurity density of $\rho_{\mathrm{depl}} = 0.62 \cdot 10^{10}\,\mathrm{cm}^{-3}$ extracted from the depletion voltage measurements.

The 36 averaged core and segment pulses as well as the fitted simulated pulses are shown in App. B. The pulses at 0° and at 40° are shown in Fig. 12.10. The visual agreement between the simulated and the data pulses is good. The $\chi^2/\mathrm{ndf} = 2.5$ at $\phi = 0^\circ$ for the core pulse and $\chi^2/\mathrm{ndf} = 1.2$ for the segment pulse. At $\phi = 40^\circ$, the core pulse shape seems well described, but the $\chi^2/\mathrm{ndf} = 3.27$. The simulated segment pulse visually deviates from the data pulse. The χ^2/ndf is 14.3.

The average χ^2/ndf for the core pulses is $\chi^2/\mathrm{ndf} = 7.3$ and the one for the segment pulses is $\chi^2/\mathrm{ndf} = 5.9$. The relatively large χ^2/ndf values could be due to an underestimation of the noise level.

The biggest deviation between simulated and data pulses occurs at the beginning of the pulses. The averaged data pulses rise steeper at early times than the simulated ones.

The biggest disagreement between pulses was in segment four, from 30° to 90°. Since the distorted segment pulse shape occurred only in segment four and was the same throughout the segment and the core pulse shape was not affected, it is clear that the simple model for the pre-amplifier is not sufficient here.

The T_{scale} factors for the core pulse, for $\rho = 0.6 \cdot 10^{10}\,\mathrm{cm}^{-3}$ and $\tau = 35\,\mathrm{ns}$ is given in Fig. 12.11(a). The T_{scale} factors for the segments are given in Fig. 12.11(b).

In general, $T_{scale} \approx 0.9$ had to be applied to the simulated core pulses to match the data pulses, i.e. the simulated pulses had to be stretched by about 10%. The T_{scale} factors for the simulated core pulses varied as a function of the azimuthal angle. These variations are expected. In Fig. 11.25(a), the $10\% - 90\%$ rise time as a function of the azimuthal angle was shown. From $\phi = 30^\circ$ to $\phi = 90^\circ$ the $10\% - 90\%$ rise times were longer than expected from the pure drift anisotropy effect. These longer $10\% - 90\%$ rise times are represented in the smaller time scale factors, since these pulses had to be stretched more.

The segment T_{scale} factors are in general larger than one, meaning that the simulated pulses had to be compressed, by about 5%. The segment time scale factor variations are explained in the same way as before for the core. For example, all $10\% - 90\%$ rise times in segment 15 were larger than expected from the fit to data, see Fig. 11.25(b). Therefore, the simulated pulse had to be longer than the other segment pulses. Thus, the time scale factor is lower in segment 15 than in the other segments.

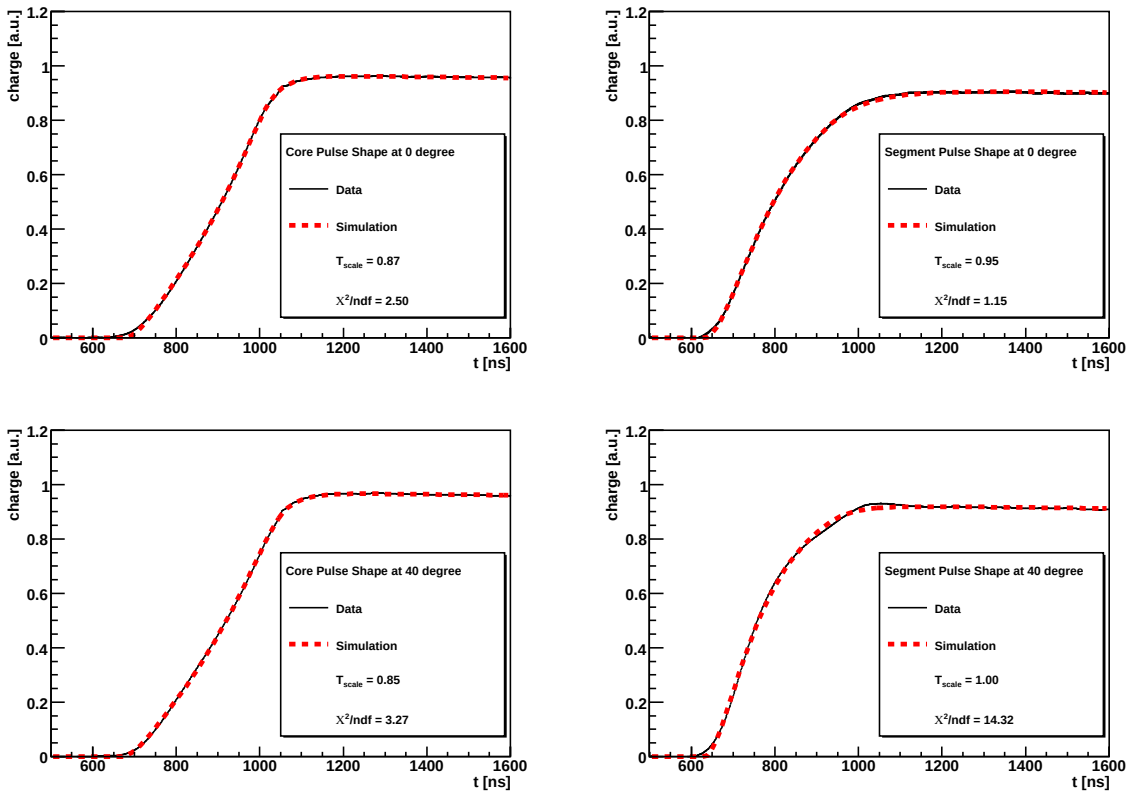

Figure 12.10.: Comparison between the averaged data pulses (black solid line) from the 121.78 keV peak of ^{152}Eu and the averaged simulated pulses from photons with $E_\gamma = 121.78$ keV (red dashed line) left for the core electrode and right for the segment electrode at $\phi = 0^\circ$ (top) and at $\phi = 40^\circ$ (bottom).

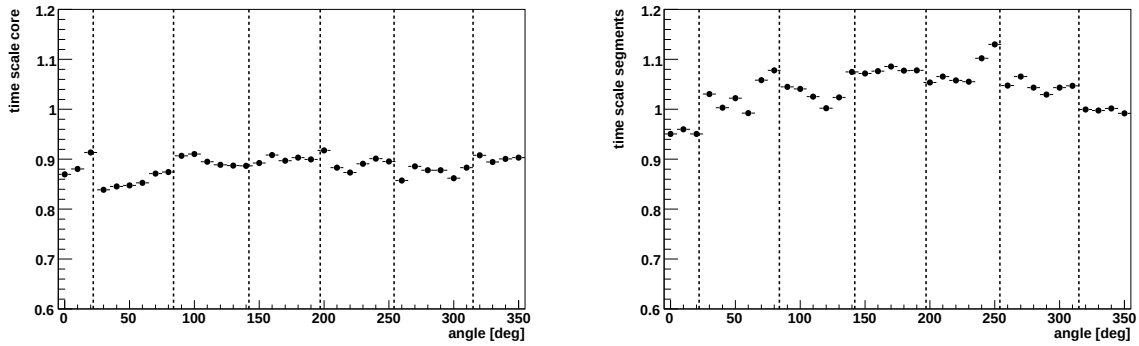

(a) (b)

Figure 12.11.: T_{scale} factors for (a) the simulated averaged core pulse and (b) the simulated averaged segment pulse as a function of ϕ. The dashed lines indicate the segment boundaries. The factors were extracted from a fit of the simulated pulses to the data pulses at an impurity density of $\rho = 0.6 \cdot 10^{10}\,\mathrm{cm}^{-3}$ and the bandwidth determined according to Sec. 12.4.3.

12.5. Conclusions and Outlook

The agreement between analytical and numerical calculation of the radial electric field was good. The accuracy of the field calculation is sufficient for the pulse shape simulation.

In order to compare simulation to data the distribution of the interactions inside the detector have to be taken into account and the correct impurity density has to be estimated.

The bandwidth at which the simulated core pre-amplifier fit the data best is 4.5 MHz. For the simulated segment pre-amplifiers, it varies between 2.9 MHz for segment 15 and 1.8 MHz for segment five and six.

The best agreement between data and simulated pulses was found for an electric field with $\rho = 0.6 \cdot 10^{10}\,\mathrm{cm}^{-3}$. The impurity density $\rho_{\mathrm{depl}} = 0.62 \cdot 10^{10}\,\mathrm{cm}^{-3}$, calculated from the depletion voltage of 2250 V confirms this ρ.

The agreement in shape between the data and the simulated pulses is reasonable. To improve the simulation, a measured pre-amplifier transfer function should be applied to the simulated pulses instead of a simple pre-amplifier model. Additionally, the use of time shift correction for the data pulses, or the simulation of time shift in the simulated pulses could help to improve the agreement between data and simulation.

The overall length of the pulses had to be adjusted. The simulated core pulses were 10% too short and the segment pulses 5% too long. That could indicate that the mobilities assumed are responsible. The mobilities for holes and electrons are different and vary depending on the model. To account for the differences in rise time using the electric field, the electric field has to be larger than simulated at small radii and smaller than simulated at larger r. Then also the shape of the pulse would change.

13. Pulse Shape Simulation of Special Cases of the Impurity Density Distribution

While the simulated pulses describe the observed pulses reasonably well, there is still room for improvement. The assumption of a homogeneous ρ is very restricting. Radial changes in the impurity in germanium crystals have been observed [104]. The question is whether such an impurity gradient changes the pulses significantly. In addition, deviations of the ϕ dependence of the rise time from the expected behaviour have been observed [108]. Cutting a detector with an offset from the crystal center, a radial impurity density gradient can be transformed into an effective ϕ dependence.

A SuSie type detector was simulated, i.e. the $\langle 100 \rangle$ axis was set to $\phi = 353.4^\circ$ and the $\langle 110 \rangle$ axis was set to $\phi = 38.4^\circ$, see Sec. 11.9.1.

Two cases were simulated. The pulse shapes from a point like charge at $r = 37.4\,\mathrm{mm}$ and the realistic case of pulse shapes from photons with $E_\gamma = 121.78\,\mathrm{keV}$.

13.1. Radial Change of Impurity Density

Pulses were simulated using an electric field with an impurity density of $\rho = 0.6 \cdot 10^{10}\,\mathrm{cm}^{-3}$ and with an electric field with $\rho = 0.6 \cdot 10^{10}\,\mathrm{cm}^{-3}$ at $r = 5\,\mathrm{mm}$ linearly decreasing to $\rho = 0.14 \cdot 10^{10}\,\mathrm{cm}^{-3}$ on the detector outside at $r = 37.5\,\mathrm{mm}$.

The radial electric fields are shown in Fig. 13.1. For the homogeneous $\rho = 0.6 \cdot 10^{10}\,\mathrm{cm}^{-3}$, $E(r) = 135\,\mathrm{V/mm}$ on the outside, drops to $E(r) = 67\,\mathrm{V/mm}$ at $r = 10\,\mathrm{mm}$ and rises back up to $E(r) = 80\,\mathrm{V/mm}$ at $r = 5\,\mathrm{mm}$. In contrast the radial electric field with the radial impurity density gradient is nearly constant throughout the detector with $E(r) = 85\,\mathrm{V/mm}$ and only rises close to core electrode of the detector to nearly $E(r) = 140\,\mathrm{V/mm}$.

The simulated pulse shapes from a point-like charges differ for the two cases, see Fig. 13.2. The initial drop of the core pulse is steeper for $\rho = const.$, since the radial electric field is higher on the outside. For the radially varying impurity density, the E(r) is larger close to the core electrode. Therefore, the pulse has a more pronounced turnover towards the end of the rise time and has a shorter total rise time.

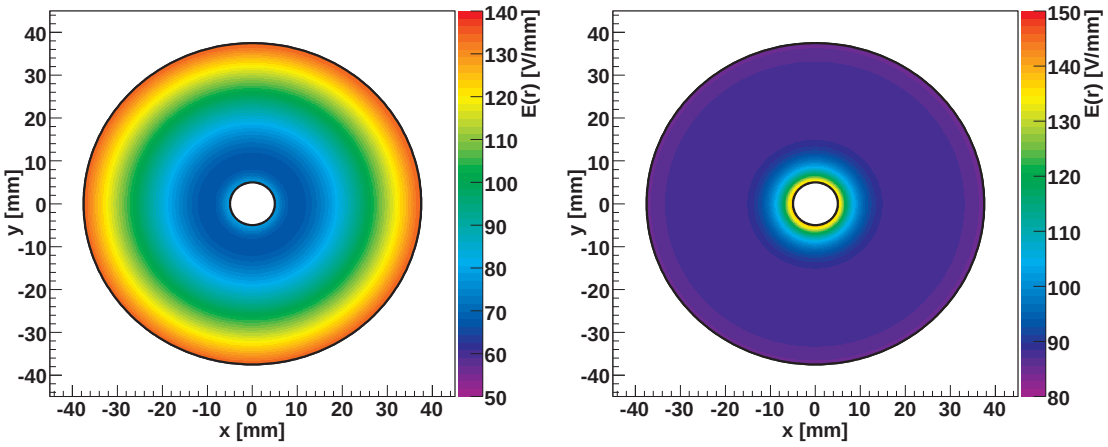

(a) (b)

Figure 13.1.: Radial electric field (a) for a homogeneous $\rho = 0.6 \cdot 10^{10}\,\mathrm{cm}^{-3}$ and (b) for an impurity density of $\rho = 0.6 \cdot 10^{10}\,\mathrm{cm}^{-3}$ at $r = 5\,\mathrm{mm}$ and linearly dropping to $0.14 \cdot 10^{10}\,\mathrm{cm}^{-3}$ at $r = 37.5\,\mathrm{mm}$.

The 10%-90% rise times, see Fig. 13.3, differ by about 10 ns, or 4%, and as expected the 10%-90% rise times for the pulses calculated with the radial impurity density gradient are shorter.

The result for the averaged pulse shapes from photons with $E_\gamma = 121.78\,\mathrm{keV}$ are shown in Fig. 13.4. The distinct features of the pulses are averaged out. The difference in the 10%-90% rise time distributions, shown in Fig. 13.5, is reduced to about 6 ns or approximately 2.5%. The mechanism shortens the rise times in the core. The simulated pulses in the core were too short already. Thus the mechanism does not account for the need of a $T_{scale} \approx 1$. Furthermore, fitting the pulses to data increased the χ^2/ndf values. An opposite gradient of the impurity density was also evaluated. Fitting the pulses to data also increased the χ^2/ndf values.

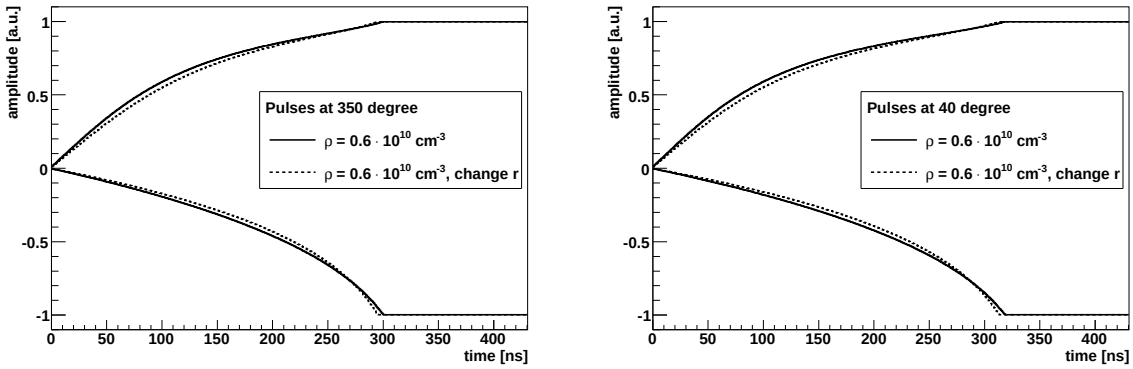

(a) (b)

Figure 13.2.: Pulses of the core and the segment electrode from a single energy deposit at $r = 37.4\,\text{mm}$ at (a) $\phi = 350°$ and (b) $\phi = 40°$ at an impurity density of $\rho = 0.6 \cdot 10^{10}\,\text{cm}^{-3}$ and $\rho = 0.6 \cdot 10^{10}\,\text{cm}^{-3}$ at $r = 5\,\text{mm}$ decreasing to $\rho = 0.14 \cdot 10^{10}\,\text{cm}^{-3}$ at $r = 37.5\,\text{mm}$.

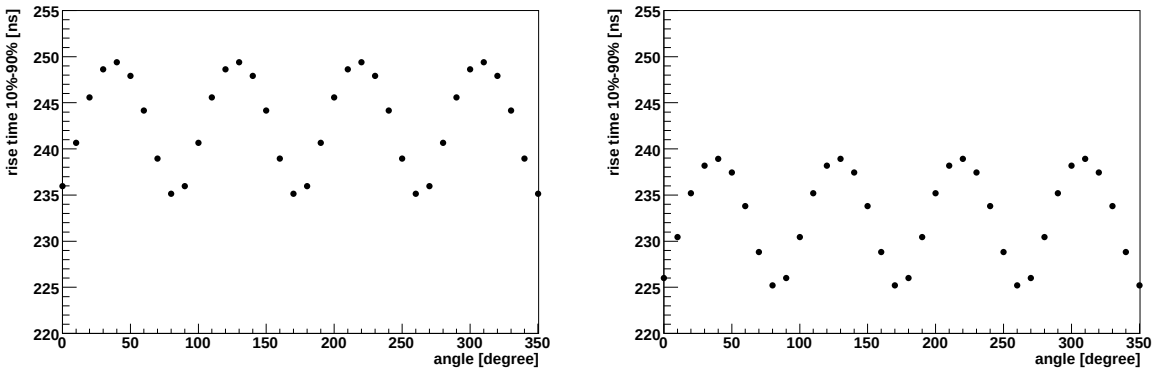

(a) (b)

Figure 13.3.: 10%-90% rise time of the pulses from a single energy deposit at $r = 37.4\,\text{mm}$ as a function of ϕ. (a) for $\rho = 0.6 \cdot 10^{10}\,\text{cm}^{-3}$ and (b) $\rho = 0.6 \cdot 10^{10}\,\text{cm}^{-3}$ at $r = 5\,\text{mm}$ decreasing to $\rho = 0.14 \cdot 10^{10}\,\text{cm}^{-3}$ at $r = 37.5\,\text{mm}$.

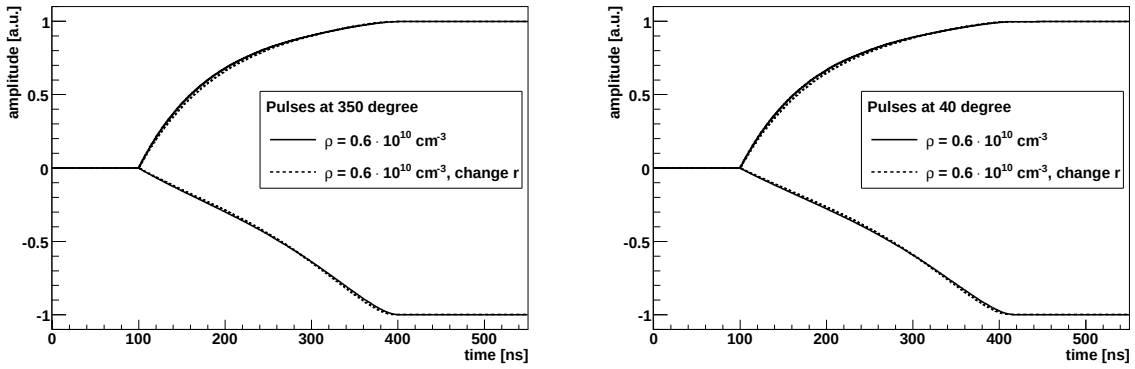

(a) (b)

Figure 13.4.: Induced averaged pulse shapes for $E_\gamma = 121.78\,\text{keV}$ for the core and segment at (a) $\phi = 350^\circ$ and (b) $\phi = 40^\circ$ at an impurity density of $\rho = 0.6 \cdot 10^{10}\,\text{cm}^{-3}$ and $\rho = 0.6 \cdot 10^{10}\,\text{cm}^{-3}$ at $r = 5\,\text{mm}$ decreasing to $\rho = 0.14 \cdot 10^{10}\,\text{cm}^{-3}$ at $r = 37.5\,\text{mm}$.

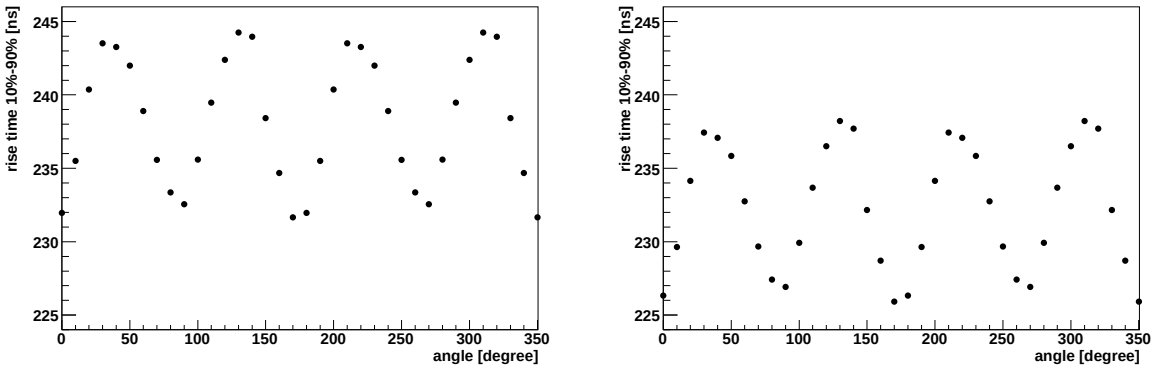

(a) (b)

Figure 13.5.: 10%-90% rise time of the averaged pulses from photon with $E_\gamma = 121.78\,\text{keV}$ as a function of ϕ. (a) for $\rho = 0.6 \cdot 10^{10}\,\text{cm}^{-3}$ and (b) for $\rho = 0.6 \cdot 10^{10}\,\text{cm}^{-3}$ at $r = 5\,\text{mm}$ decreasing to $\rho = 0.14 \cdot 10^{10}\,\text{cm}^{-3}$ at $r = 37.5\,\text{mm}$.

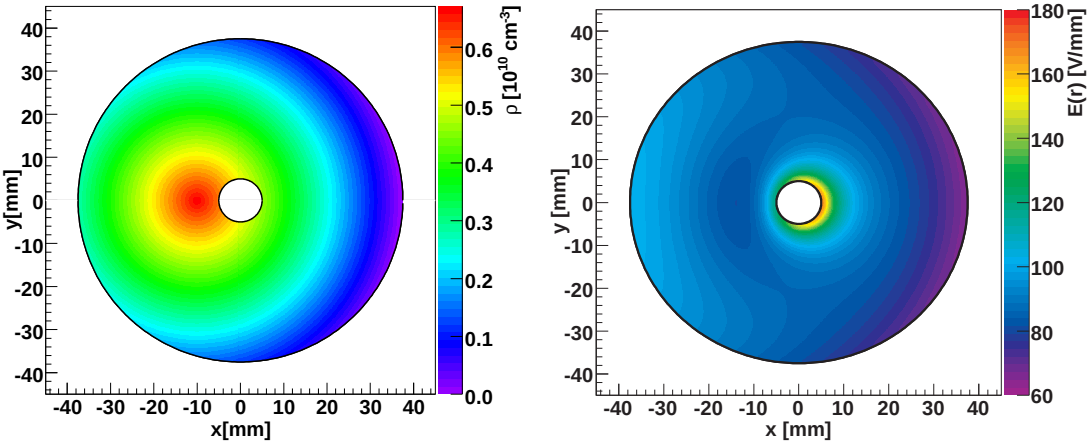

(a) (b)

Figure 13.6.: (a) Impurity density of $\rho = 0.67 \cdot 10^{10}\,\mathrm{cm}^{-3}$ in the center of the germanium crystal, which has an offset to the detector center of 1 cm. The impurity density is assumed to drop linearly to $\rho = 0\,\mathrm{cm}^{-3}$ at the far side of the detector. (b) The corresponding electric field.

13.2. Radial and Azimuthal Change of Impurity Density

The electric field for a ρ distribution with $\rho = 0.6 \cdot 10^{10}\,\mathrm{cm}^{-3}$ at $r = 5\,\mathrm{mm}$ decreasing to $\rho = 0.14 \cdot 10^{10}\,\mathrm{cm}^{-3}$ at $r = 37.5\,\mathrm{mm}$ was calculated. The field for the same impurity gradient but with an additional offset of the detector to the crystal center of $x = 10\,\mathrm{mm}$ was calculated. The impurity density distribution and the resulting $E(r)$ are shown in Fig. 13.6.

The pulse shapes from the point-like charges at $\phi = 350°$ and $\phi = 40°$ are shown in Fig. 13.7. The longitudinal drift anisotropy is visible. At $\phi = 350°$ the core rise time is about 13 ns shorter than at $\phi = 40°$. The pulse shapes for an offset in ρ differ visibly from the ones for radial change only. The $E(r)$ for a radial impurity density change only, is larger in the positive x hemisphere at large r. Therefore, the increase in the amplitude is stronger at early times.

This is not true in the negative x hemisphere. In Fig. 13.8 the induced pulse shapes for energy deposit at $\phi = 0°$ and $\phi = 180°$ are shown. The largest effect due to the offset in ρ is expected for these opposite sides. At $\phi = 180°$, $E(r)$ is larger at large r in case of an offset, but on the inside, close to the inner electrode the electric field is smaller. Therefore, the rise at early times is faster, but at late times it is slow, such that the same $t_r^{100\%} = 298\,\mathrm{ns}$ is observed. At 0° the rise time is $t_r^{100\%} = 300\,\mathrm{ns}$, i.e. the change caused by the difference in impurity density form “left-to-right” is 2 ns.

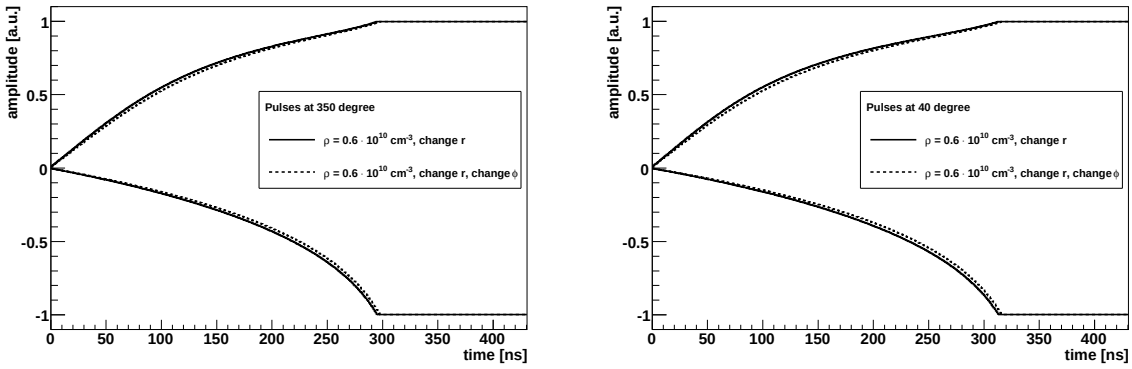

(a) (b)

Figure 13.7.: Induced pulse on the core and segment electrodes from a single energy deposit at $r = 37.4\,\text{mm}$ at (a) $\phi = 350^\circ$ and (b) $\phi = 40^\circ$ with an radial impurity density change from $\rho = 0.6 \cdot 10^{10}\,\text{cm}^{-3}$ at $r = 5\,\text{mm}$ to $\rho = 0.14 \cdot 10^{10}\,\text{cm}^{-3}$ at $r = 37.5\,\text{mm}$ and same impurity density, but with an offset of 1 cm.

The difference in shape is also represented in the $t_r^{10\%-90\%}$ distribution, shown in Fig. 13.10. The 10%-90% rise time for the radial and azimuthal impurity density change, exhibits the longest 10%-90% rise time at 220°. Compared to the 10%-90% rise time at 40° it changed by 4 ns, or by 1.6%.

Repeating the simulation with the photons of energy $E_\gamma = 121.78\,\text{keV}$ and averaging the pulses, the previously visible difference in rise time disappeared. The averaged segment and core pulse shapes at 0° and 180° are shown in Fig. 13.11. The small differences in the pulse shapes from a single energy deposit were averaged out. The 10%-90% rise time distributions are given in Fig. 13.12. Again, the difference previously observed was averaged out.

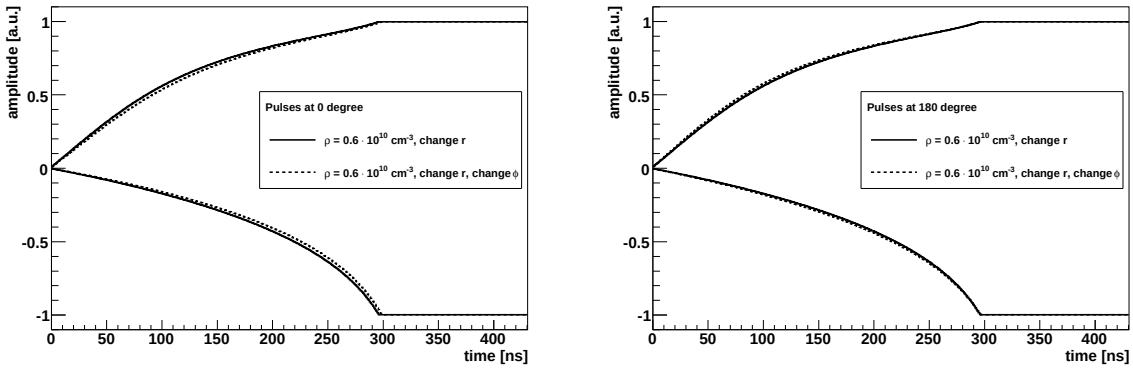

(a) (b)

Figure 13.8.: Induced pulse shapes of the core and segment electrode from a single energy deposit at $r = 37.4\,\text{mm}$ at (a) $\phi = 0°$ and (b) $\phi = 180°$ with an radial impurity density change from $\rho = 0.6 \cdot 10^{10}\,\text{cm}^{-3}$ at $r = 5\,\text{mm}$ to $\rho = 0.14 \cdot 10^{10}\,\text{cm}^{-3}$ at $r = 37.5\,\text{mm}$ and same impurity density, but with an offset of 1 cm from the detector center.

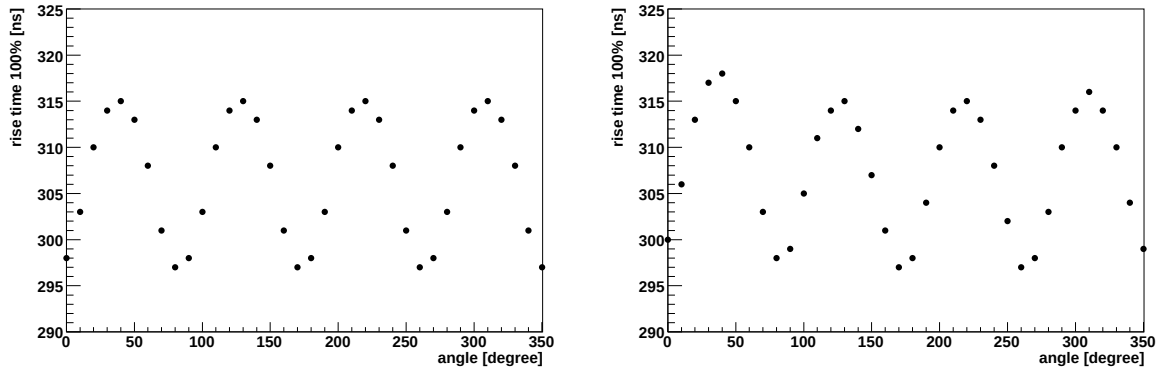

(a) (b)

Figure 13.9.: The overall rise time of the pulses from a single energy deposit at $r = 37.4\,\text{mm}$ as a function of the angle. In (a) for a radial impurity density change from $\rho = 0.6 \cdot 10^{10}\,\text{cm}^{-3}$ at $r = 5\,\text{mm}$ to $\rho = 0.14 \cdot 10^{10}\,\text{cm}^{-3}$ at $r = 37.5\,\text{mm}$ and (b) for the same impurity density, but with an offset of 1 cm from the detector center, yielding a radial and azimuthal impurity density change.

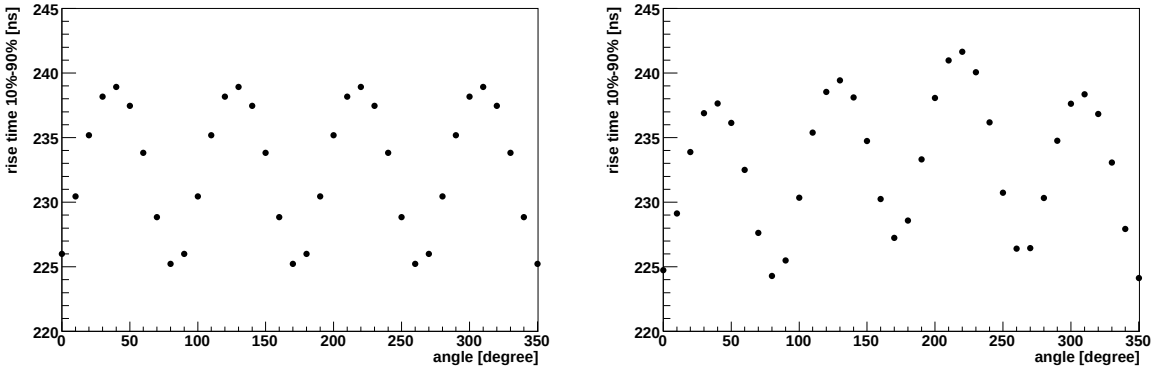

(a) (b)

Figure 13.10.: 10%-90% rise time of the pulses from a single energy deposit at $r = 37.4\,\mathrm{mm}$ as a function of the angle. In (a) for a radial impurity density change from $\rho = 0.6 \cdot 10^{10}\,\mathrm{cm}^{-3}$ at $r = 5\,\mathrm{mm}$ to $\rho = 0.14 \cdot 10^{10}\,\mathrm{cm}^{-3}$ at $r = 37.5\,\mathrm{mm}$ and (b) for the same impurity density, but with an offset of 1 cm from the detector center.

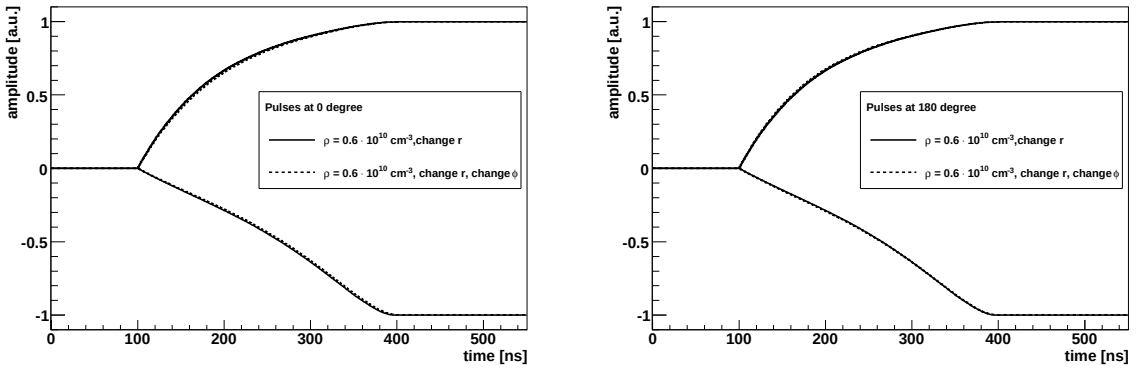

(a) (b)

Figure 13.11.: Induced averaged pulse shapes of the core and segment electrode form photons with an energy $E_\gamma = 121.78\,\mathrm{keV}$ at (a) 0° and (b) 180° with an radial impurity density change from $\rho = 0.6 \cdot 10^{10}\,\mathrm{cm}^{-3}$ at $r = 5\,\mathrm{mm}$ to $\rho = 0.14 \cdot 10^{10}\,\mathrm{cm}^{-3}$ at $r = 37.5\,\mathrm{mm}$ and same impurity density, but with an offset of 1 cm from the detector center.

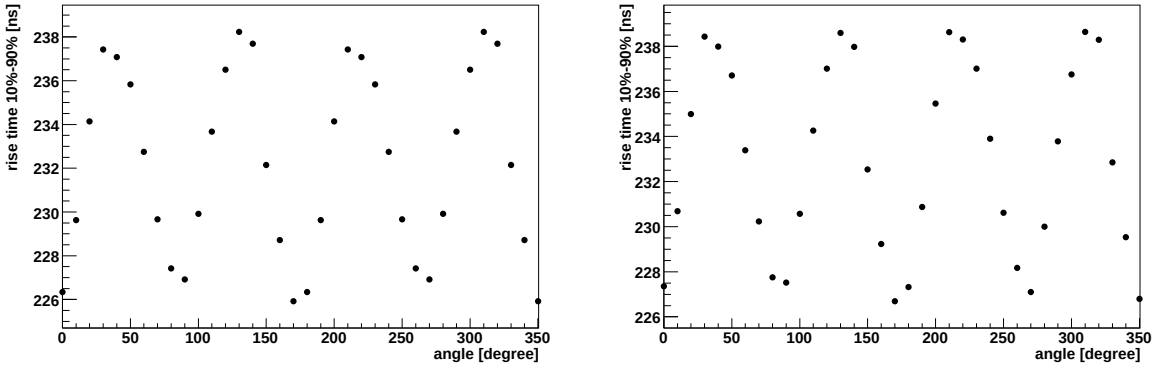

(a) (b)

Figure 13.12.: 10%-90% rise time of the averaged pulses from photons with an energy of $E_\gamma = 121.78\,\mathrm{keV}$ as a function of the angle. In (a) for a radial impurity density change from $\rho = 0.6 \cdot 10^{10}\,\mathrm{cm}^{-3}$ at $r = 5\,\mathrm{mm}$ to $\rho = 0.14 \cdot 10^{10}\,\mathrm{cm}^{-3}$ at $r = 37.5\,\mathrm{mm}$ and (b) for the same impurity density, but with an offset of 1 cm from the detector center, yielding a radial and azimuthal impurity density change.

13.3. Conclusions

Compared to a uniform impurity density of $\rho = 0.6 \cdot 10^{10}\,\mathrm{cm}^{-3}$, a radial change in the impurity density from $\rho = 0.6 \cdot 10^{10}\,\mathrm{cm}^{-3}$ at $r = 5\,\mathrm{mm}$ to $\rho = 0.14 \cdot 10^{10}\,\mathrm{cm}^{-3}$ at $r = 37.5\,\mathrm{mm}$ yields effects on the pulse shapes of about 10 ns, or 4%.

The previously observed change in rise time as a function of the azimuthal angle of about 2.5% [108], cannot easily be explained by a change of the impurity density as a function of the azimuthal angle. Even though the total rise time shows effects of the right order of magnitude, this gets washed out by the averaging process employed here. The previous analysis [108] used another analysis procedure which might preserve the effect. Another explanation for the effect would be a change in the crystal temperature between the different measurements, see Eq. (7.5).

14. The Top Surface

The top segment of the Super Siegfried detector was studied especially using several radioactive sources. The data sets were introduced in Chapter 11. The results of these measurements are presented in this chapter.

14.1. Resolution and Count Rate

The FWHM of the 121.78 keV photon peak as a function of the azimuthal angle, ϕ, from the side scan with the ^{152}Eu source, see Tab. 11.1, is shown in Fig. 14.1 for core and segment 19. The FWHM was extracted from a fit of a first order polynomial plus a Gaussian to describe the spectrum. The FWHM of the core varied around 1.4 keV. Between $210^\circ \leq \phi \leq 260^\circ$ it was significantly worse, about 1.8 ± 0.2 keV. The reason for that is unclear. However, it is interesting to note that this is approximately the region where the contact of segment 19 was made, see Sec. 11.2. The resolution at 121.78 keV of segment 19 varied between 5.8 ± 0.4 keV and 9.6 ± 0.9 keV.

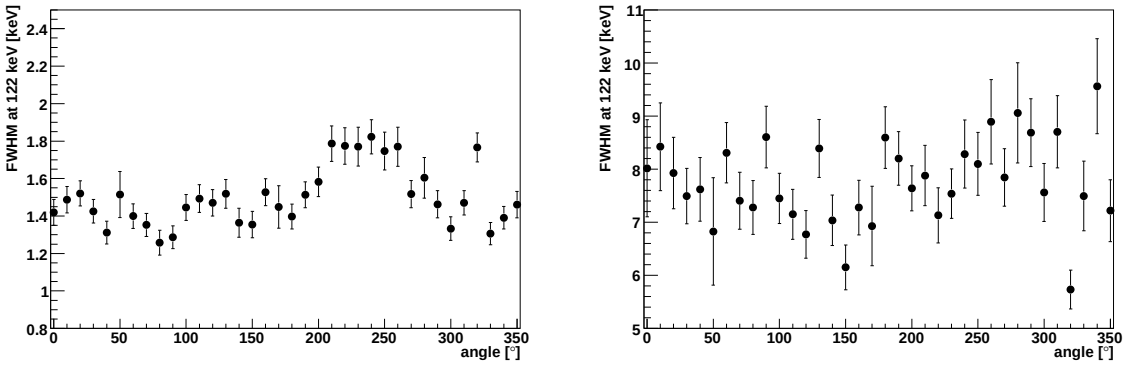

(a) (b)

Figure 14.1.: FWHM extracted for the 121.78 keV line of ^{152}Eu as a function of ϕ in (a) the core and in (b) segment 19.

The count rate calculated for the 121.78 keV peak of ^{152}Eu as a function of ϕ is shown in Fig. 14.2. The count rate of the core was constant at about 1.2 cts/s. It dropped at 50°, 170° and at 280° where the vertical bars of the detector holder were located. All events were triggered using the core signal. In an ideal case all events in the core peak should

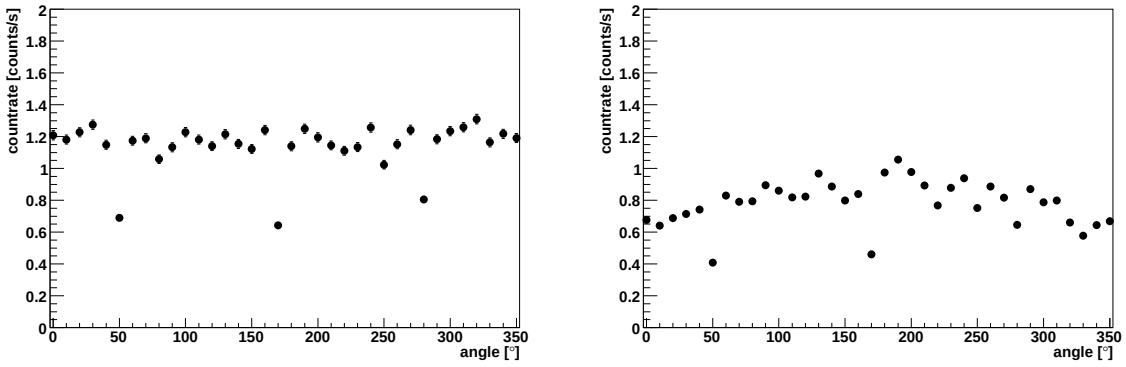

(a) (b)

Figure 14.2.: Count rate extracted for the 121.78 keV line of ^{152}Eu as a function of ϕ in (a) the core and in (b) segment 19.

also fall into the segment peak. However, the count rate in the peak was significantly lower in the segment. In addition, the count rate rose from 0.6 cts/s at 0° to 1 cts/s at 180° and then dropped again. The count rate of the segments below segment 19 showed the opposite behavior, see Fig. 14.3(b). The scanning device or the detector inside the cryostat must have been tilted such that the beam spot covered a fraction of the segments below segment 19. The count rate in the segments below was always lower than the count rate in segment 19. The sum was approximately constant at 1.1, seeFig. 14.3(b).

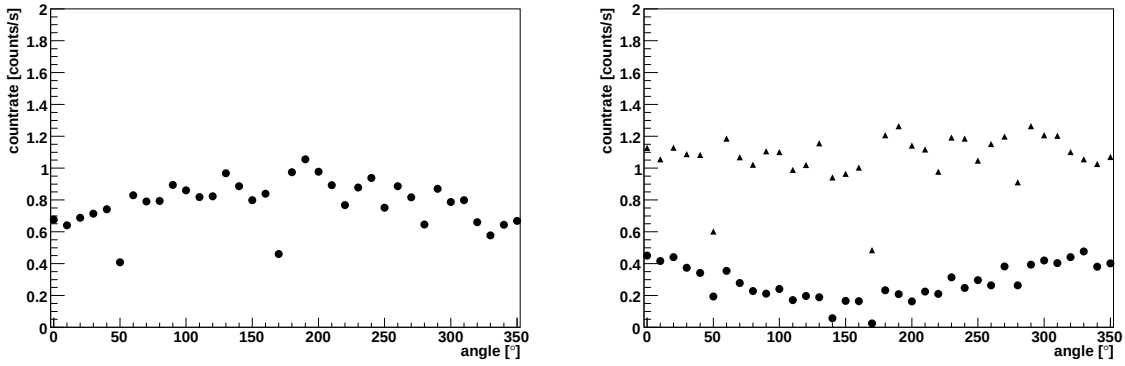

(a) (b)

Figure 14.3.: Count rate extracted for the 121.78 keV line of ^{152}Eu as a function of ϕ in (a) segment 19 and in (b) the segments below segment 19 (dots) and the sum of the count rates from segment 19 and the segments below segment 19 (triangles) .

14.2. Long Rise Times

Single segment events in segment 19 with a core energy of 121.78 ± 5 keV were selected from the same side scan data. The 10%-90% and 10%-30% rise times as defined in Sec. 11.9.1 were calculated for the core and segment 19. The 10%-90% rise time distributions at each ϕ are shown in Fig. 14.4 and Fig. 14.5 for core and segment 19. The black histogram represent the 10%-90% rise times calculated for events in the 121.78 keV photon peak. In addition, events with a core energy of $135\,\text{keV} < E_{\text{core}} < 145\,\text{keV}$ were selected. Their 10%-90% rise times are given as the red histograms. The red histograms were normalized to the number of background events in the respective 121.78 keV peaks. The rise times of these events should be similar to rise times of the background events. They are not concentrated near the surface as they are dominated by Compton scattering of photons with higher energies.

The 10%-90% rise times of the core pulses range from approximately 150 ns to about 300 ns. The distributions for background events did not change significantly for different angles. The distributions for peak events were more ϕ dependent, but at each ϕ, rise times of about 235 ns were dominant.

The 10%-90% rise times of segment 19 pulses exhibit a different structure. Two different groups of events exist. At each ϕ, there is a group of events with short rise times, of about 250 ns and a group of events with long 10%-90% rise times, of about 1000 ns. Between $0^\circ \leq \phi \leq 180^\circ$ and $330^\circ \leq \phi \leq 350^\circ$, the vast majority of events have a long rise time. Between $190^\circ \leq \phi \leq 320^\circ$, most events have an intermediate or short rise time. In the region where predominantly long rise times exist, the number of events with short rise times is well described by the background events. In regions with mostly short rise times, the long rise times are well described by the background events. Thus, a variation of the rise times with ϕ is associated to the events close to the surface induced by the ^{152}Eu source.

The peaks in the 10%-90% rise-time distributions were fitted with a Gaussian. The mean of the Gaussians are shown in Fig. 14.6 and Fig. 14.7. The same was done for the 10%-30% rise times. The result is shown in Fig. 14.8.

The rise times of the core pulses as a function of ϕ show the usual sinusoidal pattern caused by the anisotropic drift of the charge carriers. The 10%-90% rise times extracted from the core pulses are 65 ns or about 20% smaller than those observed in the middle layer, see Sec. 11.9 . In general, different rise times at different z are expected, due to the change in the impurity density ρ. The difference in ρ could account for perhaps 20 ns, see Sec.12.3. In addition, the conical shape of the inner bore hole radius reduces the drift distance by up to 5 mm or 15% at the top surface. Together, both effects can account for the short rise times.

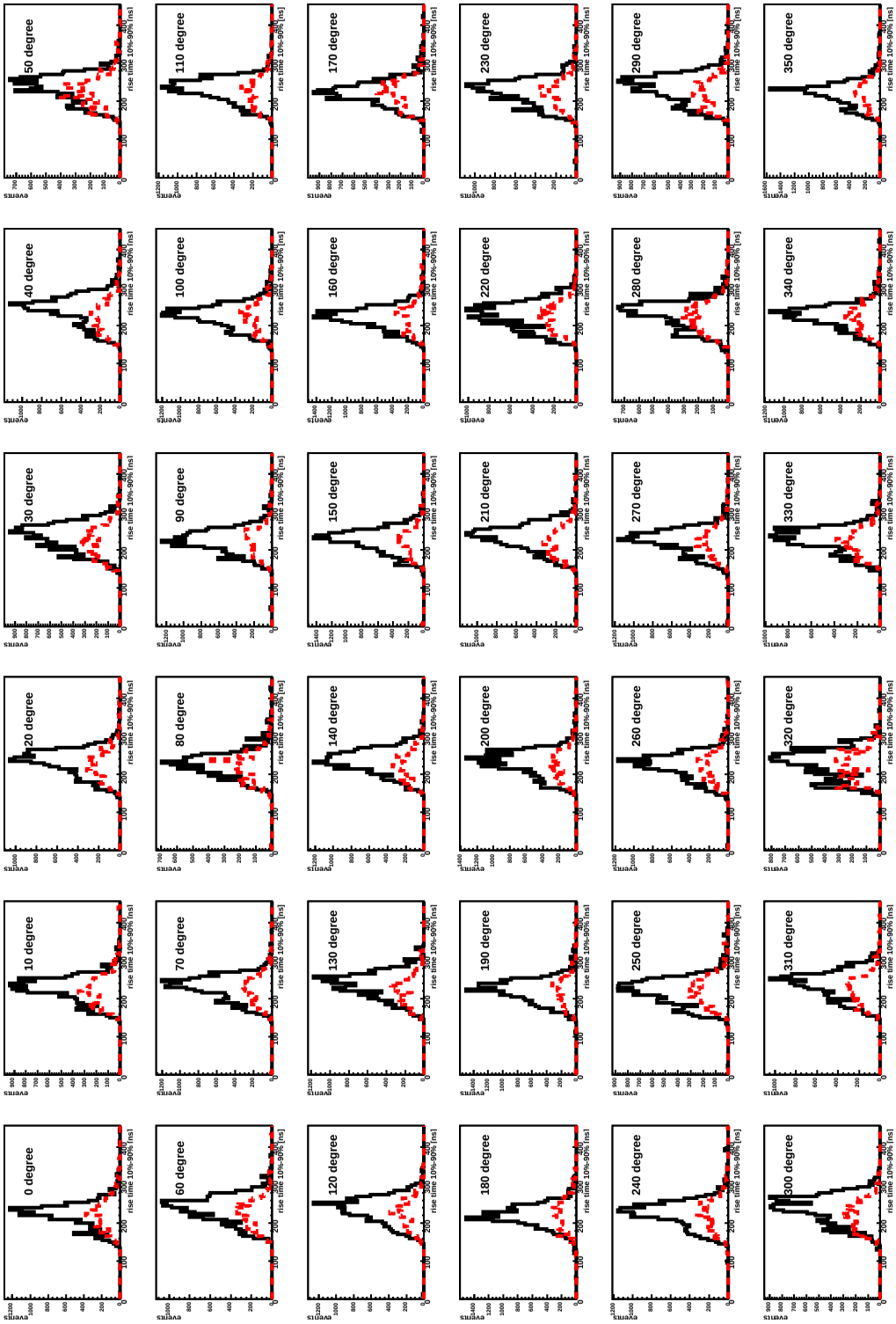

Figure 14.4.: Distributions of 10%-90% rise times of the core. In black is the distribution of photon with energy $E_\gamma = 121.78\,\text{keV}$ from the ^{152}Eu source and in red is the distribution of events with energy $135\,\text{keV} < E_\text{core} < 145\,\text{keV}$, normalized to the number of background events in the 121.78 keV peak, as extracted from a Gaussian plus first order polynomial fit.

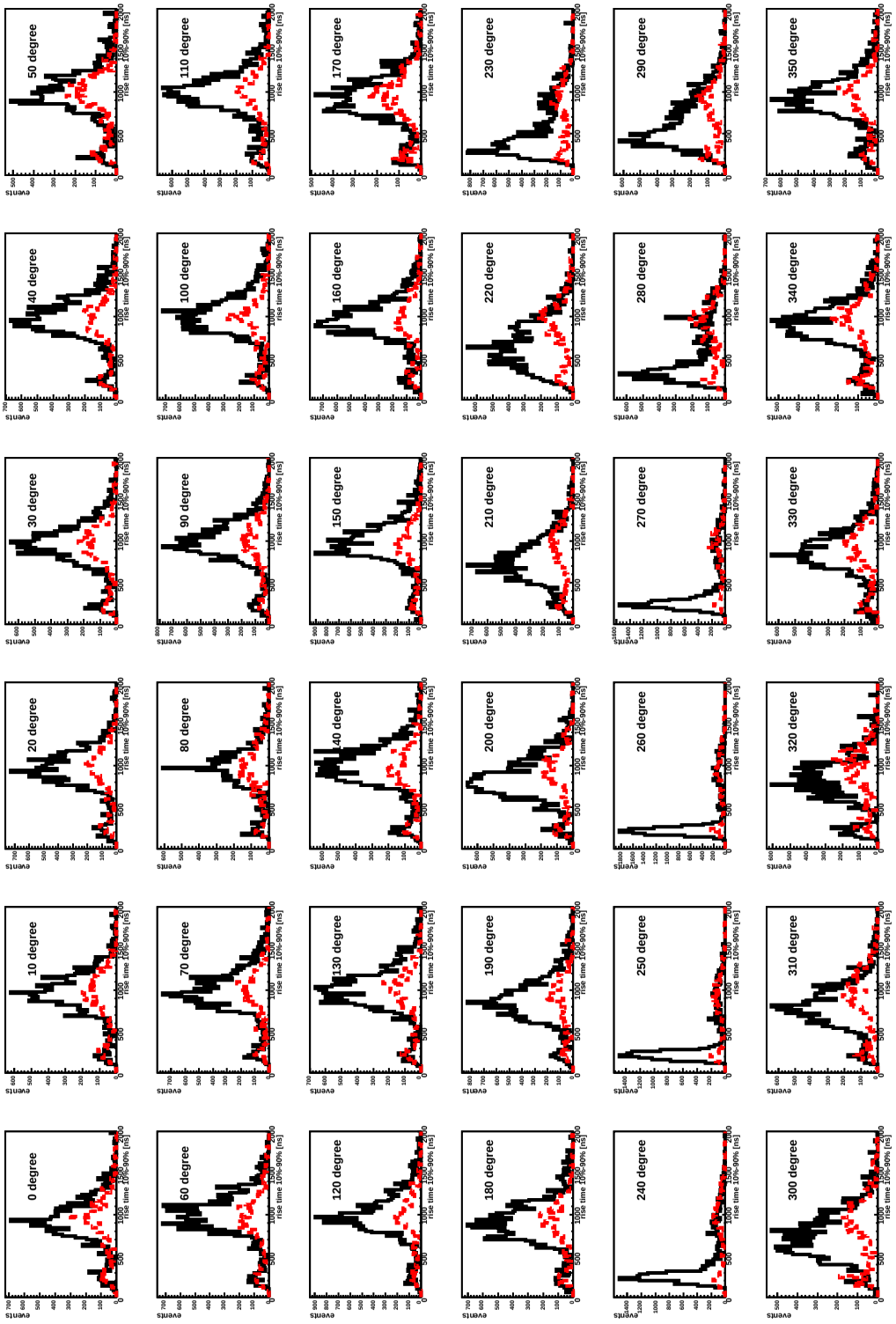

Figure 14.5.: Distributions of 10%-90% rise times of segment 19. In black is the distribution of photon with energy $E_\gamma = 121.78\,\text{keV}$ from the ^{152}Eu source and in red is the distribution of events with energy $135\,\text{keV} < E_{19} < 145\,\text{keV}$, normalized to the number of background events in the 121.78 keV peak, as extracted from a Gaussian plus first order polynomial fit.

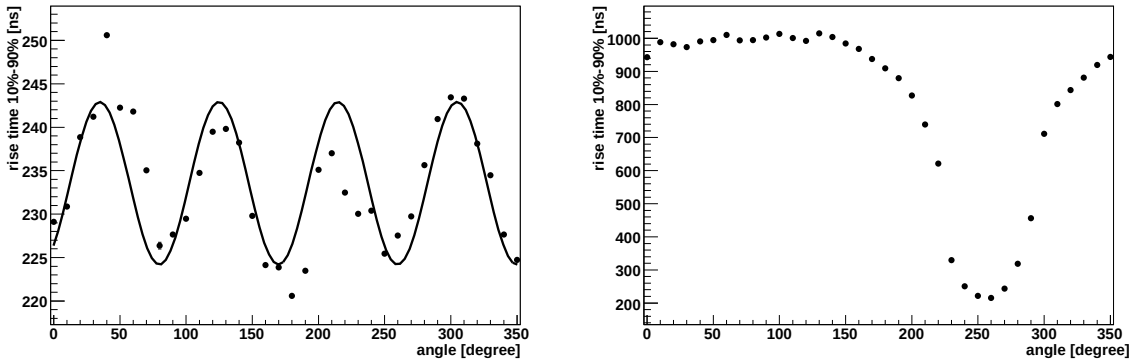

(a) (b)

Figure 14.6.: The mean 10%-90% rise time (a) for the core and (b) for segment 19 as a function of ϕ.

The 10%-90% rise times of the pulses in segment 19 show the behavior discussed above. The two groups of events are represented here. The rise times of most events were very long between $0^\circ \leq \phi \leq 180^\circ$ and $330^\circ \leq \phi \leq 350^\circ$. In the region were the read-out contact was made, around 250° the vast majority of events had small rise times. There, the 10%-90% rise times were short, about 210 ns. The rise times in the middle segments were longer; there the minimum 10%-90% rise time was 268 ns. The difference in the rise times between the top and middle layer at $\phi = 250^\circ$ is again about 20%, as for the core rise time.

In Fig. 14.7 both groups of events at each angle were fitted with a Gaussian and both rise times are shown. The short rise time is independent ϕ. The long rise times also do not show a distinct ϕ dependence. When the second peak in the distribution is clearly separated, the length of the long pulses is compatible under and far away from the contact. At the edges of the contact, the peaks overlap and the fitting is not straight forward.

The reason for the long rise times of the segment pulses is not fully understood. It seems that the electric field in the region without metallic contact and close to the top surface is complicated. The drift of the electrons is not disturbed a lot, whereas the drift of the holes can be extremely slow. These effects could be attributed to a p-type surface channel, see Sec. 7.3.4. The drift path of the holes would be distorted and the velocity of the holes would decrease. The holes might even be trapped.

To further investigate the effect, pulses recorded in a measurement with a ^{228}Th source centrally located above the detector, see Tab. 11.1, were studied. Single segment events in segment 19 were selected. The 10%-90% rise times of the pulses in segment 19 were calculated and are plotted against E_{19} in Fig. 14.9. Again, two bands in the rise times are visible and also vertical lines, i.e. photon lines. One band in rise time corresponds to about

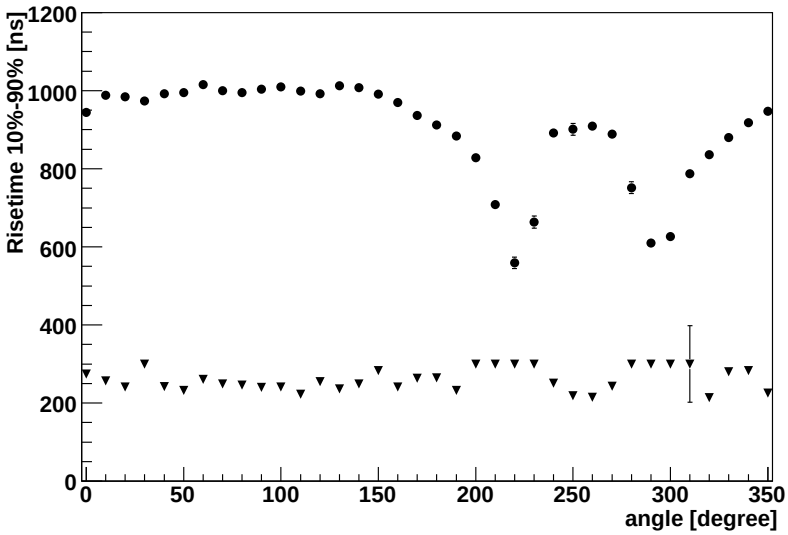

Figure 14.7.: The mean 10%-90% rise time for both groups of events in segment 19 as a function of ϕ.

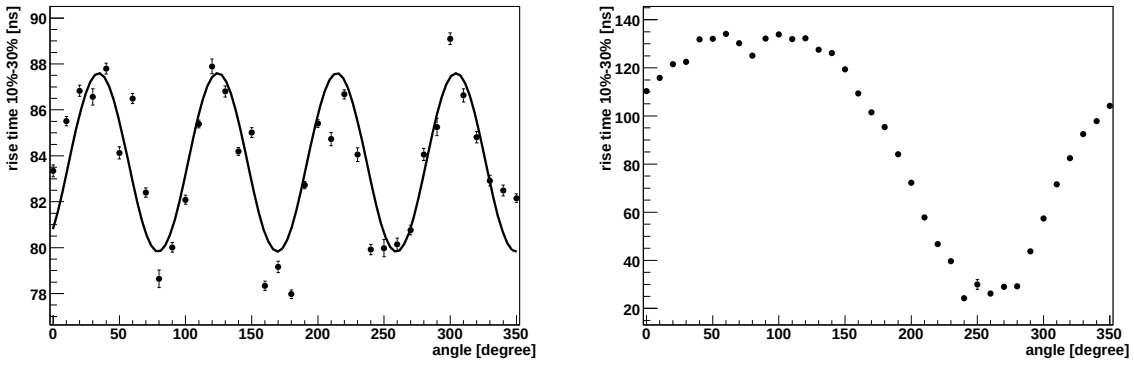

(a) (b)

Figure 14.8.: The mean 10%-30% rise time (a) for the core and (b) for segment 19 as function of ϕ.

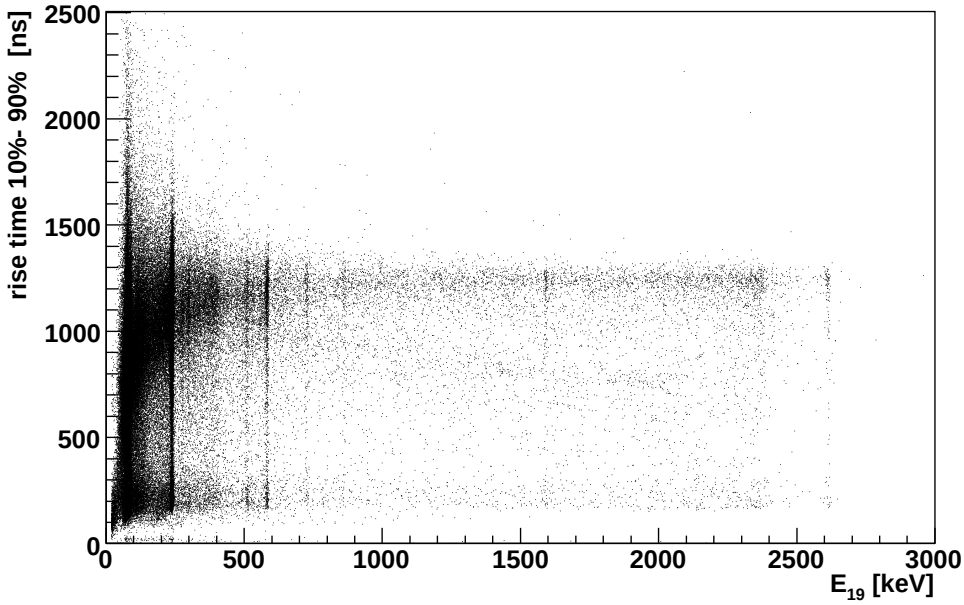

Figure 14.9.: The 10%-90% rise times of pulses from single segment events in segment 19 against E_{19} from a ^{228}Th source placed above the detector.

200 ns and a second corresponds to about 1270 ns. The energy was correctly calculated in both bands, independent of the rise time.

According to the previous discussion, events with the long rise times deposited their energy in a volume not covered by the segment contact, whereas the events with short rise times deposited their energy in the volume under the segment contact.

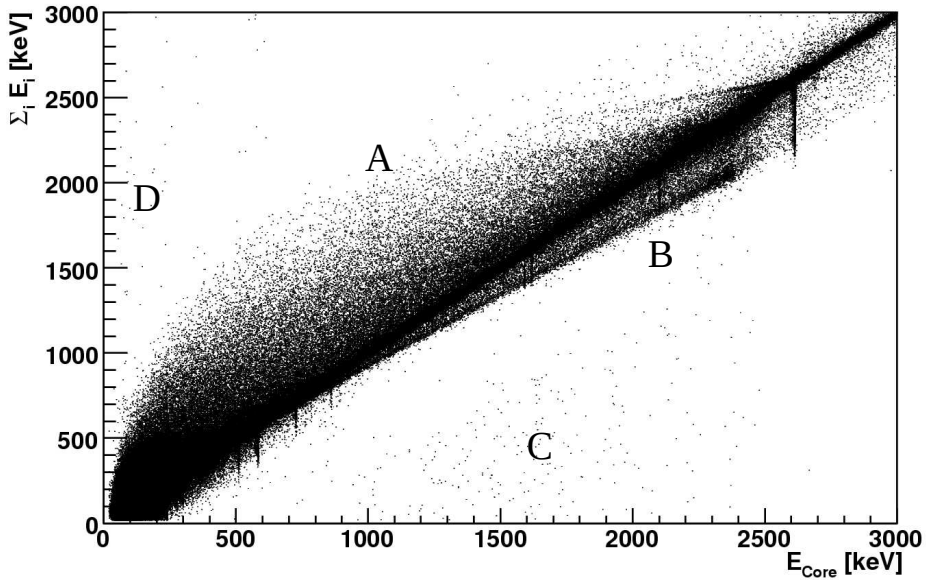

Figure 14.10.: The sum of the segment energies, $\sum_i E_i$ as a function of E_{core} for all events.

14.3. Events with Unequal Core and Segment Energies

The data with the ^{228}Th source positioned centrally above the detector was further examined. For most events, only the energy in each channel was stored. For a fraction of the events, the pulse shapes were recorded as well.

The sum of the segment energies, $\sum_i E_i$, is plotted against the measured core energy, E_{core}, in Fig. 14.10. E_{core} and $\sum_i E_i$, should agree within the energy resolutions and should form a narrow band with a slope of one. Obviously that is not the case. There are events with $\sum_i E_i > E_{\text{core}}$ and events with $\sum_i E_i < E_{\text{core}}$. The events with $\sum_i E_i > E_{\text{core}}$ are mostly located in a diffuse "cloud" above the diagonal. The events with $\sum_i E_i < E_{\text{core}}$ are mostly located in an additional line below the diagonal.

Four classes of events deviating from $\sum_i E_i = E_{\text{core}}$ were identified. Events which have $\sum_i E_i - E_{\text{core}} > 20 \cdot \sigma_{\text{core}}$ and $\sum_i E_i - E_{\text{core}} < 800\,\text{keV}$, where σ_{core} was extracted from the resolution shown in Fig. 11.21, are called class "A" events. Events which exhibit $E_{\text{core}} - \sum_i E_i > 20 \cdot \sigma_{\text{core}}$ and $E_{\text{core}} - \sum_i E_i < 600\,\text{keV}$ are called class "B" events. Event which have $E_{\text{core}} - \sum_i E_i > 600\,\text{keV}$ are called class "C" events and events which show $\sum_i E_i - E_{\text{core}} > 800\,\text{keV}$ are called class "D" events. The classes are indicated in Fig. 14.10.

Single segment events in segment 19 are shown in Fig. 14.11. Here, the different classes are again indicated with their labels.

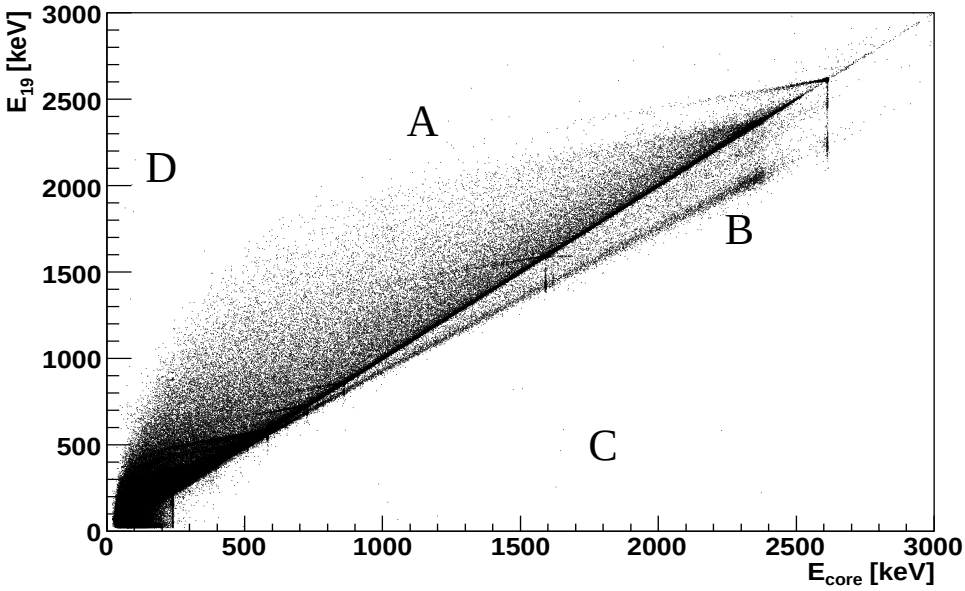

Figure 14.11.: The segment 19 energy, E_{19}, against E_{core} for single segment events in segment 19. The four classes of problematic events are labeled according to their definition in Sec. 14.3.

14.3.1. Class "A" Events

The total number of class "A" events and the fraction of class "A" events as a function of the segment multiplicity, M, are given in Tab. 14.1. In addition, the number of class "A" events with $E_{19} > 20\,\text{keV}$ is given. In total $3.46 \pm 0.01\%$ of all events belong to class "A". About $97.02 \pm 0.26\%$ of the class "A" events have $E_{19} > 20\,\text{keV}$, i.e. are associated with energy deposits in this segment.

The 20 recorded pulses of a typical class "A" event are shown in Fig. 14.12. Pulses are visible in the core and segment 19. Negative pulses are observed in segment 12 and 7. The DAQ did not calculate negative energies. These negative pulses cannot be explained as cross-talk. Instead, electrons drifting inside the crystal being stopped before reaching the core electrode. Normally, the electrons would just induce mirror charges, and the corresponding pulses would return to the baseline. When the electrons are trapped the pulse is interrupted and a seemingly negative energy is induced. The core pulse amplitude is significantly reduced, since the electrons are not reaching the core. The pulse amplitude in segment 19 is also reduced, but less, as the holes play a larger role for the segment pulse. The corresponding energies to the negative amplitudes were calculated. The sum of the segment energies, including the negative pulses equals approximately E_{core}.

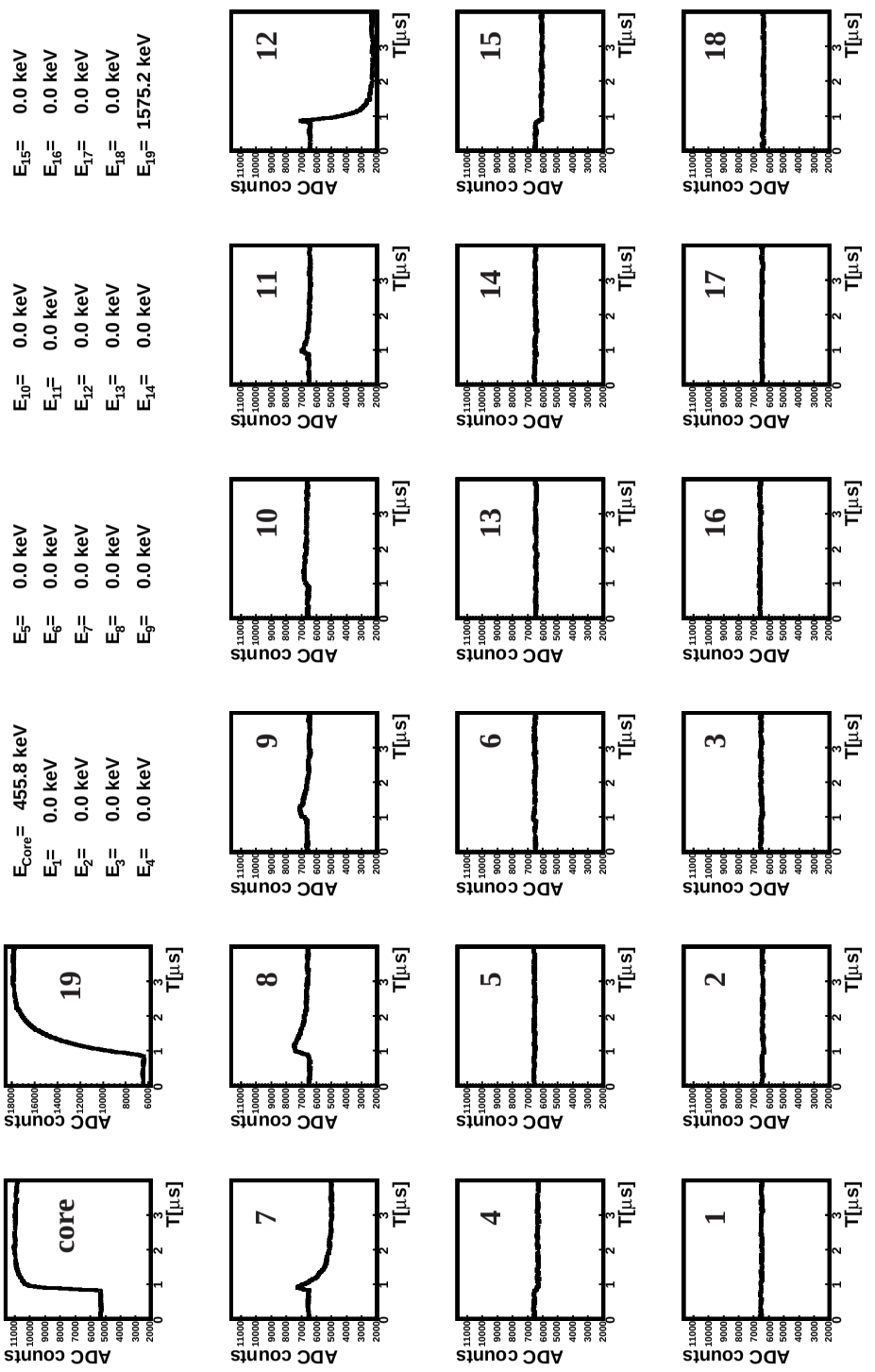

Figure 14.12.: The pulses in ADC counts as functions of the time for all 20 channels for a typical class “A” event. The measured energies in the core and the segments are given in the top right of the plot, the energy in segments with $E_i < 20\,\mathrm{keV}$ was set to zero. Negative pulses are visible in segments 7 and 12.

Segment Multiplicity, M	Total number of events	Total number of class "A" events	Fraction of class "A" events [%]	Total number of class "A" events with $E_{19} > 20\,\text{keV}$	Fraction of class "A" events with $E_{19} > 20\,\text{keV}$[%]
All events	8501174	293824	3.46 ± 0.01	285079	97.02 ± 0.26
1	5960844	237658	3.99 ± 0.01	232315	97.75 ± 0.29
2	1925955	42532	2.21 ± 0.01	40718	95.73 ± 0.66
3	470707	9659	2.05 ± 0.02	9144	94.67 ± 1.38
4	114515	2544	2.22 ± 0.04	2290	90.02 ± 2.60

Table 14.1.: Fraction of class "A" events, i.e. $\sum_i E_i - E_{\text{core}} > 20 \cdot \sigma_{\text{core}}$ and $\sum_i E_i - E_{\text{core}} < 800\,\text{keV}$, for different segment multiplicities M.

The scenario of stopped electrons is confirmed by a dedicated pulse shape simulation, see Fig. 14.13. A pulse with nominal amplitude 1 was created from a single energy deposit at $r = 37.4\,\text{mm}$. The energy deposit was 10 mm away from the lower segment boundary. The electron drift was stopped after 40 ns. The pulse induced in the core electrode is small and the pulse in the segment electrode is also not fully developed, but stopped at an amplitude of about 0.5. A negative pulse is visible in the segment below. Small negative pulses were induced in the other segments. The sum over the amplitude of all pulses, including core is zero.

Since both, core and segment pulses, were reduced, the true energy deposited cannot be recovered. The core and segment energy spectra of class "A" events did not exhibit photon peaks. Since the core energy is reduced, these events cause low energy shoulders in photon peaks; this is seen e.g. in Fig. 11.20.

The 10%-90% rise times of the core pulses of class "A" events do not differ from the rise times of events with $\sum_i E_i \approx E_{\text{core}}$. The core rise times of events in segment 19, the most affected segment are however, longer. The event depicted in Fig. 14.12 also shows this feature. This is associated with a slow and thus long drift of the holes after trapping of the electrons. The effect is less pronounced in the 10%-90% rise times as mostly the last 10% of the pulse are affected.

The evidence for electrons being stopped before reaching the core is strong. This could be caused by an n-type surface channel, see Sec. 7.3.4.

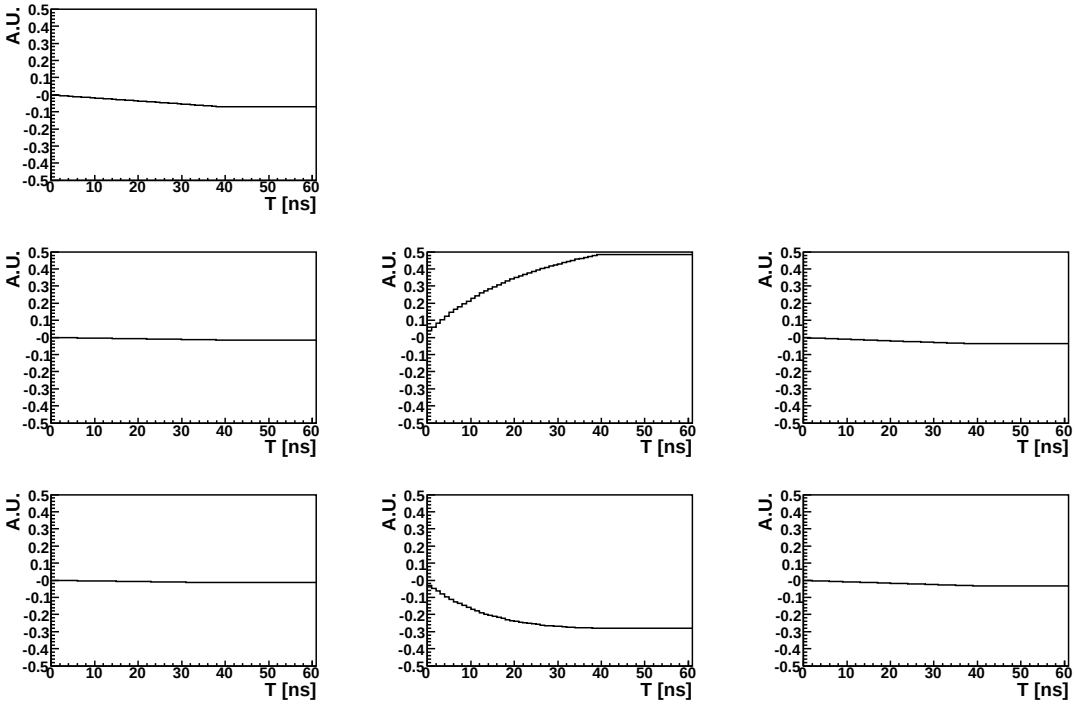

Figure 14.13.: Simulated pulses for a single energy deposit with nominal amplitude of 1, at $r = 37.4\,\mathrm{mm}$ in the top middle segment. In ϕ, the energy deposition was centered in the segment. In z, the energy deposition was 1 cm above the lower segment. The drift of the electrons was stopped after 40 ns. Negative pulses induced in the neighboring segments, especially into the segment below, are clearly visible. The core amplitude (top left) is strongly reduced, whereas the segment amplitude is less affected. The sum over all pulses, including core, is zero.

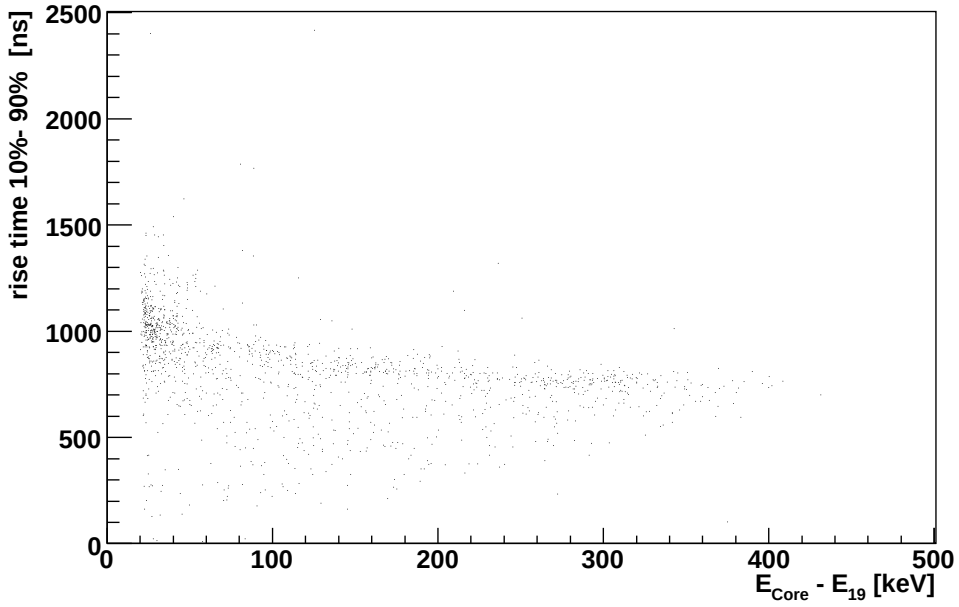

Figure 14.14.: The 10%-90% segment rise times class “B” events in segment 19 against $E_{\text{core}} - E_{19}$.

14.3.2. Class “B” Events

The class “B” events are also predominantly associated with segment 19. About 98%, of class “B” events had $E_{19} > 20\,\text{keV}$. The core energy is only slightly reduced in these events. The energy spectrum of the core still exhibits a ^{208}Tl peak at 2612.82 keV (nominal 2614.5 keV)and a double escape peak at 1590.37 keV(nominal: 1592.5 keV). The energy measured in segment was, however, reduced.

Single segment events with $E_{19} > 20\,\text{keV}$ were selected. The 10%-90% segment rise times against $E_{\text{core}} - E_{19}$ are shown in Fig. 14.14. The larger the energy difference is, the shorter is the rise time. A slight correlation is observed. Events with larger energy difference tend to have a segment pulse with lower 10%-90% rise time. The effect reduces the rise time by 20% for an energy difference of 400 keV. The 10%-90% rise time of the core pulses did not depend on $E_{\text{core}} - E_{19}$ and were fixed around 235 ns.

The 20 recorded pulses of a typical class “B” event are shown in Fig. 14.15. There is a short pulse in the core and a long one in segment 19. There is core to segment cross-talk visible in segments 8 and 9. Segments 7 and 12 show mirror charges which take a long time to return to the baseline, due to the slow drift of the holes which also causes the long segment rise times. They do not completely return to the baseline, but the positive amplitude is minimal and not sufficient to explain $E_{\text{core}} - E_{19} \approx 200\,\text{keV}$.

The reason for the energy loss in not completely clear. Since the segment pulse is reduced and the core pulse is only slightly affected, a trapping of the holes at large r is the most probable cause. A further indication that the long drift and eventually trapping of the holes is the cause comes from the side scan measurements discussed in Sec. 14.2. At $\phi = 70^\circ$ and $\phi = 160^\circ$ class "B" events amount to $0.13 \pm 0.01\%$ and $0.14 \pm 0.01\%$. At $\phi = 250^\circ$, where the segment rise times were predominantly short, class "B" events comprised only $0.09 \pm 0.01\%$ of the sample.

A DAQ problem can be excluded since the energy in ADC counts E_{19}^{ADC} is correctly calculated.

14.3.3. Class "C" Events

For events falling into class "C", a strongly reduced segment energy was determined. For some of these events, the pulse shapes were recorded. In Fig. 14.16 a typical event from that class is shown. It was a single segment event, with a pulse in the core electrode and a pulse in segment 6. The rise times of the core and the segment pulse were very long, i.e. longer than $2\,\mu$s. The energy in segment 6 was not calculated by the DAQ.

Since there are fully developed core and segment pulses, the drift of the electrons and holes must have been very slow, but no trapping occurred. The event did not have any energy deposit close to the ends of the detector. The only other volumes expected to have reduced fields are very close to the segment boundaries. However, no particularly strong mirror pulse is observed.

All class "C" events show long core and segment rise times and the energy in the segment with the long pulse was not properly calculated. It seems that the energy was not properly calculated in the segment if the core pulse was long. There were 342 events out of 8570880 events, i.e. $4 \cdot 10^{-3}\%$, affected by this DAQ problem.

14.3.4. Class "D" Events

Events falling into class "D" have a strongly increased segment energy. The pulse shapes were recorded for only one event in class "D". The event is shown in Fig. 14.17. It is a single segment event, with a pulse in the core electrode and a pulse in segment 19. The core energy was correctly calculated. The energy in segment 19 in ADC counts should have been $E_{19}^{ADC} \approx 1700$. The DAQ calculated a value of $E_{19}^{ADC} = 11081$. In total 26 out of 8570880 events were affected by this DAQ problem, i.e. $3 \cdot 10^{-4}\%$ of the events.

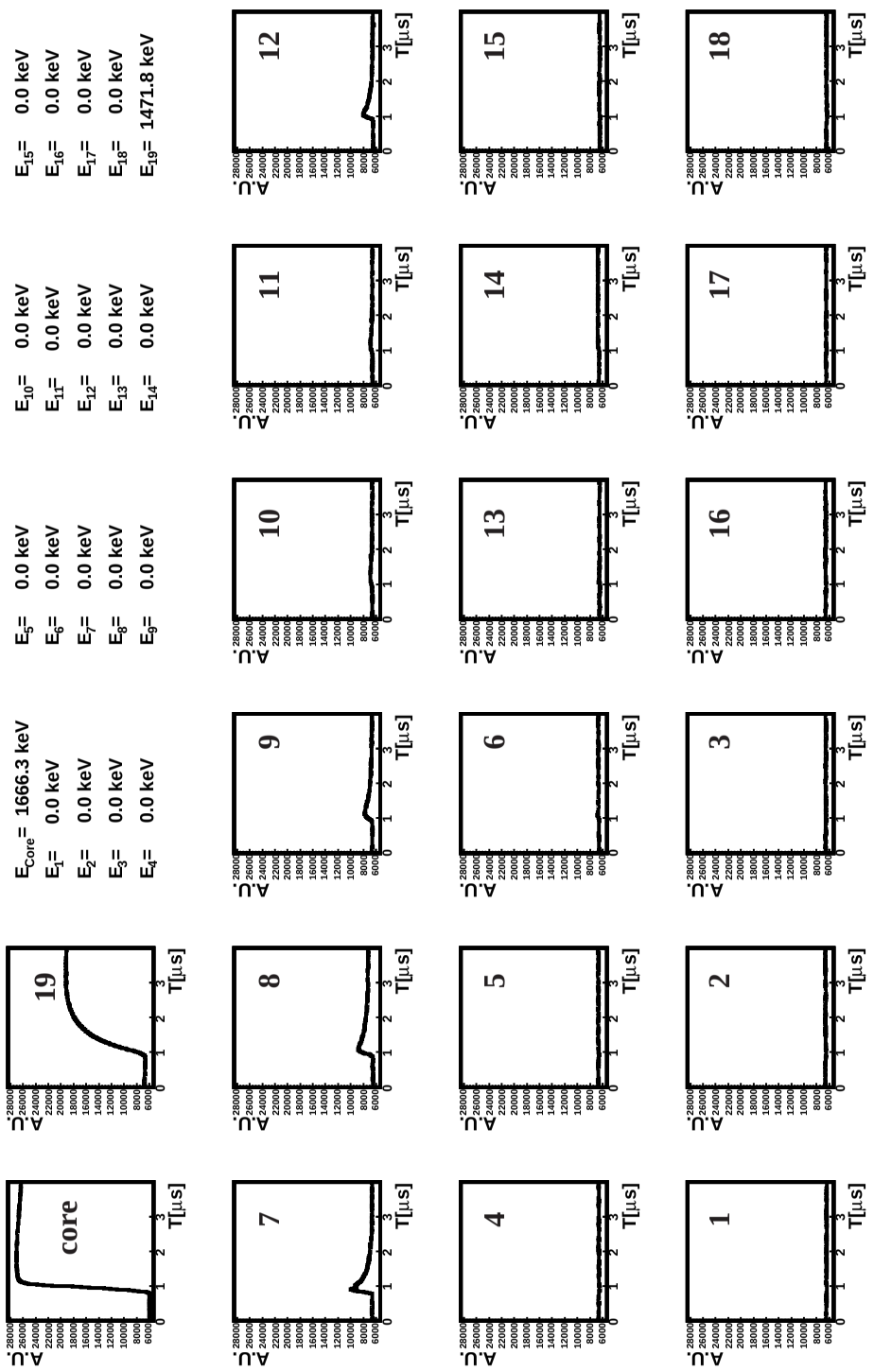

Figure 14.15.: The 20 pulses in ADC counts as a function of the time for a typical class "B" event. The energy in the core and the segments is given in the top right of the plot. It was set to zero if $E_i < 20\,\mathrm{keV}$.

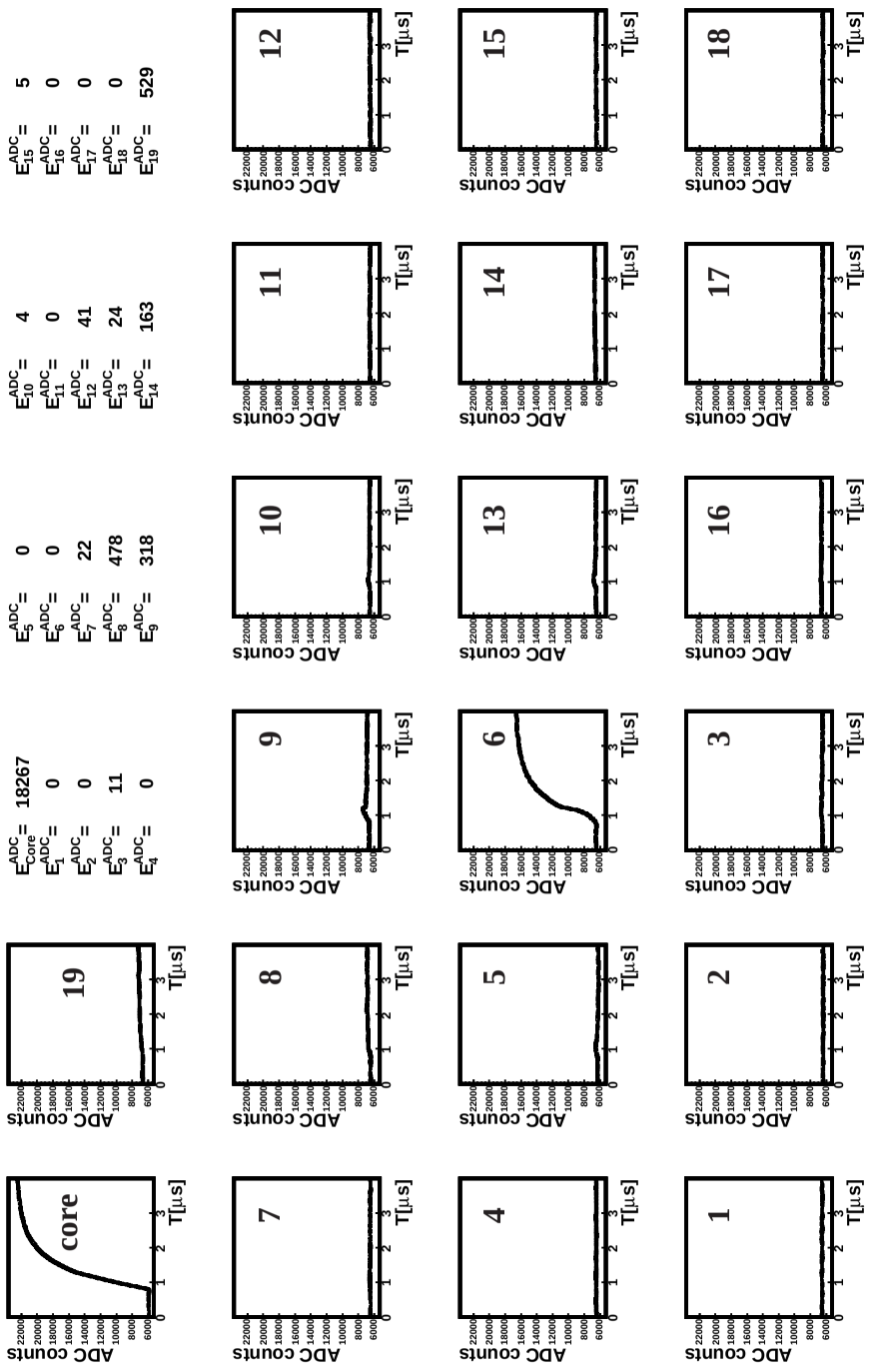

Figure 14.16.: The 20 pulses in ADC counts as a function of the time for a typical class “C” event. Long pulses in the core and in segment 6 are visible. Segments 5, 13, and 10 show a mirror charge. In segment 9, a mirror charge together with core to segment cross-talk is visible. In segment 8 and 19 a shift in the baseline from core to segment cross-talk can be seen. The measured amplitude in ADC counts as calculated by the DAQ for all 20 pulses is given in the top right of the plot. The amplitude for the pulse in segment 6 was not calculated.

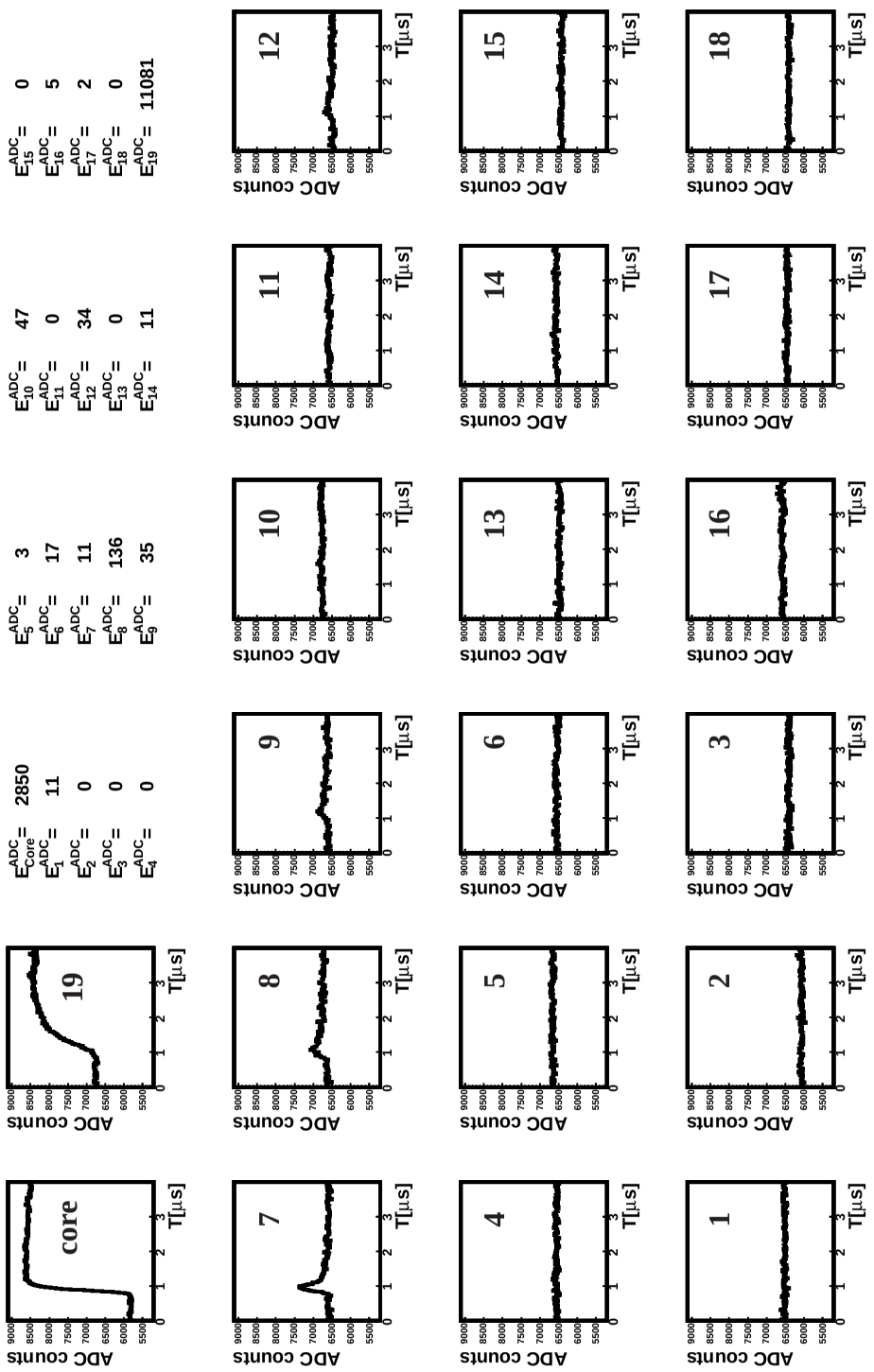

Figure 14.17.: The 20 pulses in ADC counts as a function of the time for a class “D” event. The measured amplitude in ADC counts as calculated by the DAQ for all 20 pulses is given in the top right of the plot. The amplitude for the pulse in segment 19 was not correctly calculated. Instead of approximately $E_{19}^{ADC} \approx 1700$ a value of $E_{19}^{ADC} = 11081$ was calculated.

14.4. Estimate of the Inactive Layers

The situtation at the end plates of the detector is very complicated. However, it is possible to evaluate any loss in efficiency in terms of an effective dead or inactive layer IL. Its thickness on top of the detector can be estimated using the number of events in a γ-peak, N_X^{data}, with X being segment 19 or core and the number of events in a γ-peak in the segment below segment 19, $N_{SegBelow}^{data}$. The corresponding numbers of events from a Monte Carlo simulation assuming no dead layer, N_X^{MC}, are also needed. Double ratios, DR, are calculated:

$$DR = \left(\frac{N_X^{data}}{N_{SegBelow}^{data}} \right) / \left(\frac{N_{19}^{MC}}{N_{SegBelow}^{MC}} \right). \tag{14.1}$$

The double ratios are used to calculate the thickness of the inactive layer d_{IL}^{data}. The double ratios are advantageous, since efficiencies and acceptances cancel out.

The number of events seen in the segments is given by

$$\begin{aligned} N_{19}^{data} &= I_0 \cdot e^{-\mu_{att} \cdot d_{IL}} \left(1 - e^{-\mu_{abs} \cdot (d_{19}^{data} - d_{IL})} \right) \\ N_{SegBelow}^{data} &= I_0 \cdot e^{-\mu_{att} \cdot d_{19}^{data}} \\ N_{19}^{MC} &= I_0' \cdot \left(1 - e^{-\mu_{abs} \cdot d_{19}^{MC}} \right) \\ N_{SegBelow}^{MC} &= I_0' \cdot e^{-\mu_{att} \cdot d_{19}^{MC}}, \end{aligned} \tag{14.2}$$

where d_{19}^{MC} is the thickness of segment 19 used in the MC, d_{19}^{data} is the thickness of segment 19 and μ_{abs} is the linear absorption and $\mu_{att}$is the linear attenuation coefficient of the material at a given energy. I_0 and I_0' are the intensities of the incoming radiation in data and MC, respectively. It is assumed that all 121.78 keV photons were absorbed by the segment below segment 19.

Using Eqs. (14.2) and assuming that $d_{19}^{MC} = d_{19}^{data} = d_{19}$, Eq. (14.1) is rewritten as

$$DR = \frac{e^{-\mu_{att} \cdot d_{IL}} \left(1 - e^{-\mu_{abs} \cdot (d_{19} - d_{IL})} \right)}{\left(1 - e^{-\mu_{abs} \cdot d_{19}} \right)}. \tag{14.3}$$

This equation is used to extract the d_{IL}, by varying d_{IL} until Eq. (14.3) is fulfilled.

14.4.1. Data Selection

The data sets of the radial scan with the ^{152}Eu source, see Sec. 11.3, were used. A measurement was taken every $r = 5\,\text{mm}$ from inside out, starting at a radius $r = 5\,\text{mm}$, for $\phi = 215^\circ$, $\phi = 237.5^\circ$ and $\phi = 260^\circ$. Single segment events were selected in the top two

segment layers, i.e. only one segment had $E_i > 20\,\text{keV}$. The number of events under the 121.78 keV photon peak were extracted fitting the spectra with a first order polynomial plus Gaussian to describe the peak and background. The extracted numbers of events under the peak were normalized to the net DAQ recording time, the "lifetime".

14.4.2. Monte Carlo Samples

Monte Carlo samples were generated with the setup described in Sec. 11.4. The simulated thickness of segment 19 was $d_{19}^{MC} = 5\,\text{mm}$. No dead layers on top or at the lithium drifted n^+ contact at the core were simulated.

The full spectrum of ^{152}Eu was simulated. Each simulated Monte Carlo sample contained $1.2 \cdot 10^6$ events, about twice as many as in the data sets. The energy in the Monte Carlo was smeared with the measured resolution, see Sec. 11.8.4. The Monte Carlo samples were treated in the same way as the data samples.

14.4.3. Results

The linear attenuation coefficient used to calculate d_{IL} was $\mu_{att} = 1.9252\,\text{cm}^{-1}$ and the linear absorption coefficient was $\mu_{abs} = 1.108\,\text{cm}^{-1}$ [112] for germanium at 121.78 keV.

The thickness of the inactive layer in segment 19 were extracted from the segment spectra. The results as a function of the radius at the scanning angles of $\phi = 215^\circ$, $\phi = 237.5^\circ$ and $\phi = 260^\circ$ are shown in Fig. 14.18. The uncertainty was estimated varying the number of events extracted from the data by their uncertainty and extracting the largest and the smallest observed value for the inactive layer.

At low r, no 121.78 keV peak in the spectra of segment 19 was found. This is expected, since the bore hole radius is 5.05 mm and the conical shape of the bore hole at the ends increases the bore hole radius to 10 mm. In addition, the lithium drifted n^+ contact causes dead-layers up to 500 μm. Therefore, at $r = 5\,\text{mm}$ and $r = 10\,\text{mm}$ no values were extracted. The scan positions of $\phi = 237.5^\circ$ and $\phi = 260^\circ$ are in the region under the segment contact, where the rise times in segment 19 were good. For these positions the IL at $r = 15\,\text{mm}$ was about 1.5 mm thick, i.e. 30% of the volume was inactive. At $\phi = 215^\circ$, the situation was even worse. The IL was calculated to be $3.2 \pm 0.23\,\text{mm}$. At $r \geq 20\,\text{mm}$ the IL had a thickness of the order of 0.5 mm. The IL increased again at $r = 35\,\text{mm}$. This is unexpected.

The inactive layers were also extracted from the core energy spectra of single segment events in segment 19. The results are shown in Fig. 14.19. At $r = 5\,\text{mm}$ no peak was observed in the core spectra. At $\phi = 215^\circ$ and $\phi = 237.5^\circ$ and $r = 10\,\text{mm}$, an inactive layer of $d_{IL} = 4.24 \pm 0.48\,\text{mm}$ and $d_{IL} = 5.21 \pm 0.51\,\text{mm}$ was observed; segment 19 was basically inactive. At $\phi = 215^\circ$ and larger r, the thickness of the inactive layer decreases up to

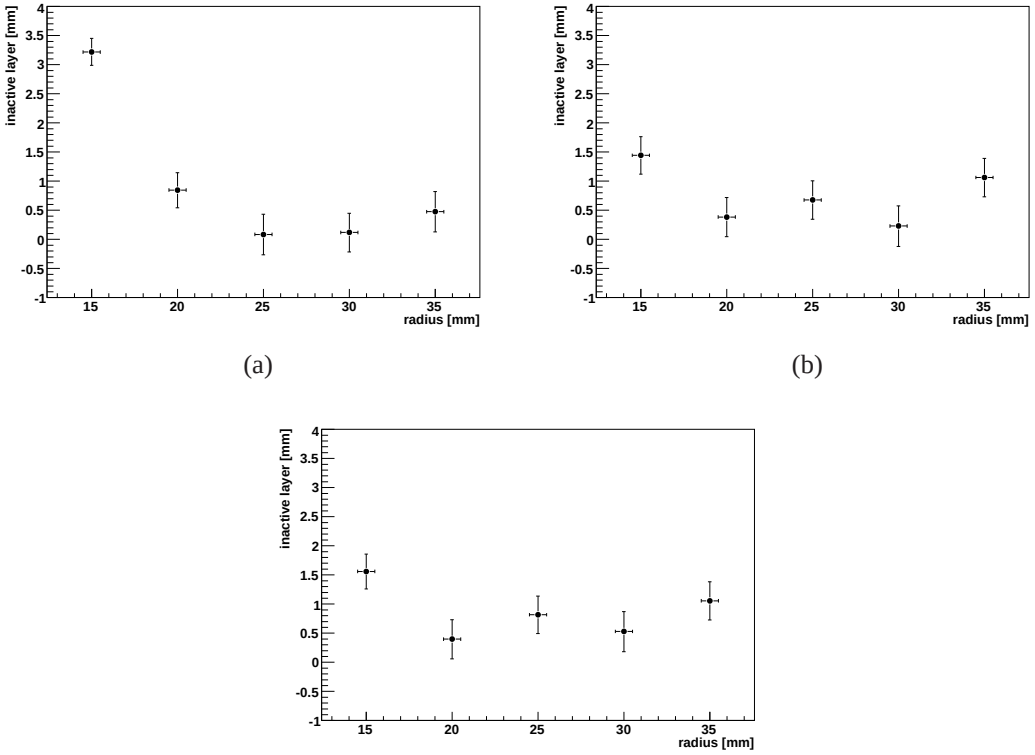

Figure 14.18.: Thickness of the inactive layer observed in the 19th segment, estimated from double ratios from r scans at (a) $\phi = 215^\circ$, (b) $\phi = 237.5^\circ$ and at (c) $\phi = 260^\circ$, respectively.

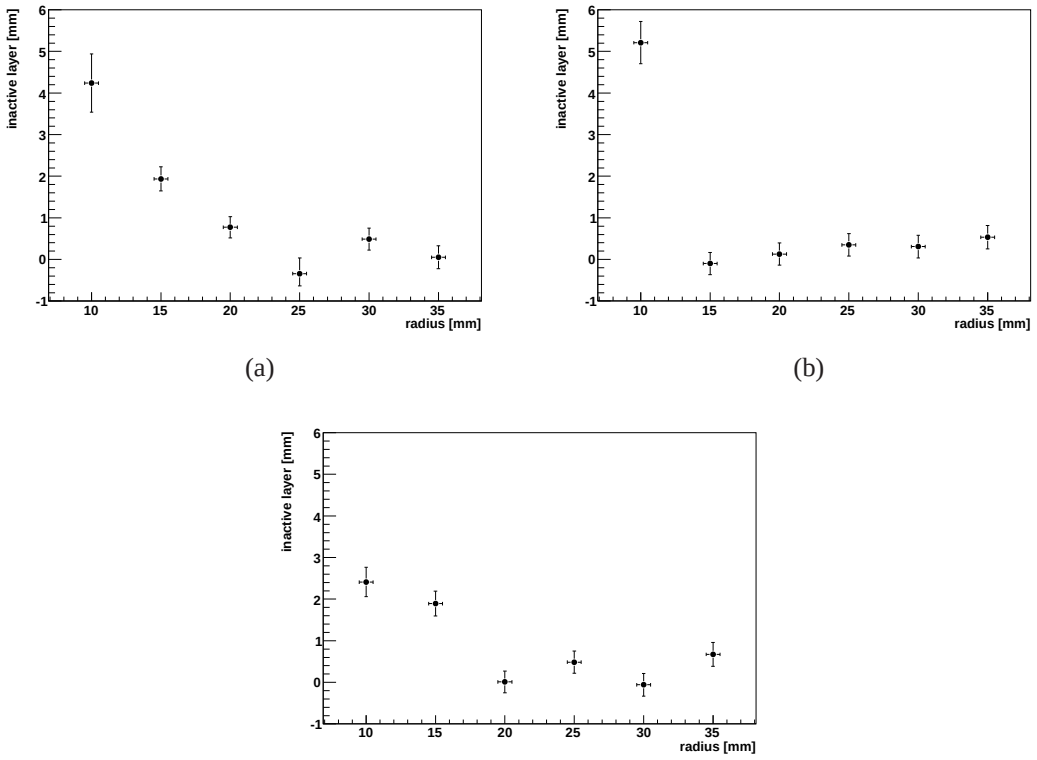

Figure 14.19.: Thickness of inactive layer observed in the core, estimated from double ratios from r scans at (a) $\phi = 215^\circ$, (b) $\phi = 237.5^\circ$ and at (c) $\phi = 260^\circ$, respectively.

$r = 25\,\text{mm}$ where a value of $d_{IL} = -0.34 \pm 0.36\,\text{mm}$ was found. At this point segment 19 as seen by the core was basically fully active. A negative value of $d_{IL} = -0.10 \pm 0.23\,\text{mm}$ is also observed at $\phi = 237.5^\circ$ and $r = 15\,\text{mm}$. At all angles and $r \leq 20\,\text{mm}$ the inactive layer is basically constant at around $0.25\,\text{mm}$.

The assumption made here was that the segment below segment 19 was fully active. Moreover it was assumed that the segment below segment 19 absorbed all 121.78 keV photons. No 121.78 keV peak was found in any other segment, therefore this assumption is also fulfilled. In addition, it was assumed that the thickness of segment 19 is 5 mm, which should be fulfilled to high precision.

The inactive layers as determined from the core spectra are in general thinner than the ones determined from the segment spectra. The signals in the segment are more influenced by the holes than the core signals. Therefore, this is possible. The rather large thicknesses of the inactive layers could be explained by n-type and/or p-type surface channels, for which there was also evidence in the previous sections.

An n-type surface channel would induce a large inactive layer seen by the core at large r. Such an inactive layers should decrease with decreasing radius. This is not observed. The thick inactive layer observed at small r might be attributed to a distorted electric field close to the conical inner bore hole.

A p-type surface channel would induce inactive layers seen by segment 19 at small r. The inactive layers would decrease towards large r. This is in fair agreement with the data. The slight rise towards the maximum r is incompatible with this model. Again, an effect of the conical bore hole might be superimposed on a surface channel effect.

14.5. Summary of the Results Concerning the Top Surface

Extremely long 10%-90% rise times of pulses, of the order of 1 μs, were observed in the electrode of segment 19 for events close to the outer mantle of the detector. The segment was not metallized except for an extended read-out contact. Close to this contact the rise times were short, indicating a better electric field in this region. The long rise times were caused by a slow drift of the holes. The corresponding pulses observed in the core electrode had normal rise times, indicating that the electron drift was not strongly affected. The events were selected using the energy as determined from the core and segment pulses. This yielded a good sample indicating that the data acquisition and event selection were reasonably efficient.

However, the energy determination did not always yield reasonable results. Four classes of events were found where the sum of the segment energies, $\sum_i E_i$, did not agree with the core energy, E_{core}.

For events with $\sum_i E_i - E_{\text{core}} > 20 \cdot \sigma_{\text{core}}$ and $\sum_i E_i - E_{\text{core}} < 800\,\text{keV}$, class “A” events, there is strong evidence that they were caused by electrons being trapped inside the detector. This was probably due to the development of an n-type surface channel.

For events with $E_{\text{core}} - \sum_i E_i > 20 \cdot \sigma_{\text{core}}$ and $E_{\text{core}} - \sum_i E_i < 600\,\text{keV}$, class “B” events, there is some evidence that they were caused by hole trapping close to the outer segment boundary. The evidence for hole trapping is not as strong, though, as for stopped electrons in class ”A” events. Hole trapping is expected for a p-type surface channel. However, the shape of the inactive layers can only partially be explained by a surface channel. In addition, the effect of the conical bore hole is superimposed.

In these two cases the pulses are so distorted that a correct energy determination is impossible due to the physics inside the detector. The other two classes show extreme combinations of long pulses for which the settings of the DAQ were just not suitable.

The design of future detectors could make use of the physical effects. The metallization close to the end faces could be omitted and thus a zone created in which long pulses in the mantle electrode tag events close to the end face. This would help reject surface events which are expected to contribute to the background in experiments like GERDA. However, the fiducial volume would then be reduced. In addition the data acquisition and event treatment have to be adjusted. Depending on the system design, it might be better to establish a metallization as close to the end plate as possible.

The situation at the end plates of the detector is extremely complicated. However, the effects can be simplify and attributed to an effective “dead” or inactive layer which represents the observed inefficiency close to the surface. This layer is not a physical volume and its effective thickness depends on whether electron or hole drift is considered and how events

are selected and treated. The effective inactive layer on top of the detector was estimated using core and segment 19 spectra. The thickness of the layer as observed through the electrode of segment 19 was large on the inside and dropped towards larger r and rose again. The thickness varied between $3.2 \pm 0.23\,\mathrm{mm}$ and $84 \pm 168\,\mu\mathrm{m}$.

The dead layer as probed by the core electrode shows a similar behavior. It was large at small r and dropped towards larger r, but stayed constant at about $r > 20\,\mathrm{mm}$.

As an implication of this analysis, the design of future detectors should take inefficiencies around the end plates into account. This can only be done considering all system aspects including data acquisition and offline event selection.

15. Summary and Outlook

A fully working pulse shape simulation was developed and evaluated. The 19-fold segmented Super-Siegfried-detector was characterized and surface effects were studied. The background index expected for the second phase of the GERDA experiment due to radioactive decays in the detectors and detector strings was estimated.

The pulse shape simulation package includes the calculation of the electric field and the weighting potentials inside the detector for various scenarios of the impurity density distribution. Individual hits were generated within the framework of the GEANT4 based package MAGE and the drift of the holes and electrons were simulated including the effect of longitudinal and transverse anisotropy.

The 19-fold segmented Super-Siegfried true-coaxial high-purity n-type germanium-detector was operated in a vacuum cryostat. The depletion voltage was measured, and the detector fully characterized, including the positioning of the crystal axes and segment boundaries. For further studies, cross-talk was corrected. Special data was taken to characterize the top surface.

The evaluation of the pulse shape simulation was based on data taken with Super Siegfried. As expected, the simulation had to be adjusted to the impurity levels of the detector. Since these were not known a priori, this was done by a fit, yielding a result compatible with the range of values given by the manufacturer. The general agreement in shape between averaged simulated and averaged data pulses was reasonable. The simulated core pulses had to be stretched by about 10% to fit the data. The simulated segment pulses had to shortened by about 5% to fit the data.The simulation can be improved using measured pre-amplifier transfer functions instead of a simple model. The simulated pulses should be used as an input to pulse shape analyses as well understood and controllable training samples.

The background index expected for the second phase of the GERDA experiment due to radioactive decays in the detector and the detector strings was estimated. The detailed geometry of the holder structure, the cables and the electronics was included into the GERDA implementation in the Monte Carlo framework MAGE. The complete decay chains of ^{232}Th and ^{238}U were simulated. In addition, the decay of ^{60}Co was simulated. In the crystals the decay of ^{68}Ge was included and the decay of ^{110m}Ag was simulated where screening results indicated the presence of that isotope. The estimated background index was $4.7 \cdot 10^{-3}\mathrm{cts}/(\mathrm{keV} \cdot \mathrm{kg} \cdot \mathrm{y})$. This included the usage of segment anti-coincidences. It exceeds the target of $1 \cdot 10^{-3}\mathrm{cts}/(\mathrm{keV} \cdot \mathrm{kg} \cdot \mathrm{y})$ for the background in Phase II. The decay of

^{68}Ge inside the detectors is the main contribution. However, the production rate of ^{68}Ge above ground is only know up to a factor of 2. In addition ^{68}Ge has a half-life of only 270 days.

The top surface was studied. Close to the surface in segment 19, the rise times of the segment pulses were very long, of the order of 1 μs. Close to the segment read-out contact the rise times were small, of the order of 210 ns. Events with $E_{\text{core}} \neq \sum_i E_i$ were found. One group of events could be attributed to electron trapping. A second group of events might have been induced by hole trapping. In a third group of events, long core and segment rise times were found, indicating slow drift of both electrons and holes making a correct calculation of the energy impossible in this setup. Effective inactive layers on the top surface were found. Different thicknesses were extracted depending on whether the inactive layers were estimated from the core or segment spectra. The different long rise times, electron and hole trapping and the inactive layers could be interpreted as evidence for surface channels. However, the shape of the inactive layers can hardly be explained exclusively by surface channels. The effect of the conical bore hole is superimposed.

Further investigations of the top surface should be made, using α and β particles, which do not penetrate deeply. In this way the effective inactive layers could be measured very precisely and the effects causing them could be better understood. This could be done in the new GALATEA test stand which is currently under construction. The source will be inside the cryostat, i.e. no material will be between the detector and the sources. In addition, a tunable laser can be used inside GALATEA to scan the crystal.

A. Tables of expected background index from GERDA array

Isotope	SP_{ROI} $[10^{-6}]$	b_{ROI} $[10^{-4}\text{cts}/(\text{keV}\cdot\text{kg}\cdot\text{y})]$	SP_{SC} $[10^{-6}]$	b_{SC} $[10^{-4}\text{cts}/(\text{keV}\cdot\text{kg}\cdot\text{y})]$	SP_{SS} $[10^{-6}]$	b_{SS} $[10^{-4}\text{cts}/(\text{keV}\cdot\text{kg}\cdot\text{y})]$
^{60}Co	4672	0.7367 ± 0.0108	1528	0.2409 ± 0.0062	119	0.0188 ± 0.0017
^{68}Ge (first year)	6465	323.8176 ± 4.0273	3051	152.8179 ± 2.7666	364	18.2319 ± 0.9556
^{68}Ge (second year)	6465	127.2199 ± 1.5822	3051	60.0384 ± 1.7903	364	7.1629 ± 0.3754
^{232}Th chain						
^{232}Th	1.0	0.0001 ± 0.0001	1.0	0.0001 ± 0.0001	1.0	0.0001 ± 0.0001
^{228}Ac	408	0.0386 ± 0.0019	251	0.0237 ± 0.0015	42	0.0040 ± 0.0006
^{228}Th	1	0.0001 ± 0.0001	1	0.0001 ± 0.0001	1	0.0001 ± 0.0001
^{220}Rn	2	0.0002 ± 0.0001	2	0.0002 ± 0.0001	2	0.0002 ± 0.0001
^{216}Po	3	0.0003 ± 0.0002	3	0.0003 ± 0.0002	3	0.0003 ± 0.0002
^{212}Bi	570	0.0539 ± 0.0026	502	0.0475 ± 0.0021	381	0.0360 ± 0.0018
^{208}Tl + ^{212}Po	1168	0.1105 ± 0.0032	471	0.0446 ± 0.0021	85	0.0080 ± 0.0009
^{238}U chain						
^{238}U	1	0.0002 ± 0.0002	1	0.0002 ± 0.0002	1	0.0002 ± 0.0002
^{234}Pa + ^{234m} Pa	858	0.1352 ± 0.0046	827	0.1304 ± 0.0045	705	0.1111 ± 0.0041
^{234}U	3	0.0005 ± 0.0003	2	0.0003 ± 0.0003	2	0.0003 ± 0.0003
^{230}Th	1	0.0002 ± 0.0002	1	0.0002 ± 0.0002	1	0.0002 ± 0.0002
^{226}Ra	1	0.0002 ± 0.0002	1	0.0002 ± 0.0002	1	0.0002 ± 0.0002
^{222}Rn	2	0.0003 ± 0.0002	2	0.0003 ± 0.0002	2	0.0003 ± 0.0002
^{218}Po	7	0.0011 ± 0.0004	7	0.0011 ± 0.0004	7	0.0011 ± 0.0004
^{214}Bi	7444	1.1749 ± 0.0136	4014	0.6335 ± 0.0100	1478	0.2333 ± 0.0061
^{210}Tl + ^{214} Po	10	0.0016 ± 0.0005	6	0.0009 ± 0.0003	4	0.0006 ± 0.0003
^{210}Pb	1	0.0002 ± 0.0002	1	0.0002 ± 0.0002	1	0.0002 ± 0.0002
^{206}Tl + ^{210} Po	1	0.0002 ± 0.0002	1	0.0002 ± 0.0002	1	0.0002 ± 0.0002
Sum:(first year)		326.07 ± 4.03		153.94 ± 2.77		18.65 ± 0.96
Sum:(second year)		129.48 ± 1.59		61.16 ± 1.10		7.58 ± 0.38

Table A.1.: Expected background index from the crystals. The first column shows the isotope under consideration. The second column shows the background index, using events selected after the ROI cut. The background index in third and fourth column shown are calculated using Single-Crystal (SC) and Single-Segment (SS) events only. Each crystal has a mass of 1.616 kg. The overall enriched germanium mass is 33.94 kg. The assumed contamination of the enriched germanium is $0.01 \cdot 10^{-3}$ mBq/kg for ^{238}U and $0.006 \cdot 10^{-3}$ mBq/kg for ^{232}Th. The background is calculated for 33.94 kg enriched germanium in an energy window from 2.029 MeV to 2.049 MeV.

Isotope	SP_{ROI} $[10^{-6}]$	b_{ROI} $[10^{-4}\text{cts}/(\text{keV}\cdot\text{kg}\cdot\text{y})]$	SP_{SC} $[10^{-6}]$	b_{SC} $[10^{-4}\text{cts}/(\text{keV}\cdot\text{kg}\cdot\text{y})]$	SP_{SS} $[10^{-6}]$	b_{SS} $[10^{-4}\text{cts}/(\text{keV}\cdot\text{kg}\cdot\text{y})]$
^{60}Co	1288.3	4.0270 ± 0.0354	174.7	0.5460 ± 0.0131	6.5	0.0203 ± 0.0025
^{232}Th chain						
^{228}Ac	0.9	0.0053 ± 0.0018	0.8	0.0048 ± 0.0017	0.1	0.0006 ± 0.0006
^{208}Tl + ^{212}Po	685.1	4.0689 ± 0.0492	255.1	1.5150 ± 0.0299	114.9	0.6824 ± 0.0201
^{238}U chain						
^{214}Bi	420.3	2.1021 ± 0.0324	164.9	0.8250 ± 0.0203	57	0.2889 ± 0.0120
^{210}Tl + ^{214}Po	0.3	0.0010 ± 0.0007	-	-	-	-
^{210}Pb	0.3	0.0010 ± 0.0007	-	-	-	-
Sum:		10.20 ± 0.07		2.89 ± 0.04		0.99 ± 0.02

Table A.2.: Expected background index from the copper holders. The first column shows the isotope under consideration. The second column shows the background index, using events selected after the ROI cut. The background index in third and fourth column shown are calculated using Single-Crystal (SC) and Single-Segment (SS) events only. The holder is made from 32.04 g copper. The overall copper mass is 0.67284 kg. The assumed contamination of the copper is 0.016 mBq/kg for ^{238}U, 0.019 mBq/kg for ^{232}Th and 0.01 mBq/kg for ^{60}Co. The background is calculated for 33.94 kg enriched germanium in an energy window from 2.029 MeV to 2.049 MeV.

Isotope	SP_{ROI} $[10^{-6}]$	b_{ROI} $[10^{-4}\text{cts}/(\text{keV} \cdot \text{kg} \cdot \text{y})]$	SP_{SC} $[10^{-6}]$	b_{SC} $[10^{-4}\text{cts}/(\text{keV} \cdot \text{kg} \cdot \text{y})]$	SP_{SS} $[10^{-6}]$	b_{SS} $[10^{-4}\text{cts}/(\text{keV} \cdot \text{kg} \cdot \text{y})]$
^{232}Th chain						
^{228}Ac	1.71	0.0127 ± 0.0031	1.41	0.0105 ± 0.0028	0.6	0.0045 ± 0.0018
^{212}Bi	0.9	0.0068 ± 0.0023	0.8	0.0060 ± 0.0021	0.6	0.0045 ± 0.0018
^{208}Tl + ^{212}Po	848.7	6.3462 ± 0.0691	330.6	2.4723 ± 0.0431	112.3	0.9145 ± 0.0262
^{238}U chain						
^{234}Pa + ^{234m}Pa	1.1	0.0082 ± 0.0025	1.1	0.0082 ± 0.0025	0.7	0.0052 ± 0.0020
^{214}Bi	669.1	5.0031 ± 0.0612	287.1	2.1465 ± 0.0400	88.1	0.6586 ± 0.0222
^{210}Tl + ^{214}Po	0.7	0.0052 ± 0.0019	0.3	0.0022 ± 0.0013	-	-
^{210}Pb	0.2	0.0015 ± 0.0011	0.2	0.0015 ± 0.0011	0.2	0.0015 ± 0.0011
Sum:		11.38 ± 0.09		4.65 ± 0.06		1.59 ± 0.03

Table A.3.: Expected background index from the Teflon plugs. The first column shows the isotope under consideration. The second column shows the background index, using events selected after the ROI cut. The background index in third and fourth column shown are calculated using Single-Crystal (SC) and Single-Segment (SS) events only. The holder plugs are made from 4.79 g Teflon. The overall Teflon mass is 0.101 kg. The assumed contamination of the Teflon is 0.16 mBq/kg for ^{238}U and 0.16 mBq/kg for ^{232}Th. The background is calculated for 33.94 kg enriched germanium in an energy window from 2.029 MeV to 2.049 MeV.

Isotope	SP_{ROI} $[10^{-6}]$	b_{ROI} $[10^{-4}\text{cts}/(\text{keV} \cdot \text{kg} \cdot \text{y})]$	SP_{SC} $[10^{-6}]$	b_{SC} $[10^{-4}\text{cts}/(\text{keV} \cdot \text{kg} \cdot \text{y})]$	SP_{SS} $[10^{-6}]$	b_{SS} $[10^{-4}\text{cts}/(\text{keV} \cdot \text{kg} \cdot \text{y})]$
^{232}Th chain						
^{228}Ac	0.9	0.0019 ± 0.0006	0.5	0.0010 ± 0.0005	0.3	0.0006 ± 0.0004
^{208}Tl + ^{212}Po	640.5	1.3398 ± 0.0167	238	0.4978 ± 0.01020	118	0.2468 ± 0.0072
^{238}U chain						
^{214}Bi	370.5	0.7751 ± 0.0127	142.7	0.2986 ± 0.0079	48	0.1005 ± 0.0046
^{210}Tl + ^{214}Po	0.5	0.0010 ± 0.0005	0.1	0.0002 ± 0.0002	-	-
^{210}Pb	0.3	0.0006 ± 0.0004	0.2	0.0004 ± 0.0003	-	-
Sum:		2.14 ± 0.02		0.79 ± 0.01		0.34 ± 0.09

Table A.4.: Expected background index from the signal-cable guides. The first column shows the isotope under consideration. The second column shows the background contribution, using events selected after the ROI cut. The background index in third and fourth column shown are calculated using Single-Crystal (SC) and Single-Segment (SS) events only. The Signal-cable-guides are made from 1.34 g Teflon. The overall Teflon mass is 0.02814 kg. The assumed contamination of the Teflon is 0.16 mBq/kg for ^{238}U and 0.16 mBq/kg for ^{232}Th. The background is calculated for 33.94 kg enriched germanium in an energy window from 2.029 MeV to 2.049 MeV.

Isotope	SP_{ROI} [10^{-6}]	b_{ROI} [10^{-4}cts/(keV · kg · y)]	SP_{SC} [10^{-6}]	b_{SC} [10^{-4}cts/(keV · kg · y)]	SP_{SS} [10^{-6}]	b_{SS} [10^{-4}cts/(keV · kg · y)]
^{232}Th chain						
^{228}Ac	0.5	0.0011 ± 0.0005	0.2	0.005 ± 0.0003	-	-
^{212}Bi	0.2	0.0004 ± 0.0003	0.2	0.0004 ± 0.0003	0.2	0.0004 ± 0.0003
^{208}Tl + ^{212}Po	708.1	1.5917 ± 0.0189	258.8	0.5795 ± 0.0114	120	0.2697 ± 0.0077
^{238}U chain						
^{234}Pa + ^{234m}Pa	0.3	0.0006 ± 0.0004	0.3	0.0006 ± 0.0004	0.2	0.0004 ± 0.0003
^{214}Bi	480.9	1.0819 ± 0.0156	191.1	0.4299 ± 0.0098	73.7	0.1656 ± 0.0061
^{210}Tl + ^{214}Po	0.3	0.0007 ± 0.0004	0.1	0.0002 ± 0.0002	-	-
^{210}Pb	0.1	0.0002 ± 0.0002	-	-	-	-
Sum:		2.68 ± 0.02		1.02 ± 0.02		0.44 ± 0.01

Table A.5.: Expected background index from the high-voltage-cable guides. The first column shows the isotope under consideration. The second column shows the background contribution, using events selected after the ROI cut. The background index in third and fourth column shown are calculated using Single-Crystal (SC) and Single-Segment (SS) events only. The Signal-cable-guides are made from 1.44 g Teflon. The overall Teflon mass is 0.03024 kg. The assumed contamination of the Teflon is 0.16 mBq/kg for ^{238}U and 0.16 mBq/kg for ^{232}Th. The background is calculated for 33.94 kg enriched germanium in an energy window from 2.029 MeV to 2.049 MeV.

Isotope	SP_{ROI} $[10^{-6}]$	b_{ROI} $[10^{-4}\text{cts}/(\text{keV}\cdot\text{kg}\cdot\text{y})]$	SP_{SC} $[10^{-6}]$	b_{SC} $[10^{-4}\text{cts}/(\text{keV}\cdot\text{kg}\cdot\text{y})]$	SP_{SS} $[10^{-6}]$	b_{SS} $[10^{-4}\text{cts}/(\text{keV}\cdot\text{kg}\cdot\text{y})]$
^{60}Co *left*	32.5	0.0065 ± 0.0004	1.9	0.0004 ± 0.0001	0.1	0.00002 ± 0.00002
^{60}Co *right*	37.7	0.0076 ± 0.0004	3.2	0.0006 ± 0.0001	0.1	0.00002 ± 0.00002
^{232}Th chain						
^{228}Ac *right*	0.2	0.00008 ± 0.00005	0.2	0.00008 ± 0.00005	0.1	0.00004 ± 0.00004
^{208}Tl + ^{212}Po *left*	104.3	0.0401 ± 0.0012	59.3	0.0228 ± 0.0009	31.2	0.0120 ± 0.0007
^{208}Tl + ^{212}Po *right*	103.0	0.0396 ± 0.0012	57.3	0.0220 ± 0.0009	27.5	0.0106 ± 0.0006
^{238}U chain						
^{214}Bi *left*	37.0	0.0119 ± 0.0006	20.6	0.0067 ± 0.0001	8.1	0.0026 ± 0.0003
^{214}Bi *right*	33.6	0.0109 ± 0.0006	17.3	0.0056 ± 0.0004	7.6	0.0025 ± 0.0003
Sum:		0.12 ± 0.01		0.06 ± 0.01		0.03 ± 0.01

Table A.6.: Expected background index from the copper spacer. Since left and right support string have been simulated independently, for each isotope there are two values, indicated with *left* and *right*. The first column shows the isotope under consideration. The second column shows the background index, using events selected after the ROI cut. The background index in third and fourth column shown are calculated using Single-Crystal (SC) and Single-Segment (SS) events only. The spacer have a mass of 12.5 g per string. The overall mass is 0.0435715 kg. The assumed contamination of the support strings is 0.016 mBq/kg for ^{238}U and 0.019 mBq/kg for ^{232}Th and 0.01 mBq/kg for ^{60}Co. The background is calculated for 33.94 kg enriched germanium in an energy window from 2.029 MeV to 2.049 MeV.

Isotope	SP_{ROI} $[10^{-6}]$	b_{ROI} $[10^{-4}\text{cts}/(\text{keV} \cdot \text{kg} \cdot \text{y})]$	SP_{SC} $[10^{-6}]$	b_{SC} $[10^{-4}\text{cts}/(\text{keV} \cdot \text{kg} \cdot \text{y})]$	SP_{SS} $[10^{-6}]$	b_{SS} $[10^{-4}\text{cts}/(\text{keV} \cdot \text{kg} \cdot \text{y})]$
^{60}Co	2988.1	20.5608 ± 0.1188	628.3	4.3232 ± 0.0544	41.7	0.2870 ± 0.0140
^{232}Th chain						
^{228}Ac	1.5	0.0208 ± 0.0052	1	0.0136 ± 0.0044	0.3	0.0040 ± 0.0024
^{212}Bi	60.8	0.8368 ± 0.0340	55.4	0.7624 ± 0.0324	29.9	0.4108 ± 0.0236
^{208}Tl + ^{212}Po	893.1	12.2908 ± 0.1300	289.4	3.9824 ± 0.074	83.3	1.1460 ± 0.0396
^{238}U chain						
^{234}Pa + ^{234m}Pa	103	3.1896 ± 0.0990	99.8	3.0906 ± 0.0981	55	1.7028 ± 0.0729
^{214}Bi	2287.5	70.8300 ± 0.4689	987.6	30.5802 ± 0.3078	291.7	9.0306 ± 0.1674
^{210}Tl + ^{214}Po	2.1	0.0648 ± 0.0144	0.6	0.0189 ± 0.0072	0.1	0.0027 ± 0.0027
^{210}Pb	0.1	0.0027 ± 0.0027	0.1	0.0027 ± 0.0027	0.1	0.0027 ± 0.0027
Sum:		107.80 ± 0.51		42.77 ± 0.34		12.58 ± 0.19

Table A.7.: Expected background index from the Kapton cable. The first column shows the isotope under consideration. The second column shows the background index, using events selected after the ROI cut. The background index in third and fourth column shown are calculated using Single-Crystal (SC) and Single-Segment (SS) events only. The Kapton cables are made from 0.35 g Kapton. The overall Kapton mass is 0.0074 kg. The assumed contamination of the Kapton is 9 mBq/kg for ^{238}U, 4 mBq/kg for ^{232}Th and 2 mBq/kg for ^{60}Co. The background is calculated for 33.94 kg enriched germanium in an energy window from 2.029 MeV to 2.049 MeV.

Isotope	SP_{ROI} [10^{-6}]	b_{ROI} [10^{-4}cts/(keV · kg · y)]	SP_{SC} [10^{-6}]	b_{SC} [10^{-4}cts/(keV · kg · y)]	SP_{SS} [10^{-6}]	b_{SS} [10^{-4}cts/(keV · kg · y)]
^{60}Co	3031.4	0.7793 ± 0.0045	644	0.1656 ± 0.0021	37.2	0.0096 ± 0.0005
^{232}Th chain						
^{228}Ac	1.5	0.0007 ± 0.0002	1.1	0.0005 ± 0.0002	0.4	0.0002 ± 0.0001
^{212}Bi	35.5	0.0173 ± 0.0009	32.4	0.0158 ± 0.0009	16.6	0.0081 ± 0.0006
^{208}Tl + ^{212}Po	909	0.4440 ± 0.0047	301.2	0.1471 ± 0.0027	92.2	0.045 ± 0.0015
^{238}U chain						
^{234}Pa + ^{234m}Pa	69.8	0.0287 ± 0.0011	67.7	0.0278 ± 0.0011	36.4	0.0150 ± 0.0008
^{214}Bi	2144.4	0.8829 ± 0.0060	931.6	0.3835 ± 0.0039	287.4	0.1183 ± 0.0022
^{210}Tl + ^{214}Po	0.9	0.0004 ± 0.0001	0.3	0.0001 ± 0.0001	-	-
^{210}Pb	0.3	0.0001 ± 0.0001	0.1	0.00004 ± 0.00004	-	-
Sum:		2.15 ± 0.01		0.74 ± 0.01		0.20 ± 0.01

Table A.8.: Expected background index from the copper signal lines on the back of the Kapton cable. The first column shows the isotope under consideration. The second column shows the background index, using events selected after the ROI cut. The background index in third and fourth column shown are calculated using Single-Crystal (SC) and Single-Segment (SS) events only. The copper-plated signal lines are made from 2.64 g copper. The overall copper mass is 0.0553 kg. The assumed contamination of the copper is 0.016 mBq/kg for ^{238}U, 0.019 mBq/kg for ^{232}Th and 0.01 mBq/kg for ^{60}Co. The background is calculated for 33.94 kg enriched germanium in an energy window from 2.029 MeV to 2.049 MeV.

Isotope	SP_{ROI} [10^{-6}]	b_{ROI} [10^{-4}cts/(keV · kg · y)]	SP_{SC} [10^{-6}]	b_{SC} [10^{-4}cts/(keV · kg · y)]	SP_{SS} [10^{-6}]	b_{SS} [10^{-4}cts/(keV · kg · y)]
^{60}Co	661.5	4.5446 ± 0.0558	129.3	0.8884 ± 0.0248	8.2	0.0564 ± 0.0062
^{232}Th chain						
^{228}Ac	0.7	0.0096 ± 0.0036	0.3	0.0040 ± 0.0024	-	-
^{212}Bi	6.2	0.0852 ± 0.0108	5.9	0.0812 ± 0.0104	4.7	0.0644 ± 0.0096
^{208}Tl + ^{212}Po	287.6	3.9524 ± 0.0736	116.6	1.6012 ± 0.0468	50	0.6872 ± 0.0308
^{238}U chain						
^{234}Pa + ^{234m}Pa	9.8	0.3033 ± 0.0306	9.4	0.2907 ± 0.0297	8.8	0.2718 ± 0.0288
^{214}Bi	411.1	12.7233 ± 0.198	185.5	5.7411 ± 0.1332	79.9	2.4696 ± 0.0873
^{210}Tl + ^{214}Po	0.4	0.0873 ± 0.0063	0.2	0.0063 ± 0.0045	0.1	0.0027 ± 0.0027
Sum:		21.71 ± 0.22		8.61 ± 0.15		3.55 ± 0.10

Table A.9.: Expected background index from the Kapton of the Kapton connection-cable. The first column shows the isotope under consideration. The second column shows the background contribution, using events selected after the ROI cut. The background index in third and fourth column shown are calculated using Single-Crystal (SC) and Single-Segment (SS) events only. The Kapton has a mass of 1.06 g. The overall Kapton mass is 0.0074 kg. The assumed contamination of the Kapton is 9 mBq/kg for ^{238}U, 4 mBq/kg for ^{232}Th and 2 mBq/kg for ^{60}Co. The background is calculated for 33.94 kg enriched germanium in an energy window from 2.029 MeV to 2.049 MeV.

Isotope	SP_{ROI} $[10^{-6}]$	b_{ROI} $[10^{-4}\text{cts}/(\text{keV}\cdot\text{kg}\cdot\text{y})]$	SP_{SC} $[10^{-6}]$	b_{SC} $[10^{-4}\text{cts}/(\text{keV}\cdot\text{kg}\cdot\text{y})]$	SP_{SS} $[10^{-6}]$	b_{SS} $[10^{-4}\text{cts}/(\text{keV}\cdot\text{kg}\cdot\text{y})]$
^{60}Co	643.9	0.0607 ± 0.0008	124.3	0.0117 ± 0.0003	8.9	0.0008 ± 0.0001
^{232}Th chain						
^{228}Ac	0.5	0.0001 ± 0.00004	0.4	0.0001 ± 0.00004	-	-
^{212}Bi	3.2	0.0005 ± 0.0001	3.2	0.0005 ± 0.0001	2.5	0.0004 ± 0.0001
^{208}Tl + ^{212}Po	289.3	0.0518 ± 0.0009	118.9	0.0212 ± 0.0006	50.9	0.0091 ± 0.0004
^{238}U chain						
^{234}Pa + ^{234m}Pa	6.2	0.0009 ± 0.0001	5.8	0.0009 ± 0.0001	5.5	0.0008 ± 0.0001
^{214}Bi	379.5	0.0572 ± 0.0009	170.2	0.0257 ± 0.0006	77.9	0.0118 ± 0.0004
^{210}Tl + ^{214}Po	0.2	0.00003 ± 0.00002	0.1	0.00002 ± 0.00002	-	-
Sum:		0.17 ± 0.01		0.06 ± 0.01		0.02 ± 0.01

Table A.10.: Expected background index from the copper of the Kapton connection-cable. The first column shows the isotope under consideration. The second column shows the background contribution, using events selected after the ROI cut. The background index in third and fourth column shown are calculated using Single-Crystal (SC) and Single-Segment (SS) events only. The copper has a mass of 2.90 g per string. The overall Kapton mass is 0.0203 kg. The assumed contamination of the copper is 0.016 mBq/kg for ^{238}U, 0.019 mBq/kg for ^{232}Th and 0.01 mBq/kg for ^{60}Co. The background is calculated for 33.94 kg enriched germanium in an energy window from 2.029 MeV to 2.049 MeV.

Isotope	SP_{ROI} $[10^{-6}]$	b_{ROI} $[10^{-4}\text{cts}/(\text{keV} \cdot \text{kg} \cdot \text{y})]$	SP_{SC} $[10^{-6}]$	b_{SC} $[10^{-4}\text{cts}/(\text{keV} \cdot \text{kg} \cdot \text{y})]$	SP_{SS} $[10^{-6}]$	b_{SS} $[10^{-4}\text{cts}/(\text{keV} \cdot \text{kg} \cdot \text{y})]$
^{110m}Ag	1140.6	42.5571 ± 0.3995	140.2	5.2310 ± 0.1401	2.9	0.1087 ± 0.02019
^{232}Th chain						
^{228}Ac	0.5	0.0214 ± 0.0096	0.1	0.0043 ± 0.0043	-	-
^{208}Tl + ^{212}Po	270.0	11.5152 ± 0.2221	112.6	4.8041 ± 0.1435	50.9	2.1685 ± 0.0964
^{238}U chain						
^{214}Bi	151.3	1.0487 ± 0.0269	56.8	0.3933 ± 0.0165	19.3	0.134 ± 0.0096
^{210}Tl + ^{214}Po	0.2	0.0014 ± 0.0010	0.1	0.0007 ± 0.0007	0.1	0.0007 ± 0.0007
Sum:		55.14 ± 0.46		10.43 ± 0.20		2.41 ± 0.10

Table A.11.: Expected background index from the high-voltage coaxial cable. The first column shows the isotope under consideration. The second column shows the background contribution, using events selected after the ROI cut. The background index in third and fourth column shown are calculated using Single-Crystal (SC) and Single-Segment (SS) events only. The high-voltage coaxial cable has a mass of 1.64 g, with 0.66 g Teflon and 0.98 g copper, per string. The overall mass is 0.01148 kg. The assumed contamination of the high-voltage coaxial cable is 9 mBq/kg for ^{238}U to ^{230}Th, 1.3 mBq/kg from ^{226}Ra to ^{214}Po, ^{210}Tl respectively. From ^{210}Pb on the assumed contamination is 51 mBq/kg. Te assumed contamination is 6 mBq/kg for ^{232}Th and 7 mBq/kg for ^{110m}Ag. The background is calculated for 33.94 kg enriched germanium in an energy window from 2.029 MeV to 2.049 MeV.

Isotope	SP_{ROI} $[10^{-6}]$	b_{ROI} $[10^{-4}\mathrm{cts}/(\mathrm{keV}\cdot\mathrm{kg}\cdot\mathrm{y})]$	SP_{SC} $[10^{-6}]$	b_{SC} $[10^{-4}\mathrm{cts}/(\mathrm{keV}\cdot\mathrm{kg}\cdot\mathrm{y})]$	SP_{SS} $[10^{-6}]$	b_{SS} $[10^{-4}\mathrm{cts}/(\mathrm{keV}\cdot\mathrm{kg}\cdot\mathrm{y})]$
^{60}Co	0.3	0.0006 ± 0.0003	-	–	-	-
^{232}Th chain						
^{208}Tl + ^{212}Po	18.4	0.0683 ± 0.0050	12.0	0.0448 ± 0.0040	6.1	0.0227 ± 0.0029
^{238}U chain						
^{214}Bi	5.8	0.0181 ± 0.0024	3.7	0.0115 ± 0.0019	1.4	0.0044 ± 0.0012
Sum:		0.09 ± 0.01		0.06 ± 0.01		0.03 ± 0.01

Table A.12.: Expected background index from the junction-board. The first column shows the isotope under consideration. The second column shows the background index, using events selected after the ROI cut. The background index in third and fourth column shown are calculated using Single-Crystal (SC) and Single-Segment (SS) events only. The Junction-board has a mass of 60 g, per string. The overall mass is 0.42 kg. The assumed contamination of the Junction-Board is 0.016 mBq/kg for ^{238}U and 0.019 mBq/kg for ^{232}Th and 0.01 mBq/kg for ^{60}Co. The background is calculated for 33.94 kg enriched germanium in an energy window from 2.029 MeV to 2.049 MeV.

Isotope	SP_{ROI} $[10^{-6}]$	b_{ROI} $[10^{-4}\text{cts}/(\text{keV} \cdot \text{kg} \cdot \text{y})]$	SP_{SC} $[10^{-6}]$	b_{SC} $[10^{-4}\text{cts}/(\text{keV} \cdot \text{kg} \cdot \text{y})]$	SP_{SS} $[10^{-6}]$	b_{SS} $[10^{-4}\text{cts}/(\text{keV} \cdot \text{kg} \cdot \text{y})]$
^{232}Th chain						
^{208}Tl + ^{212}Po	15.4	5.0082 ± 0.4036	10.1	3.2846 ± 0.3268	5.1	1.6586 ± 0.2322
^{238}U chain						
^{214}Bi	5.3	1.7339 ± 0.2381	2.9	0.9487 ± 0.1762	1.2	0.3925 ± 0.1133
Sum:		6.74 ± 0.47		4.23 ± 0.37		2.05 ± 0.26

Table A.13.: Expected background index from the Front-End-Electronics. The first column shows the isotope under consideration. The second column shows the background contribution, using events selected after the ROI cut. The background index in third and fourth column shown are calculated using Single-Crystal (SC) and Single-Segment (SS) events only. The FEE has a mass of 10 g, per string. The overall mass is 0.07 kg. The assumed contamination of the FEE is 10 mBq/kg for ^{238}U and 10 mBq/kg for ^{232}Th and 10 mBq/kg for ^{60}Co. The background is calculated for 33.94 kg enriched germanium in an energy window from 2.029 MeV to 2.049 MeV.

Isotope	SP_{ROI} $[10^{-6}]$	b_{ROI} $[10^{-4}\text{cts}/(\text{keV} \cdot \text{kg} \cdot \text{y})]$	SP_{SC} $[10^{-6}]$	b_{SC} $[10^{-4}\text{cts}/(\text{keV} \cdot \text{kg} \cdot \text{y})]$	SP_{SS} $[10^{-6}]$	b_{SS} $[10^{-4}\text{cts}/(\text{keV} \cdot \text{kg} \cdot \text{y})]$
^{232}Th chain						
^{208}Tl + ^{212}Po	15.8	1.396 ± 0.1108	10.5	0.9220 ± 0.0901	5.2	0.4568 ± 0.0632
^{238}U chain						
^{214}Bi	3.6	0.7119 ± 0.1188	2.2	0.4347 ± 0.0922	1.0	0.1971 ± 0.0621
Sum:		2.11 ± 0.16		1.36 ± 0.13		0.65 ± 0.09

Table A.14.: Expected background index from the electronics Kapton cable. The first column shows the isotope under consideration. The second column shows the background contribution, using events selected after the ROI cut. The background index in third and fourth column shown are calculated using Single-Crystal (SC) and Single-Segment (SS) events only. The electronics Kapton cable has a mass of 6.75 g, per string. The overall mass is 0.04725 kg. The assumed contamination of the Electronics Kapton Cable is 9 mBq/kg for ^{238}U and 4 mBq/kg for ^{232}Th and 2 mBq/kg for ^{60}Co. The background is calculated for 33.94 kg enriched germanium in an energy window from 2.029 MeV to 2.049 MeV.

Isotope	SP_{ROI} $[10^{-6}]$	b_{ROI} $[10^{-4}\text{cts}/(\text{keV}\cdot\text{kg}\cdot\text{y})]$	SP_{SC} $[10^{-6}]$	b_{SC} $[10^{-4}\text{cts}/(\text{keV}\cdot\text{kg}\cdot\text{y})]$	SP_{SS} $[10^{-6}]$	b_{SS} $[10^{-4}\text{cts}/(\text{keV}\cdot\text{kg}\cdot\text{y})]$
^{60}Co	0.2	0.0032 ± 0.0023	-	-	-	-
^{232}Th chain						
^{208}Tl + ^{212}Po	11.7	0.3550 ± 0.0328	7.9	0.2397 ± 0.0269	3.5	0.1062 ± 0.0179
^{238}U chain						
^{214}Bi	2.2	0.0563 ± 0.0120	1.1	0.0281 ± 0.0085	0.6	0.01534 ± 0.0063
Sum:		0.42 ± 0.04		0.27 ± 0.03		0.12 ± 0.02

Table A.15.: Expected background index from the copper of the junction-sled. The first column shows the isotope under consideration. The second column shows the background contribution, using events selected after the ROI cut. The background index in third and fourth column shown are calculated using Single-Crystal (SC) and Single-Segment (SS) events only. The junction-sled has a mass of 495 g made of 491 g copper and 4 g of Iglidur per string. The overall mass is 3.465 kg. The assumed contamination of the copper is 0.016 mBq/kg for ^{238}U and 0.019 mBq/kg for ^{232}Th and 0.01 mBq/kg for ^{60}Co. The background is calculated for 33.94 kg enriched germanium in an energy window from 2.029 MeV to 2.049 MeV.

Isotope	SP_{ROI} [10^{-6}]	b_{ROI} [10^{-4}cts/(keV · kg · y)]	SP_{SC} [10^{-6}]	b_{SC} [10^{-4}cts/(keV · kg · y)]	SP_{SS} [10^{-6}]	b_{SS} [10^{-4}cts/(keV · kg · y)]
^{232}Th chain						
^{208}Tl + ^{212}Po	6.8	2.2645 ± 0.2746	4.4	1.4652 ± 0.2208	2.2	0.7326 ± 0.1562
^{238}U chain						
^{214}Bi	2.3	0.6768 ± 0.1411	1.5	0.4414 ± 0.1140	0.2	0.0588 ± 0.0416
Sum:		2.94 ± 0.31		1.91 ± 0.25		0.79 ± 0.16

Table A.16.: Expected background index from the Iglidur of the junction-sled. The first column shows the isotope under consideration. The second column shows the background contribution, using events selected after the ROI cut. The background index in third and fourth column shown are calculated using Single-Crystal (SC) and Single-Segment (SS) events only. The junction-sled has a mass of 495 g made of 491 g copper and 4 g of Iglidur per string. The overall mass is 3.465 kg. The assumed contamination of the Iglidur is 22.6 mBq/kg for ^{238}U and 15.9 mBq/kg for ^{232}Th to ^{228}Ac and 25.6 mBq/kg from ^{228}Th on. The background is calculated for 33.94 kg enriched germanium in an energy window from 2.029 MeV to 2.049 MeV.

Isotope	SP_{ROI} $[10^{-6}]$	b_{ROI} $[10^{-4}\text{cts}/(\text{keV}\cdot\text{kg}\cdot\text{y})]$	SP_{SC} $[10^{-6}]$	b_{SC} $[10^{-4}\text{cts}/(\text{keV}\cdot\text{kg}\cdot\text{y})]$	SP_{SS} $[10^{-6}]$	b_{SS} $[10^{-4}\text{cts}/(\text{keV}\cdot\text{kg}\cdot\text{y})]$
^{60}Co	0.1	0.0013 ± 0.0013	-	-	-	-
^{232}Th chain						
^{208}Tl + ^{212}Po	9.3	0.3039 ± 0.0315	5.8	0.1889 ± 0.0249	2.7	0.0882 ± 0.0170
^{238}U chain						
^{214}Bi	2.1	0.0087 ± 0.0019	1.4	0.0058 ± 0.0016	0.8	0.0033 ± 0.0012
Sum:		0.31 ± 0.03		0.19 ± 0.02		0.09 ± 0.02

Table A.17.: Expected background index from the Murtfeldt of the junction-pins volume. The first column shows the isotope under consideration. The second column shows the background contribution, using events selected after the ROI cut. The background index in third and fourth column shown are calculated using Single-Crystal (SC) and Single-Segment (SS) events only. The junction-pins part has a mass of 213.41 g made of 142 g copper, 67 g of Murtfeldt and 4.41 g of Pogo-Pins per string. The overall mass is 1.494 kg. The assumed contamination of the Murtfeldt is 3.4 mBq/kg for ^{238}U to ^{230}Th and 0.019 mBq/kg from ^{226}Ra on. For ^{232}Th a contamination of 0.15 mBq/kg is used. The contamination of ^{60}Co was 0.061 mBq/kg.The background is calculated for 33.94 kg enriched germanium in an energy window from 2.029 MeV to 2.049 MeV.

Isotope	SP_{ROI} $[10^{-6}]$	b_{ROI} $[10^{-4}\text{cts}/(\text{keV} \cdot \text{kg} \cdot \text{y})]$	SP_{SC} $[10^{-6}]$	b_{SC} $[10^{-4}\text{cts}/(\text{keV} \cdot \text{kg} \cdot \text{y})]$	SP_{SS} $[10^{-6}]$	b_{SS} $[10^{-4}\text{cts}/(\text{keV} \cdot \text{kg} \cdot \text{y})]$
^{60}Co	0.1	0.0005 ± 0.0005	-	-	-	-
^{232}Th chain						
^{208}Tl + ^{212}Po	9.3	0.0816 ± 0.0085	5.8	0.0509 ± 0.0067	2.7	0.0237 ± 0.0046
^{238}U chain						
^{214}Bi	2.1	0.0155 ± 0.0034	1.4	0.0103 ± 0.0028	0.8	0.0059 ± 0.0021
Sum:		0.10 ± 0.01		0.06 ± 0.01		0.03 ± 0.01

Table A.18.: Expected background index from the copper of the junction-pins volume. The first column shows the isotope under consideration. The second column shows the background contribution, using events selected after the ROI cut. The background index in third and fourth column shown are calculated using Single-Crystal (SC) and Single-Segment (SS) events only. The Junction-Sled Pins part has a mass of 213.41 g made of 142 g copper, 67 g of Murtfeldt and 4.41 g of Pogo-Pins per string. The overall mass is 1.494 kg. The assumed contamination of the copper is 0.016 mBq/kg for ^{238}U, 0.019 mBq/kg for ^{232}Th and 0.01 mBq/kg for ^{60}Co. The background is calculated for 33.94 kg enriched germanium in an energy window from 2.029 MeV to 2.049 MeV.

Isotope	SP_{ROI} $[10^{-6}]$	b_{ROI} $[10^{-4}\text{cts}/(\text{keV}\cdot\text{kg}\cdot\text{y})]$	SP_{SC} $[10^{-6}]$	b_{SC} $[10^{-4}\text{cts}/(\text{keV}\cdot\text{kg}\cdot\text{y})]$	SP_{SS} $[10^{-6}]$	b_{SS} $[10^{-4}\text{cts}/(\text{keV}\cdot\text{kg}\cdot\text{y})]$
^{232}Th chain						
^{208}Tl + ^{212}Po	9.3	5.2018 ± 0.5394	5.8	3.2441 ± 0.4260	2.7	1.5102 ± 0.2906
^{238}U chain						
^{214}Bi	2.1	1.5977 ± 0.3540	1.4	1.0651 ± 0.2847	0.8	0.6087 ± 0.2152
Sum:		6.80 ± 0.65		4.31 ± 0.51		2.12 ± 0.36

Table A.19.: Expected background index from the "Pogo-Pins" of the junction-pins volume. The first column shows the isotope under consideration. The second column shows the background contribution, using events selected after the ROI cut. The background index in third and fourth column shown are calculated using Single-Crystal (SC) and Single-Segment (SS) events only. The Junction-Sled Pins part has a mass of 213.41 g made of 142 g copper, 67 g of Murtfeldt and 4.41 g of Pogo-Pins per string. The overall mass is 1.494 kg. The assumed contamination of the Pogo-Pins is 53 mBq/kg for ^{238}U to ^{210}Tl, ^{214}Po respectively. From ^{210}Pb on a contamination of 1400 mBq/kg is assumed. And 39 mBq/kg from ^{232}Th to ^{228}Ac and 19 mBq/kg from ^{228}Th on. The background is calculated for 33.94 kg enriched germanium in an energy window from 2.029 MeV to 2.049 MeV.

Isotope	SP_{ROI} $[10^{-6}]$	b_{ROI} $[10^{-4}\text{cts}/(\text{keV} \cdot \text{kg} \cdot \text{y})]$	SP_{SC} $[10^{-6}]$	b_{SC} $[10^{-4}\text{cts}/(\text{keV} \cdot \text{kg} \cdot \text{y})]$	SP_{SS} $[10^{-6}]$	b_{SS} $[10^{-4}\text{cts}/(\text{keV} \cdot \text{kg} \cdot \text{y})]$
^{232}Th chain						
^{208}Tl + ^{212}Po	6.0	0.3902 ± 0.0504	3.9	0.2537 ± 0.0406	1.7	0.1106 ± 0.0268
^{238}U chain						
^{214}Bi	1.6	0.2084 ± 0.0521	0.9	0.1172 ± 0.0391	0.2	0.0260 ± 0.0184
Sum:		0.60 ± 0.07		0.37 ± 0.06		0.13 ± 0.03

Table A.20.: Expected background index from the junction-spacer (copper screws) of the matrix. The first column shows the isotope under consideration. The second column shows the background contribution, using events selected after the ROI cut. The background index in third and fourth column shown are calculated using Single-Crystal (SC) and Single-Segment (SS) events only. The copper screws have a mass of 20.0 g per string. The overall mass is 0.14 kg. The assumed contamination of the copper screws is 2 mBq/kg for ^{238}U, 1 mBq/kg for ^{232}Th and 0.5 mBq/kg for ^{60}Co. The background is calculated for 33.94 kg enriched germanium in an energy window from 2.029 MeV to 2.049 MeV.

Isotope	SP_{ROI} $[10^{-6}]$	b_{ROI} $[10^{-4}\text{cts}/(\text{keV} \cdot \text{kg} \cdot \text{y})]$	SP_{SC} $[10^{-6}]$	b_{SC} $[10^{-4}\text{cts}/(\text{keV} \cdot \text{kg} \cdot \text{y})]$	SP_{SS} $[10^{-6}]$	b_{SS} $[10^{-4}\text{cts}/(\text{keV} \cdot \text{kg} \cdot \text{y})]$
^{232}Th chain						
^{208}Tl + ^{212}Po	5.6	0.1522 ± 0.0204	4.3	0.1169 ± 0.0178	1.4	0.0381 ± 0.0102
^{238}U chain						
^{214}Bi	1.4	0.0321 ± 0.0086	1.0	0.0229 ± 0.0072	0.2	0.0046 ± 0.0032
Sum:		0.19 ± 0.02		0.14 ± 0.02		0.04 ± 0.01

Table A.21.: Expected background index from the copper of the junction-cable volume. The first column shows the isotope under consideration. The second column shows the background contribution, using events selected after the ROI cut. The background index in third and fourth column shown are calculated using Single-Crystal (SC) and Single-Segment (SS) events only. The junction-cable volume has a mass of 474.0 g, consisting of 440 g of copper and 34 g of Teflon, per string. The overall mass is 3.318 kg. The assumed contamination of the copper is 0.016 mBq/kg for ^{238}U, 0.019 mBq/kg for ^{232}Th and 0.01 mBq/kg for ^{60}Co. The background is calculated for 33.94 kg enriched germanium in an energy window from 2.029 MeV to 2.049 MeV.

Isotope	SP_{ROI} $[10^{-6}]$	b_{ROI} $[10^{-4}\mathrm{cts}/(\mathrm{keV}\cdot\mathrm{kg}\cdot\mathrm{y})]$	SP_{SC} $[10^{-6}]$	b_{SC} $[10^{-4}\mathrm{cts}/(\mathrm{keV}\cdot\mathrm{kg}\cdot\mathrm{y})]$	SP_{SS} $[10^{-6}]$	b_{SS} $[10^{-4}\mathrm{cts}/(\mathrm{keV}\cdot\mathrm{kg}\cdot\mathrm{y})]$
^{232}Th chain						
^{208}Tl + ^{212}Po	5.6	0.0991 ± 0.0132	4.3	0.0761 ± 0.0116	1.4	0.0248 ± 0.0066
^{238}U chain						
^{214}Bi	1.4	0.0248 ± 0.0066	1.0	0.0177 ± 0.0056	0.2	0.0035 ± 0.0025
Sum:		0.12 ± 0.10		0.09 ± 0.01		0.03 ± 0.01

Table A.22.: Expected background index from the Teflon of the junction-cable volume. The first column shows the isotope under consideration. The second column shows the background contribution, using events selected after the ROI cut. The background index in third and fourth column shown are calculated using Single-Crystal (SC) and Single-Segment (SS) events only. The junction-cable volume has a mass of 474.0 g, consisting of 440 g of copper and 34 g of Teflon, per string. The overall mass is 3.318 kg. The assumed contamination of the Teflon is 0.16 mBq/kg for ^{238}U and 0.16 mBq/kg for ^{232}Th. The background is calculated for 33.94 kg enriched germanium in an energy window from 2.029 MeV to 2.049 MeV.

Isotope	SP_{ROI} $[10^{-6}]$	b_{ROI} $[10^{-4}\text{cts}/(\text{keV}\cdot\text{kg}\cdot\text{y})]$	SP_{SC} $[10^{-6}]$	b_{SC} $[10^{-4}\text{cts}/(\text{keV}\cdot\text{kg}\cdot\text{y})]$	SP_{SS} $[10^{-6}]$	b_{SS} $[10^{-4}\text{cts}/(\text{keV}\cdot\text{kg}\cdot\text{y})]$
^{232}Th chain						
$^{208}\text{Tl}+^{212}\text{Po}$	2	1.7065 ± 1.2067	1	0.8533 ± 0.8533	-	-
Sum:		1.71 ± 1.21		0.85 ± 0.85	-	-

Table A.23.: Expected background index from the stainless steel cable chain. The first column shows the isotope under consideration. The second column shows the background contribution, using events selected after the ROI cut. The background index in third and fourth column shown are calculated using Single-Crystal (SC) and Single-Segment (SS) events only. The cable chain has a mass of 1193 g, per string. The overall mass is 8.351 kg. The assumed contamination of the stainless steel is 72 mBq/kg from ^{238}U to $^{\text{Th230}}$ and 0.97mBq/kg from $^{\text{Ra226}}$ on. The assumed contamination is 2.9 mBq/kg from ^{232}Th to ^{228}Ac. From ^{228}Th on the contamination is assumed to be 2.2 mBq/kg. The background is calculated for 33.94 kg enriched germanium in an energy window from 2.029 MeV to 2.049 MeV.

Isotope	SP_{ROI} $[10^{-6}]$	b_{ROI} $[10^{-4}\text{cts}/(\text{keV} \cdot \text{kg} \cdot \text{y})]$	SP_{SC} $[10^{-6}]$	b_{SC} $[10^{-4}\text{cts}/(\text{keV} \cdot \text{kg} \cdot \text{y})]$	SP_{SS} $[10^{-6}]$	b_{SS} $[10^{-4}\text{cts}/(\text{keV} \cdot \text{kg} \cdot \text{y})]$
^{232}Th chain						
^{208}Tl	2	0.0016 ± 0.0011	2	0.0016 ± 0.0011	-	-
Sum:		0.01 ± 0.01		0.01 ± 0.01		-

Table A.24.: Expected background index from the woven ribbon Cables. The first column shows the isotope under consideration. The second column shows the background index, using events selected after the ROI cut. The background index in third and fourth column shown are calculated using Single-Crystal (SC) and Single-Segment (SS) events only. The ribbon cable has a mass of 126.99 g copper and 0.97 g Teflon. The overall mass is 0.896 kg. The assumed contamination of the copper is 0.016 mBq/kg for ^{238}U, 0.019 mBq/kg from ^{232}Th and 0.01mBq/kg for ^{60}Co. The assumed contamination of the Teflon is 0.16 mBq/kg for ^{238}U and ^{232}Th. The background is calculated for 33.94 kg enriched germanium in an energy window from 2.029 MeV to 2.049 MeV.

B. Graphs of all Simulated Pulses Compared to Data Pulses

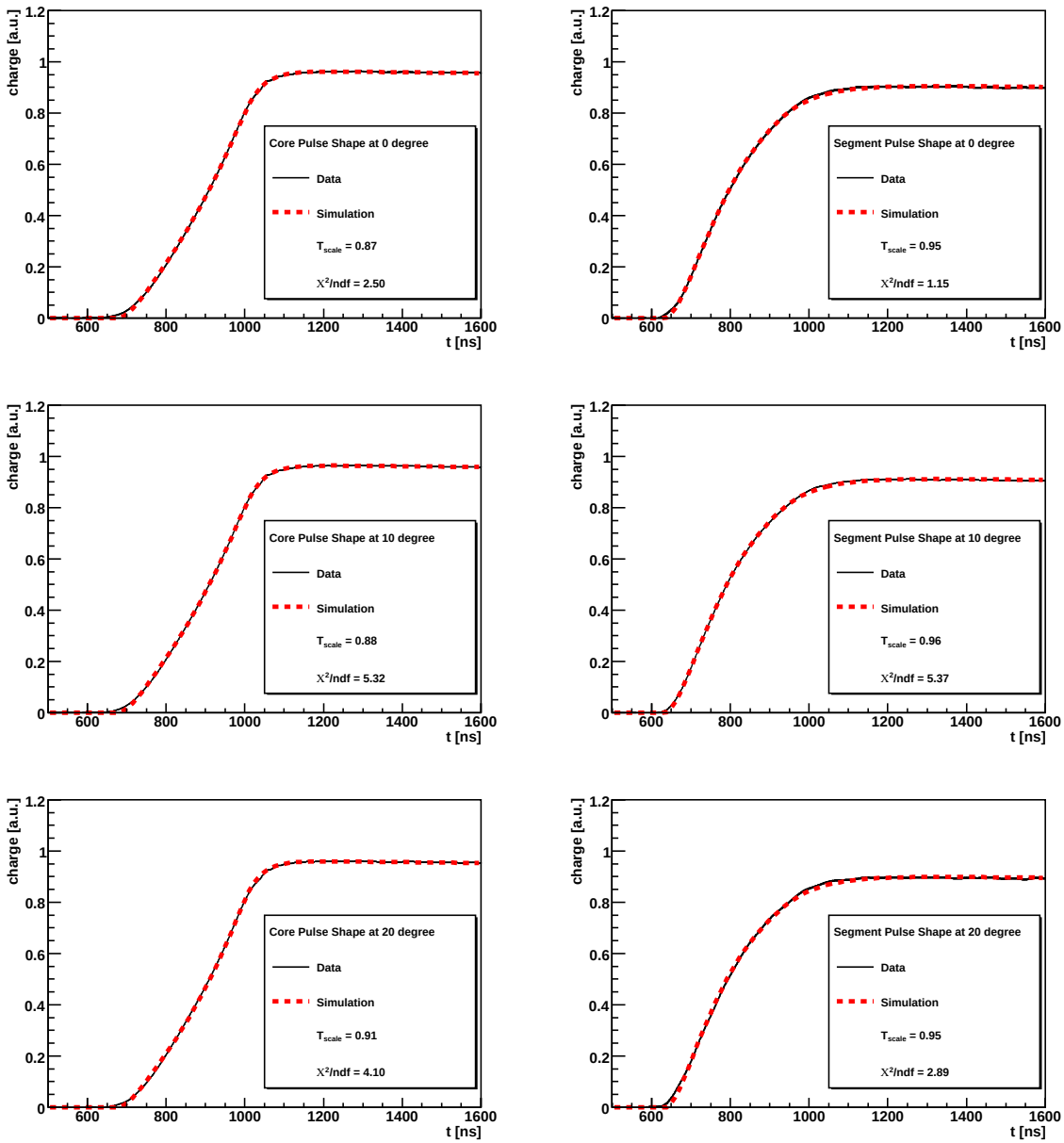

Figure B.1.: Comparison between the averaged data pulse shape (black solid line) from the 121.78 keV peak of ^{152}Eu and the averaged simulated pulse shape from photons with energy of 121.78 keV (red dashed line) left for the core electrode and right for the segment electrode from 0° (top) to 20° (bottom).

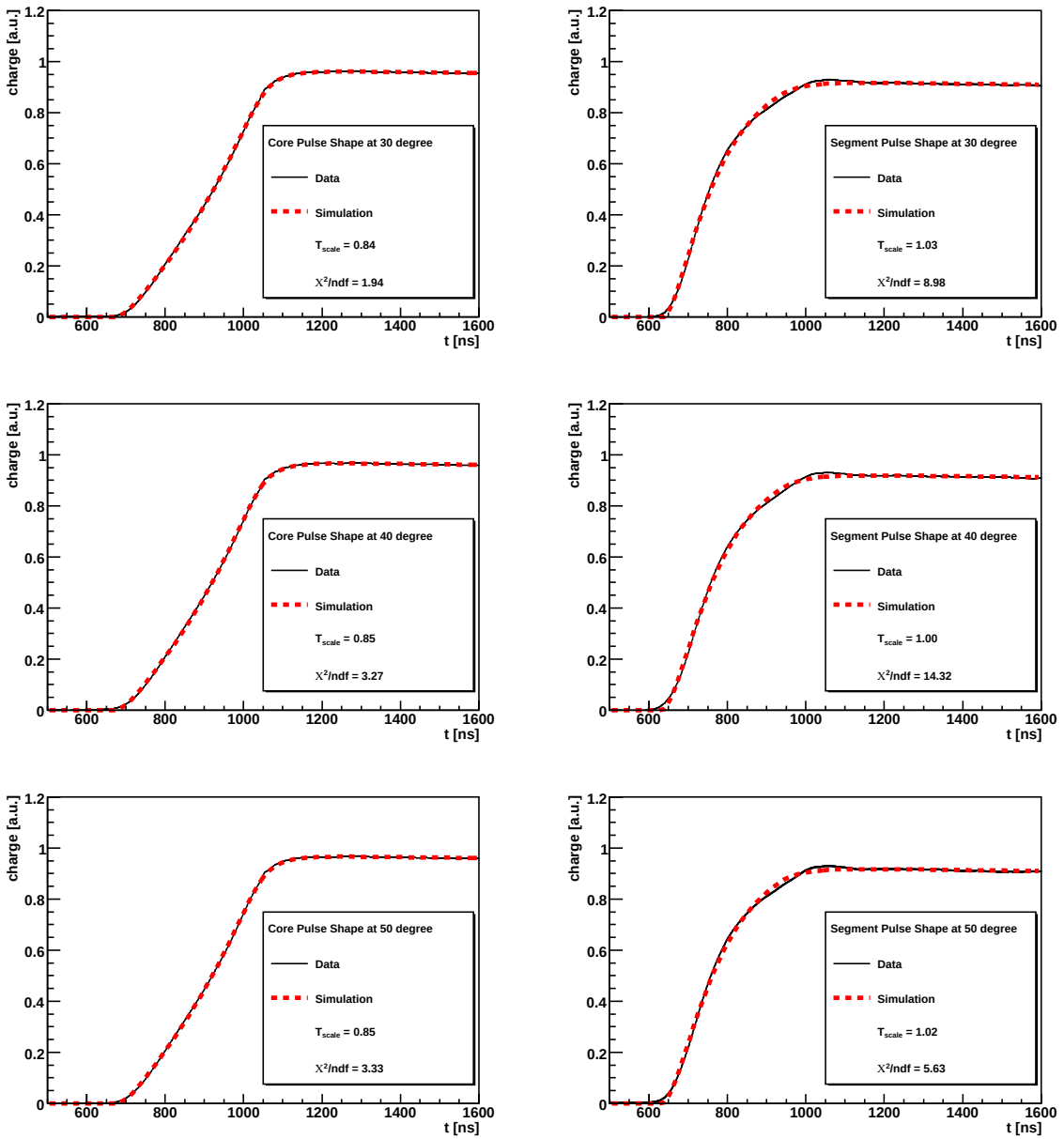

Figure B.2.: Comparison between the averaged data pulse shape (black solid line) from the 121.78 keV peak of ^{152}Eu and the averaged simulated pulse shape from photons with energy of 121.78 keV (red dashed line) left for the core electrode and right for the segment electrode from 30° (top) to 50° (bottom).

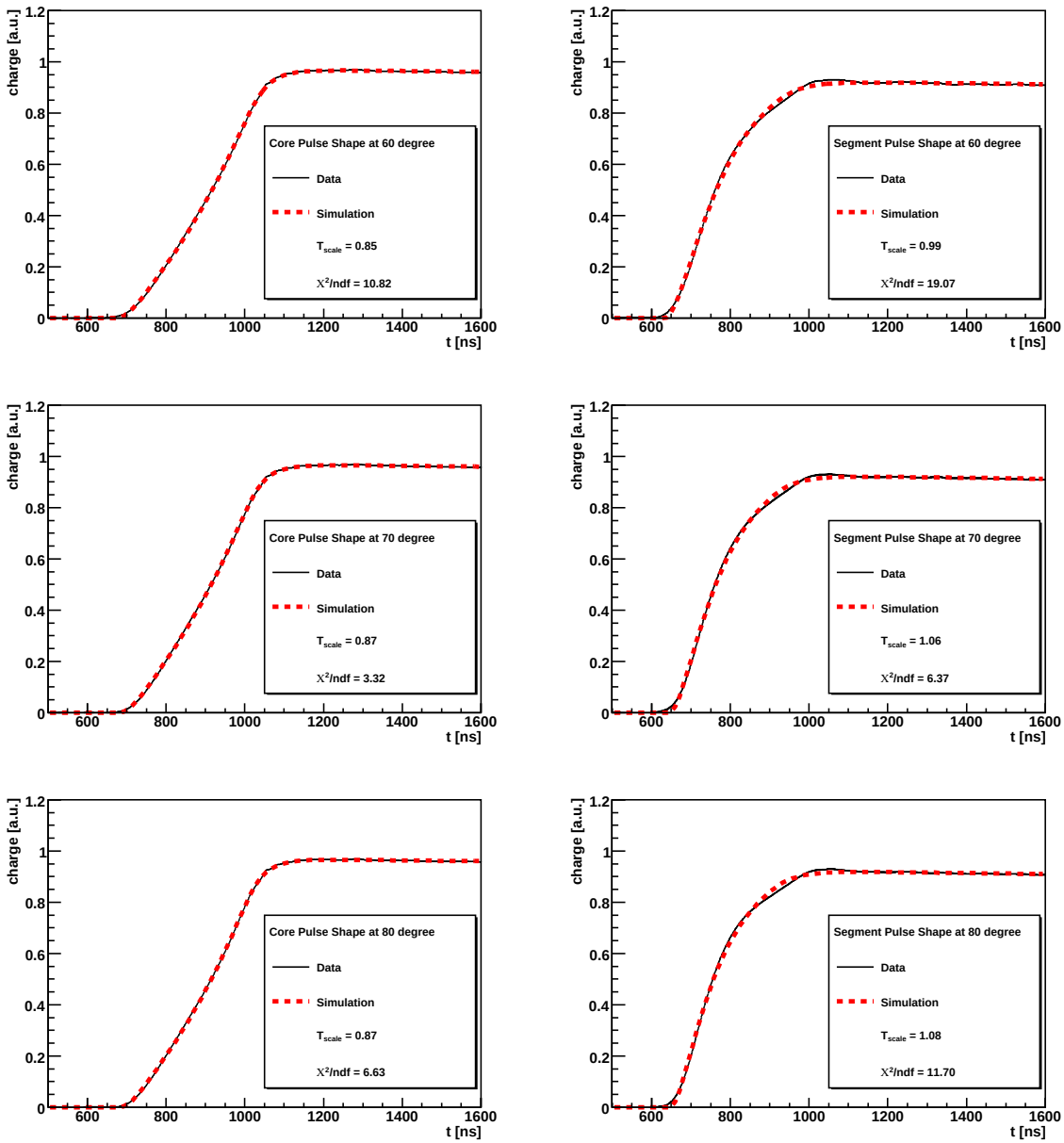

Figure B.3.: Comparison between the averaged data pulse shape (black solid line) from the 121.78 keV peak of ^{152}Eu and the averaged simulated pulse shape from photons with energy of 121.78 keV (red dashed line) left for the core electrode and right for the segment electrode from 60° (top) to 80° (bottom).

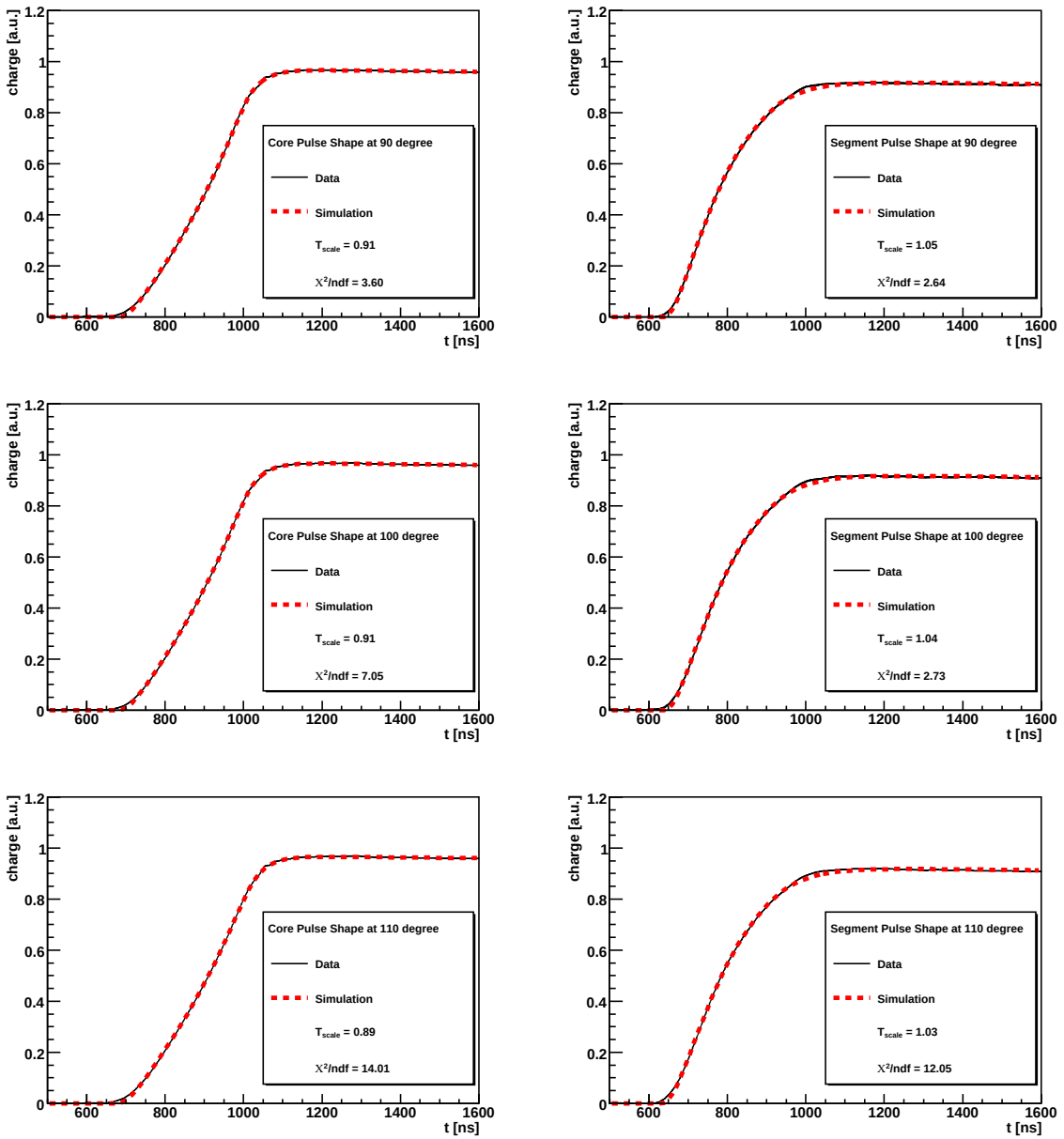

Figure B.4.: Comparison between the averaged data pulse shape (black solid line) from the 121.78 keV peak of ^{152}Eu and the averaged simulated pulse shape from photons with energy of 121.78 keV (red dashed line) left for the core electrode and right for the segment electrode from 90° (top) to 110° (bottom).

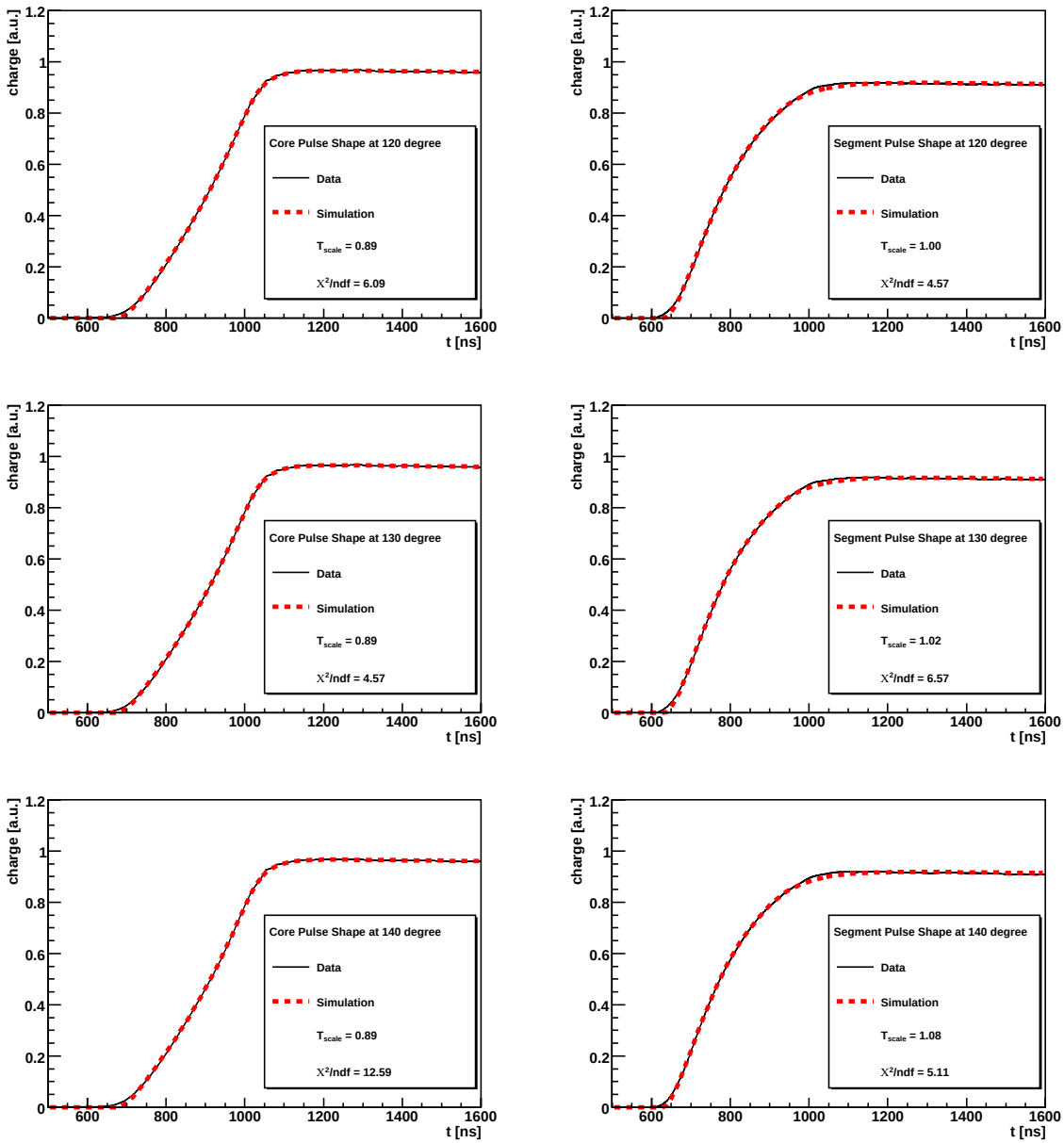

Figure B.5.: Comparison between the averaged data pulse shape (black solid line) from the 121.78 keV peak of ^{152}Eu and the averaged simulated pulse shape from photons with energy of 121.78 keV (red dashed line) left for the core electrode and right for the segment electrode from 120° (top) to 140° (bottom).

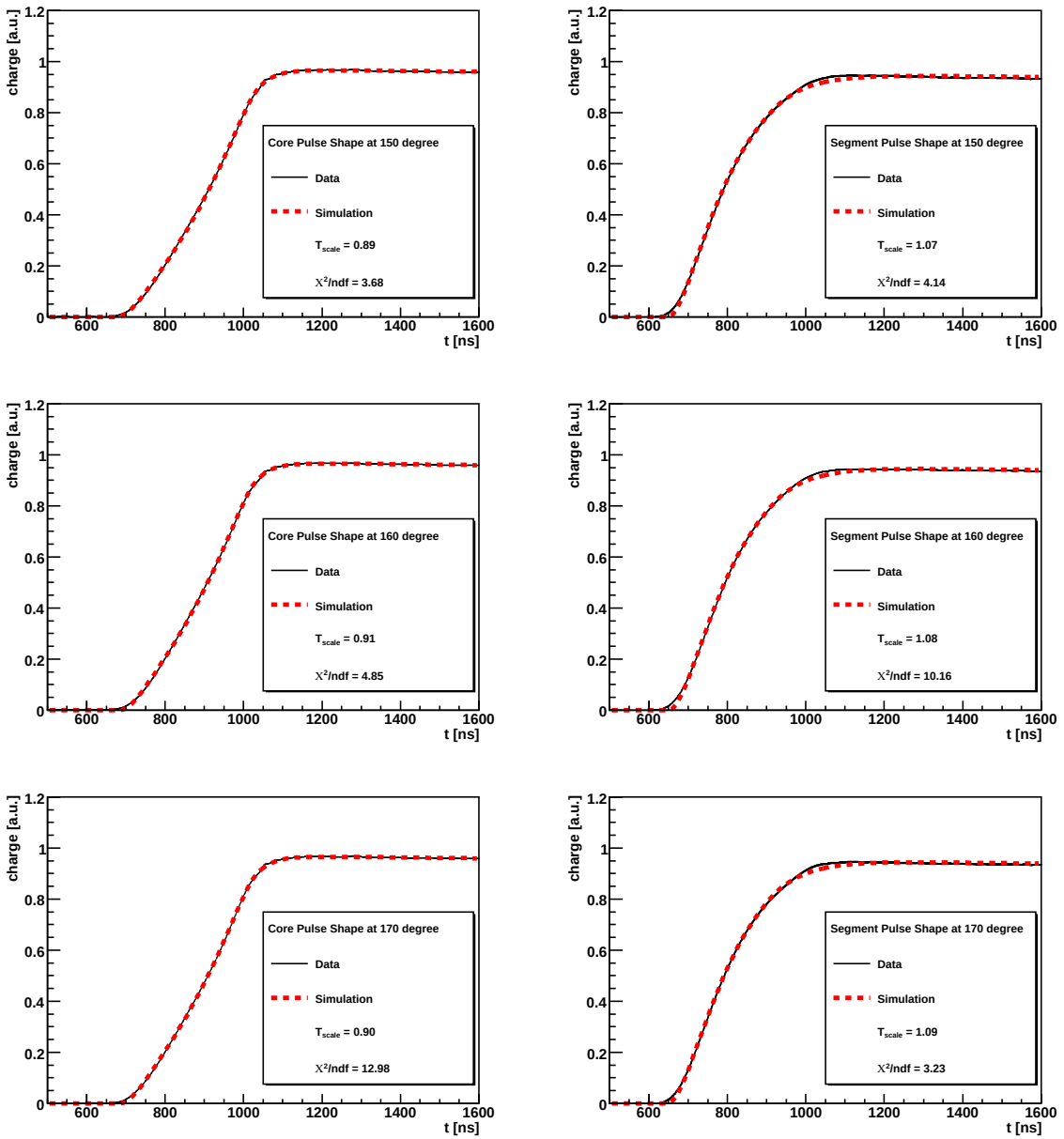

Figure B.6.: Comparison between the averaged data pulse shape (black solid line) from the 121.78 keV peak of ^{152}Eu and the averaged simulated pulse shape from photons with energy of 121.78 keV (red dashed line) left for the core electrode and right for the segment electrode from 150° (top) to 170° (bottom).

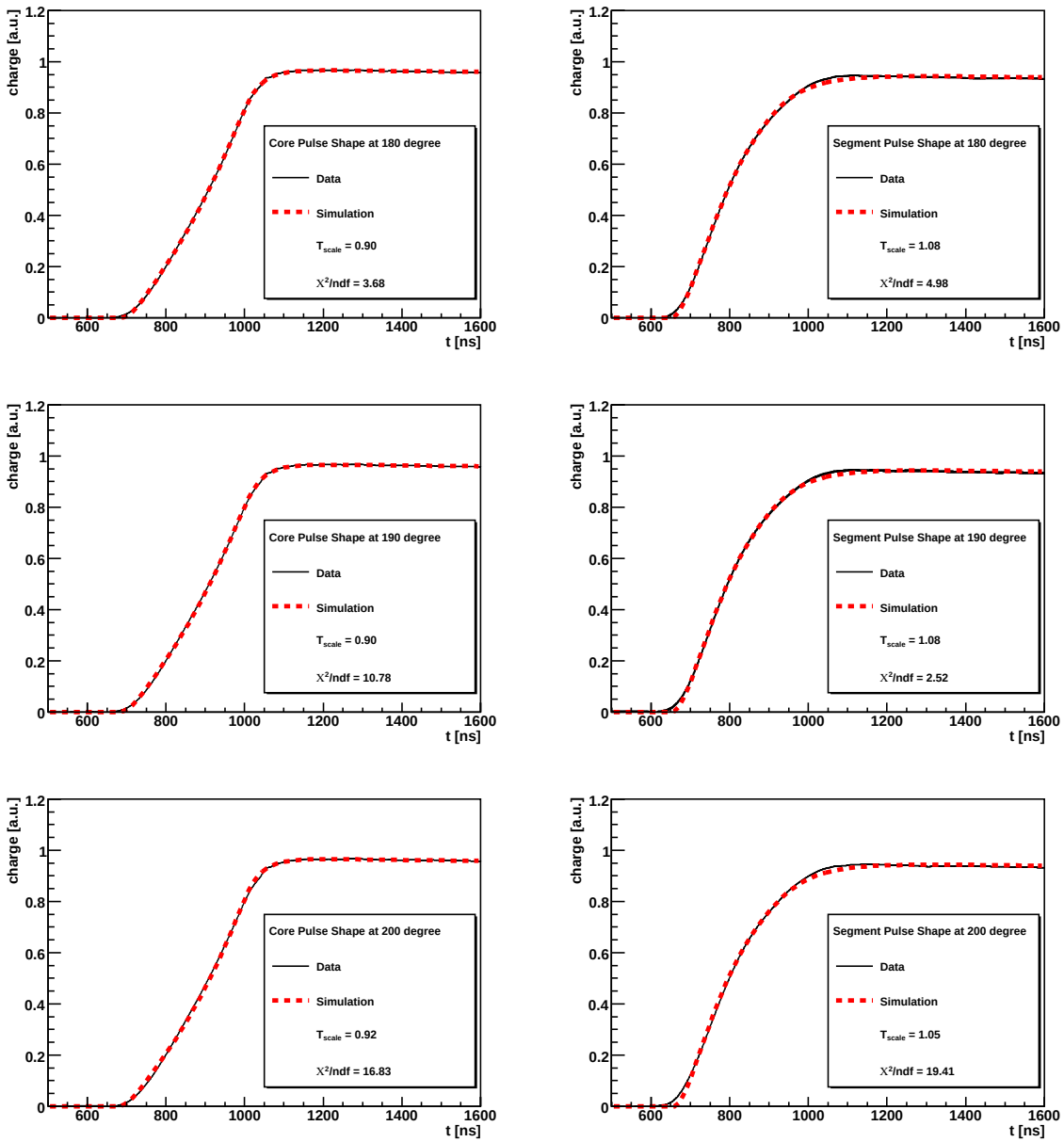

Figure B.7.: Comparison between the averaged data pulse shape (black solid line) from the 121.78 keV peak of ^{152}Eu and the averaged simulated pulse shape from photons with energy of 121.78 keV (red dashed line) left for the core electrode and right for the segment electrode from 180° (top) to 200° (bottom).

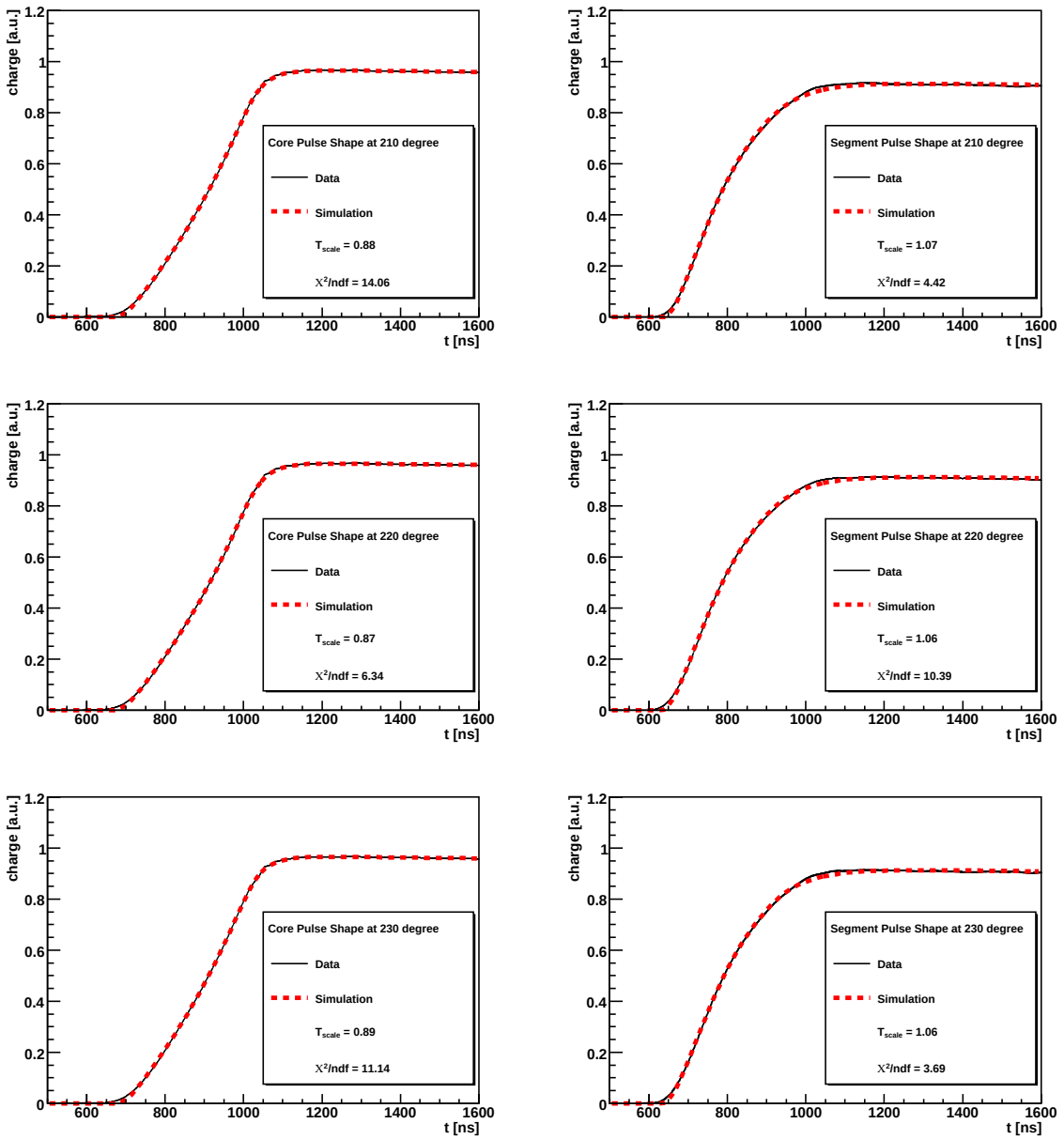

Figure B.8.: Comparison between the averaged data pulse shape (black solid line) from the 121.78 keV peak of ^{152}Eu and the averaged simulated pulse shape from photons with energy of 121.78 keV (red dashed line) left for the core electrode and right for the segment electrode from 210° (top) to 230° (bottom).

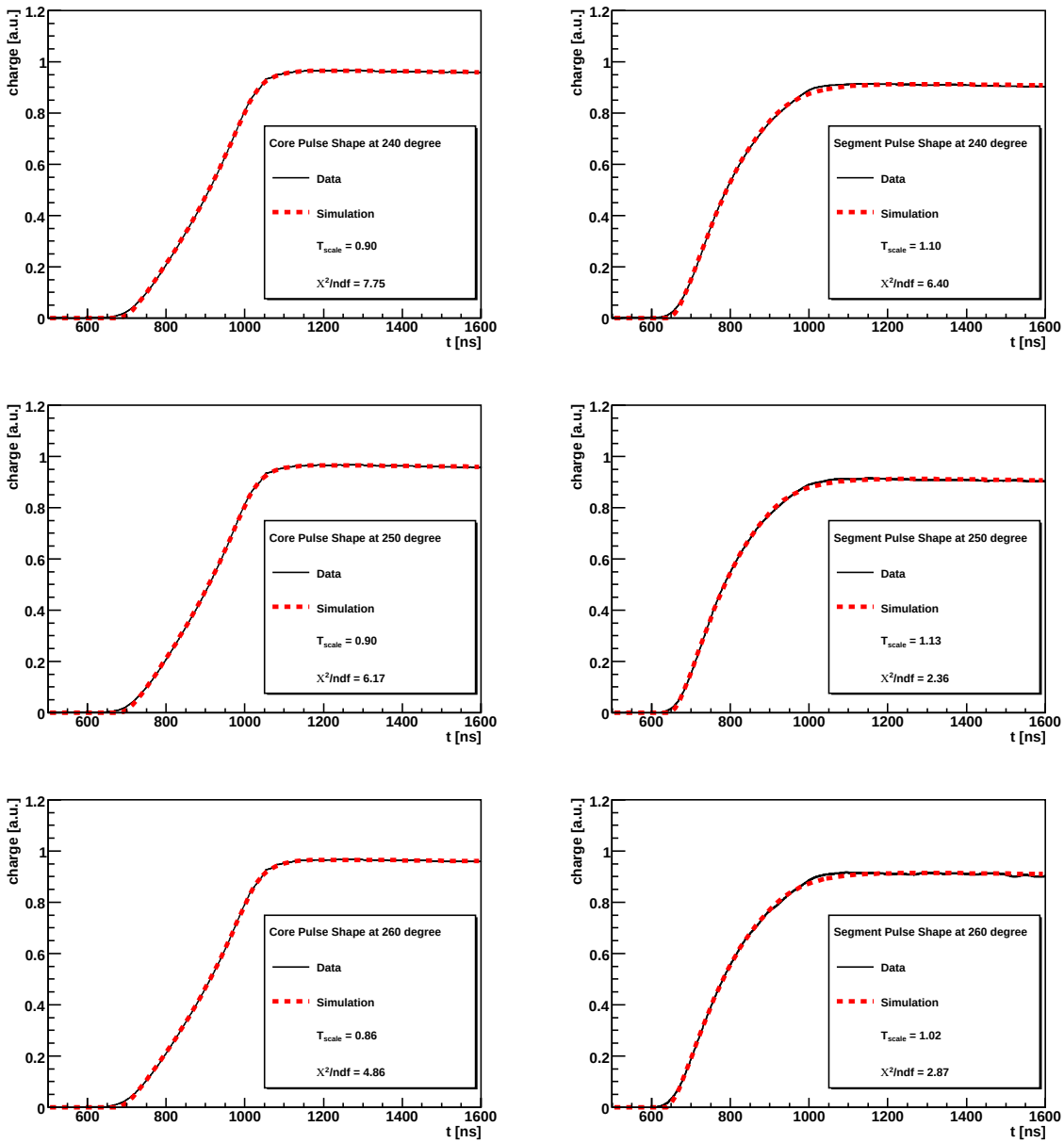

Figure B.9.: Comparison between the averaged data pulse shape (black solid line) from the 121.78 keV peak of ^{152}Eu and the averaged simulated pulse shape from photons with energy of 121.78 keV (red dashed line) left for the core electrode and right for the segment electrode from 240° (top) to 260° (bottom).

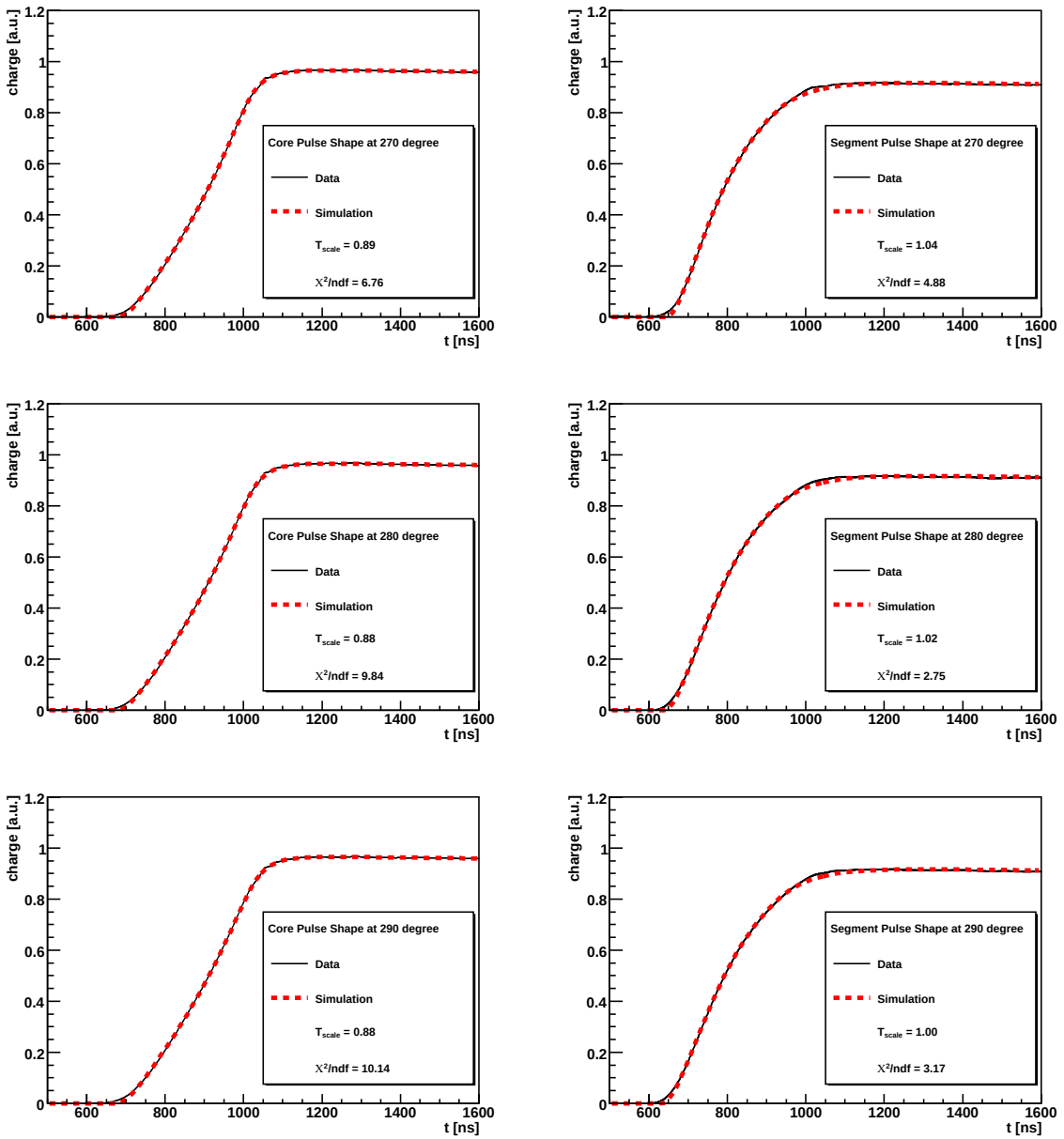

Figure B.10.: Comparison between the averaged data pulse shape (black solid line) from the 121.78 keV peak of ^{152}Eu and the averaged simulated pulse shape from photons with energy of 121.78 keV (red dashed line) left for the core electrode and right for the segment electrode from 270° (top) to 290° (bottom).

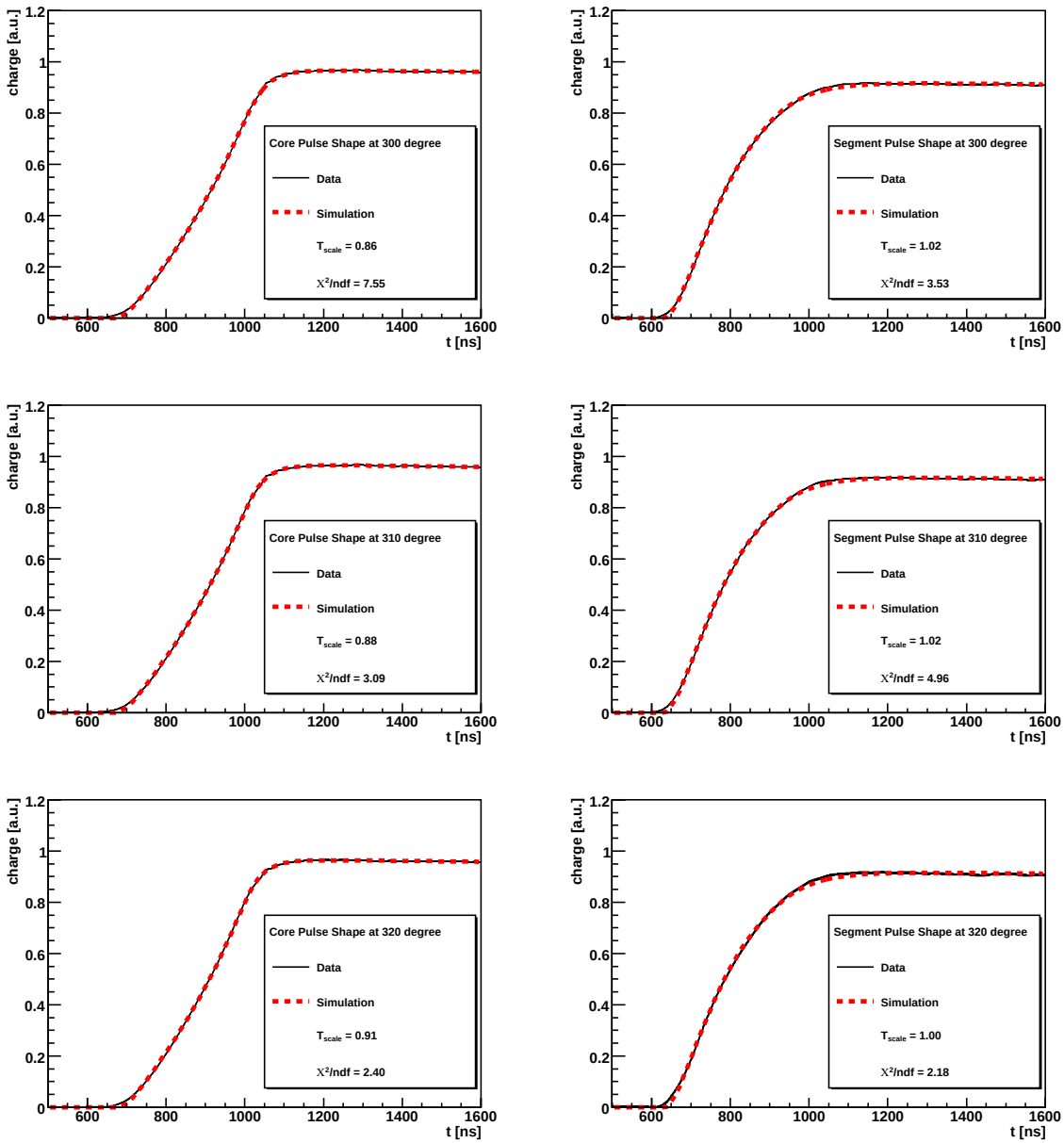

Figure B.11.: Comparison between the averaged data pulse shape (black solid line) from the 121.78 keV peak of ^{152}Eu and the averaged simulated pulse shape from photons with energy of 121.78 keV (red dashed line) left for the core electrode and right for the segment electrode from 300° (top) to 320° (bottom).

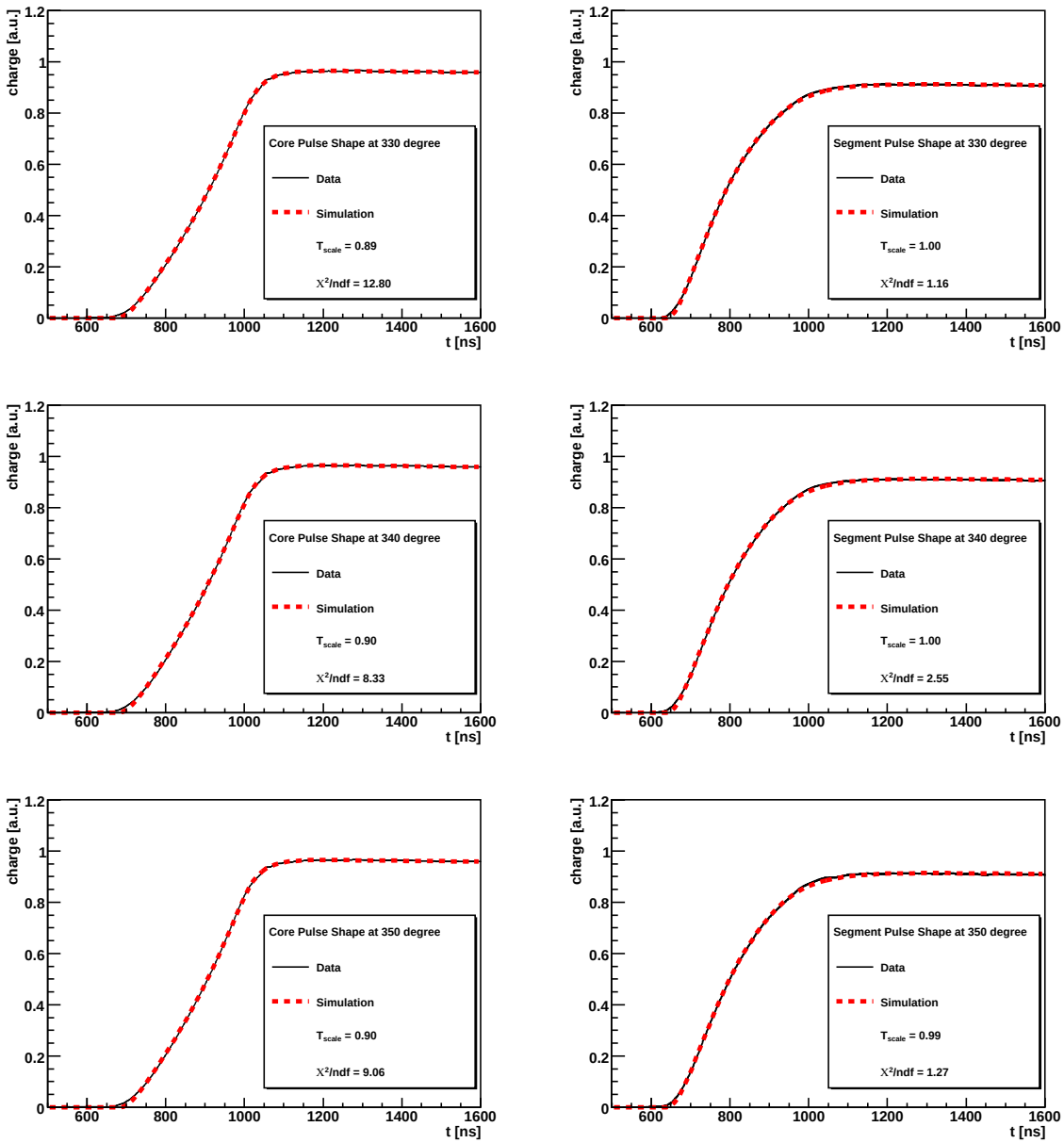

Figure B.12.: Comparison between the averaged data pulse shape (black solid line) from the 121.78 keV peak of ^{152}Eu and the averaged simulated pulse shape from photons with energy of 121.78 keV (red dashed line) left for the core electrode and right for the segment electrode from 330° (top) to 350° (bottom).

C. Bibliography

[1] W. H. Furry. *Phys. Rev.*, **54**(1) 56 1938.

[2] W. H. Furry. *Phys. Rev.*, **56**(12) 1184 1939.

[3] C. L. Cowan, Jr., *et al. Science*, **124** 103 1956.

[4] C. Kraus, *et al. Eur. Phys. J.*, **C40** 447 2005.

[5] V. M. Lobashev, *et al. Phys. Lett.*, **B460** 227 1999.

[6] H. V. Klapdor-Kleingrothaus, *et al.* Prepared for International Symposium on Weak and Electromagnetic Interactions in Nuclei (WEIN-89), Montreal, Quebec, Canada, 15-19 May 1989.

[7] F. T. Avignone, *et al.* In *Les Arcs 1988, Proceedings, 5th force, neutrino physics* 63-70. (see Conference Index).

[8] I. Abt, *et al.* [arxiv:hep-ex/0404039] 2004.

[9] S. L. Glashow. *Nucl. Phys.*, **22** 579 1961.

[10] S. Weinberg. *Phys. Rev. Lett.*, **19** 1264 1967.

[11] A. Salam. Originally printed in *Svartholm: Elementary Particle Theory, Proceedings Of The Nobel Symposium Held 1968 At Lerum, Sweden*, Stockholm 1968, 367-377.

[12] G. S. Abrams, *et al. Phys. Rev. Lett.*, **63**(20) 2173 1989.

[13] The ALEPH, DELPHI, L3, OPAL, SLD Collaborations, the LEP Electroweak Working Group, the SLD Electroweak and Heavy Flavour Groups. *Phys. Rept.*, **427** 257 2006.

[14] J. Bahcall, A. Serenelli, S. Basu. *Astrophys. J. Lett.*, **621**(1) L85 2005.

[15] R. Davis, D. S. Harmer, K. C. Hoffman. *Phys. Rev. Lett.*, **20**(21) 1205 1968.

[16] M. Cribier. *Nucl. Phys. Proc. Suppl.*, **70** 284 1999.

[17] M. Altmann, *et al. Phys. Lett.*, **B616** 174 2005.

[18] J. N. Abdurashitov, *et al. J. Exp. Theor. Phys.*, **95** 181 2002.

[19] J. N. Bahcall, M. H. Pinsonneault, G. J. Wasserburg. *Rev. Mod. Phys.*, **67**(4) 781 1995.

[20] K. S. Hirata, *et al. Phys. Rev. Lett.*, **63**(1) 16 1989.

[21] J. P. Cravens, *et al. Phys. Rev.*, **D78** 032002 2008.

[22] W. C. Haxton. *Annual Review of Astronomy and Astrophysics*, **33**(1) 459 1995.

[23] B. Aharmim, *et al. Phys. Rev.*, **C72**(5) 055502 2005.

[24] T. J. Haines, *et al. Phys. Rev. Lett.*, **57** 1986 1986.

[25] K. S. Hirata, *et al. Phys. Lett.*, **B205** 416 1988.

[26] Y. Fukuda, *et al. Phys. Lett.*, **B335** 237 1994.

[27] S. Hatakeyama, *et al. Phys. Rev. Lett.*, **81** 2016 1998.

[28] Y. Ashie, *et al. Phys. Rev. Lett.*, **93** 101801 2004.

[29] K. Eguchi, *et al. Phys. Rev. Lett.*, **90**(2) 021802 2003.

[30] S. Abe, *et al. Phys. Rev. Lett.*, **100** 221803 2008.

[31] M. Apollonio, *et al. Eur. Phys. J.*, **C27** 331 2003.

[32] P. Adamson, *et al. Phys. Rev. Lett.*, **101** 131802 2008.

[33] M. H. Ahn, *et al. Phys. Rev.*, **D74** 072003 2006.

[34] C. Athanassopoulos, *et al. Phys. Rev. Lett.*, **75** 2650 1995.

[35] B. Armbruster, *et al. Phys. Rev. D*, **65**(11) 112001 2002.

[36] A. Aguilar, *et al. Phys. Rev.*, **D64** 112007 2001.

[37] A. A. Aguilar-Arevalo, *et al. Phys. Rev. Lett.*, **98** 231801 2007.

[38] M. Aoki, K. Hagiwara, N. Okamura. *Phys. Lett.*, **B554** 121 2003.

[39] D. S. Ayres, *et al.* [arxiv:hep-ex/0503053] 2004.

[40] M. Guler, *et al.* CERN-SPSC-2000-028.

[41] T. Schwetz, M. Tortola, J. W. F. Valle. *New J. Phys.*, **10** 113011 2008.

[42] R. N. Mohapatra, *et al. Rept. Prog. Phys.*, **70** 1757 2007.

[43] S. M. Bilenky, C. Giunti, W. Grimus. *Prog. Part. Nucl. Phys.*, **43** 1 1999.

[44] C. Giunti, M. Laveder. [arxiv:hep-ph/0310238] 2003.

[45] A. Strumia, F. Vissani. *Nucl. Phys.*, **B726** 294 2005.

[46] C. Weinheimer, *et al. Phys. Lett.*, **B460** 219 1999.

[47] A. Osipowicz, *et al.* [arxiv:hep-ex/0109033] 2001.

[48] K. Assamagan, *et al. Phys. Rev.*, **D53** 6065 1996.

[49] R. M. Carey, *et al.* http://www.hep.umn.edu/numass/ [2009, March 09]. http://www.hep.umn.edu/numass/ [2009, March 09].

[50] R. Barate, *et al. Eur. Phys. J.*, **C2** 395 1998.

[51] L. P. Ekström, R. B. Firestone. WWW table of radioactive isotopes. http://ie.lbl.gov/toi/index.htm. Database version 02/28/99.

[52] J. Schechter, J. W. F. Valle. *Phys. Rev.*, **D25** 2951 1982.

[53] O. Panella, C. Carimalo, Y. N. Srivastava. *Phys. Rev.*, **D62** 015013 2000.

[54] M. Hirsch, H. V. Klapdor-Kleingrothaus, O. Panella. *Phys. Lett.*, **B374** 7 1996.

[55] M. Hirsch, H. V. Klapdor-Kleingrothaus, S. G. Kovalenko. *Phys. Lett.*, **B372** 181 1996.

[56] M. Hirsch, H. V. Klapdor-Kleingrothaus, S. G. Kovalenko. *Phys. Rev.*, **D54** 4207 1996.

[57] A. Ali, A. V. Borisov, D. V. Zhuridov. [arxiv:hep-ph/0606072] 2006.

[58] A. Smolnikov, P. Grabmayr. *Phys. Rev. C*, **81**(2) 028502 2010.

[59] E. Caurier, F. Nowacki, A. Poves. *Eur. Phys. J.*, **A36** 195 2008.

[60] F. Simkovic, *et al. Phys. Rev.*, **C77** 045503 2008.

[61] F. T. Avignone, III, S. R. Elliott, J. Engel. *Rev. Mod. Phys.*, **80** 481 2008.

[62] S. R. Elliott, P. Vogel. *Ann. Rev. Nucl. Part. Sci.*, **52** 115 2002.

[63] J. R. Wilson. *J. Phys. Conf. Ser.*, **120** 052048 2008.

[64] T. Bloxham, *et al. Phys. Rev.*, **C76** 025501 2007.

[65] R. Ardito, *et al.* [arxiv:hep-ex/0501010] 2005.

[66] C. Arnaboldi, *et al. Phys. Rev. Lett.*, **95** 142501 2005.

[67] M. Danilov, *et al. Phys. Lett.*, **B480** 12 2000.

[68] D. Dassie, *et al. Nucl. Instr. Meth. Phys. Res.*, **A309** 465 1991.

[69] C. J. M. Longuemare. *Part. Nucl. Lett.*, **106** 62 2001.

[70] L. Vala. [arxiv:hep-ex/0901.0473] 2009.

[71] C. E. Aalseth, *et al. Phys. Rev.*, **D65** 092007 2002.

[72] H. V. Klapdor-Kleingrothaus, *et al. Eur. Phys. J.*, **A12** 147 2001.

[73] H. V. Klapdor-Kleingrothaus, *et al. Mod. Phys. Lett.*, **A16** 2409 2001.

[74] H. V. Klapdor-Kleingrothaus, *et al. Physics Letters B*, **586**(3-4) 198 2004.

[75] C. E. Aalseth, *et al. Mod. Phys. Lett.*, **A17** 1475 2002.

[76] H. L. Harney. [arxiv:hep-ph/0205293] 2001.

[77] H. V. Klapdor-Kleingrothaus. [arxiv:hep-ph/0205288] 2002.

[78] A. M. Bakalyarov, *et al. Phys. Part. Nucl. Lett.*, **2** 77 2005.

[79] D. M. Mei, *et al. Phys. Rev.*, **C77** 054614 2008.

[80] O. Chkvorets. [arxiv:nucl-ex/0812.1206] 2008.

[81] A. Caldwell, K. Kröninger. *Phys. Rev.*, **D74** 092003 2006.

[82] G. Heusser. *Ann. Rev. Nucl. Part. Sci.*, **45** 543 1995.

[83] C. Arpesella. *Nuclear Physics B - Proceedings Supplements*, **28**(1) 420 1992.

[84] L. Pandola, *et al. Nucl. Instr. Meth. Phys. Res.*, **A570**(1) 149 2007.

[85] C. Grupen, B. Shwartz. *Particle Detectors, 2nd edition*. Cambridge University Press 1996.

[86] M. J. Berger, *et al.* XCOM: Photon Cross Section Database (version 1.4). http://physics.nist.gov/xcom [2009, September 21] 2009. National Institute of Standards and Technology, Gaithersburg, MD.

[87] G. Knoll. *Radiation detection and measurements*. John Wiley and Sons, Inc., New York 2000.

[88] I. Abt, *et al. Nucl. Instr. Meth. Phys. Res.*, **A570** 479 2007.

[89] M. Tyagi. *Introduction to Semiconductor Materials and Devices*. John Wiley & Sons, Inc. 1991.

[90] R. A. Kroeger, *et al. Nucl. Instr. Meth. Phys. Res.*, **A422**(1-3) 206 1999.

[91] W. Shockley. *Jour. of Appl. Physics*, **9** 635 1938.

[92] S. Ramo. *Proc. of the I. R. E.*, **27** 584 1939.

[93] R. Dinger. *IEEE Transaction on Nuclear Science*, **22** 135 1975.

[94] E. Hull, *et al. Nucl. Instr. Meth. Phys. Res.*, **A364** 488 1995.

[95] E. Baldinger, E. Haller. *Helv. Phys. Acta.*, **43** 833 1970.

[96] Y.-D. Chan, *et al.* [arxiv:nucl-ex/0802.0860] 2008.

[97] S. Agostinelli, *et al. Nucl. Instr. Meth. Phys. Res.*, **A506**(3) 250 2003.

[98] J. Allison, *et al. IEEE Trans. Nucl. Sci.*, **53** 270 2006.

[99] I. Abt, *et al. Eur. Phys. J.*, **C52** 19 2007.

[100] E. L. Brady, M. Deutsch. *Phys.Rev.*, **78** 558 1950.

[101] R. M. Kloepper, E. S. Lennox, M. L. Wiedenbeck. *Phys. Rev.*, **88**(4) 695 1952.

[102] O. A. Ponkratenko, V. I. Tretyak, Y. G. Zdesenko. *Phys. Atom. Nucl.*, **63** 1282 2000.

[103] I. Abt, *et al. Nucl. Instr. Meth. Phys. Res.*, **A577** 574 2007.

[104] D. Gutknecht. *Nucl. Instr. Meth. Phys. Res.*, **A288**(1) 13 1990.

[105] L. Mihailescu, *et al. Nucl. Instr. Meth. Phys. Res.*, **A447**(3) 350 2000.

[106] L. Reggiani, *et al. Phys. Rev. B*, **16**(6) 2781 1977.

[107] B. Bruyneel, P. Reiter, G. Pascovici. *Nucl. Instr. Meth. Phys. Res.*, **A569**(3) 764 2006.

[108] J. Liu. *Development of Segmented Germanium Detectors for Neutrinoless Double Beta Decay Experiments*. Ph.D. thesis, Technische Universität München, Germany 2009.

[109] XIA. X-Ray Instrumentation Associates, http://www.xia.com.

[110] I. Abt, *et al. Nucl. Instr. Meth. Phys. Res.*, **A583** 332 2007.

[111] B. Bruyneel, *et al. Nucl. Instr. Meth. Phys. Res.*, **A608**(1) 99 2009.

[112] C. T. Chantler, *et al.* X-Ray Form Factor, Attenuation and Scattering Tables(version 2.1). [Online] available: http://physics.nist.gov/ffast [2009, March 21] 2009. National Institute of Standards and Technology, Gaithersburg, MD., Originally published as C.T. Chantler *et al.* J Phys. Chem. Ref. Data, **29**(4),597-1048. 2000 and C.T. Chantler *et al.* J Phys. Chem. Ref. Data, **24**(4),71-643. 1995.

Acknowledgments

Many people contributed in some way to this thesis. I would like to use the opportunity and thank them.

First, I would like to thank my supervisor Prof. Allen Caldwell for the possibility to write this thesis in his group. I would like to thank Dr. Iris Abt for all the support and her patience with me and this document. Also, I would thank Dr. Bela Majorovits for support and discussions. I am grateful to Xiang Liu, who was always very helpful and up for discussions in any aspect of analysis, lab-work, soccer, squash or beer drinking. Thanks Xiang. I thank Jing Liu, for the good teamwork on the pulse shape simulation and for the many discussions. I also would like to thank Kevin Kröninger who helped me a lot in the beginning.

I would also like to thank the Monte Carlo work groups of both, the GERDA and the Majorana experiment. Especially, I would like to thank Luciano, Reyco, Jason and Mike.

In general, I would like to thank the GeDet, GERDA and FCD groups for the good spirit at work and afterwards. Also, I want to say thanks to the “neutrino theory people” from upstairs for explanation and discussion, especially Martin Spinrath and Florian Hahn-Wörnle. Thanks to the “MPI soccer team” for the continuous fun on Thursdays and the distraction from physics.

Finally, I take the opportunity to thank Maike for everything.